THE UNIVERSITY *of* EDINBURGH

The evolution of bright star-forming galaxies in the first billion years

Rebecca Alison Andrews Bowler

Doctor of Philosophy
The University of Edinburgh
November 2014

Abstract

In this thesis, I present the results of a new search for, and study of, luminous galaxies in the first billion years of cosmic time. This work is primarily based on a new selection of bright ($L \gg L^*$) Lyman-break galaxies (LBGs) at $z \simeq 6$ and $z \simeq 7$ in the UltraVISTA first and second data releases (DR1, DR2) and the UKIDSS (UKIRT Infrared Deep Survey) UDS DR10 (Ultra Deep Survey). The UltraVISTA survey provides deep Y, J, H and K_s near-imaging over $1.5\,\mathrm{deg}^2$ of the Cosmic Evolution Survey (COSMOS) field and the UKIDSS UDS provides J, H and K band data overlapping with the Subaru *XMM-Newton* Deep Survey (SXDS), with both fields also containing deep optical and mid-infrared imaging essential for the clean detection of $z > 5$ galaxies. The fields combined provide an unprecedented $1.65\,\mathrm{deg}^2$ of deep multiwavelength data with which to securely select LBGs using a photometric redshift fitting technique, which can additionally remove probable low-redshift galaxy interlopers and galactic dwarf stars that can contaminate ground-based samples.

At $z \simeq 7$, the DR1 of the UltraVISTA survey was used to select a sample of ten high-redshift galaxy candidates, which extended to a 5σ limiting magnitude of $Y + J \sim 25$ (AB magnitude, 2-arcsec diameter circular aperture) over $1\,\mathrm{deg}^2$. A stack of the four most robust objects from the sample indicated that they were massive ($M_* \simeq 5 \times 10^9\,\mathrm{M}_\odot$), had blue rest-frame UV slopes ($\beta \simeq -2.0 \pm 0.2$) and were highly star-forming (SFR $\simeq$ 25–50 $\mathrm{M}_\odot\,\mathrm{yr}^{-1}$) when compared to previous, fainter, samples of galaxies at $z = 7$.

The number counts of $z \simeq 7$ galaxies selected within the UltraVISTA DR1 survey was higher than that expected from extrapolations of the rest-frame UltraViolet (UV) luminosity function (LF) from fainter data, a result that was strongly confirmed with an improved search for $z \simeq 7$ galaxies using the UltraVISTA DR2 imaging and the UDS field. A total of 34 galaxies at $6.5 < z < 7.5$ were found in the combined fields, which included the previously identified robust galaxies from the DR1 imaging. This expanded sample allowed the first determination of the rest-frame UV LF in the range $-23.0 < M_{\mathrm{UV}} < -21.5$ at $z \simeq 7$, and the results reveal a power-law decline

to bright magnitudes in contrast to the commonly assumed exponentially declining Schechter function extrapolated from fainter data. The excess of galaxies observed at bright magnitudes cannot be accounted for by gravitational lensing or by significant contamination of the sample by Active Galactic Nuclei (AGN) . The observed LF is well described by a double power law, which at the bright end follows the form of the underlying dark matter halo mass function, suggesting that the physical mechanism that inhibits star formation activity in massive galaxies (e.g. AGN feedback or some other form of 'mass quenching') has yet become efficient at $z \simeq 7$.

The deeper imaging data confirm that the $z \simeq 7$ LBGs show blue rest-frame UV slopes (median $\beta = -2.0$) and are massive (up to $M_* \simeq 10^{10}\,\mathrm{M}_\odot$). Furthermore, an analysis of the ground-based imaging shows that the majority are resolved consistent with larger sizes ($r_{1/2} \simeq 1$–$1.5\,\mathrm{kpc}$) than displayed by less massive galaxies.

Finally, a new search for $z \simeq 6$ galaxies within the UltraVISTA and UDS datasets was undertaken, resulting in a sample of 266 LBGs ($-22.7 < M_{\mathrm{UV}} < -20.5$) galaxies with which to investigate the rest-frame UV LF. The potential contamination by galactic brown dwarfs was investigated quantitatively using a simple model of the Galaxy, showing that the expected contamination rate of the sample was < 3 per cent, and that the stars can be effectively removed by fitting standard stellar spectra to the observed photometry. The galaxy surface density in the UltraVISTA/COSMOS field exceeds that in the UDS/SXDS by a factor of $\simeq 1.4$, indicating strong cosmic variance between the two fields. The number counts of galaxies we find are a factor of 2 lower than predicted by the recent LF determination by Bouwens et al., and the derived rest-frame UV LF at $z \simeq 6$ revealed that an under dense UDS field can account for some of the observed differences between previous analyses. An evolution in the characteristic magnitude between $z \simeq 5$ and $z \simeq 7$ of $\Delta M^* \sim 0.5$ was found in contrast to other smaller area surveys, and a double power law was shown to equally well describe the LF at $z = 6$ as compared to the commonly assumed Schechter function. The bright-end of the LF at $z \simeq 6$ tentatively shows a steeper decline than found at $z \simeq 7$, which could indicate the onset of mass quenching of the most massive galaxies or the rise of dust obscuration. Comparison with the predictions of the latest theoretical models and simulations of galaxies reveals that most models require substantial ($A_{1500} \sim 1.5$–2) average dust extinction at the bright end to reproduce the shape of the galaxy UV LF at $z \simeq 7$.

Lay Summary

The current picture of the Universe, deduced from a huge range of observations and theoretical calculations, is that it began 13.8 billion years ago in the 'Big Bang'. Since then, the Universe has changed dramatically with what was an almost completely smooth soup of extremely hot particles, becoming a dark, cold and largely empty place with islands of stars and their puny orbiting planets. The stars themselves are seen to reside in galaxies, collections of tens of billions of stars, that come in a wide range of shapes, sizes and colours. Millions of galaxies have now been observed with telescopes both on the ground (usually in exotic places like Hawaii or the Canary Islands) and in space (such as the famous Hubble Space Telescope), which essentially produce digital photos of different parts of the sky using different coloured filters (e.g. red, blue, green, infrared...). These images have revealed a huge diversity of galaxies, and even more amazingly, because it takes light so long to travel from distant galaxies to our telescopes, they show us galaxies *as they were* millions and even billions of years ago.

Being able to observe galaxies *as they were* in the past, means that a single image of a patch of sky is like a time capsule, showing galaxies at different epochs in the history of the Universe and hence revealing how they have grown and changed over time. The most distant galaxies that have been discovered so far emitted the light that we collect today only 500 million years after the Big Bang. These galaxies are among the first galaxies to form after everything cooled down a few million years after the Big Bang, and they are very different to our own, the beautiful spiral galaxy the Milky Way.

The aim of my PhD has been to find new distant galaxies using new exceptional imaging from the VISTA telescope in Chile, to try and understand how and when these first galaxies were formed. In particular I was searching for unusually bright galaxies, much brighter than those previously detected with the Hubble Space Telescope. In total we found around 300 galaxies, observed as they appeared between 700 million to 1 billion years after the Big Bang, which was many more than expected from previous observations of fainter galaxies at the same epoch. Measurements of the sizes and colours of the galaxies showed that some of them were also much bigger than expected,

which could be because they are, in fact, a handful of smaller galaxies merging, and they were also found to be very blue as expected for young galaxies that are forming stars rapidly. By comparing the number (or number density to be precise) of bright galaxies at the beginning and end of the 300 million years that the galaxies span, we found that the star formation is progressively being stifled in the brightest objects, either because the fuel to create new stars has been flung out of the galaxy or perhaps the stars are being formed but are hidden behind a shroud of dust. Exactly what is happening in these very distant objects is still an exciting puzzle, which is likely to be solved by combining future observations with large scale computer simulations of the formation of early galaxies.

Declaration

I declare that this thesis was composed by myself, that the work contained herein is my own except where explicitly stated otherwise in the text, and that this work has not been submitted for any other degree or professional qualification except as specified.

Parts of this work have been published in Bowler et al. (2012), Bowler et al. (2014) and Bowler et al. (2015).

(*Rebecca Alison Andrews Bowler, November 2014*)

Acknowledgements

Firstly I must thank my supervisors Jim Dunlop and Ross McLure for their invaluable guidance and support throughout my PhD. Secondly, I thank Paul Hewett for agreeing to take me on as a summer student back in 2008, and for his constant encouragement since then. Thirdly, I thank Phil Best for taking the time to give me a tour of the Royal Observatory when I was applying for Universities aged 17. The sight of the Observatory perched on Blackford Hill, the skyline of Edinburgh and the highlands beyond stuck firmly in my mind and I am very lucky to have had the opportunity to live in such a fantastic place.

I thank the many past and current members of the Institute for Astronomy who have become great friends as well as helping with anything astronomy or computing related, there are too many of you to name individually. Finally I thank my family: my mum, dad, Fran, Ella and Ben, and my grandparents, for constant encouragement and interest since I started my education over 22 years ago!

Contents

List of Figures

List of Tables

CHAPTER 1

Introduction

A complete picture of the formation and evolution of galaxies must necessarily include an understanding of when, where and how the first galaxies appeared and subsequently transformed into the galaxies that surround us today. My PhD focuses on one particular epoch in the history of the Universe, roughly 500 million to one billion years after the Big Bang. It is during this period that the exotic first galaxies were starting to mature, and effects that we know can strongly affect a galaxy today, such as the copious energy released from the central supermassive black hole, were starting to come into effect. Before I discuss the recent observational progress made in looking for these exciting galaxies, I start with a more general introduction covering essential cosmology and the physical processes that form an observed galaxy spectrum.

1.1 A Brief History of the Universe

The history of the universe is a complicated chain of events beginning at the Big Bang and ending with the structures (e.g. planets, stars, galaxies, clusters of galaxies....) that can be observed today. Knowledge of the very early Universe, at 380000 years after the

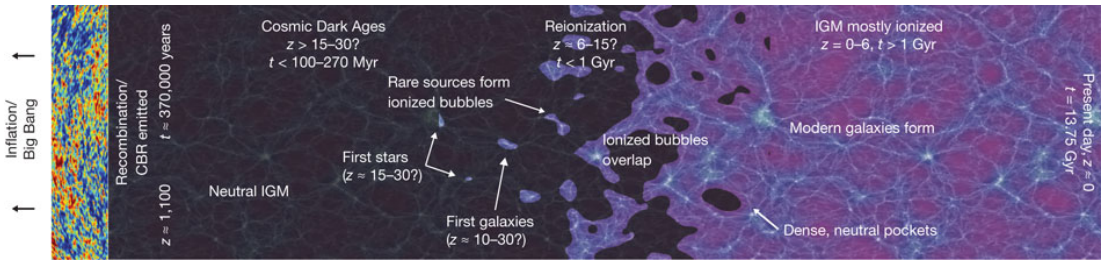

Figure 1.1 *A schematic of the history of the Universe taken from Robertson et al. (2010). Time runs from left to right, showing recombination followed by the Dark Ages. The creation of the first stars and galaxies, which produce ionising radiation, then begins to ionise small bubbles in the neutral Universe. These bubbles eventually overlap and the intergalactic medium becomes predominantly ionised.*

Big Bang, comes from the primordial radiation released from the process of protons and electrons combining to form Hydrogen and Helium atoms. This process, called 'recombination', occurred when the pre-existing hot plasma had cooled sufficiently ($\sim 3000\,K$), and as a result the photons released could propagate freely with little scattering. The radiation released can be observed today with a temperature of $T = 2.73\,K$ as the Cosmic Microwave Background (CMB). Once the process of recombination had occurred, the Universe was neutral, rapidly expanding and cooling. During the "Dark Ages" after recombination, over-densities in the matter distribution which can be seen in the CMB, then started to collapse under self-gravity. As more baryonic matter became gravitationally bound inside the dark matter haloes, it is thought that the first stars started nuclear fusion. During the Dark Ages, the baryonic universe was comprised primarily of neutral Hydrogen and Helium with trace amounts of metals created during the hot nucleosynthesis stage of the Big Bang. The first stars were therefore formed essentially of Hydrogen and Helium and their exact properties are unknown, however they are thought to rapidly enrich the surrounding medium with 'metals' (elements other than Hydrogen and Helium) and hence allow more familiar stars to be born. During their short lifespan, these "Population III" stars release large quantities of energy in the form of energetic UV photons that travel outward from the proto-galaxies and interact with the surrounding neutral inter-galactic medium (IGM). At early times, all of the released photons would be stopped by the surrounding neutral Hydrogen, ionizing a bubble around the star system. Eventually the energetic photons carved deeper ionized pockets into the IGM, reionizing the universe to a high degree. When and how the reionization occurred is still not clear, with data on the CMB polarization giving a redshift of $z \sim 11.1 \pm 1.1$ (Planck Collaboration et al., 2014) if it happened instantaneously, while Gunn-Peterson trough measurements of high-redshift quasars suggest complete reionization by $z \sim 6$ (Fan et al., 2006). The first galaxies are thought to form ~ 100 Myrs after the Big Bang, and current calculations of the number of ionising photons produced from these early galaxies shows that they could (just) reionize the Universe (Robertson et al., 2013). The light from these first galaxies travels through the expanding space and reaches our telescopes, and because the galaxy is receding from us at a very high velocity, the light will be 'stretched' or redshifted. The redshift (z) of a galaxy is defined from the relation between the intrinsic wavelength of the source at rest as compared to the wavelength that such a feature is observed at:

$$\lambda_{\rm observed} = (1 + z)\,\lambda_{\rm rest} \tag{1.1}$$

For any isotropic and expanding Universe, the relationship between the redshift and the

time at which the galaxy is being observed is given by:

$$1 + z = \frac{a(t_{\rm observed})}{a(t_{\rm emitted})} \tag{1.2}$$

where $a(t)$ is the scale factor at that epoch. The scale factor simply relates a given scale at some time in the history of the Universe, $R(t)$, with the same scale at the present time, R_0. From this equation, one can define the look-back time to an extragalactic object, which is the time since the photon was emitted and hence from this the age of the Universe at which the photon was emitted can be calculated.

The current best and simplest model that describes the expansion of the Universe is the Λ cold dark matter (CDM) cosmology. Here the Λ is the cosmological constant introduced by Einstein, which modifies the equations of motion to match the observation that the Universe is expanding at a faster and faster rate. The equations that describe the expansion depend on several constants, and throughout this thesis I assume:

$$\Omega_{\rm m} = 0.3,\ \Omega_\Lambda = 0.7,\ H_0 = 70 {\rm km/s/Mpc}^3 \tag{1.3}$$

Here the Ω terms describe the fraction of the energy density of the Universe contained in matter (both dark and baryonic) and vacuum energy, when the total energy density is taken to be the critical density. In a flat Universe, $\Omega_{\rm total} = \Omega_{\rm m} + \Omega_\Lambda = 1$. The Hubble constant, H_0, relates the recessional velocity (v) with the proper distance (d) for low redshift galaxies:

$$v = H_0 d \tag{1.4}$$

At higher redshift, the Hubble parameter changes with time as:

$$H^2 \equiv \left(\frac{\dot{a}}{a}\right)^2 = \frac{8\pi G}{3}\rho - \frac{kc^2}{a^2} + \frac{\Lambda c^2}{3} \tag{1.5}$$

where ρ is the energy density of the Universe, a is again the scale factor and k describes the curvature of the Universe ($+1$: closed, 0: flat, -1: open).

1.1.1 Distance measures

The concept of a distance or similarly a volume becomes non-trivial in an expanding ΛCDM Universe. Specifically for the analysis of distant galaxies there are several distance measures that are essential; the luminosity distance, the angular diameter distance and the radial distance. An isotropic and homogeneous space-time can be described with the Robertson-Walker metric:

$$ds = -c^2dt^2 + a(t)^2\left[\frac{dr^2}{1-kr^2} + r^2(d\theta^2 + \sin^2\theta\, d\phi^2)\right] \tag{1.6}$$

which describes the infinitesimal interval between two events in space-time. Here the (r, θ, ϕ) coordinates are comoving coordinates and t is the cosmological time. Hence the distance between two objects depends explicitly on the time, which dictates the effective scale of the Universe via the scale factor.

The luminosity distance is required to convert the observed apparent magnitude into an absolute magnitude, as it encompasses the dimming of the object.

$$M = m - 5.0\log_{10}(D_L(\mathrm{pc})/10\mathrm{pc}) + 2.5\log_{10}(1+z) \tag{1.7}$$

where the $1 + z$ factor comes from considering the expansion of the $d\lambda$ in the measurement of the apparent magnitude. The luminosity distance relates the intrinsic luminosity (L) of an astronomical object with the observed flux (S), and hence satisfies the equation:

$$S = \frac{L}{4\pi d_L^2} \tag{1.8}$$

There are two effects that change the observed luminosity of a galaxy, the first is the loss of energy of the photon, which reduces the flux by a factor of $1 + z$, and the second is the number of photons themselves are reduced, which results in an additional factor of $1 + z$. The luminosity is therefore related to the flux by:

$$S = \frac{L}{4\pi a_0^2 r_0^2 (1+z)^2}, \text{ and hence } d_L = a_0 r_0 (1+z) \tag{1.9}$$

Here r_0 denotes the comoving radius to the object, and hence $a_0 r_0$ is the proper distance. When considering the flux per unit wavelength or frequency however, another factor

of $1+z$ must be taken into account, due to the change in width of the bandpass with the redshifting of the objects spectrum. Mathematically the flux per unit frequency then becomes:

$$S_\nu = (1+z)\frac{L_{(1+z)\nu}}{L_\nu}\frac{L_\nu}{4\pi d_L^2} \tag{1.10}$$

When converting this formula into magnitudes, the $(1+z)\,L_{(1+z)\nu}/L_\nu$ term becomes the so-called K-correction (Hogg et al., 2002), which accounts for the fact that the observed frequency range/filter is measuring a different part and frequency range of the spectrum in the rest-frame of the galaxy. The K-correction becomes important when for example, calculating the V-band luminosity function in a wide redshift bin or observing the evolution with redshift. As the observed V-band flux will be measured on a redshifted spectrum it will be probing a part of the spectrum at a shorter rest-frame wavelength.

The second is the angular diameter distance, which relates an objects observed angular diameter on the sky (θ), with the proper size at that redshift (x) as:

$$d_A = \frac{x}{\sin\theta} \simeq \frac{x}{\theta} \tag{1.11}$$

where the approximation is valid for small angles (θ must therefore be in radians). Integrating the angular part of the metric we find:

$$\theta = \frac{x}{r_0 a(t_e)} = \frac{x(1+z)}{a_0 r_0}, \text{ and hence } d_A = \frac{a_0 r_0}{(1+z)} \tag{1.12}$$

Here we have used the relation that $a(t) = a_0/(1+z)$. As an example, the angular diameter distance at $z = 7$ calculated from our standard cosmology is $d_A = 1080\,\mathrm{Mpc}$, and therefore a galaxy with an observed angular size of 1 arcsec has a physical size of $\sim 5\mathrm{kpc}$.

The bolometric surface brightness of a galaxy, or the total flux per solid angle on the sky (where solid angle is given by $\omega = A/D^2$ for an object of projected area A, at distance D), therefore depends on redshift as:

$$I_{\mathrm{obs}} \equiv \frac{S}{\omega} = \frac{L}{4\pi d_L^2}\frac{d_A^2}{A} = \frac{L}{4\pi A}\frac{1}{(1+z)^4} = \frac{I_{\mathrm{emit}}}{(1+z)^4} \tag{1.13}$$

Hence, galaxies and low-surface brightness features of galaxies become increasingly hard to detect at higher redshift as a result of cosmology. The above equation relates to the bolometric or total surface brightness of a galaxy, summed over all wavelengths, however typically observations of galaxies are made in specific filters or bandpasses. As I have shown above, the observed flux per unit frequency is $S_\nu \propto (1+z)\, L_{(1+z)\nu}$ and hence the surface brightness dimming per unit frequency declines with redshift as $(1+z)^{-3}$.

Finally, when considering the luminosity or mass functions of galaxies, the comoving volume is required. The use of the comoving volume allows the effects of cosmology to be separated from the evolution of the number density of galaxies, as a non-evolving and non-merging population stays at a constant comoving number density. The comoving volume element is given by:

$$dV_C = \frac{c}{H_0} \frac{(1+z)^2 d_A^2}{\sqrt{\Omega_M (1+z)^3 + \Omega_k (1+z)^2 + \Omega_\Lambda}}\, d\omega\, dz \tag{1.14}$$

Here, the large factor on the denominator gives the dependence of the comoving radial length on redshift, which the numerator converts the observed solid angle ω into a comoving area. The interval between $6.5 < z < 7.5$ contains a comoving volume of $\simeq 300\,\mathrm{Gpc}^3$, which corresponds to a volume of $0.008\,\mathrm{Gpc}^3$ over one square degree (the full sphere has a solid angle of $\simeq 41\,253\,\mathrm{deg}^2$).

1.2 The First Stars

During the Dark Ages, the period of time before any stars had formed in the Universe, the neutral gas was collapsing under gravity into structures following the dark matter distribution. The formation of stars depends on the ability of the gas to cool such that a sufficiently dense core can be formed and fusion can begin. Very generally, the condition for star formation to occur in a region of over density in the Universe is given by $t_{\rm cool} < t_{\rm dyn}$ (Rees & Ostriker, 1977; Silk, 1977). The cooling is most efficient in moderate dark matter haloes, with masses $\simeq 10^{12}\,\mathrm{M}_\odot$, and hence the star-formation efficiency is peaked at this halo mass with a $M_*/M_{\rm dm} \sim 0.02$ (Behroozi et al., 2013a,b). In the pristine gas that forms the first stars, metal line cooling, which becomes the most efficient cooling rate at low temperatures in local star-forming regions, cannot occur. Molecular cooling can provide the solution as can be seen in Fig. 1.2, although the formation of the H_2 molecule is challenging without dust particles (formed of metals)

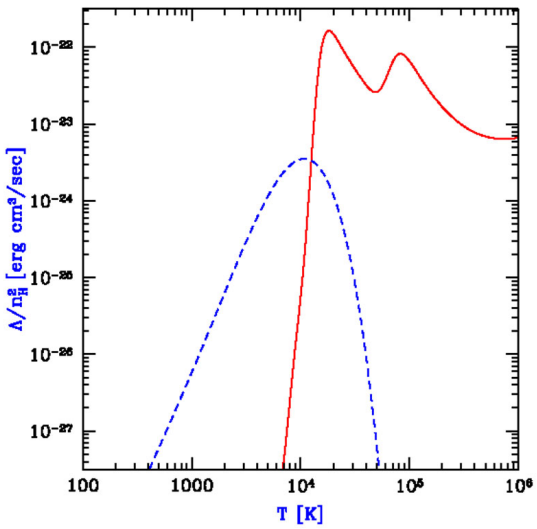

Figure 1.2 *The cooling rate as a function of temperature for pristine gas. The red curve shows the cooling rate due to atomic Hydrogen, via line emission, and the blue curve shows the cooling rate due to molecular transitions. Figure adopted from Loeb (2010).*

that act as a catalyst. The initial mass function of the first stars is thought to be top-heavy compared to the locally observed initial mass distribution, with characteristic masses around $10\,\mathrm{M}_\odot$ (Bromm, 2013).

In situations where pristine haloes of gas and dark matter are unable to cool via molecular transitions, which could occur when halos with masses of order $M_\mathrm{h} \simeq 10^8 M_\odot$ are close to newly star-forming halos that produce a strong radiation field capable of dissociating H_2 (Lyman-Werner field, with energies of 11.2–$13.6\,\mathrm{eV}$), black holes of order $m_\mathrm{BH} \simeq 10^{4-6} M_\odot$ could form by direct collapse. The formation of such massive seed black holes directly reduces the tension between observations of quasars spectra that imply a central supermassive black hole of $M \simeq 10^9 M_\odot$ already in place by $z = 7.0$ (Mortlock et al., 2011).

1.2.1 Metallicity

The metallicity of a star, of the ISM or of a galaxy is often quoted in units of solar metallicity, $\mathrm{Z}_\odot$. The solar values of metal content as a fraction of the total mass is shown in Table 1.1. Hence the metallicity, or fraction by mass of the sun that is not Hydrogen or Helium, is 0.02.

Table 1.1 *The metallicity of the sun, shown as a fraction by mass of Hydrogen, Helium and metals.*

Element	Fraction by Mass	Solar Value
Hydrogen	X	0.70
Helium	Y	0.28
Metals	Z	0.02

The quantity obtained directly from observations is often the $[\mathrm{Fe/H}]$ value, defined as:

$$[\mathrm{Fe/H}] = \log\left(\frac{(N_{Fe}/N_H)}{(N_{Fe}/N_H)_\odot}\right), \text{ where } [\mathrm{Fe/H}]_\odot = \log(N_{Fe}/N_H) \simeq -4.22 \quad (1.15)$$

The metallicity of the constituent stars affects the observed galaxy SED, as an increase in metals in the atmospheres of stars results in a higher opacity, and hence larger and redder stars. Stronger spectral absorption lines will also result, in general giving redder colours and a stronger 4000Å break (due mainly to Ca H + K lines as well as CN). When determining the metallicity of a galaxy you must consider where you are measuring it from. Typically the gas phase metallicity is measured by observing emission lines from the nebulae surrounding stars, and determining the Oxygen abundance relative to that of Hydrogen. The physical conditions of the gas (e.g. temperature and density) are determined from the relative strength of the emission from different excitation levels of Oxygen, and using these properties the abundance of Oxygen relative to Hydrogen can be inferred from their ratio. Other methods use ratios of different excitations of Oxygen, or the Oxygen to Nitrogen ratio to give the metallicity via some calibration. There are issues with this method however, because the calibration depends on the ionisation parameter (which is the number of ionising photons divided by the density of the gas) which is likely to change with redshift as galaxies become more metal poor with young stellar populations.

The metallicity of high-redshift galaxies is thought to be lower than in an evolved galaxy such as the Milky Way, as a consequence of the young age of the stellar populations. However, the metallicity of a galaxy is hard to determine with broad-band photometry due to degeneracies with age and dust reddening. Furthermore, there exist metallicity gradients in galaxies, with the inner bulge region tending to exhibit a higher metallicity than the outer parts, an effect that must be considered when determining the metallicity from small aperture photometry on the objects, such as that performed by the Sloan Digital Sky Survey (3-arcsecond diameter apertures). Hence typically the metallicity

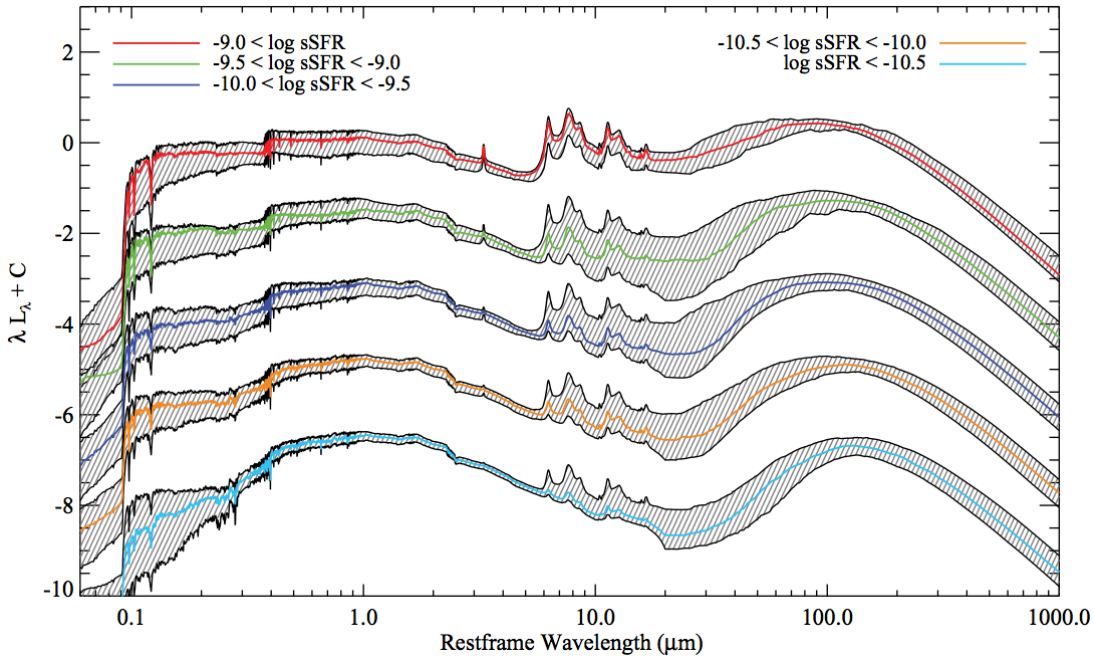

Figure 1.3 *Panchromatic SEDs of Herschel selected galaxies from Smith et al. (2012). The stacked SEDs are split by star-formation rate, and displayed in units of* λL_λ *which gives a measure of the emitted energy at each wavelength. The emission from young O and B-type stars can be seen in the UV part of the spectrum from* $\simeq$ 1000–3000*Å, the optical spans from the Balmer break at* $\simeq$ 4000*Å to* 1μm *where we enter the near-infrared and the spectrum becomes more dominated by older stars. The PAH features are visible at* $\simeq 10\mu$m *followed by a broad modified blackbody peak emitted from dust grains, which rises through the far-infrared and falls into the sub-mm regime. The Lyman limit and Balmer break are visible at* 912*Å and* 3546*Å.*

cannot be well constrained at high redshift, except with spectroscopic observations such as those undertaken by Sanders et al. (2014) at $z \simeq 2$ or by using low-redshift analogues (Stanway & Davies, 2014).

1.3 An Overview of Galaxies

1.3.1 The panchromatic SED of galaxies

The spectral-energy distribution (SED) of an observed galaxy contains a wealth of information about that object. To illustrate the salient features of galaxy SEDs, in Fig. 1.3 I show panchromatic SEDs derived from model fitting to stacked galaxies selected by *Herschel* (Smith et al., 2012). The rest-frame UV wavelengths are dominated by recent star formation. Massive, short lived stars such as O and B spectral

Table 1.2 *The effective temperature, typical lifetime and mass of stars by stellar type.*

Stellar Type	$T_{\rm eff}$	MS lifetime	Typical mass ($\mathrm{M}_\odot$)	Features
O	$\gtrsim 30000\,\mathrm{K}$	1–10 Myr	20–60	Ionized He
B	10000–30000 K	11–400 Myr	3–18	
A	7500–10000 K	~ 1 Gyr	2–3	Strong Balmer absorption
F	6000–7500 K	3 – 7 Gyr	1.1–1.5	
G	5500–6000 K	8–15 Gyr	0.9–1.05	Ca^+ (H and K), Na
K	4000–5500 K	17 Gyr	0.6–0.8	CN and CH
M	2500–4000 K	56 Gyr	0.08–0.5	Molecules, TiO
L	1000–2500 K			
T	500–1000 K			
Y	200–500 K			

types, have spectra that peak at very short wavelengths. In Table 1.2 I detail the basic properties of stars of different spectral type. The effective temperature of a star, $T_{\rm eff}$, is measured from the point when the optical depth in the stellar atmosphere is unity. The observer then effectively sees the stars as a black body with the effective temperature, and hence the spectrum should follow:

$$B_\lambda(T) = \frac{2hc^2}{\lambda^5}\frac{1}{e^{hc/\lambda k_B T} - 1} \tag{1.16}$$

where $B_\lambda(T)$ is the flux per unit wavelength per steradian. Wien's displacement law relates the wavelength of the peak of this function and the temperature of the blackbody as $\lambda_{\rm peak}\, T = 2.9 \times 10^{-3}\,\mathrm{mK}$, hence the spectrum of an O or B-type star peaks in the UV. I show example stellar spectra in Fig. 1.4. The steepening slope of each spectrum to hotter $T_{\rm eff}$ can be seen, as can the changing absorption features and the strength of the breaks. In the UV, the most striking feature is the step observed at 912Å, which occurs at the Lyman-limit. A photon of higher energy will ionise Hydrogen (through a bound-free transition), and hence the emission of these photons out of the stellar birth cloud is strongly suppressed. If violent star formation can punch a hole through the neutral Hydrogen and dust in the galaxy, then ionising (or Lyman-continuum) photons could escape. The fraction of ionising photons (with energies exceeding $13.6\,\mathrm{eV}$) that can escape the galaxy and hence contribute to the reionization of the Universe, is the escape fraction ($f_{\rm esc}$).

The rest-frame optical emission observed in the galaxy spectrum is dominated by older stars, and can be completely out-shined by O and B types when a star-formation event occurs. As the number of less massive stars dominates over that of the young massive

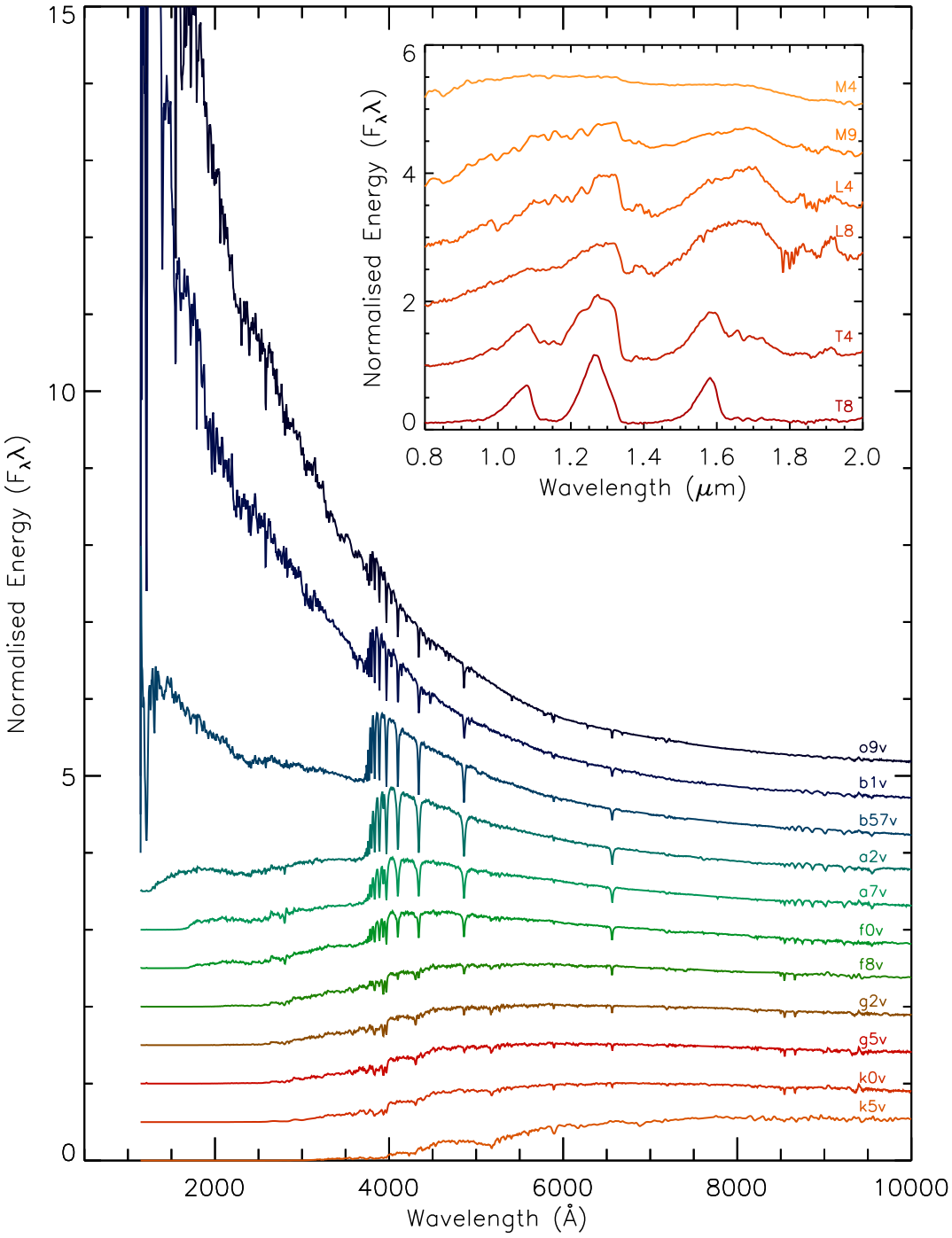

Figure 1.4 *Stellar spectra in the UV and optical taken from the PICKELS and SpeX stellar libraries. The inset shows dwarf stars, which peak in the near-infrared.*

objects (see the IMF section later), the rest-frame optical light is a good tracer of the mass of the galaxy. In particular, the strength of the Balmer and 4000 Å breaks can be good indicators of the age of the population. The formation of breaks in the spectrum, such as the Balmer break, are a result of bound-free transitions where a photon has sufficient energy to ionize the atom. The break observed at the Lyman-limit, at $912\,$Å, is similarly a result of bound-free transitions, whereas the 'Lyman-break' at 1216Åis a result of the bound-bound transition from the ground state ($n = 1$) of Hydrogen to the $n = 2$ excited state as photons with the energy of Lyα are absorbed by the neutral IGM along the line-of-sight to the galaxy. The Balmer break occurs as a result of photons of energy greater than the Balmer-limit ionising the atom from the $n = 2$ state, hence there is an increased opacity in the atmosphere of the star at shorter wavelengths than the break. The strength of the Balmer break reflects the proportion of Hydrogen atoms in the atmosphere of the star that are in the $n = 2$ state, which depends on the temperature and peaks around $10000\,\mathrm{K}$. Considering the collisional excitation of Hydrogen atoms into the various states, you would expect the number of electrons in each state to approximately follow the Boltzmann law with $n_u/n_l \propto \exp(\Delta E/k_\mathrm{B}T)$, and hence the higher the temperature the greater the proportion of electrons in the upper ($n = 2$) state. Therefore, we would expect the Balmer lines to get stronger and stronger with increasing atmospheric temperature, however the Balmer line strength is limited by the ionisation of atoms. If you include the changing proportion of atoms ionised from the $n = 2$ state (calculated from the Saha equation) with the Boltzmann population levels you can show that the Balmer lines should be strongest in stars of $T_\mathrm{eff} \simeq 10\,000\,\mathrm{K}$, which is what is observed for A-type stars.

The strength of the Balmer break or the depth of the Balmer absorption lines (e.g. Hα denoted as δHα) gives an indication of the galaxy age, as A-type stars dominate the SED of a galaxy at $\simeq 1\,\mathrm{Gyr}$. Another commonly measured break is the '4000Å' break, or $D(4000)$, which measures the line blanketing of metals in the atmospheres of stars, in particular the strength of the Calcium H and K absorption features at 3969Å and 3934Å and absorption by Carbon and Nitrogen. The 4000Å break is stronger in older stars than the Balmer break, as a consequence of the temperatures required for metals to strongly absorb the light.

Stellar objects with types M (later than subtype > 6.5), L, T and Y are not strictly stars as no Hydrogen fusion is occurring in their cores, and are instead brown dwarfs. The spectra of brown dwarfs peaks in the near-infrared due to their low T_eff, and the SEDs are dominated by deep and broad absorption features produced by molecules in the atmospheres including water, TiO and methane.

So far I have only touched on absorption features in the spectra of stars and hence in galactic spectra. The spectra of stars tend to only show absorption features because the radiation from the star has to pass through layers of cooler atmosphere. Emission lines are observed in star-forming galaxies and are produced in the ionised nebulae surrounding young hot stars. These nebular emission lines result from ionised atoms recombining, and the electrons cascading down through the energy levels of the atoms, and hence are a tracer of the ionising radiation field in the galaxy and hence the SFR. In principle therefore, if the amount of ionising radiation being produced by a star or a galaxy is known, then the amount of energy released in emission lines and the relative fluxes of these lines can be calculated. Such a calculation is performed in studies of high-redshift galaxies to predict the contribution of rest-frame optical emission lines to the total flux measured here using broad-band photometry, and hence to determine more accurately the mass of the galaxy which is measured from the strength of the continuum only. In the optically thick nebulae that typically surround young stars, emission line ratios can be determined by assuming 'Case B' recombination, which takes into account the high optical depth to transition of the Lyman series and hence line emission by Lyman-β, Lyman-γ... is suppressed in favour of further smaller steps on the transition ladder (Osterbrock & Ferland, 2006). Emission lines in the rest-frame UV part of the spectrum tend to be from highly ionised metal species, and although common in spectra of quasars, lines such as CIV $\lambda\lambda$ 1548,1550Å, which requires an ionising potential of $47.9\,\mathrm{eV}$, are thought not to be present in galaxy spectra. Recent work on low-mass, high sSFR galaxies at $z \sim 2$ by Stark et al. (2014b) however, detected UV emission lines of several species including CIV, implying large ionisation parameters (the ionising photon flux compared to the gas density), which can be produced by young populations of metal poor stars. The strongest line observed, after Lyα, was the blended CIII] $\lambda\lambda$ 1907,1909 line, which showed rest-frame equivalent widths up to 14Å. The fact that the Lyα and CIII] equivalent widths were correlated, and the fraction of LBGs exhibiting observable Lyα emission drops as the epoch of reionization is approached, has led to the CIII] line being highlighted as a potential alternative to Lyα to gain spectroscopic redshifts of galaxies at $z \gtrsim 6.5$. To-date however, only Lyα detected, gravitationally lensed, objects have been observed to show CIII] due to the weakness of the line and the necessity for it to lie between sky-lines for adequate detection (Stark et al., 2014a).

Moving to the mid-infrared, from $\sim$ 2–$10\,\mu\mathrm{m}$, we enter the region where stellar light can be contaminated by hot dust from quasars. At $\simeq 10\mu\mathrm{m}$ the emission from Polycyclic Aromatic Hydrocarbons (PAHs) is apparent. This is produced in the neutral shell of a photo-dissociation region where the molecules are irradiated by UV light.

The emission from dust dominates at far-infrared and sub-mm wavelengths. Dust emission occurs as high-energy photons emitted from stars are absorbed by dust grains surrounding the birth-cloud of the star, or in the ISM. These dust grains then become hot, and re-radiate the light at a longer wavelength as a result of their size. The exact grain composition and geometry are poorly understood (although progress is being made in local galaxies, e.g. Draine & Hensley, 2012), however the emission is well fitted by a modified blackbody curve (or combination of curves according to different temperature dust) or 'grey body' curve, where the Planck function is multiplied by an emissivity function which is $\propto \nu^{\beta}$ with $\beta \sim 1$–2. At the short-wavelength side of the dust peak, the spectrum follows a power law due to the presence of small grains that are not in radiative equilibrium. At the long-wavelength side however, the spectrum follows the Raleigh-Jeans tail of the modified blackbody curve.

One notable emission line in the far-infrared is the [CII] or C^+ line at 158μm. This fine-structure line can be very strong in star-forming galaxies as it is the dominant coolant of the neutral interstellar gas (Herrera-Camus et al., 2014), and has started to be detected in $z \gtrsim 6$ galaxies (e.g. Ota et al., 2014). Observations of the CO ladder also offers the potential for accurate redshift determination of galaxies, such as the redshift confirmation of the highly star-forming galaxy HFLS3 by Riechers et al. (2013).

Finally, normal galaxies emit in the radio wavelengths as a consequence of star-formation events, separate from any active galaxy contribution. The radio signal at high frequencies comes from the long-wavelength tail of the dust emission, with free-free (or Bremsstrahlung) and synchrotron emission dominating at lower frequencies. Thermal free-free / Bremsstrahlung emission dominates at low to mid frequencies ($100\mathrm{GHz}$) and originates from ionised Hydrogen in HII regions. The synchrotron emission originates from SNe remnants and cosmic rays accelerated from SNe, that interact with the galactic magnetic field. Synchrotron emission has a steeper spectral index than the thermal emission ($\propto \nu^{-0.8}$ vs. $\nu^{-0.1}$) and hence dominates the low frequencies.

1.3.2 Observing basics

The majority of galaxies are found using photometric surveys, where in essence you are taking a digital photograph of the sky using different filters to probe the colours of the objects. The counts in a photometric image are related to the magnitude of that object via the zero-point of the image, which defines the magnitude of one count in the

image through:

$$m = -2.5 \log_{10}(C) + m_Z \tag{1.17}$$

where the number of counts is C, and the zero-point is m_Z. Then, relating the given magnitude to a flux in that filter depends on the magnitude system used. Throughout this work I use AB magnitudes, which are defined relative to a flat-spectrum source in flux per unit frequency (F_ν). In general the magnitude of a galaxy in band-pass A is defined as:

$$m_A = -2.5 \log_{10} \left[\frac{\int F_\nu(\nu) R(\nu) d\nu/\nu}{\int g_\nu(\nu) R(\nu) d\nu/\nu} \right] \tag{1.18}$$

where R is the filter response as a function of frequency, F_ν is the observed spectrum of the source in question, and g_ν is the reference source (e.g. the spectrum for Vega for Vega magnitudes). The filter response describes how much a photon of frequency ν contributes to the final measured signal from the detector. As well as the efficiency of the filter at transmitting light of a given frequency, the efficiency of the detector must be taken into account in the accurate determination of this function. For AB magnitudes, the reference source is a hypothetical flat spectrum source with $F_\nu = 3631\,\mathrm{Jy}$ such that the flux of the object in the chosen filter is:

$$F_\nu = 3631 \times 10^{-m_{\mathrm{AB}}/2.5}\,\mathrm{Jy} \tag{1.19}$$

or alternately in the centimetre-gram-second (cgs) unit system:

$$F_\nu = 10^{-(m_{\mathrm{AB}} + 48.6)/2.5}\,\mathrm{ergs\,s^{-1}\,cm^{-2}\,Hz^{-1}} \tag{1.20}$$

Typical filter transmission curves from the UltraVISTA survey are shown in Fig. 1.5 as an example.

1.4 The Selection of High-Redshift Galaxies

At $z > 5$, observations in the optical and near-infrared probe the rest-frame UV and optical wavelengths of galaxies. In Fig. 1.5 I show simplified galaxy spectra from $z = 3$ to $z = 10$ against observed wavelength, along with some photometric filters used for the

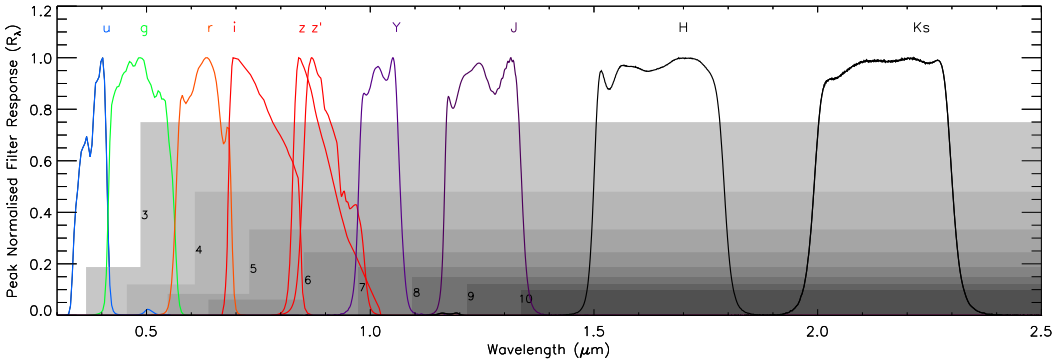

Figure 1.5 *The shaded boxes show the simplified spectrum of Lyman-break galaxies, showing a flat rest-frame UV slope (flat in F_ν), with a sharp break at 1216Å due to the absorption by neutral Hydrogen along the line of sight to the galaxy. The filter transmission curves from the COSMOS/UltraVISTA field are shown for reference.*

selection of such objects. Detection of galaxies at $z > 6$ is challenging and requires the deepest available observations. This is in part due to cosmological dimming, but also because the redshifting of the spectrum shifts the peak in the SED to the near-infrared where CCDs become less sensitive. The rest-frame UV spectrum of a star-forming galaxy is dominated by the Lyman-limit at 912Å, which arises due to absorption by neutral Hydrogen atoms in the inter-stellar medium. Furthermore, there exists neutral Hydrogen in the inter-galactic medium along the line-of-sight to the galaxy which can additionally absorb continuum photons blue-ward of the Lyman-break at 1216Å.

The effect of the IGM absorption can be most clearly seen in the spectra of high-redshift quasars, which are typically several magnitudes brighter than galaxies at the same epoch and hence detailed spectra can be obtained. The Lyα line is a resonant transition with a large interaction cross-section, and hence only a small column density of neutral Hydrogen can produce optically thick absorption lines. Observations of the UV spectra of quasars show many absorption lines blueward 1216Å that form the Lyα Forest. Looking to higher redshift systems it is observed that, as a result of both the high cross-section of neutral Hydrogen and the ionised fraction decreasing, the entire region blueward of Lyα disappears leaving a "Gunn-Peterson Trough" (Gunn & Peterson, 1965). Spectra of quasars at $z > 5$ are shown in Fig. 1.6, showing the decreasing lack of flux transmission in the rest-frame UV as redshift increases. The presence of flux in the trough region at redshifts lower than $z \sim 6$ indicates that the Universe was almost completely ionized by this time, as a neutral fraction as low as 10^{-4} would produce the trough observed at higher redshifts (Fan et al., 2006; Becker et al., 2007).

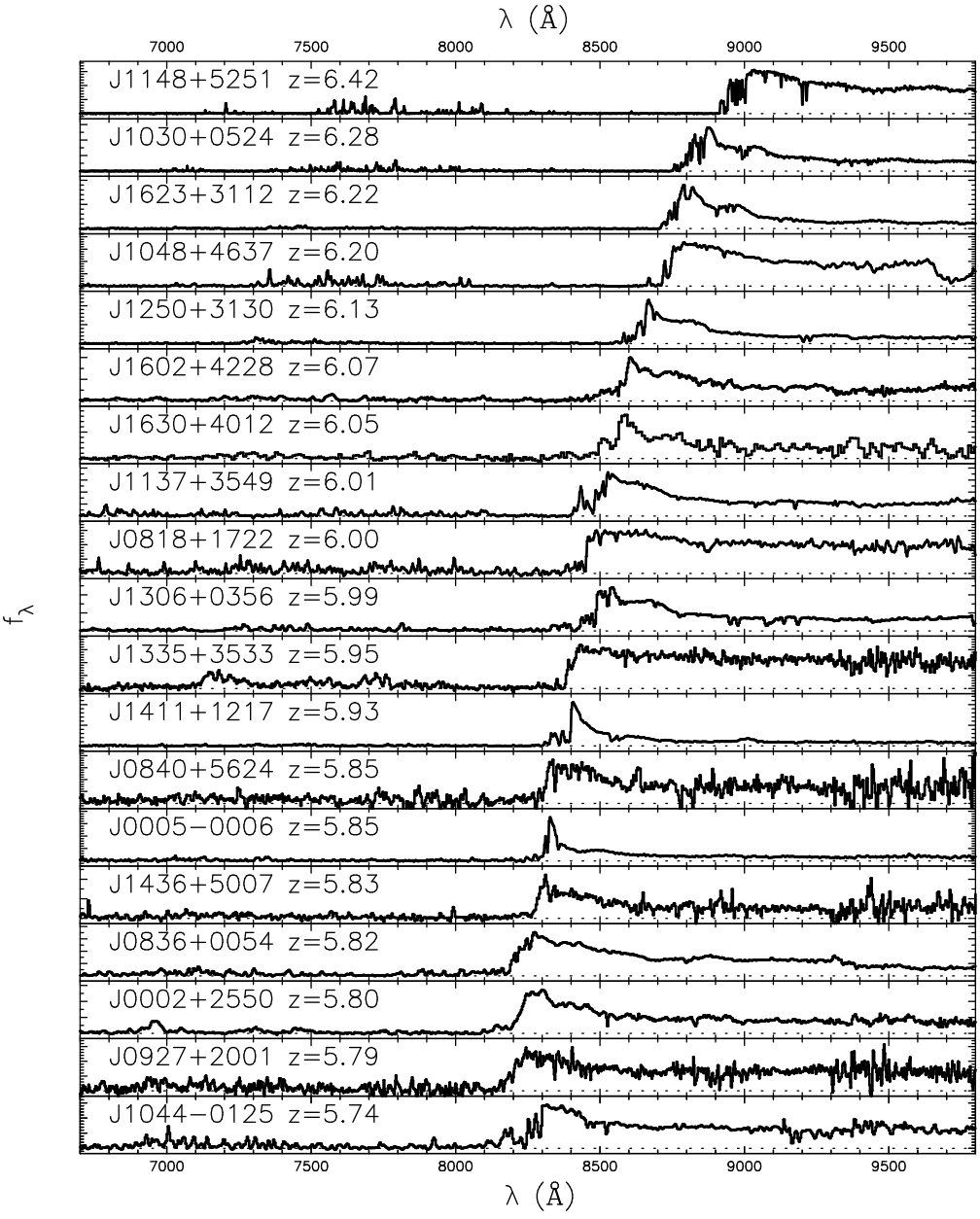

Figure 1.6 *Quasar spectra from Fan et al. (2006) shown against observed wavelength. Many of the spectra show a strong and broad Lyα emission line followed by the Gunn-Peterson trough at shorter wavelengths. The transmission of flux blueward of the Lyα emission line becomes successively more suppressed as the redshift of the quasar increases.*

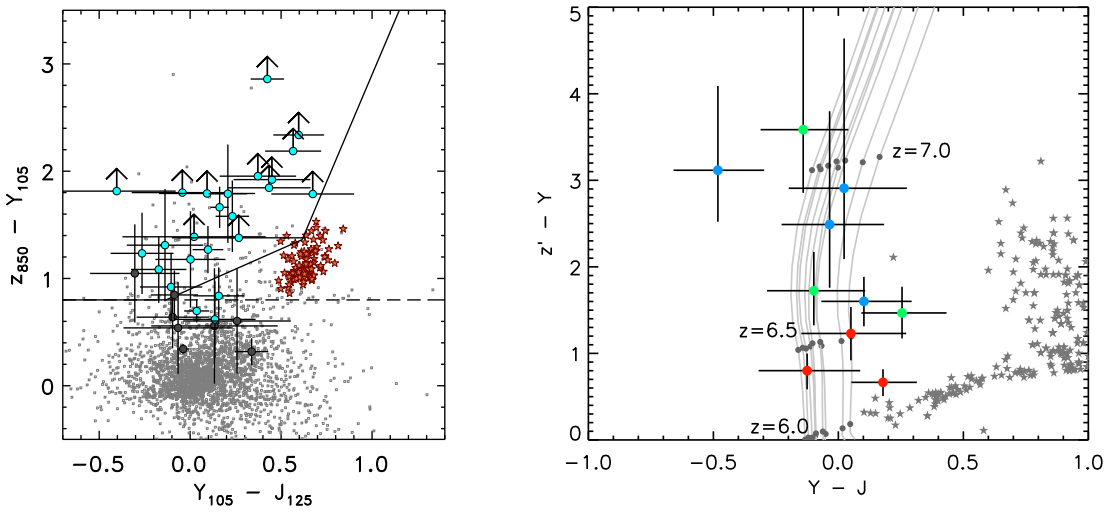

Figure 1.7 *Colour-colour plots to demonstrate the selection of $z \simeq 7$ galaxies using the colour-colour technique. The $Y - J$ colour probes the rest-frame UV slope, whereas the $z - Y$ colour gives the strength of the Lyman-break. The left hand figure is from Finkelstein et al. (2010), and demonstrates the issues with using a strict colour cut in the selection. The solid lines show the selection cuts from Oesch et al. (2010b) and the dotted line is from Yan et al. (2010). The small grey squares are low redshift contaminants, with $z_{phot} < 6.0$, and the red stars indicate the colours of galactic brown dwarf stars, both of which satisfy the high-redshift galaxy colour cuts. The right-hand figure, taken from Bowler et al. (2012), shows the expected colours of LBGs with $z > 6$ as the grey tracks.*

1.4.1 Lyman-break galaxies

The strong decrease in flux blueward of Lyα is the key spectral feature that allows detection of star-forming galaxies at high redshift. Once the effects of IGM absorption are taken into account, the resulting galaxy spectrum has a sharp break, with very little flux blueward of the Lyα emission line. These so-called "Lyman Break Galaxies" (LBGs) can therefore be selected based on the strength of the Lyman-break, using either colour information or by SED fitting of galaxy models to the observed photometry. The use of the Lyman-break in the selection of high-redshift galaxies was pioneered by Steidel et al. (1996).

A demonstration of the "colour-colour cut" technique is shown in Fig. 1.7. As a consequence of the strong Lyman-break in LBGs, they can be selected based on the

red colour between the pre- and post- break filters that is typically greater than one magnitude, coupled with a close to flat rest-frame UV slope. A major problem with using colour-colour cuts is contamination, which is clearly shown in Fig. 1.7, as the colours of cool galactic stars as well as highly reddened galaxies at $z \sim 2$ can mimic those of high redshift galaxies (Dunlop et al., 2007). There is also a range in the possible colours of high-redshift galaxies which, in combination with photometric scatter and potential systematics in the image, could lead to galaxies being excluded and therefore a bias being imposed on the final sample. The advantage of using colour cut selection however, is that it is simple and easy to reproduce, and furthermore can produce clean samples of objects in a relatively narrow redshift window where a strong break is measured.

An alternative method for identifying high-redshift galaxies from photometry is by using all the available multi-wavelength data and fitting model galaxy SEDs. The process of SED fitting is widely used to find the photometric redshifts and to derive the physical properties of objects at lower redshifts and, by using simulated high-redshift galaxy templates, the method can be extended to the selection of high-redshift galaxies. In Fig. 1.8, I show several high-redshift galaxies selected using an SED fitting analysis by McLure et al. (2013). The objects were selected from within the *Hubble* Ultra Deep Field, and the filter transmission curves are shown in Fig. 4.1. The SED fitting methodology is utilised extensively in this thesis and hence I present a more detailed discussion in the next section.

1.4.2 SED fitting

Observed galaxy SEDs contain a wealth of information about the galaxy, including the current and past star-formation, the dust and metal content. To derive such properties from broad-band photometry the fitting of synthetic spectral energy distributions is used. The process of creating a synthetic SED is outlined in Fig. 1.9. The general principle first involves the creation of an SED that represents a burst of star formation, where all the stars are created at the same time and then evolve according to defined isochrones. These simple stellar populations (SSPs) can then be combined with an assumed star-formation history to form a composite stellar population (CSP). The CSP, once the effects of dust attenuation, absorption by the IGM, and the addition of potential nebular emission lines have been included, forms the final synthetic galaxy SED. In this section I discuss in more detail several important parts of the SED model creation process.

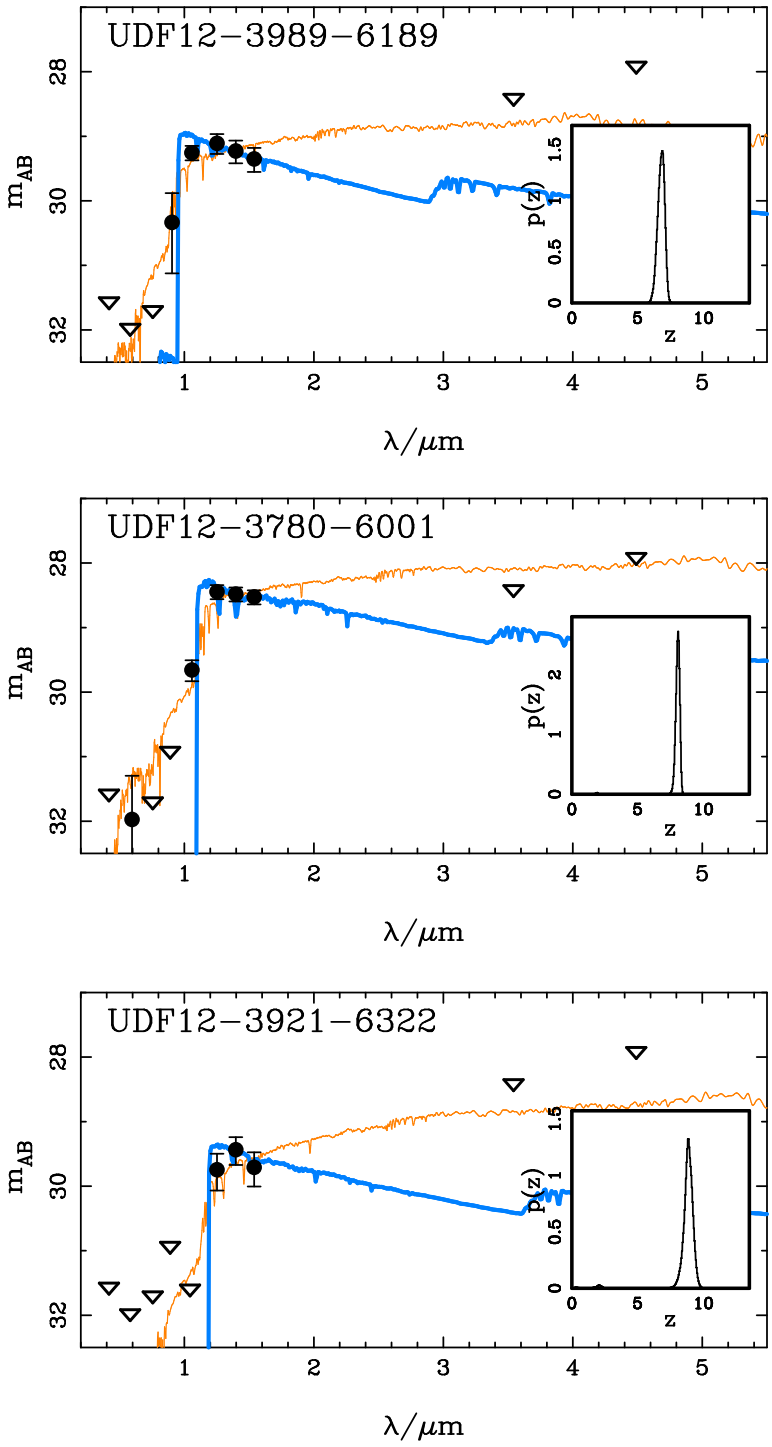

Figure 1.8 *Photometry and the best-fitting SED models for high-redshift galaxies candidates from McLure et al. (2013). In each plot, the photometry is shown as the black points or* 1σ *upper limit arrows, with the best-fitting high and low redshift galaxy SEDs shown as the blue and red curves respectively. The inset plot shows the probability function of photometric redshift derived from the model fitting process.*

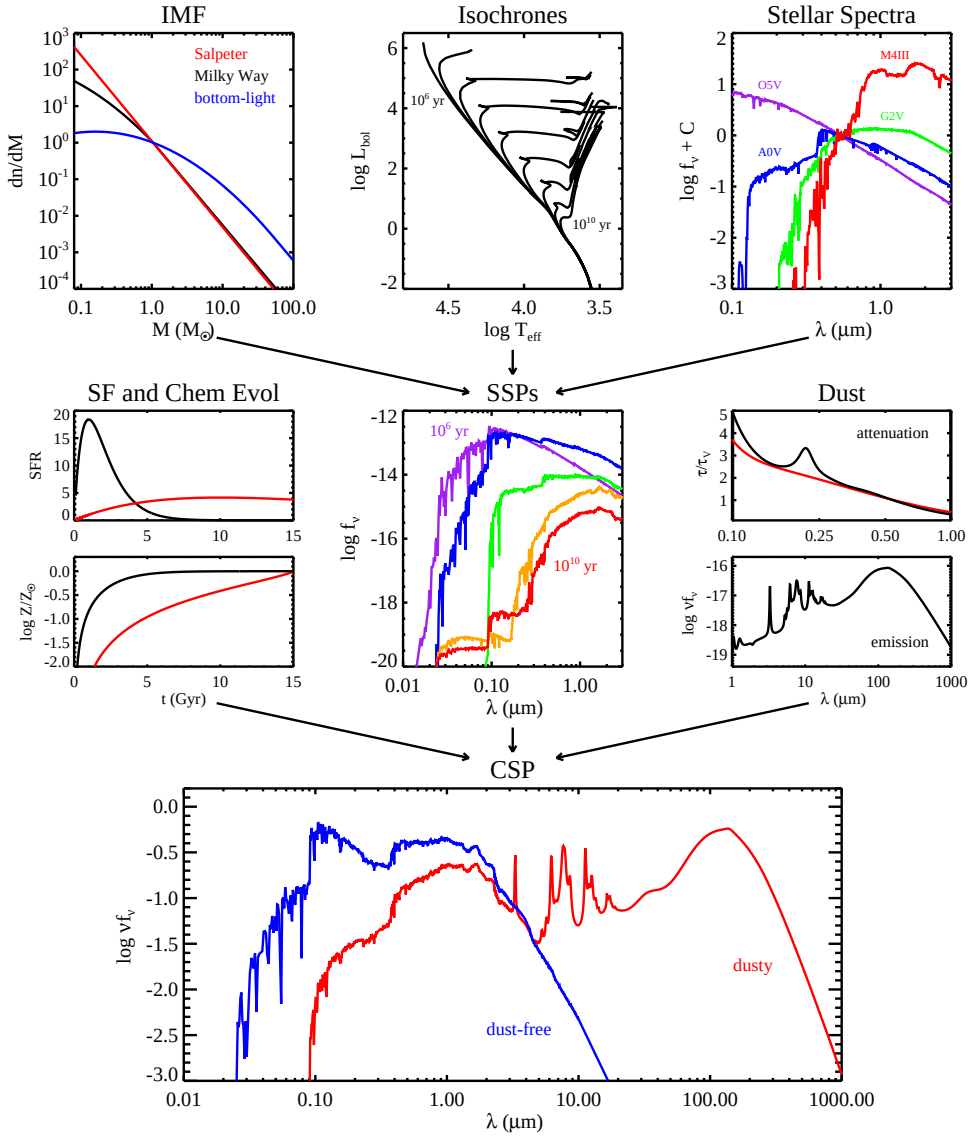

Figure 1.9 *An outline of the ingredients required to create a synthetic SED model, from Conroy (2013). The final composite stellar population shown as the large lower plot is formed from single stellar populations, convolved with an assumed star-formation history (and potential chemical evolution in the metal content) and a dust attenuation law. The creation of the single stellar populations, shown in the top row, requires an input IMF, isochrones and stellar spectra.*

The initial-mass function

The initial-mass function (IMF) describes the distribution of initial masses for a population of stars, and is expressed as a probability density function. The distribution of star masses present will change as stars move from the main sequence and evolve via various channels (e.g. mass loss via stellar winds, SNe explosions). The IMF is an important factor in creating a model galaxy SED because it determines the relative proportion of high to low-mass stars for a given burst of star formation, and hence the inferred mass of a galaxy can vary as a consequence of the assumed IMF. There are several standard IMFs used in SED fitting, and there is recent discussion about the existence of a variable IMFs dependent on the environment or type of galaxy (Cappellari et al., 2012). The simplest IMF is a power law derived in Salpeter (1955) expressed as $dn/dM \propto M^{-2.35}$, which was determined by studying the population of local stars. More recent IMFs include a flattening at $M < 1M_{\odot}$, such as the Kroupa (2001) and Chabrier (2003) IMF.

Star-formation history

The SFHs commonly assumed are constant and exponential declining with $\mathrm{SFR} \propto \exp(-t/\tau)$ (equivalent to constant sSFR). The real SFR is likely to be complicated and potentially stochastic, however the degeneracies already present in the model fitting coupled with the available broad-band photometry of high-redshift galaxies, preclude the creation of a more complicated SFH. Simulations would suggest an exponentially increasing SFH is most valid at high redshift, which would follow the rate of accreted gas onto the galaxies.

At low redshift SFHs can be distinguished with sufficient quality spectra (e.g. using the VESPA code on the SDSS galaxy spectra Tojeiro et al., 2007), whereas at high redshift, with broad-band photometry of faint objects, many SFHs can provide a good fit to the data (Curtis-Lake et al., 2013). The selection of high-redshift LBGs via SED fitting is fairly robust to the exact SFHs employed. However, the derived properties of the galaxy such as age and SFR can vary with the assumed SFH (as well as other parameters).

Dust attenuation

The presence of dust in a galaxy, ubiquitous within star-formation regions in spiral galaxies, can alter the observed UV/optical spectrum of a galaxy. The absorption of dust

grains is a strong function of energy, and hence short wavelength light is preferentially absorbed leading to a reddening of the spectrum. The energy is not lost from the spectrum however, but is re-radiated in the far-infrared wavelengths. The reddening of a spectrum due to dust can be described as either 'extinction' or 'attenuation'. Extinction assumes that the absorption of photons by dust simply removes the light from the observed spectrum, whereas in an attenuated spectrum the absorbed photons can be re-radiated back into the line-of-sight. The former case is valid when measuring the dust reddening in the Milky Way or Magellanic Clouds by comparing two stellar spectra, whereas attenuation is most relevant for observations in extragalactic objects where the dust configuration is likely to provide photons scattered back into the line-of-sight. The degree of reddening applied to the simulated spectrum of a galaxy is described by the decrease in the flux in the rest-frame V-band, parameterised by the increase in magnitude, A_V. Then attenuation at any other wavelength, λ, is given by:

$$f_{\rm obs}(\lambda) = f_{\rm int}(\lambda) 10^{-0.4 A_\lambda} \tag{1.21}$$

where

$$A_\lambda = k(\lambda) E(B-V) = \frac{k(\lambda) A_V}{R_V}. \tag{1.22}$$

So the flux observed, $f_{\rm obs}(\lambda)$, is the intrinsic flux of the galaxy, $f_{\rm int}(\lambda)$, attenuated by a value that depends on the extinction or attenuation curve, $k(\lambda)$. R_V is a constant that depends on the particular model of reddening used (for the Calzetti Law discussed below, $R_V = 4.05 \pm 0.80$), and A_V is the attenuation in the V-band and sets the magnitude of the reddening. For example, if $A_V = 0$ then there is no reddening, but values of $A_V > 2.5$ represent extreme reddening, which, if occurring in galaxies $z \sim 2$, can cause confusion with high-redshift galaxies (Dunlop et al., 2007). $E(B-V)$ is the UV excess and is given by the difference in the $B-V$ colour before and after reddening, or more generally for any band donated by F:

$$E(F-V) = (F-V) - (F-V)_0 \tag{1.23}$$

The most common reddening law applied in the case of high redshift galaxies is that described by (Calzetti et al., 2000), which was derived from near-by starburst galaxies, which are thought to have similarly high star-formation rates (SFRs) to those at high redshift. Other dust extinction curves exist, derived in the Milky Way and in the small

and large Magellanic Clouds for example, where there is an observed bump in the extinction at $\lambda = 2175$Å. The lack of such a bump in the Calzetti et al. (2000) curve is thought to be due to the high level of UV photons present in the star-forming galaxies observed by Calzetti et al. (2000) which could destroy the graphite type dust grains thought to be the origin of the feature.

Intergalactic medium absorption

The effect of the IGM absorption along the line of sight to the galaxy is generally applied using the Madau (1995) prescription. Madau (1995) calculated the average flux decrements blueward of Lyα as a consequence of absorption by neutral Hydrogen clouds along the line of sight, using a model for the clumpy distribution of the neutral gas and for the line blanketing that results. The derived flux decrements D_A and D_B are calculated in the rest-frame wavelength ranges between Lyα and Lyβ (1026–1216Å) and between Lyβ and the Lyman-limit (912–1026Å), where $D_A = 1 - f_{\rm obs}/f_{\rm init}$. At $z > 6$ the attenuation factors exceed 0.8, and hence the Lyman-break at 1216Å is enhanced by almost 2 magnitudes.

1.4.3 Lyman-α emitting galaxies

The Lyα emission line is expected to be strong in star-forming galaxies and therefore provides an opportunity for spectroscopic redshifts of LBGs. The fact that Lyα is so readily absorbed by neutral Hydrogen also makes it a potential probe of the progress of reionization, although other effects such as neutral gas within the galaxy and dust can also affect the line strength. Lyman-α emitting galaxies or LAEs can be selected directly from the strength of their line emission, via narrow band selection. A filter configuration designed to select $z = 6.6$ LAEs using the Subaru Telescope is shown in Fig. 1.10. As the line enters the narrow-band filter, the measured magnitude compared to the z'-band (or whichever broad-band contains the narrow-band) will be brighter and hence you can select line-emitters by defining some 'narrow-band excess'. For example, when selecting $z \simeq 6.6$ LAEs from deep NB921 and z'-band imaging, Ouchi et al. (2010) required $NB921 - z' > 1.0$ (see Fig. 1.10). The narrow-band excess condition selects all sufficiently strong line emitters (Ouchi et al., 2010 claim they are sensitive to a rest-frame $EW_0 \gtrsim 36$Å), and hence to select high-redshift LAEs the object must also present a sufficiently strong break to imply the Lyman-break. The observed EW depends on the redshift, as $EW = (1 + z)\, EW_0$, due to the observed

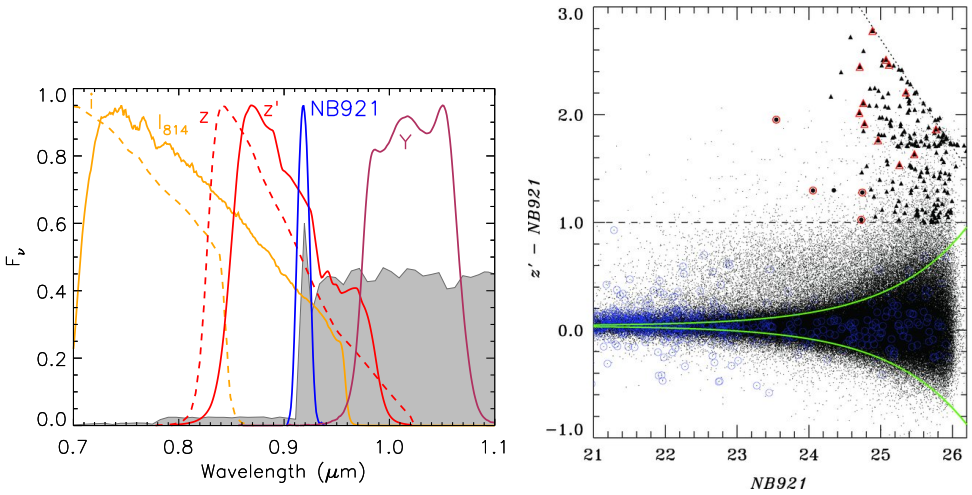

Figure 1.10 *On the left is an example filter configuration, using both narrow and broad-band filters, designed to selected LAEs at $z = 6.6$ using Suprime-Cam on the Subaru telescope. On the right I show a figure from Ouchi et al. (2010) used in the selection of narrow-band excess objects with the $NB921$ narrow-band filter. Candidate LAEs are selected by requiring $NB921 - z' > 1.0$, which excludes the majority of objects in the images (shown as the trumpet shaped distribution) which do not show emission lines.*

continuum level decreasing by $(1 + z)$ with the redshift, but the enclosed flux of the line staying constant.

The spectroscopically confirmed galaxy redshift record is held by an LBG at $z = 7.51$ (Finkelstein et al., 2013), with a potential detection of Lyα at $z = 7.62$ by Schenker et al. (2014). The detection of Lyα at $z \gtrsim 7.0$ has been challenging, with only tens of objects confirmed to date (Schenker et al., 2014; Pentericci et al., 2014; Caruana et al., 2014; Finkelstein et al., 2013). The reduced success rate has been attributed to an increase in neutral fraction from $z \simeq 6$ to $z \simeq 7$, although theoretical work has shown that the constraints are still relatively weak, mainly as a consequence of the small sample sizes (Dijkstra et al., 2014), but also because of degeneracies between the presence of dust, the galaxy $f_{\rm esc}$ and the neutral fraction (Hutter et al., 2014).

Although initially thought to be two separate populations, there is a growing consensus that LAEs and LBGs represent two extreme ends of a continuous distribution of galaxies, with and without strong Lyα emission. The selection of LAEs from narrow-band data preferentially selects objects that are faint in the continuum, partially because of the imposed narrow-band excess condition but also because intrinsically fainter galaxies are more numerous. Furthermore, when continuum detections of LAEs were available they were found to show bluer rest-frame UV slopes, have younger ages and be of lower masses than LBGs (Stark et al., 2010; Ono et al., 2010; Ouchi et al., 2008).

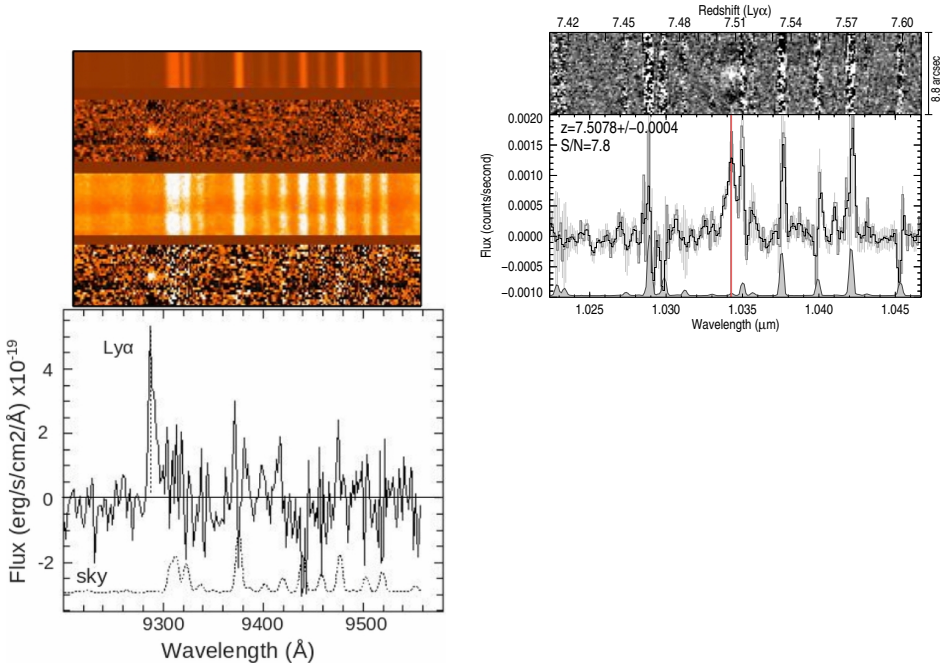

Figure 1.11 *On the left is the spectrum of the spectroscopically confirmed LBG taken from Pentericci et al. (2014). The upper images show the 2D spectra, with the four rows showing the sky emission, the S/N, the total rms error and finally the reduced spectrum in the lower panel. An emission line is clearly visible at* 9300Å *in the 1D spectrum plotted below, and an asymmetric is present in the line which allows the line to be identified as Ly*α*. The right-hand plot shows the Ly*α *emission line at* $z = 7.51$ *detected by Finkelstein et al. (2013). Here there is confusion with a sky line, which makes the expected line asymmetry impossible to observe in this spectrum.*

The presence of a bluer UV slope when Lyα emission is observed hints that the origin of the difference between LAEs and LBGs depends on the ability of the Lyα photons to escape the galaxy. Observations of lower redshift LBGs have further strengthened this view, with large velocity offsets found for the Lyα emission from LBGs, indicating that the bulk of the Lyα emission at the systemic velocity has been absorbed by gas or dust in the galaxy (Shibuya et al., 2014; Erb et al., 2014).

1.4.4 Overview of the searches to-date

The selection of statistical samples of $z > 5$ galaxies only became possible with the installation of the Advanced Camera for Surveys (ACS) on the *HST* in 2002.

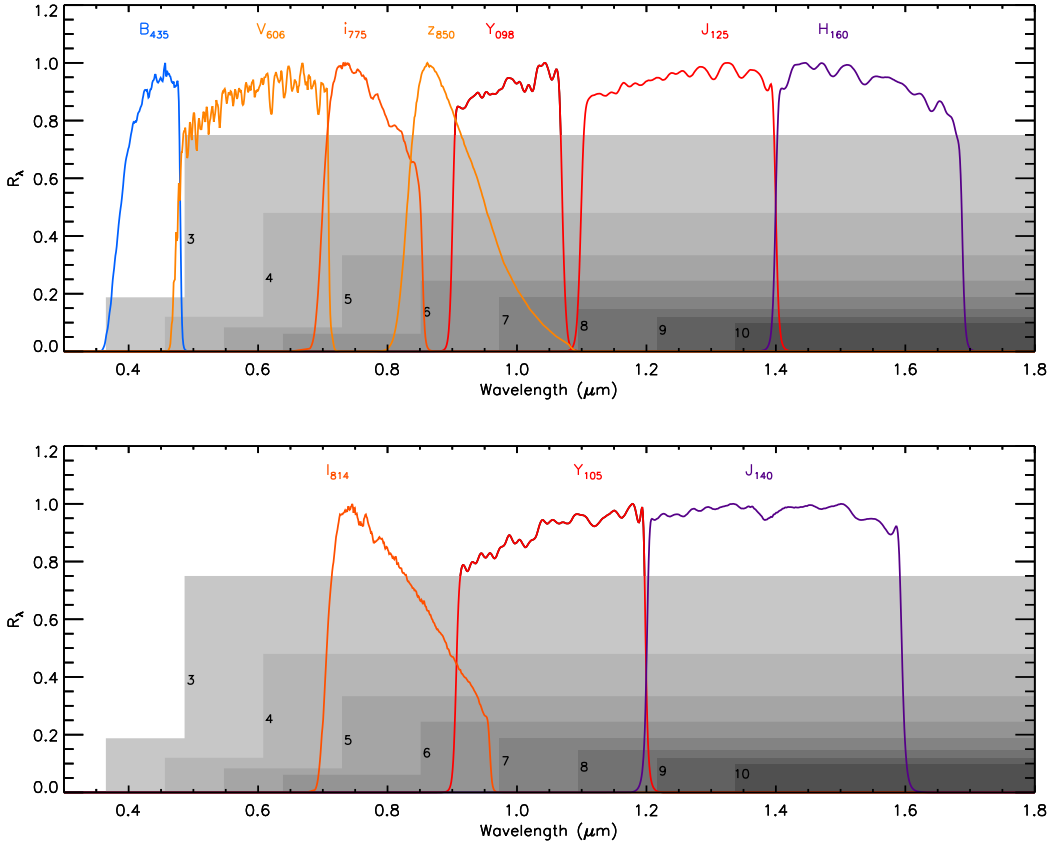

Figure 1.12 HST/*ACS and WFC3 filter response curves, used in the search for high-redshift galaxies. The lower plot shows additional filters used in the UDF12 and COSMOS programs.*

The *HST*/ACS was a significantly more red-sensitive optical camera than had previously been available, allowing deep z-band images to be made and hence enabling the secure detection of V_{606}-dropout objects with blue UV slopes defined by the $i_{775} - z_{850}$ colour. Aside from sensitivity in the red-optical, extremely deep imaging is also necessary to detect LBGs at high-redshift because they are so faint. The *Hubble* Ultra Deep Field (UDF), a single pointing of *HST*/ACS covering 11arcmin^2, fulfilled this requirement (Beckwith et al., 2006). I show a selection of filter response curves available on the *HST* from the ACS or the Wide Field Camera 3 (WFC3) as a reference in Fig. 1.12.

On a historic note, the *Hubble* Deep Field (HDF) which preceded the UDF by a decade, was taken with the Wide Field and Planetary Camera 2 (WFPC2). It covered an area of $\simeq 5\,$arcmin^2 in several filters with the reddest being similar to the i_{775} band. The HDF then subsequently became the site of the Great Observatories Deep Survey (GOODS)-North field, a wider area *HST*/ACS survey field. In addition to GOODS-N, the GOODS-South field surrounded the UDF, providing additional area with which to select brighter but rarer LBGs at $z \simeq 5$–6. The *Hubble* fields opened up the $z = 6$ regime (e.g. Bouwens et al., 2006; Beckwith et al., 2006), detecting galaxies as faint as $M_{\rm UV} = -17.5$ and allowing the first constraints on the evolution in number density and colour of LBGs beyond $z = 5$. At roughly the same time as the deep surveys from *HST*, ground-based programs from the Subaru and UK Infrared Telescope (UKIRT) produced deep z'-band and near-infrared imaging over degree scales in the Subaru Deep Field (SDF) and the UKIRT Infrared Deep Sky Survey (UKIDSS) Ultra Deep Survey (UDS), also known as the Subaru/*XMM-Newton* Deep Field (SXDF). These wide area, but relatively shallow surveys, detected brighter and rarer objects to a depth of $z' \sim 26$ (e.g. Shimasaku et al., 2005 and McLure et al., 2006, 2009). For comparison, the combined UDF, two parallel fields and GOODS-N/S fields have a total area of $\simeq 300\,$arcmin^2, but extend to depths of $z_{850} \sim 27.5$–29.

Recently, the use of medium-band filters in the search for $z \simeq 7$ galaxies has been pioneered by Tilvi et al. (2013) using the zFourGE survey. zFourGE uses medium band filters from 1–1.8 μm (J_1, J_2, J_3, H_l, H_s) on the FourStar imager on the Magellan Baade Telescope. The medium band imaging allows more accurate photometric redshifts for $z > 7$ galaxies, although the area of the survey is relatively small, only $\sim 0.12\,$deg^2 over three fields (CDFS, COSMOS, UDS).

The $z \geq 7$ regime of galaxy selection requires near-infrared photometry, to both detect and select high-redshift galaxies showing a Lyman-break at $\lambda \geq 1\mu$m. The installation of the near-infrared sensitive WFC3 infrared camera (WFC3/IR) on the *HST* in 2009

led to the UDF09 observing program, which obtained deep Y_{105}, J_{125} and H_{160} imaging in a single $4.5\,\mathrm{arcmin}^2$ pointing in the UDF. The UDF09 data suddenly allowed the first samples of $z \simeq 7$ and $z \simeq 8$ galaxies to be detected and studied, and the first luminosity functions appeared. In Table 1.3, I present a summary of the studies of high-redshift galaxies over the past decade, restricting myself to studies where the LF was calculated and in the case of *HST* data I only show results since the installation of WFC3/IR in 2009. Where relevant, several of the more recent studies are discussed and compared in later chapters. The selection of $z > 5$ galaxies is a fast moving field, with several different groups working on the same data-sets and reaching higher and higher redshifts as the near-infrared data available has improved. In 2012, the imaging in the UDF was further extended in the near-infrared as part of the UDF12 program (Ellis et al., 2013; Koekemoer et al., 2013), allowing the detection of galaxies as faint as $M_{\mathrm{UV}} \sim -17.0$ at $z \simeq 8$ (McLure et al., 2013; Schenker et al., 2013). With the aim of detecting brighter galaxies over a wider area, the Cosmic Assembly Near-Infrared Deep Extragalactic Legacy Survey (CANDELS) was started in 2010 and is now completed (Grogin et al., 2011). CANDELS provided *HST*/ACS and WFC3/IR imaging over two deep fields (GOODS-N and GOODS-S), with additional wider area but shallower components, and three wider fields (UDS, COSMOS, EGS). The 'deep' and 'wide' areas of the CANDELS survey have a total area of $120\,\mathrm{arcmin}^2$ and $670\,\mathrm{arcmin}^2$ respectively (Koekemoer et al., 2011). The photometric filters utilised in each field different slightly, with the wide fields not including coverage in the z_{850} or Y_{105} filters that are important for the selection of $z \simeq 7$ galaxies, although they do contain deep ground-based imaging in z' or Y.

Specifically at $z \simeq 8$, progress has been made exploiting the pure parallel observational method with *HST*. It is possible for the *HST* to observe using multiple cameras at once, and the *Hubble* Infrared Pure Parallel Imaging Extragalactic Survey (HIPPIES) and the continuing Brightest of the Reionizing Galaxies (BoRG) programs both exploited this capability to enhance the number of known $z = 8$ galaxies. The observations with WFC3/IR were taken simultaneously with the use of another instrument in an entirely separate program, often when taking long exposures of quasars with the Cosmic Origins Spectrograph. Four filters were used, the Y_{098} or Y_{105}, J_{125} and H_{160} to select Y-dropout objects, and the V_{606} or V_{600} to exclude red low-redshift galaxies. The multiple independent sight-lines (71 used in the recent analysis by Schmidt et al., 2014) reduce the effect of cosmic variance, caused by the underlying large scale structure of the Universe, and provide a wide area ($\gtrsim 350\,\mathrm{arcmin}^2$) with which to search for brighter and rarer galaxies (see Fig. 1.13). Unfortunately, the analysis of the imaging is complicated by the pure-parallel nature of the observations, as the parallel program has no control

Table 1.3 *A summary of the recent studies to select $z = 5$–8 LBGs. I have included all papers after 2009 (the installation of the* HST*/WFC3), with the addition of several ground-based studies before this date if they are relevant for later chapters. The NTTDF is the the New Technology Telescope Deep Field and the BDF was taken by Lehnert & Bremer (2003). HFFp denotes HFF parallel fields.*

Year	Fields utilised	Redshift				Author
		5	6	7	8	
2009	SDF, GOODS-N			✔		Ouchi et al. (2009a)
2009	UDS DR1	✔	✔			McLure et al. (2009)
2010	GOODS-S			✔		Castellano et al. (2010a)
2010	UDF09			✔		Oesch et al. (2010b)
2010	UDF09				✔	Bouwens et al. (2010)
2010	GOODS-S			✔		Wilkins et al. (2010)
2010	UDF09		✔	✔	✔	McLure et al. (2010)
2010	CFHTLS deep	✔				van der Burg et al. (2010)
2010	GOODS-S, BDF, NTTDF			✔		Castellano et al. (2010b)
2010	UDF09			✔	✔	Bunker et al. (2010)
2011	HIPPIES			✔		Yan et al. (2011)
2011	COSMOS			✔		Capak et al. (2011)
2011	UDF09+, ERS				✔	Lorenzoni et al. (2011)
2011	UDF09+, GOODS		✔			Su et al. (2011)
2012	UltraVISTA DR1			✔		Bowler et al. (2012)
2012	BoRG12				✔	Bradley et al. (2012)
2012	GOODS-S				✔	Oesch et al. (2012)
2012	GOODS-S				✔	Yan et al. (2012)
2013	CFHTLS deep		✔			Willott et al. (2013)
2013	CANDELS/GOODS-S			✔	✔	Lorenzoni et al. (2012)
2013	zFourGE			✔		Tilvi et al. (2013)
2013	UDF12, CANDELS			✔	✔	Schenker et al. (2013)
2013	UDF12, CANDELS, BoRG12			✔	✔	McLure et al. (2013)
2014	UltraVISTA DR2 + UDS DR10			✔		Bowler et al. (2014)
2014	BoRG12+				✔	Schmidt et al. (2014)
2014	UDF12, CANDELS, BoRG12	✔	✔	✔	✔	Bouwens et al. (2014)
2014	UDF, GOODS, HFFp	✔	✔	✔	✔	Finkelstein et al. (2014)

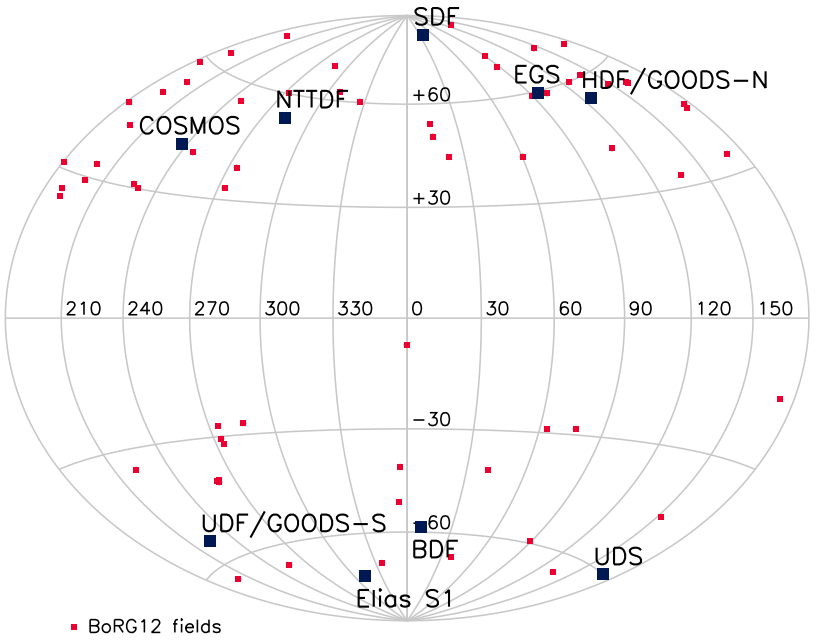

Figure 1.13 *The galactic coordinates (l, b) of the CANDELS and ground-based fields described, shown using an Aitoff projection.*

over the total integration time or imaging methodology. The lack of dithering, the process of taking small sub-pixel steps to allow reconstruction of the point-spread function, is not made for example, nor are larger dither steps to smooth out detector defects. The unusual properties of the background noise that result can cause more spurious detections (Schmidt et al., 2014), which may have lead to the misidentification of a proto-cluster highlighted initially by Trenti et al. (2012). The BoRG program will be continued into Cycle 22 and beyond with a new strategy to detect $z \simeq 9-10$ galaxies as J_{125}-dropout galaxies (PI: Trenti).

Finally, in the coming year the *Hubble* Frontier Fields (HFFs) will be completed. The HFFs are 6 separate pointings of *HST* centred on galaxy clusters, with a corresponding 6 parallel blank fields imaged simultaneously. The cluster fields are designed to use the strong lensing of the foreground cluster to detect very faint high-redshift galaxies, and therefore determine with more accuracy the faint-end slope of the LF. The flux and size magnification of the galaxies also makes them prime candidates for spectroscopic follow-up and size/morphology studies.

1.5 Observed Properties of LBGs

Rest-frame UV slope

Optical and near-infrared photometry of $z > 5$ galaxies probes the rest-frame UV wavelengths, which is dominated by light from young stars and furthermore is very sensitive to attenuation by dust. The rest-frame UV continuum can be estimated as a power law, with $F_\lambda \propto \lambda^\beta$, and for normal star-forming galaxies values of the exponent are $\beta \simeq -2$ which corresponds to a flat spectrum in F_ν. For extremely young stellar populations, with low metallicity and no dust attenuation, $\beta \simeq -3$ is expected (Schaerer, 2002) and hence a detection of such a blue galaxy at high redshift would be evidence for the very first population of stars. The measurement of β can be made by directly fitting a power-law to the broad-band photometry, or by using a single colour:

$$\beta_{\rm colour} = \beta_{F_1-F_2} = A(F_1 - F_2) - 2.0, \text{ where } A = 1/[2.5\ \log(\lambda_1/\lambda_2)] \qquad (1.24)$$

In the use of both β measurement methods, the precise selection criterion of the galaxies can cause a bias in the derived β values. For example, the use of the J_{125} band to select

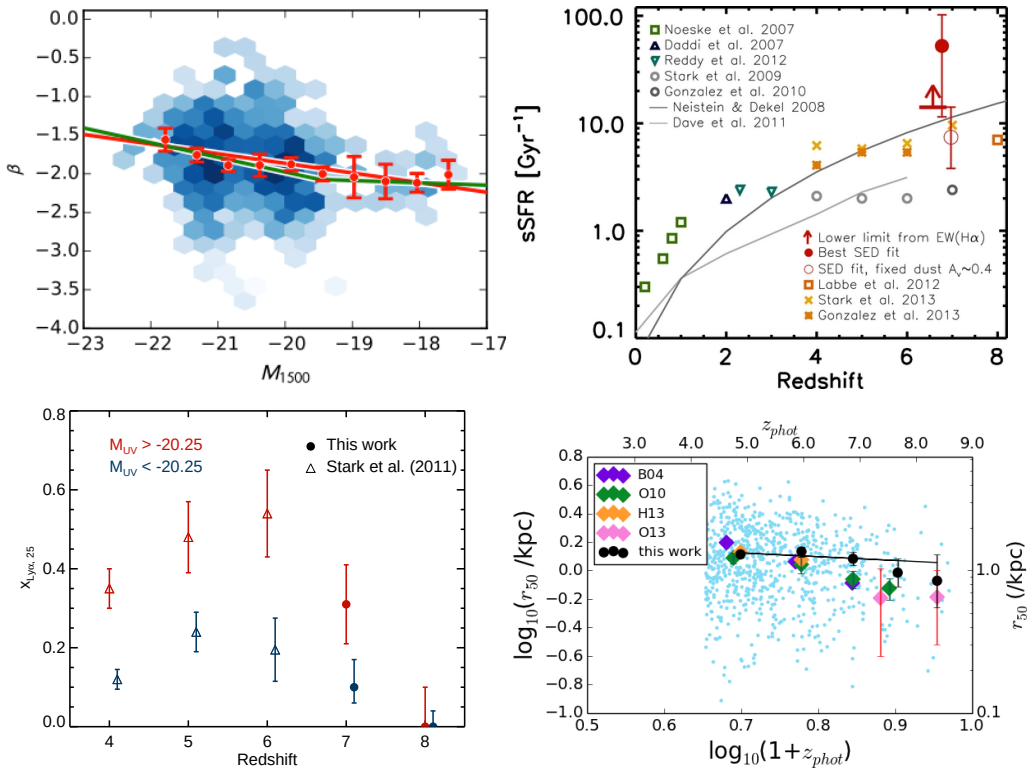

Figure 1.14 *Plots summarising some of the known properties of high-redshift galaxies. Clockwise from top left, I show the colour-magnitude relation at $z \simeq 5$ from Rogers et al. (2014), the evolution of the sSFR with redshift from a compilation by Smit et al. (2014), the observed redshift evolution of sizes taken from Curtis-Lake et al. (2014) and the fraction of LBGs showing Lyα emission (with $EW_0 > 25$Å) as a function of redshift from Schenker et al. (2014).*

galaxies at $z \simeq 7$ and the $J_{125} - H_{160}$ colour to determine β, leads to a blue bias as galaxies that are up scattered into the sample will naturally have a bluer colour. Other more subtle biases can be introduced by SED fitting or using the most robust samples of galaxies in the measurement, as both of these methods result in preferentially blue objects remaining in the sample (see discussion in Dunlop et al., 2013). The results to-date are summarised in Fig. 1.14, which shows the colour-magnitude relation at $z \simeq 5$ from Rogers et al. (2014) and also summarises work by Bouwens et al. (2013) as the green line. At faint magnitudes, $\beta \simeq -2.0$ is recovered as expected for star-forming galaxies at high redshift, and there exists a trend to redder colours in the brightest objects. Looking in more detail at the distribution of galaxy colours with magnitude, Rogers et al. (2014) showed that although the brightest galaxies have a redder mean colour, in fact the distribution of β also widens, consistent with increased scatter as red dusty galaxies become more common or similarly a stochastic SFH where brighter galaxies are observed at different stages of their duty cycle of star-formation.

sSFR and nebular emission

The mass and to some extent the age of galaxies can be well constrained from the rest-frame optical light, which is dominated by the most numerous and longer lived stars as compared to the rest-frame UV. Determining the masses and SFRs of galaxies at $z > 3$ can give an insight into how galaxies are evolving in the first few billion years, for example whether galaxies are smoothly growing or exhibit more stochastic bursts of star-formation. At $z > 5$ the rest-frame optical light can be observed with the *Spitzer Space Telescope* in the mid-infrared. The Infrared Array Camera (IRAC) has filters at 3.6μm, 4.5μm, 5.8μm and 8.0μm, and usually only the two shorter wavelength filters are used, due to the reduction in sensitivity to the red and the increasing size of the PSF making images more confused. Since 2009, only the two short wavelength channels are functioning as part of the *Spitzer* Warm mission.

The larger PSF of the IRAC images, which have a Full-width at Half-Maximum, FWHM ~ 1.8 arcsec, makes blending with nearby objects a problem for measuring the flux of individual LBGs and in general the images have to be deconfused using higher resolution imaging. Stark et al. (2009) measured the masses and SFRs of a sample of LBGs from $z = 4$–6 in the GOODS fields, using the deep IRAC imaging available for isolated members of the sample ($\sim 35\%$ of the galaxies), finding a correlation such that higher mass galaxies were also brighter in the UV and hence had higher SFRs. Such a correlation has also been found at lower redshift and has been dubbed the ‘Galaxy Main

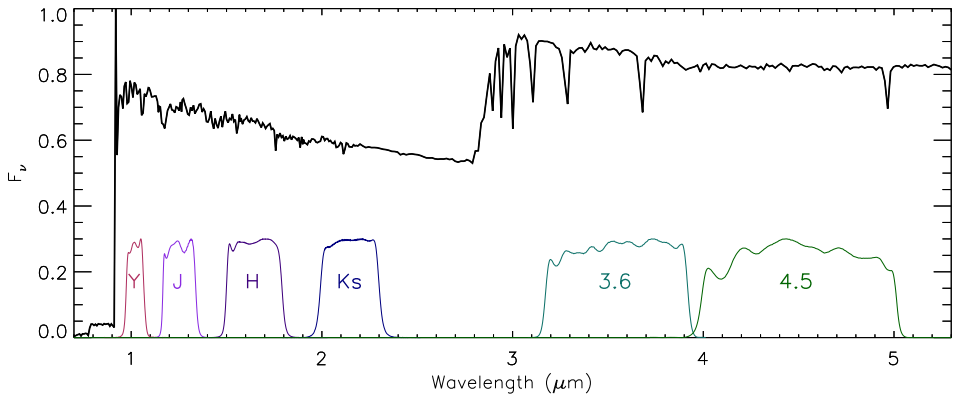

Figure 1.15 *A model SED at $z = 6.4$ showing the Spitzer/IRAC 3.6μm and 4.5μm filters. These filters probe the rest-frame optical part of the galaxy spectrum, redward of the Balmer break which can be seen at $\simeq 3\mu$m.*

Sequence' (MS, Noeske et al., 2007; Elbaz et al., 2007; Daddi et al., 2007). Comparing the results from $z = 4$–6, Stark et al. (2009) found little evolution in the observed MS, which translates into an approximately constant specific SFR (sSFR = SFR/$M_\star$) as can be seen in Fig. 1.14. The sSFR tells you the growth timescale for the galaxy:

$$\mathrm{sSFR} = \frac{dM/dt}{M_0} \tag{1.25}$$

which implies, for a constant sSFR:

$$\int_0^t \mathrm{sSFR}\, dt' = \mathrm{sSFR}\, t = (1/M_0) \int_{M_0}^{2M_0} dM = (1/M_0)(2M_0 - M_0) = 1 \tag{1.26}$$

Hence a $\mathrm{sSFR} = 2\,\mathrm{Gyr}^{-1}$ implies a mass doubling time of $500\,\mathrm{Myr}$. Work at $z \simeq 7$ by González et al. (2010) also found a similar sSFR, albeit with significantly smaller samples. A constant sSFR from $z \simeq 3$–7 was in tension with the theoretical predictions, where sSFR grows according to the availability of cold gas which increases rapidly with time (see model predictions from Neistein & Dekel, 2008 and Davé et al., 2011 in Fig. 1.14).

The masses used in calculating the sSFR by Stark et al. (2009) and González et al. (2010) were derived using SED models which did not include nebular emission lines. Several strong lines occur in the rest-frame optical such as Hα, Hβ and [OIII]$\lambda\lambda$4959, 5007Å, and the presence of these lines at $z > 4$ was uncovered by considering the 3.6μm - 4.5μm colour with redshift, which changes as the nebular lines move through

the filters as shown in Fig. 1.16. The nebular emission lines boost the measured flux in the rest-frame optical, and hence increase the inferred mass. Fitting SED models which include nebular emission lines reduces the expected rest-frame optical continuum level and the inferred mass and hence an increased sSFR is found (Stark et al., 2013; González et al., 2014). The contamination of both $[3.6\mu\mathrm{m}]$ and $[4.5\mu\mathrm{m}]$ filters at $z = 5$–6 increases the effect to higher redshift, and hence the results are now closer in-line with theoretical predictions. Smit et al. (2014) detected the signature of nebular emission in a sample of gravitationally lensed galaxies at $z \simeq 7$, and Fig. 1.14 shows the effect on the derived sSFR when the effect of this emission is removed using the inferred line EW.

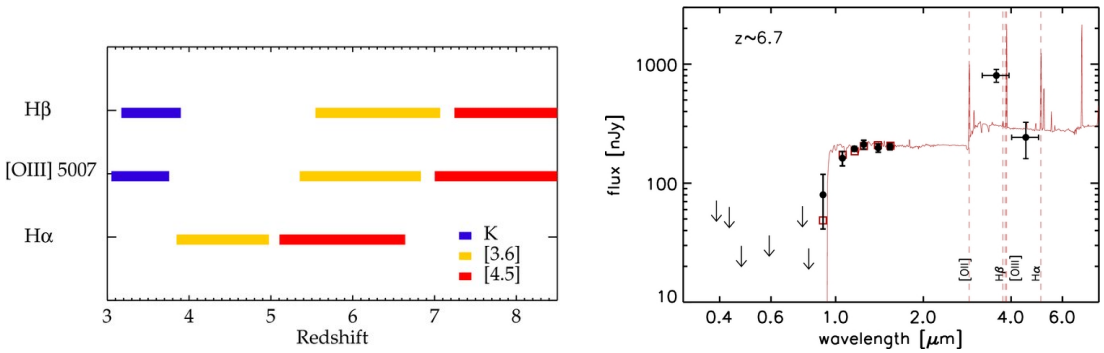

Figure 1.16 *The left-hand plot shows the nebular emission line contamination of the K-band, $[3.6\mu\mathrm{m}]$ and $[4.5\mu\mathrm{m}]$ filters as a function of redshift, taken from Stark et al. (2013). On the right is an example SED from Smit et al. (2014), which includes nebular emission lines in the rest-frame optical.*

Fraction of LBGs showing Lyα emission

Due to the high optical depth to scattering of Lyα , the presence of strong emission from star-forming galaxies is dependent on the amount of neutral Hydrogen along the line of sight. Before the completion of reionization, the Lyα line is predicted to be suppressed as the photons are resonantly absorbed and re-emitted in a random direction. Therefore the measurement of the fraction of LBGs that show significant Lyα emission at $z > 5$, combined with measurements of the neutral Hydrogen via the 21cm line emission, should reveal how reionization took place between $z \simeq 6$ and $z \simeq 11$. The measured fraction is $x_{\mathrm{Ly}\alpha}$, which denotes the fraction of LBGs showing a Lyα emission line with rest-frame EW greater than an observationally imposed limit (typically $EW_0 > 25$Å for moderate Lyα emission, and $EW_0 > 55$Å for strong emission). Observations of $z \simeq 4$–7 LBGs have shown that Lyα emission is more common in fainter galaxies (Stark et al., 2010, 2011), which can be seen in Fig 1.14.

Brighter galaxies ($-21.75 < M_{\rm UV} < -20.25$) are found to show a lack of high-EW emission despite it being easily observable (Stark et al., 2010) and the proportion of brighter galaxies showing Lyα of any EW is lower than for fainter galaxies. As discussed in more detail in Chapter 5, there is evidence that Lyα emission may be more common in the very brightest LBGs with $M_{\rm UV} \simeq -21.5$ selected from wide-area ground-based surveys (Curtis-Lake et al., 2012). The fraction of galaxies in a given magnitude range showing Lyα emission increase with redshift from $z = 3$–6 (Stark et al., 2010, 2011) and then appears to drop at $z > 6$ (Schenker et al., 2012; Tilvi et al., 2014; Caruana et al., 2014; Pentericci et al., 2014; Schenker et al., 2014). The rise in the prevalence in Lyα emission from $z = 3$–6, when compared to the decreasing number counts of galaxies to higher redshift, indicates that at higher redshift Lyα can more easily escape from galaxies possibly due to reduced absorption by dust or neutral gas in the galaxy.

Sizes and morphology

The sizes of LBGs are predicted to increase with time following the size growth of the parent dark-matter haloes, although exactly how the dark matter and baryonic sizes relate is likely complicated. Measurements of the sizes of LBGs at $z > 5$ are challenging due to the reduced surface brightness, however using the unrivalled spatial resolution in the optical/near-infrared provided by *HST*/ACS and WFC3 (PSF FWHM = 0.1–0.2 arcsec), the sizes of LBGs at $z > 5$ have been measured. Typically galaxy sizes are taken as the half-light radius ($r_{1/2}$), which is usually estimated from the galaxy isophotes, converted into a circular measure. The half-light radius can also be found by fitting a Sersic profile which has the form $I(R) \propto I_0 \exp(-\kappa[(R/R_{1/2})^{1/n} - 1])$, with the Sersic index $n = 1$ representing a pure disk profile and $n = 4$ representing a de Vaucouleurs profile, and the κ being a normalisation constant that depends on the chosen n. When measuring the $r_{1/2}$, injection and recovery simulations show that the software packages SExtractorand GALFIT underestimate the sizes of the faintest objects, as the low surface brightness wings become lost in the noise, which must be corrected for to uncover the true size distribution.

LBGs in the luminosity range 0.3–$1 L^*_{z=3}$ (where $L^*_{z=3}$ corresponds to $M_{\rm UV} = -21.0$) were found to have measured $r_{1/2} \simeq 0.2$ arcsec, which converts to a physical size that is $\lesssim$ 1kpc at $z > 5$ (Bouwens et al., 2004). For reference, using a standard ΛCDM cosmology and the angular diameter distance, one arcsecond measured half-light radius corresponds to 6.3 kpc, 5.7 kpc, 5.2 kpc and 4.8 kpc at $z = 5.0, 6.0, 7.0$

and 8.0. Furthermore, a size-luminosity relation was found at $z \simeq 7$ (Grazian et al., 2012; Oesch et al., 2010b) with the faintest galaxies effectively unresolved with *HST* showing $r_{1/2} < 0.5$ kpc. Comparing the mean sizes from samples of LBGs at different redshifts revealed a trend for an increasing average size with redshift (Bouwens et al., 2004; Grazian et al., 2012), appearing to extend to $z \gtrsim 8$, although the sample sizes are small (Ono et al., 2013; Oesch et al., 2013). Using *HST*/WFC3 follow-up of a sample of relatively bright $z \simeq 6$ galaxies however, Jiang et al. (2013a) found a significantly shallower size-luminosity relation than previous studies. Recent work by Curtis-Lake et al. (2014) has highlighted that although a tail of larger galaxies appears as redshift decreases, the typical sizes of LBGs taken from the mode of the distribution shows little evidence for evolution from $z = 8$–4.

The fraction of galaxies with disturbed morphologies is observed to rise with redshift (Talia et al., 2014; Tasca et al., 2009), a trend coinciding with an increasing merger rate, which has been confirmed to at least $z \simeq 3$ (Conselice, 2014; Mortlock et al., 2013). The results of follow-up imaging with HST/WFC3 of $z \simeq 6$ galaxies strongly suggest that the trend continues to the highest redshifts, with 40 - 50% of the brightest galaxies ($M_{\rm UV} < -20.5$) showing evidence for an interaction (Jiang et al., 2013a; Willott et al., 2013). At $z > 6$, there is tentative evidence that the brightest galaxies continue to be dominated by merging/interacting systems, with the two brightest galaxies at $z = 7$ in the UDF (with $M_{\rm UV} \sim -20.5$) having an extended and clumpy profile (Ono et al., 2013; Oesch et al., 2010b). Furthermore, one of the brightest known objects at this epoch, the $z = 6.6$ galaxy nicknamed 'Himiko' (Ouchi et al., 2009a) that was first discovered in ground-based data, reveals itself to be a triple merger system in high-resolution *HST*/WFC3 imaging, where it appears as three separate components each of $L \sim L^*$ (Ouchi et al., 2009a).

1.6 The Luminosity Function

The luminosity function describes how many galaxies of a given luminosity are present in a certain volume. Often, the luminosity function is expressed in magnitudes and the LF is denoted as $\phi(M)$ in units of $/\mathrm{mag}/\mathrm{Mpc}^3$. The volume here is the comoving volume, and hence the LF can be compared directly between different redshifts with the idea that X galaxies in one unit volume at a certain redshift, will be X galaxies in one unit volume at another, provided no evolution or merging events took place. Determining the LF of galaxies at high redshift is particularly important for 1) calculating whether the ionising radiation from galaxies alone is sufficient to reionize

the Universe, 2) providing a starting point for simulations of galaxy formation and evolution and 3) constraining the key physical processes that shape the LF (e.g. AGN, SNe feedback) during an epoch when the galaxies are relatively young. Furthermore, by using the rest-frame UV LF as a proxy for the SFR function, an estimate of the SFR density ($\rho_{\rm SFR}$, with units of $\rm M_{\odot}\,yr^{-1}\,Mpc^{-3}$) can be made and hence the cosmic SFR density can be traced back to early times as shown by the Madau-Lilly diagram (Lilly et al., 1996; Madau et al., 1996; Madau & Dickinson, 2014, see Fig. 1.17). The SFR can be estimated either from a full SED fit to the observed photometry, or directly from the UV luminosity using the Madau et al. (1998) relation:

$$\rm SFR\,(M_{\odot}\,yr^{-1}) = \frac{\mathit{L}_{UV}(erg\,s^{-1}Hz^{-1})}{13.9 \times 10^{27}} \tag{1.27}$$

which assumes no dust attenuation. Recent evidence from extremely high-redshift studies with the UDF12 imaging data and lensed galaxies behind massive foreground clusters have shown tentative evidence for an even steeper increase in $\rho_{\rm SFR}$ at $z > 8$ (Ellis et al., 2013; Oesch et al., 2014; Coe et al., 2013). Whereas the SFR density increases and then falls from $z \simeq 2$ to the present day, the stellar mass density ($\rho_{\rm M_{\star}}$, with units of $\rm M_{\odot}\,Mpc^{-3}$) monotonically increases with time, and should be recovered by integrating the $\rho_{\rm SFR}$ to the required redshift, provided the UV selected samples offer a relatively complete view of star-formation at early times (Robertson et al., 2010). The stellar mass density can be derived directly from integrating the mass function (with masses derived from SED fitting to rest-frame optical photometry from *Spitzer*/IRAC), or indirectly by using the mass-to-light ratio in combination with the known rest-frame UV LFs. The latter approach requires the inclusion of the observed intrinsic scatter on the $M_{\rm UV}$–$M_{\star}$ relation, which can be large (~ 0.5 dex; González et al., 2011), and hence affects the derived number of massive galaxies and the total mass density. Recent determinations of $\rho_{\rm M_{\star}}$ show that using the observed UV luminosity functions and the $M_{\rm UV}$–$M_{\star}$ relation under-predicts the $\rho_{\rm M_{\star}}$ derived directly from the mass function (Duncan et al., 2014). A more rapidly evolving $M_{\rm UV}$–$M_{\star}$ relation with redshift could potentially reconcile the difference and future work over a wider area of imaging analysed by Duncan et al. (2014), should provide clues to the underlying relation and intrinsic scatter between the observed $M_{\rm UV}$ and stellar mass at high redshift.

1.6.1 Functional forms

The mass and luminosity function are generally fitted with a Schechter function, which as can be seen in Fig. 1.17, reproduces the decline of bright/massive galaxies observed.

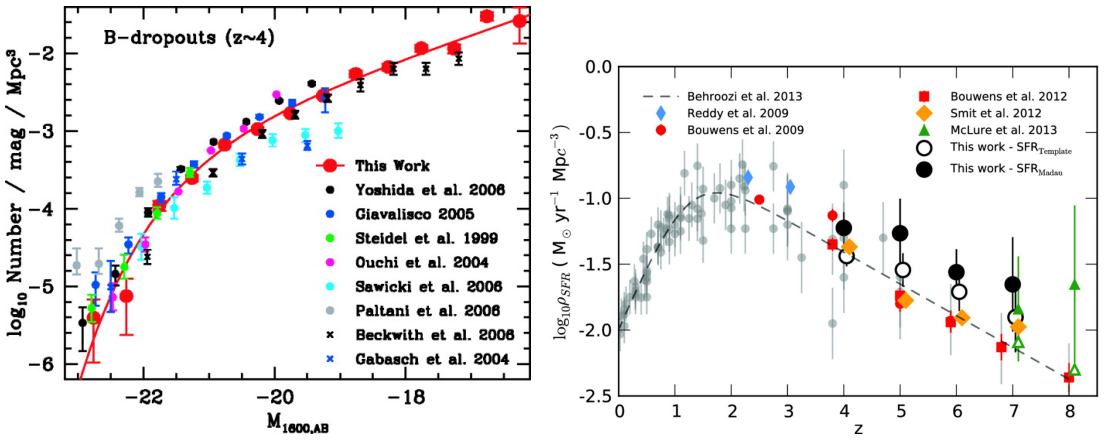

Figure 1.17 *The left-hand plot shows the observed $z \simeq 4$ rest-frame UV luminosity function from Bouwens et al. (2007), which includes a compilation of previous determinations. The red line is a Schechter function fit to the Bouwens et al. (2007) points which are shown in red. On the right I show the observed SFR density from Duncan et al. (2014), which can be derived from the rest-frame UV LF by creating a SFR function; where the SFR of each galaxy is typically calculated from either SED fitting to the full multiwavelength photometry or using the Madau et al. (1998) relation to convert the observed rest-frame UV luminosity into a SFR.*

The classic Schechter function has the form:

$$\phi(L) = \frac{\phi^*}{L^*}\left(\frac{L}{L^*}\right)^{\alpha} \exp\left(-\frac{L}{L^*}\right) \tag{1.28}$$

where α denotes the faint-end slope, L^* is the characteristic luminosity which is the point where the slope changes from $\phi(L) \propto L^{\alpha}$ to an exponential decline. The normalisation of the function is described by ϕ^*. In magnitude space this becomes:

$$\phi(M) = 0.4 \ln 10\, \phi^* [10^{-0.4(M-M^*)}]^{(\alpha+1)} \exp(-10^{0.4(M-M^*)}) \tag{1.29}$$

and the exponential decline now appears as a double exponential, resulting in an extremely steep cut-off to bright magnitudes. The luminosity density of a population of galaxies can be determined by integrating the luminosity function, and although it diverges for $\alpha < -2.0$, it is dominated by L^* galaxies for the reasonable assumption of

$\alpha = -1$:

$$\rho_{L\,\mathrm{total}} = \int_0^\infty \phi(L)\, L\, dL \simeq \phi^*\, L^* \tag{1.30}$$

which is observed at low redshift (Montero-Dorta & Prada, 2009). The Schechter function first originates from Schechter (1976), who proposed it as an analytical expression for the LF for bright local galaxies and cluster-galaxies. The functional form originates from theoretical work presented in Press & Schechter (1974) which used a self-similar growth model to predict the mass function of galaxies and clusters. To fit the function to the galaxy LF, Schechter (1976) allowed the faint-end slope to vary. Since the introduction of Schechter function it has been used extensively to fit both the observed luminosity and derived mass functions of galaxies and clusters. In particular, it provides a good fit for the mass function of galaxies. However, as I discuss in Chapter 4, there is evidence that it may not always provide a good description of the luminosity function, and instead a double power law (DPL), which is often used to fit quasar and infrared LFs, can be used:

$$\phi(L) = \left(\frac{\phi^*}{L^*}\right) \frac{1}{(L/L^*)^\alpha + (L/L^*)^\beta} \tag{1.31}$$

where as for the Schechter function, L^* describes the luminosity at which the slope changes, α gives the faint-end slope and β controls the bright-end slope. In magnitudes the DPL becomes:

$$\phi(M) = \frac{\phi^*}{10^{0.4(\alpha+1)(M-M^*)} + 10^{0.4(\beta+1)(M-M^*)}}. \tag{1.32}$$

Finally, a Saunders function, which has been advocated as a theoretically motivated fit to the LF by Salim & Lee (2012), is given by:

$$\phi(L) = \left(\frac{\phi^*}{L^*}\right) \left(\frac{L}{L^*}\right)^\alpha \exp\left(-\frac{\log^2(1 + L/L^*)}{2\sigma^2}\right) \tag{1.33}$$

which in magnitudes then becomes:

$$\phi(M) = 0.4 \ln 10\, \phi^* [10^{-0.4(M-M^*)}]^{(\alpha+1)} \exp\left(-\frac{\log^2(1 + 10^{-0.4(M-M^*)})}{2\sigma^2}\right) \tag{1.34}$$

where the σ parameter controls the shape of the bright end of the LF.

1.6.2 The evolution of the luminosity function

The $z = 5, 6$ and 7 rest-frame UV LF (particularly the bright-end) will be discussed extensively in this thesis, and hence I do not attempt a thorough literature review and leave it to the relevant chapter. To give a brief overview of what is known about the high-redshift LF, in Fig. 1.18 I show the LF determined from $z = 4$ to $\simeq 8$ by Bouwens et al. (2011a), and the Lyα LF from Ouchi et al. (2010) as a comparison. The rest-frame UV LFs are clearly evolving with redshift, whereas the Lyα LF shows little evolution from $z = 3.1$–5.7, with a drop at $z \gtrsim 6.5$.

The tightest constraints on the UV LF have come primarily from a "wedding-cake" like combination of *HST* surveys (McLure et al., 2013; Oesch et al., 2013; Bouwens et al., 2014), with extremely deep, small area, surveys such as the *Hubble* Ultra Deep Field (HUDF, area = 4.5 arcmin^2, typical limiting magnitude in the near-infrared $\mathrm{m_{AB}} \sim 29.5$) and parallel fields detecting the faintest objects, being combined with samples of brighter galaxies from the wider area CANDELS (Grogin et al., 2011, area $\simeq 0.2$ deg^2, $\mathrm{m_{AB}} \sim 26$–27). Overall, there has been a strong consensus between different analyses, using both the classical 'colour-colour' selection (Bouwens et al., 2011a; Schenker et al., 2013; Oesch et al., 2013) and photometric redshift fitting approaches (McLure et al., 2009, 2010, 2013), particularly at the relatively faint-end of the LF where the number of galaxies found in these surveys peaks. The faint-end slope has been found to be steep (e.g. $\alpha \simeq -1.90^{+0.23}_{-0.28}$ at $z \simeq 7$; McLure et al., 2013) when compared to the local Universe ($\alpha \sim -1.3$; Hammer et al., 2012) and appears to be steepening with redshift, although the errors are large at $z > 7$.

Determining the number of $L \gg L^*$ galaxies is challenging with *HST* surveys alone, due to the declining number counts of objects brighter than the characteristic magnitude (M^*) and the relatively small area provided by the HUDF and CANDELS imaging. Instead, the very bright end of the LF at $z = 5 - 7$ has been successfully studied using ground-based survey fields, which provide degree scale imaging albeit to shallower depths (e.g. at $z = 5 - 6$: McLure et al., 2006, 2009; Willott et al., 2013, and at $z \simeq 7$: Ouchi et al., 2009a; Castellano et al., 2010a,b; Bowler et al., 2012, 2014). The uncertainties in the number of bright galaxies leads to a large uncertainty in the derived M^*, and the vulnerability of small fields to the effects of cosmic variance can result in systematic errors in M^* depending on which under or over- dense fields are included in the analysis. Nevertheless, there has been a consensus on the dominant evolution path

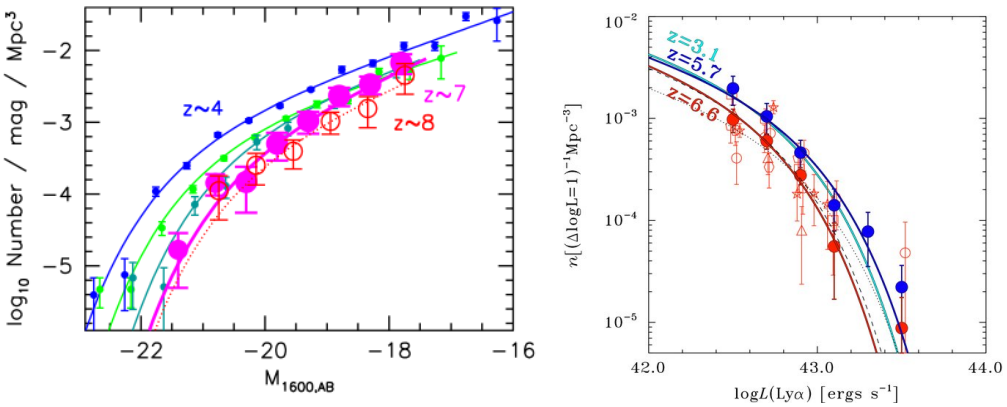

Figure 1.18 *The left-hand plot shows a recent determination of the rest-frame UV LF at $z \simeq 4$ to $z \simeq 8$ from Bouwens et al. (2011a). The right-hand plot shows how the Lyα LF evolves over a similar period from Ouchi et al. (2010).*

of $z \simeq 4$–7 UV LFs until recently (see the discussion in Chapter 4). In Bouwens et al. (2007, 2008, 2011a); McLure et al. (2009), an evolution in the characteristic magnitude was found to well reproduce the observed evolution, with little 'density' evolution. A pure luminosity evolution can be understood from considering the evolution of the underlying dark matter haloes, where hierarchical coalescence of lower mass objects produces the rapid build-up of massive halos as shown in Fig. 1.19. The differential growth of the halo mass function (HMF) results in the number densities of the most massive halos evolving the most rapidly, and hence if the observed galaxy LFs were simply following the underlying HMF an evolution in the characteristic magnitude would be expected. In such a model, the characteristic magnitude rapidly increases at early times, and then becomes fainter to lower-redshift when vigorous star-formation occurs in progressively lower mass galaxies, as the gas becomes depleted in the most massive objects; a process called 'downsizing'. Fig 1.19 also shows the results of the semi-analytical model of Dayal et al. (2014), which includes the hierarchical growth of DM halos and shows a clear luminosity evolution in the predicted rest-frame UV LFs.

The form of the bright end of the LF

Generally speaking, when comparing the observed Schechter-like luminosity functions to the underlying dark matter halo mass function, predicted by theory, a deficit of galaxies is observed at the bright and faint end of the LF. As illustrated in Fig. 1.20, at the faint end the deficit of galaxies is thought to be due to supernova feedback, which can expel gas from small DM haloes. At the bright end it has been postulated that the inability of gas to cool in high-mass halos, or feedback from AGN, could quench star

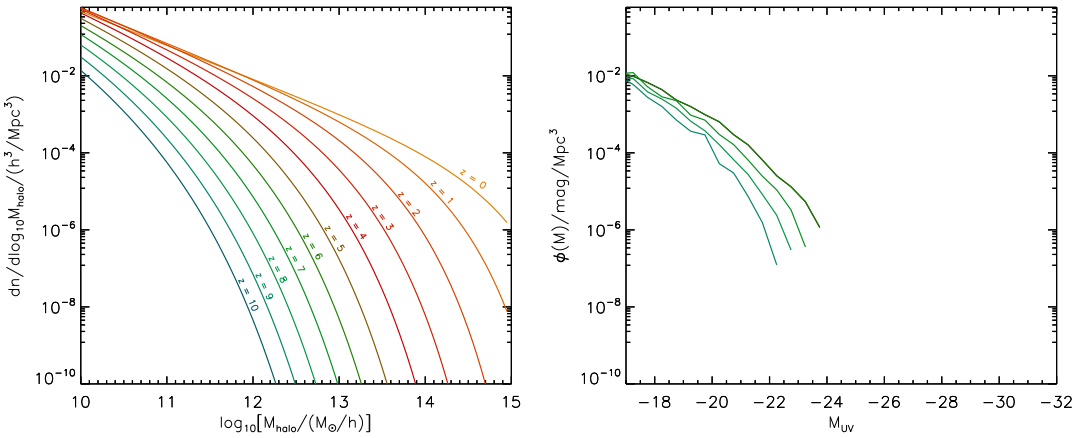

Figure 1.19 *The evolution of the halo mass function with redshift is shown on the left. The HMF was taken from the Sheth-Tormen prescription. On the right I show predicted rest-frame UV LFs from Dayal et al. (2014), where I have roughly scaled the x-axis to correspond to the the HMF masses on the left, where here $M_{\rm halo} \simeq 10^{12}\,{\rm M}_{\odot}$ corresponds to a mass of $M_{\star} = 10^{10}\,{\rm M}_{\odot}$, which has $M_{\rm UV} \simeq -22.0$.*

formation, with strong outflows expelling gas and preventing the accretion of cold gas. Whereas feedback from supernova can quench star-formation in low-mass galaxies rapidly, it remains possible that, at some epoch, the exponential cut-off at the bright end of the LF may disappear and, for example, be replaced by a shallower power-law due to early inefficiency (or absence) of the physical processes purported to be responsible for the relative inefficiency of star-formation in higher-mass dark-matter halos (e.g. Finlator et al., 2011, but see also Trenti et al., 2010 and Jaacks et al., 2012). Hence by determining the form and the evolution of the bright end of the LF at $z > 5$, and comparing the results to the predictions of theoretical models, it is possible to constrain the onset of the astrophysical process that shape the luminosity and mass function to lower redshift. In Chapter 4, I provide an overview of current theoretical simulations that predict the form of the LF with the inclusion of AGN feedback and other effects.

Finally, when calculating the LF from observational data, two forms of bias need to be accounted for. The Eddington bias occurs due to scatter in the measured fluxes of objects, which when close to the limit of a dataset, can result in an overestimate of the number of sources at faint magnitudes. Secondly, the Malmquist bias occurs because brighter objects can be seen to further distances, and hence the volume probed for faint and bright objects will differ.

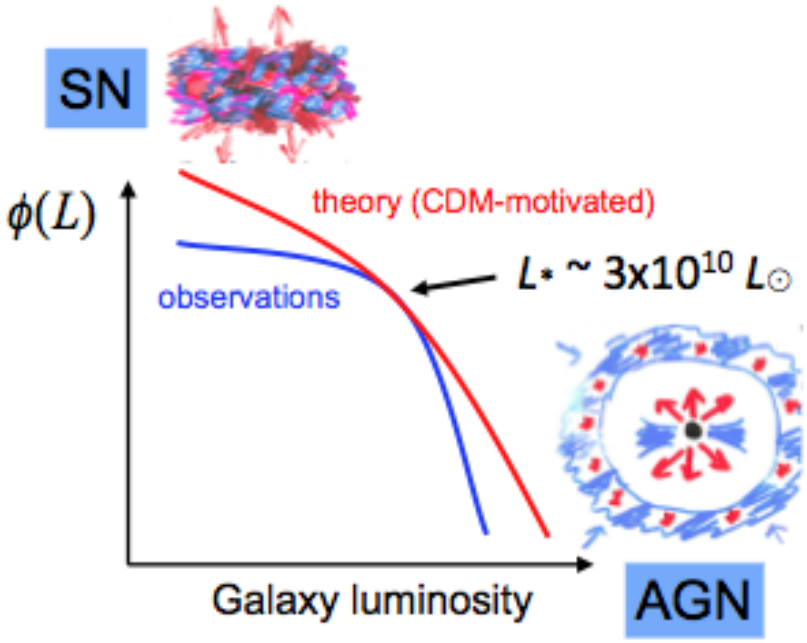

Figure 1.20 *A schematic of the observed and underlying luminosity function, derived from the dark-matter halo mass function, from Silk & Mamon (2012). The halo mass function has a power law shape, and hence the predicted luminosity function is similarly flat, however observations show a deficit of both bright and faint galaxies.*

1.7 Overview of the Thesis

There is a wealth of astrophysical measures that can be extracted from observations of high-redshift galaxies, with the added challenge that these objects are detected at the limit of optical/near-infrared data. I have introduced the galaxy LF as a way to follow the evolution of high-redshift galaxies, and the goal of this thesis is to attempt to measure this evolution through observations of very bright galaxies at $z > 5$. Due to their rarity, the detection of the brightest galaxies requires wide area data, and the clean selection of $z > 5$ galaxies further requires sufficiently deep optical/near-infrared imaging over this wide area. In this thesis, I present work selecting and studying $z \simeq 6$ and $z \simeq 7$ LBGs from a combined 1.65 deg^2 of optical/near-infrared survey data from the UltraVISTA/COSMOS and UDS/SXDS surveys (see Fig. 1.21). Aside from measuring the number densities of these galaxies to form the LF, I also use the multiwavelength photometry available to measure the properties of the galaxies such as their star-formation rates and masses.

The structure of the thesis follows the work published in Bowler et al. (2012), Bowler et al. (2014) and Bowler et al. (2015). In Chapter 2 I start by presenting a search for $z \simeq 7$ galaxies with the first data release (DR1) of the UltraVISTA dataset, which allowed the first secure estimate of the bright-end of the LF at $z \simeq 7$. The work I undertook at $z \simeq 7$ was then significantly extended using the deeper second data release of the UltraVISTA imaging, which I combined with the UDS field to increase the overall area available for the search of luminous LBGs. The larger sample of $z \simeq 7$ galaxies detected in this improved dataset allowed a significantly improved estimate of the bright-end of the LF, and also warranted more detailed study of the galaxy properties (rest-frame UV slope, sizes, nebular emission, masses and SFRs). This work forms Chapter 3 of this thesis. In my final science chapter, I then extended my work at $z \simeq 7$ to lower redshift, concentrating on $z \simeq 6$ with the goal of pinning down the evolution in the bright-end of the LF from $z = 5$–7. Chapter 4 describes the search for $z \simeq 6$ galaxies in the UltraVISTA and UDS datasets, including an analysis of the potential contamination by brown dwarfs. I end with some conclusions and a look forward to future work.

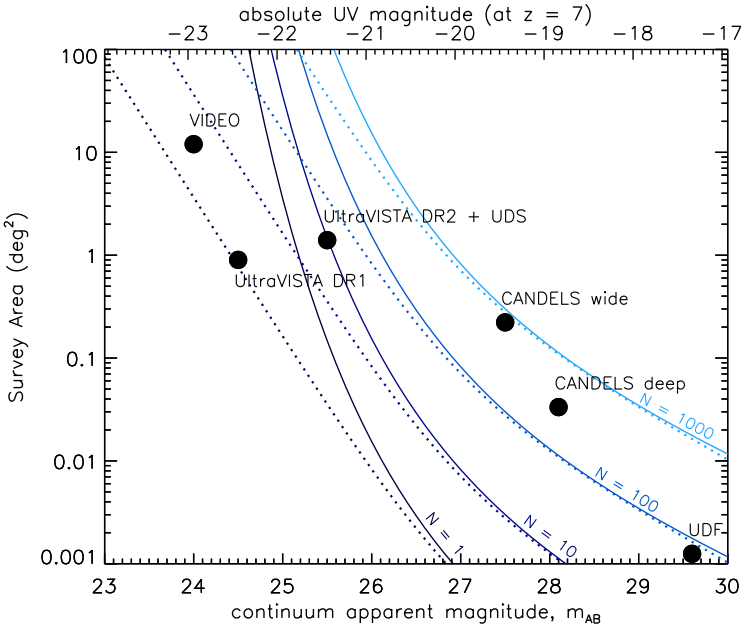

Figure 1.21 *The survey depth against area for several astronomical survey fields, comparing the UltraVISTA/COSMOS and UDS/SXDS fields utilised in this thesis with the UDF and CANDELS surveys. The lines show the required area and depth combination to detect 1, 10, 100 or 1000 LBGs according to the Schechter function fit of McLure et al. (2013), shown as the solid lines, or according to a DPL fit taken from Bowler et al. (2014).*

CHAPTER 2

The discovery of bright $z \simeq 7$ galaxies in the UltraVISTA survey

2.1 Introduction

The depth of the *HST* imaging available, coupled with the (relatively) small field-of-view of WFC3/IR, has meant that, to date, new studies of the $z \simeq 7$ LF have been largely focussed on the faint end, with the WFC3/IR samples dominated by sub-L^* galaxies ($M_{1500} \simeq -20 \rightarrow -18$ mag). Even CANDELS, when complete, will cover an area of only $\simeq 800$ arcmin^2. There thus remains a key role for wider-area, albeit shallower, ground-based near-infrared imaging to better constrain the number density of rarer more luminous galaxies at $z > 6.5$, and hence determine the bright end of the galaxy LF at these epochs. The value of degree-scale imaging surveys of the high-redshift Universe (sampling comoving volumes $\simeq 100 \times 100 \times 100$ Mpc^3) was demonstrated by McLure et al. (2006, 2009) and Curtis-Lake et al. (2012), who utilised the Subaru Suprime-Cam and UKIRT WFCAM imaging of the SXDS field to search for rare bright galaxies at $z \simeq 5$ and $z \simeq 6$, complementing deeper smaller-area imaging work with *HST* ACS (e.g. Bouwens et al., 2007), and ultimately yielding determinations of the $z \simeq 5$ and $z \simeq 6$ LF spanning a dynamic range of over five magnitudes.

An attempt to push ground-based studies of LBGs out to $z \simeq 7$ has been made by Ouchi et al. (2009a) and Castellano et al. (2010a,b). However the latter study (with Hawk-I on ESO's Very Large Telescope; VLT) has covered an area smaller than the final CANDELS area, while the former was based on pushing the silicon-based CCDs in Subaru Suprime-CAM to their red limit, and lacked the longer-wavelength ($\lambda > 1\,\mu$m) near-infrared imaging required to confirm a blue spectral slope longward of the putative Lyman break (resulting in highly-contaminated galaxy samples).

Now, however, degree-scale near-infrared imaging reaching the depth required to uncover credible galaxy candidates at $z > 6.5$ has finally arrived with the UltraVISTA

survey. This 5-year public survey on the COSMOS field (Scoville et al., 2007b) with the near-infrared camera VIRCAM (Dalton et al., 2006) on the new VISTA survey telescope at Paranal in Chile (Emerson & Sutherland, 2010) commenced in 2010, and the first public data release of the fully-reduced year-1 data was made through ESO in Feb 2012[1](McCracken et al., 2012). This new near-infrared imaging covers 1.5 deg^2 to depths of $Y = 24.7, J = 24.5, H = 24.0, K_s = 23.8$ (5σ; 2-arcsec aperture diameter). At the longer wavelengths this is not yet as deep as the 0.8 deg^2 imaging being delivered in the SXDS field by the ongoing UKIDSS Ultra Deep Survey (UDS; Lawrence et al., 2007). However, as well as covering a larger area, UltraVISTA provides the crucial new ingredient of the first large-area Y-band imaging reaching $\simeq 25$ mag (due, in part, to the vastly superior short-wavelength sensitivity of the VISTA Raytheon detectors). As discussed further below, this deep Y-band imaging is of vital importance, both for the effective selection of credible LBGs at $z > 6.5$ and for the robust rejection of cool brown-dwarf star contaminants. Also crucial is the new availability of very deep Subaru z'-band imaging over the central 1 deg^2 of the UltraVISTA field, obtained over the last three years with the refurbished Suprime-Cam (equipped with its new red-sensitive Hamamatsu CCDs); these data were obtained specifically to provide red optical imaging of the depth necessary to exploit UltraVISTA in the search for extreme-redshift LBGs.

We note that UltraVISTA does not represent the first near-infrared imaging of the COSMOS field. Indeed, Capak et al. (2011) exploited the somewhat shallower H, K_s imaging obtained with WIRCam on the Canada-France-Hawaii Telescope (CFHT) and J imaging from WFCAM on UKIRT to report three potential $z > 7$ galaxies in COSMOS at surprisingly bright magnitudes ($J < 23.3$), some with proposed spectroscopic confirmation. However, the power of the new UltraVISTA imaging is well demonstrated by the ease with which we can now show that all of these galaxies in fact lie at much lower redshift (see below). The main aim of this Chapter is, however, not only to check previous claims of $z > 6.5$ LBGs in the COSMOS field but more importantly to demonstrate that UltraVISTA, even in its first few months of data taking, has delivered images of the depth and quality necessary to produce a small but robust sample of luminous $z \simeq 7$ galaxy candidates, and to present this sample to the community for spectroscopic follow-up.

This chapter is structured as follows. In Section 2.2, we present the new UltraVISTA survey near-infrared data, and summarise the crucial supporting datasets: these comprise deep optical imaging (including the final CFHT Legacy Survey data, the long-public *HST* ACS i-band imaging, new ultra-deep Subaru z'-band imaging) and the

[1] `http://www.eso.org/sci/observing/phase3/data_releases.html`

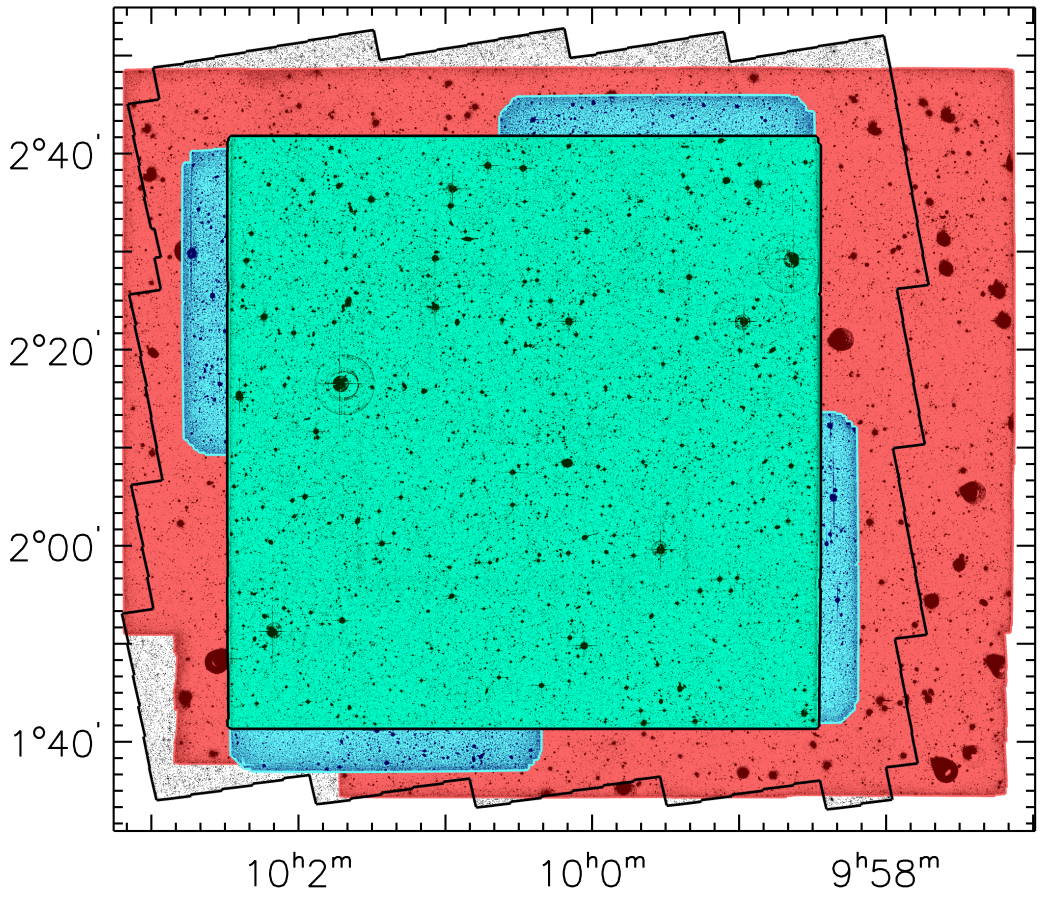

Figure 2.1 *The multi-band coverage map of the UltraVISTA/COSMOS field utilised in this study. Working from the outside in, the year-one 1.5 deg^2 UltraVISTA imaging is shown as the large red rectangle, with the* HST/*ACS I_{814}-band coverage indicated by the jagged outline. The blue irregular shape within the UltraVISTA data is the Subaru z'-band mosaic, formed from four individual Suprime-Cam pointings. Finally, the central green outlined square is the CFHTLS D2 optical data. This final square area, covering $\simeq 1$ deg^2, is the area utilised in this study, as it contains all the required overlapping multi-wavelength data.*

Table 2.1 *The 5σ limiting magnitudes for the relevant optical and near-infrared data used in this study, obtained from the rms of the flux from apertures placed in blank regions of each image (see Section 2.3.1). All magnitudes were calculated within a 2-arcsec diameter aperture, apart from the ACS I_{814} values, which used a 0.6-arcsec diameter aperture and the IRAC $3.6\,\mu$m and $4.5\,\mu$m values, which were calculated in a 2.8-arcsec diameter aperture.*

Filter	$m_{AB}(5\sigma)$	Source
u^*	26.9	CFHT/MegaCam
g	27.0	CFHT/MegaCam
r	26.6	CFHT/MegaCam
i	26.4	CFHT/MegaCam
I_{814}	26.7	*HST*/ACS
z	25.2	CFHT/MegaCam
z'	26.3	Subaru/SuprimeCam
Y	24.7	UltraVISTA
J	24.5	UltraVISTA
$Y+J$	24.9	UltraVISTA
H	24.0	UltraVISTA
K_s	23.8	UltraVISTA
3.6μm	24.2	Spitzer/IRAC
4.5μm	23.8	Spitzer/IRAC

mid-infrared (3.6 μm and 4.5 μm) *Spitzer* IRAC imaging obtained via the S-COSMOS survey (Sanders et al., 2007). In Section 2.3 we then describe the creation and subsequent progressive refinement of our galaxy sample based primarily on spectral energy distribution (SED) fitting, and also show colour-colour plots to demonstrate the validity of our selection method and help expose the possible contaminant populations. Our final ten candidate $z > 6.5$ galaxies are presented in Section 2.4, where we also discuss potential contamination, with special emphasis on an extremely careful elimination of cool brown-dwarf (L, M, T) stars; as discussed by many authors (e.g. Stanway et al., 2008b), contamination by cool dwarf stars is a much more serious issue for ground-based searches for $z \simeq 6-7$ galaxies than for ultra-deep *HST* WFC3/IR imaging surveys, both because extreme-redshift galaxies are generally unresolved in even good-seeing ground-based imaging, and because the relative number of brown-dwarf stars to genuine high-redshift galaxies is much larger at brighter magnitudes (e.g. with a typical absolute magnitude $J \simeq 19$, a T-dwarf star with an apparent magnitude of $J = 24$ still lies well within the galactic disc; see Dunlop 2013). Next, to place our results in context, in Section 2.5 we provide a discussion/re-analysis of the previous claims of bright $z > 7$ galaxies recently advanced by Capak et al. (2011) and Hsieh et al. (2012), as well as the claimed highest redshift X-ray

source candidate presented by Salvato et al. (2011). Then, in Section 2.6, we analyse the properties displayed by the stacked photometry of our top four galaxy candidates, and provide a very brief discussion of the implications of our results for the form of the LF at $z = 7$ (a detailed reanalysis of the $z \simeq 7$ luminosity function is deferred to the next Chapter, where we also incorporate data from the UKIDSS UDS survey). We conclude with a summary of our main results in Section 2.7.

All magnitudes quoted are in the AB system (Oke & Gunn, 1983), including data points from the dwarf-star literature, where Vega magnitudes and AB magnitudes are, unfortunately, frequently mixed. For the calculation of physical quantities we assume a ΛCDM cosmology with $H_0 = 70\,\mathrm{kms}^{-1}\mathrm{Mpc}^{-1}$, $\Omega_\mathrm{m} = 0.30$ and $\Omega_\Lambda = 0.70$.

2.2 Data

The analysis presented in this Chapter is based on the first year of near-infrared imaging obtained by the UltraVISTA survey, in combination with the deep multi-band optical imaging obtained as part of the CFHT Legacy Survey (CFHTLS), new deep z'-band imaging obtained with the refurbished Suprime-Cam on the Subaru telescope, and other publicly-available *HST* and *Spitzer* data obtained as part of the Cosmological Evolution Survey (COSMOS) (Scoville et al., 2007b). The production of multi-wavelength catalogues required the use of images on a common pixel grid and so the region of overlapping data defined by the CFHTLS imaging (described below in Section 2.2.2) was used to define the search area as shown in Fig. 2.1. In Table 2.1 we give the 5σ depths which we have calculated for each of the relevant imaging datasets (see caption for details). All images were matched to the astrometric grid of the UltraVISTA Y-band image using the IRAF package CCMAP. Finally, the images were resampled to match the pixel scale and image size of the CFHTLS D2 field using the IRAF package SREGISTER.

2.2.1 UltraVISTA near-infrared imaging

Over the next ~ 5 years it is planned that the UltraVISTA survey will provide deep near-infrared imaging covering the central region of the COSMOS field in four broad-band near-infrared filters (Y, J, H, K_s) and one narrow-band filter (NB118) to unprecedented depths (McCracken et al., 2012)[2] . The survey was designed to commence with a "deep"

[2] http://ultravista.org

programme (212 hours) providing fully-sampled imaging over a contiguous 1.5 deg^2 field, with the majority (1408 hours) of the observing time being subsequently devoted to the "ultradeep" programme, comprising substantially deeper imaging over four strips (0.73 deg^2) within the field. The first phase of "deep" imaging was completed by July 2011, and released to the public in fully-reduced form via ESO in Feb 2012. It is this year-one imaging that is utilised here, and the relevant coverage map and photometric depths are summarised in Fig. 2.1. The UltraVISTA images use the COSMOS CFHT i^*-band image from 2003-2004 as the astrometric reference (McCracken et al., 2012; Capak et al., 2007). For the present purpose of searching for high-redshift Lyman-break galaxies, an inverse-variance weighted stack of the Y-band and J-band UltraVISTA images was created with the aim of increasing the sensitivity of the survey for objects with a near-flat (in f_ν) near-infrared spectral slope.

2.2.2 CFHT optical imaging

Deep optical data are essential for the identification of genuine high-redshift galaxies, as it is vital to confirm that no flux is detected at wavelengths shortward of the putative Lyman-break. The COSMOS field benefits from extensive multi-band optical imaging obtained with both the CFHT and the Subaru telescope. In this study we use the deepest available data from the CFHT Legacy Survey, which provides imaging over a 1 deg^2 subsection of the COSMOS field centred on RA $10^{\rm h}00^{\rm m}28.00^{\rm s}$, Dec $+2^\circ12'30''$; this defines the area of the survey appropriate for a consistent high-quality search for high-redshift optical drop-out galaxies. The CFHTLS T0006 release[3], in the deep field D2, provides data in the u^*, g, r, i_1, i_2("y") and z optical filters from the MegaCam instrument, with data in the u^*-band obtained as part of the COSMOS survey (Capak et al., 2007). The i_1 and i_2 (or y-band) image distinction is a consequence of a new i-band filter installed since October 2007. However, since the filter transmission curves are similar and probe a region of the spectrum of $z > 6.5$ galaxies where we impose a non-detection condition, and the images are of comparable depth (to within 0.1 mag), we combined these images to form a deeper inverse-variance weighted stack, hereafter simply termed the i-band image. The astrometry of the CFHTLS T0006 data release was based on the 2MASS catalogue rather than the standard COSMOS CFHT i^*-band catalogue. Hence, the CFHTLS images were mapped onto the astrometric solution of the Y-band UltraVISTA imaging using the technique described in Section 2.2, with a correction of typically 0.2$''$, although the pixel scale was retained and used as a base

[3] `http://terapix.iap.fr/cplt/T0006-doc.pdf`

for all other multi-wavelength images.

2.2.3 HST/ACS I_{814}-band imaging

The COSMOS field has been imaged to single-orbit depth by *HST*/ACS in the I_{814}-band through a HST Treasury Programme (Scoville et al., 2007a; Koekemoer et al., 2007; Massey et al., 2010). Due to the large size of the 1.8 deg^2 high-resolution mosaic (0.03″ /pix), individual postage stamps of galaxy candidates were retrieved from the NASA/IPAC archive[4] and visually inspected (after smoothing) as described in Section 2.3. The I_{814}-band image uses the same base astrometric reference as the COSMOS CFHT i^*-band image used as the standard reference for subsequent imaging within the COSMOS field and the UltraVISTA data as described above, hence no further transformations were applied.

2.2.4 Subaru Suprime-Cam z'-band imaging

Deep z'-band imaging is crucial for the selection of galaxies at $z > 6.5$. Since 2009 we have exploited the new red sensitivity provided by the refurbished Suprime-Cam instrument on Subaru to obtain very deep z'-band imaging over the central 1 deg^2 of the COSMOS field (i.e. matching, as near as possible, the CFHT imaging). The imaging consists of four Suprime-Cam pointings, each with $\gtrsim 15$ hours of exposure time, rotated by 90 deg with respect to each other. This yields a final z'-band mosaic reaching a minimum 5σ depth of $z' = 26.3$ (in a 2-arcsec diameter aperture), with the deepest panel reaching 0.3 mag deeper. To create the mosaic, the astrometry of each of the four pointings was matched to that of the Y-band UltraVISTA imaging using the IRAF package CCMAP, background-subtracted using SEXTRACTOR (Bertin & Arnouts, 1996), and the zero points were equalised to take into account the different exposure time of each pointing. A mosaic in the native pixel size (0.202″ /pix) was produced using SWARP (Bertin et al., 2002), where overlapping sections were combined with the WEIGHTED keyword using weights taken from an rms map created by SEXTRACTOR. A science image for use with the UltraVISTA datasets, overlapping the CFHT Legacy Survey image region with a pixel scale of 0.186″ /pix, was created using the IRAF package SREGISTER. The full Subaru mosaic overlaps the CFHTLS field that forms the search area in this thesis, with some sections extending beyond as can be seen in Fig. 2.1.

[4] `http://irsa.ipac.caltech.edu/data/COSMOS/index_cutouts.html`

2.2.5 Spitzer IRAC mid-infrared imaging

The full 2 deg^2 COSMOS field is covered by publicly-available mid-infrared data from *Spitzer* IRAC and MIPS obtained as part of the S-COSMOS survey (Sanders et al., 2007). All channels were imaged with an integration time of 1200 seconds. The IRAC 5.8μm and 8.0μm data are too shallow ($m_{\rm AB} = 21.3$ and 21.0 respectively, Sanders et al. 2007) for effective use in the present study, beyond visual inspection of our final candidate sample (see Section 2.3). However, the IRAC $3.6\,\mu$m and $4.5\,\mu$m images reach 5σ depths in a $2.8''$ diameter aperture of 24.2 and 23.8 mag respectively, are sufficiently well-matched to the UltraVISTA H and K_s depths to be of potential use in the galaxy selection process. In particular, low-redshift galaxy contaminants are predicted to be particularly bright at these wavelengths, in contrast to the much flatter near-infrared slope anticipated for genuine high-redshift galaxies. The *Spitzer* IRAC photometry was obtained in a $2.8''$ diameter aperture, from images that had been background subtracted with a large filter length using the GLOBAL keyword in SEXTRACTOR and then matched to the common pixel grid and area defined above. In acknowledgement of the limitations of photometry from the confused IRAC imaging, the 3.6 μm and 4.5 μm photometric errors used in the photometric redshift fitting described below were set to a minimum level of 20% of the measured flux density.

2.3 Candidate Selection

2.3.1 Initial detection, photometry and depth analysis

The primary catalogue was created using SEXTRACTOR v2.8.6 (Bertin & Arnouts, 1996) on the $Y+J$ stacked image, with photometry in the additional filters collected in the dual-image mode. Objects were also added to the catalogue from Y- and J-band selected catalogues, to ensure no galaxies were missed. However, all objects retained in the final sample were in fact selected from the $Y+J$ catalogue. All optical and near-infrared photometry was measured in a $2''$ diameter circular aperture, which corresponds to 70% enclosed flux (for a point source) in the Y-band imaging.

The global limiting magnitude for each image was calculated by finding the sigma-clipped standard deviation of the flux enclosed within $2''$ (or $1.2''$ where relevant) diameter circular apertures placed on the image in a grid. Apertures that contain

flux from an object were removed using the segmentation-map output produced by SExtractor, where aggressive parameter values were chosen to ensure detection of the majority of low-significance objects (exceeding 2σ significance in the detection procedure). For the final sample of objects presented in this Chapter, we undertook a local estimate of the photometric errors by finding the standard deviation of the 50 closest blank apertures placed around the object, with 2.5σ clipping.

The 5σ depth of the $Y+J$ image is 24.9 mag, and so, for simplicity, we cut our catalogue at $Y+J < 25.0$, resulting in an initial near-infrared selected sample of 175075 sources. To confine our search to potential objects at redshifts $z > 6.0$, we then applied a non-detection ($< 2\,\sigma$) criterion in all optical filters blueward of and including the i-band. Removing artefacts around bright stars and the small region of missing UltraVISTA data in the corner of our central survey area, resulted in a catalogue of 146 objects with $Y+J < 25.0$ and non-detections in all optical bands except for the CFHT z-band and/or Subaru z'-band imaging.

2.3.2 Sample refinement via SED fitting

In contrast to other studies which have endeavoured to select bright $z \simeq 7$ galaxies from ground-based data, we do not attempt to define areas in colour-colour space to isolate high-redshift galaxies. Fig. 2.2 clearly illustrates the difficulties in separating high-redshift galaxies from dwarf-star contaminants based on z', J and K_s photometry alone. The addition of Y-band data is crucial (as shown in Fig. 2.2), but again the use of only two colours does not make optimal use of the available multi-wavelength data. Therefore, as in our previous studies (e.g. McLure et al. 2009; 2010; 2011) we have used a full SED-fitting analysis to derive the redshift-probability distribution for each galaxy candidate. We employed the Bruzual & Charlot (2003) stellar evolution models, considering models with metallicities ranging from solar ($Z_{\odot}$) to 1/50th solar ($0.02Z_{\odot}$). The star-formation histories considered were instantaneous bursts, constant and exponentially declining with characteristic timescales in the range 50 Myr $< \tau <$ 10 Gyr. The ages of the stellar populations models were allowed to range from 10 Myr to 13.7 Gyr, but were required to be less than the age of the Universe at each redshift. Dust reddening was described by the Calzetti et al. (2000) attenuation law, and allowed to vary within the range $0.0 \leq A_{\rm V} \leq 4.0$. Inter-galactic medium absorption short-ward of Lyα was described by the Madau (1995) prescription, and a Chabrier (2003) IMF was assumed in all cases. Further details can be found in McLure et al. (2011). Specifically for this study we have included detailed fitting of the spectra of

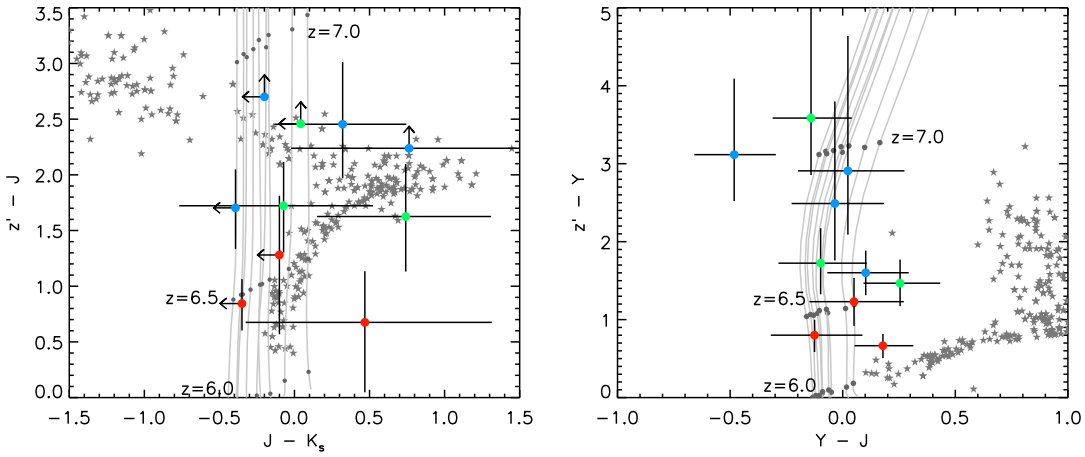

Figure 2.2 *Colour-colour plots of our final ten candidates selected by SED fitting. The most secure high-redshift candidates are shown in blue. Candidates that are likely to be at high redshift, but where we cannot completely exclude the possibility they are dwarf stars or low-redshift galaxy contaminants, are shown in green. Finally, our our three least secure candidates are shown in red. The large uncertainty in the $J - K_s$ colour is a consequence of the relative shallowness of the K_s imaging as compared to the $Y + J$ detection band (which also results in a few of our candidates being formally undetected in the K_s image). The colours of M, L and T-dwarf stars are shown with a star symbol, and were obtained from photometric surveys (Knapp et al., 2004; Burningham et al., 2010) and by calculating synthetic magnitudes from spectra obtained from several libraries as described in Findlay et al. (2012). The grey tracks indicate the evolution of colours with redshift for high-redshift Lyman-break galaxies as synthesised from the theoretical SEDs of Bruzual & Charlot (2003), assuming a constant star-formation history, and a range of other parameter values ($Z = 0.2\,\mathrm{Z}_{\odot}$, $A_V = 0.0 - 0.5$, $\mathrm{age} = 50 - 500\,Myr$). Appropriate redshift steps are illustrated with grey circles situated along the tracks at $z = 6, 6.5$ and 7. Absorption by the Intergalactic Medium is applied with the Madau (1995) prescription, with additional suppression of the flux blueward of $\lambda_{\mathrm{rest}} = 1216\,\AA$ at the very highest redshifts (parameterised as $e^{-2((1+z)/6)^4}$ from Patel, 2010).*

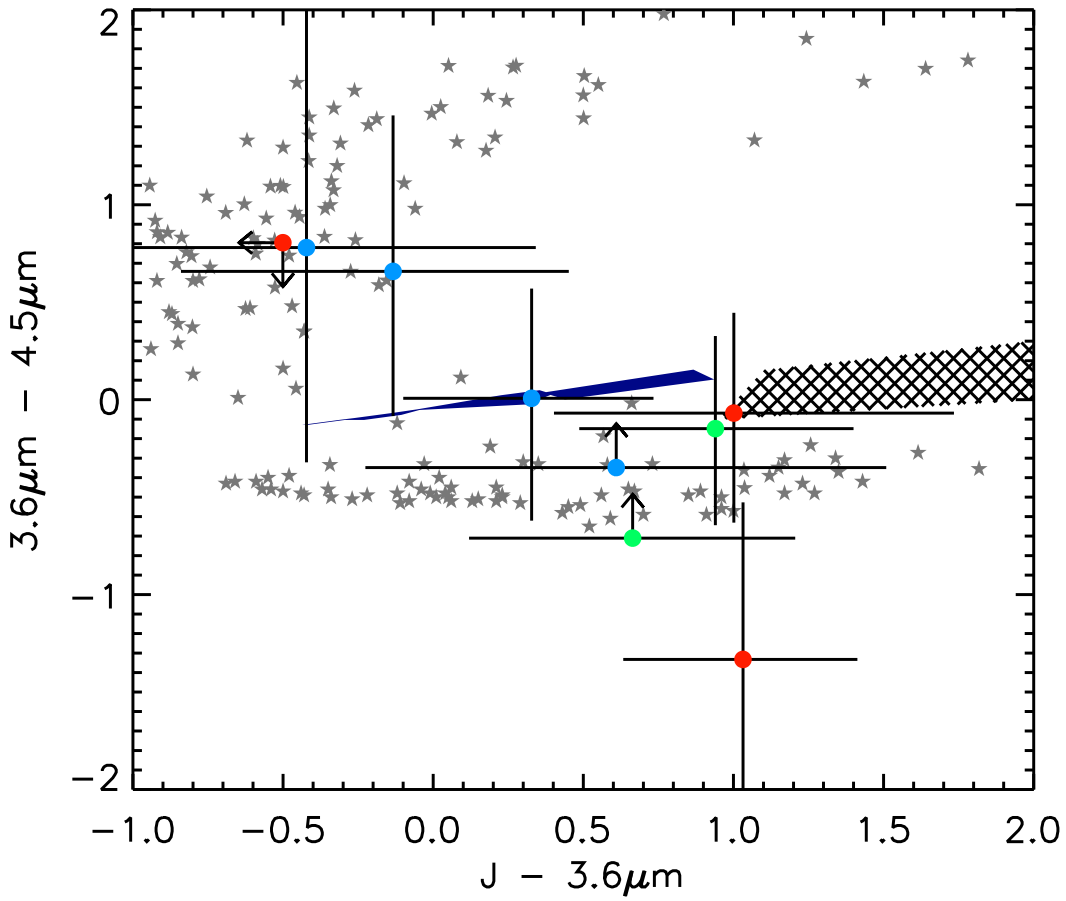

Figure 2.3 *The colours of our high-redshift galaxy candidates (shown as the coloured circles) using the Spitzer IRAC information, where the most secure candidates are shown in blue, the robust/contaminant category are shown in green and the insecure category are shown in red. The colours of M, L and T-dwarf stars are shown with grey star symbols from Kirkpatrick et al. (2011) and Patten et al. (2006), where the error bars are all below 0.05 mag. Predicted colours of low-redshift contaminant galaxies* ($1.3 < z < 1.9$) *are shown by the hatched area, where reddening increases to redder* $J - 3.6\mu$*m colours (from* A_V *= 0 to* ~ 2 *at the right-hand edge of the plot). The thin navy wedge represents the predicted colours of high-redshift galaxies using the models and parameter ranges as in Fig. 2.2. Flux densities below the* 2σ *level were set to the* 2σ *depth and the resulting colour limits plotted as an arrow. Note that T-dwarf stars have the reddest 3.6*μ*m - 4.5*μ*m colours, whereas L and M types all have slightly bluer colours and occupy the lower horizontal band of stars.*

L, M and T dwarf stars, where the reference spectra from the speX library[5] were used for each spectral type from M4 through to T8. Only for the final sample of galaxies presented in Section 2.4 did we introduce the equivalent width (EW) of the Lyα -line in the SED-fitting analysis as an extra free parameter, with the rest-frame equivalent width within the range 0 Å $< EW_0 < 240$ Å.

SED fitting was performed using all the multi-wavelength data, including the CFHTLS z-band data (although it is significantly shallower than the Subaru z'-band image, it has a slightly bluer effective wavelength and thus adds some extra spectral resolution to the fitting process). The IRAC photometry was only included in the final stages of candidate selection due to the large uncertainties involved and the high number of objects where the photometry is confused. All near- and far-infrared photometry was corrected to the 84% enclosed flux level of the z'-band imaging for the SED fitting, where the enclosed flux within a $2''$ diameter aperture was calculated from the point spread function obtained by taking the median of unsaturated stars extracted from each image.

The output redshift-χ^2 distribution from the SED fitting (without the IRAC photometry) was used to determine which of the 146 candidates were consistent with being at high redshift. We applied the criteria that the object must have an acceptable solution at $z > 6.0$, and that the $z > 6.0$ template must be preferred ($\Delta\chi^2 > 0.0$) over the alternative low-redshift galaxy solution (usually produced at a redshift where the putative Lyman-break can be interpreted as a Balmer or 4000Å break). Here we define an 'acceptable' solution as one in which $\chi^2 < 11.3$, calculated as the χ^2 value that corresponds to 2σ significance over the expected (mean) χ^2 given 5 degrees of freedom [6]. These conditions resulted in a reduced sample of 68 objects consistent with being at $z > 6.0$. Further inspection of the i-band image, in combination with the HST/ACS I_{814} image and an inverse-variance weighted stack of the optical bands up to and including i, resulted in the removal of a further 21 objects with weak detections in these bands implying $z < 6.5$.

As a result of the SED fitting and manual optical checks, the sample of potential $z > 6.5$ galaxies was reduced to 47 objects. However many of these still had formally-acceptable solutions at much lower redshift. At this point the IRAC $3.6\,\mu$m and $4.5\,\mu$m measurements were incorporated into the SED-fitting analysis, in effect to remove the red dusty low-redshift galaxy interlopers which display a much redder $J - 3.6\mu$m

[5] `http://pono.ucsd.edu/~adam/browndwarfs/spexprism/`

[6] A χ^2 distribution with k degrees of freedom, which is defined as the number of data points with the number of free parameters of the model subtracted, has a mean of k and a variance of $2k$.

colour than genuine high-redshift galaxies. In practice the IRAC photometry was simply incorporated into the full SED fitting, but the process is illustrated in colour-colour space in Fig. 2.3 which shows the (hashed) area at $J - 3.6\,\mu\mathrm{m} > 1$ where low-redshift dusty interlopers are generally found. At this stage all the observed optical–to–near-infrared SEDs were also fitted to the SEDs of L, M, T dwarf stars and objects were rejected if the dwarf-star solution was formally preferred over the high-redshift galaxy solution. The lack of mid-infrared spectroscopy of dwarf stars prevented the simple incorporation of the IRAC measurements into the dwarf-star SED-fitting process, but we were able to confirm a number of ambiguous dwarf-star solutions on the basis of the position of the object on the colour-colour plots shown in Fig. 2.2 and Fig. 2.3. The final result of this IRAC-based cull was a remaining sample of 17 potential $z > 6.5$ galaxies.

The final stage of sample refinement involved detailed re-investigation of every single galaxy image, and repetition of the dwarf-star fitting using photometry taken in a smaller $1.2''$ diameter circular aperture (with the expectation that, in the case of a real star, the fit should improve with the smaller aperture photometry). Galaxy colours were also calculated from smaller-aperture photometry for comparison. As a consequence of these final checks, three objects were excluded because of low-level flux detected in the optical stack, in combination with insecure photometry that resulted in the objects drifting substantially around the colour-colour diagrams when smaller apertures were used. A further two objects were only detected in the Y-band image, and closer inspection revealed them to be part of a faint diffraction halo around a bright star. Finally two objects were confirmed as secure $z > 6$ galaxies, but their redshift-probability distributions indicated that they could not lie above $z = 6.5$.

The final outcome is a sample of 10 objects which have survived as credible candidate Lyman-break galaxies at $z > 6.5$, and which we deem worthy of presentation in this Chapter. The magnitude errors and SED fits for these objects presented in subsequent sections are all based on the local error estimates (although these are all formally consistent with the global error estimates). We visually inspected the $5.8\,\mu$m and $8.0\,\mu$m *Spitzer*/IRAC imaging for our final 10 candidates, finding no evidence for even low-level flux (as expected given the magnitudes predicted by the SED fits, and the depths of the S-COSMOS IRAC imaging at these longer wavelengths; see Section 2.2.5).

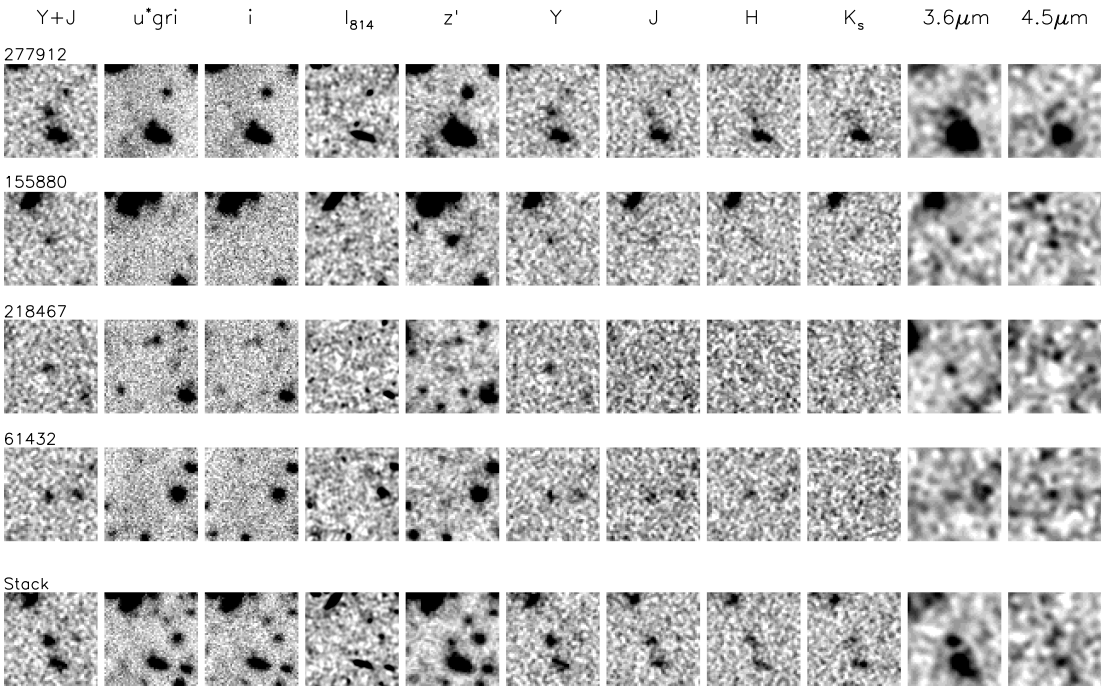

Figure 2.4 *Multi-band postage-stamp images of the four most secure $z \simeq 7$ galaxies, with the detection image ($Y + J$) shown on the left. A stack of these four objects is presented in the bottom row. The stamps are $10'' \times 10''$, with North up, and East to the left. Each filter stamp has a linear grayscale, with the lower level (white) set to 2σ below the background level and objects (black) saturated at 4.5σ above the background level. To aid the visual detection of low-level flux indicative of a $z < 6.5$ contaminant object, the I_{814} stamp has been smoothed using the* IRAF GAUSS *package, with a standard deviation of 5 pixels.*

2.4 Candidate $z > 6.5$ Galaxies

Table 2.2 details the photometry of the final ten $z > 6.5$ galaxy candidates, where we have grouped them into three categories depending on the statistical security of their $z > 6.5$ solutions. The final galaxy and dwarf-star SED fits for these ten candidates are presented in Fig. 2.5. Their photometric redshifts and derived physical properties such as stellar masses and star-formation rates are presented in Table 2.3.

2.4.1 Category 1 - Robust

Our four most secure $z > 6.5$ galaxy candidates have completely unacceptable alternative fits for either a low-redshift dusty galaxy or a late-type dwarf star from the SED fitting analysis, and are all very well described by a high-redshift galaxy template

Table 2.2 *Photometry of the ten $z > 6.5$ galaxy candidates, grouped into the three categories described in the main text. From top to bottom the top four galaxies are classed as "Robust" (followed by the photometry for a stack of this subset of galaxies), the next three as "Robust/Contaminant", and the final three can be regarded as "Insecure". The optical and near-infrared magnitudes were measured within a 2″ diameter circular aperture and corrected to 84% enclosed flux, and the IRAC magnitudes were measured within a 2.8″ diameter circular aperture and corrected to 84% enclosed flux. As a consequence of the correction up to 84% enclosed flux, the Y- and J-band magnitudes presented here appear typically ~ 0.2 brighter than the quoted 2-arcsec diameter 5σ limit (see Table 2.1). Wherever the measured flux density lies below the 2σ limit in that band, the magnitude has been replaced here by the 2σ limiting magnitude depth of the appropriate image, and is given as a lower limit on the apparent magnitude.*

ID	RA	DEC	z'	Y	J	H	K_s	3.6μm	4.5μm
277912	10:00:43.38	+02:37:51.8	$26.7^{+0.4}_{-0.3}$	$24.2^{+0.2}_{-0.1}$	$24.3^{+0.2}_{-0.2}$	$24.0^{+0.3}_{-0.2}$	$23.9^{+0.3}_{-0.2}$	$23.9^{+0.3}_{-0.2}$	$23.9^{+0.4}_{-0.3}$
155880	10:02:06.49	+02:13:24.1	$26.1^{+0.1}_{-0.1}$	$24.5^{+0.2}_{-0.2}$	$24.4^{+0.2}_{-0.2}$	$24.4^{+0.4}_{-0.3}$	> 24.8	$24.5^{+0.5}_{-0.3}$	$23.9^{+0.4}_{-0.3}$
218467	10:01:52.31	+02:25:42.3	> 27.3	$24.6^{+0.2}_{-0.2}$	$25.1^{+0.6}_{-0.4}$	> 25.0	$24.3^{+0.4}_{-0.3}$	$24.4^{+0.5}_{-0.3}$	> 24.8
61432	10:01:40.70	+01:54:52.5	> 27.3	$24.6^{+0.2}_{-0.2}$	$24.6^{+0.3}_{-0.2}$	$24.4^{+0.4}_{-0.3}$	> 24.8	$25.0^{+1.0}_{-0.5}$	$24.2^{+0.6}_{-0.4}$
Stack			$27.0^{+0.2}_{-0.2}$	$24.5^{+0.1}_{-0.1}$	$24.6^{+0.1}_{-0.1}$	$24.4^{+0.2}_{-0.2}$	$24.6^{+0.3}_{-0.2}$	$24.4^{+0.2}_{-0.2}$	$24.6^{+0.4}_{-0.3}$
277880	10:01:36.86	+02:37:49.3	$26.4^{+0.2}_{-0.2}$	$24.7^{+0.2}_{-0.2}$	$24.7^{+0.3}_{-0.2}$	$24.9^{+1.0}_{-0.5}$	$24.0^{+0.4}_{-0.3}$	$24.1^{+0.3}_{-0.2}$	> 24.8
268511	10:00:02.36	+02:35:52.2	> 27.3	$24.7^{+0.3}_{-0.2}$	$24.8^{+0.4}_{-0.3}$	$24.8^{+0.5}_{-0.3}$	> 24.8	> 25.2	> 24.8
271105	09:59:07.60	+02:36:24.4	$26.1^{+0.2}_{-0.2}$	$24.7^{+0.2}_{-0.2}$	$24.4^{+0.3}_{-0.2}$	$24.2^{+0.2}_{-0.2}$	$24.5^{+0.5}_{-0.3}$	$23.5^{+0.2}_{-0.2}$	$23.6^{+0.3}_{-0.2}$
95661	10:01:20.70	+02:01:44.0	$25.4^{+0.1}_{-0.1}$	$24.6^{+0.5}_{-0.3}$	$24.7^{+0.5}_{-0.4}$	$25.0^{+1.0}_{-0.5}$	$24.3^{+0.4}_{-0.3}$	$23.7^{+0.2}_{-0.2}$	$23.8^{+0.4}_{-0.3}$
28400	10:00:58.01	+01:48:15.6	$25.3^{+0.1}_{-0.1}$	$24.6^{+0.2}_{-0.1}$	$24.4^{+0.2}_{-0.2}$	$24.5^{+0.4}_{-0.3}$	> 24.8	$23.4^{+0.2}_{-0.2}$	$24.7^{+1.2}_{-0.6}$
2233	10:01:43.16	+01:42:53.5	$26.0^{+0.2}_{-0.1}$	$24.7^{+0.4}_{-0.3}$	$24.7^{+0.6}_{-0.4}$	> 25.0	> 24.8	> 25.2	$24.4^{+0.7}_{-0.4}$

at $z > 6.5$, as can been seen in Fig. 2.5.

Object 277912 has $z'-Y = 2.5$ and a flat near-infrared SED through to the IRAC bands, with a best-fitting spectral template corresponding to a galaxy with $z_{\rm phot} = 6.97^{+0.06}_{-0.07}$. As can be seen from the postage stamps presented in Fig. 2.4, a low-redshift galaxy is present $\sim$2.5$''$ away from the position of our high-redshift candidate in the Y-band imaging. The companion has a photometric redshift of $z_{\rm phot} = 0.94 \pm 0.10$ from the COSMOS Photometric Redshift Catalogue (Ilbert et al., 2008) and $z_{\rm phot} = 1.18 \pm 0.10$ from our own fitting of the 2$''$ diameter aperture photometry. The χ^2 distribution for object 277912 indicates that the low-redshift solution is not only extremely unlikely, but would also lie at $z \sim 1.7$. Hence it seems clear that this object is at high redshift and not associated with the low-redshift foreground galaxy. Unfortunately the presence of the foreground galaxy means that the IRAC photometry, where the FWHM of the PSF is $\sim 1.7''$, is confused, and therefore the stellar mass estimate is uncertain. Allowance for a possible contribution from Lyman-α emission in the SED fitting does not change the photometric redshift, with zero Lyman-α emission remaining the preferred option.

Object 155880 also has a blue spectral slope in the near-infrared bands and is clearly detected in the deep Subaru z'-band imaging giving a $z_{\rm phot} = 6.78^{+0.06}_{-0.09}$. We stress that the z'-band detection ($z' = 26.1 \pm 0.1$) is achieved because the Subaru Suprime-CAM z'-band imaging is so deep and the filter extends to $\sim 1\mu$m; the measured spectral break is still large $z' - Y > 1.5$, although not large enough to warrant inclusion as a high-redshift candidate in some traditional colour-colour cut selection methods (e.g. $z' - Y/J \gtrsim 2$). Fitting with the addition of a Lyα line always results in a higher derived photometric redshift, as for the same observed magnitude in a filter which includes the Lyman-break, the additional flux introduced by including the emission line must be offset by increasing the redshift of the object (which determines how much of the filter in question is filled by the SED of the galaxy at wavelengths longer than 1216Å). Indeed for this object we find a slightly higher-redshift fit with $z_{\rm phot} = 6.98$ (with a Lyα-line $EW_0 = 40$ Å), although the errors on these values are large than for continuum only fits as the photometric redshift and EW are strongly degenerate. The best-fitting stellar template of an earlier type T-dwarf star (T3) can produce the $z' - Y$ colour, but not the other near-infrared colours, with the result that the high-redshift galaxy solution is the only acceptable SED fit. The IRAC 3.6μm - 4.5μm = 0.6 colour is redder than would be predicted directly from constant SFR models, but there is evidence (Curtis-Lake et al., in preparation) that a multiple-component star-formation history or a significant contribution from nebular emission can reproduce this spectral shape. Inspection of the smoothed ACS I_{814}-band imaging shown in Fig. 2.4 shows a low-significance (2.3σ)

detection $0.5''$ from our object. However, given that our astrometric accuracy is better than $0.2''$, we conclude that this detection is unrelated to our candidate.

Object 218467 has the bluest $Y - J$ colour of all our candidates as shown in the colour-colour plot in Fig. 2.2, which results in unacceptable SED fits for both the low-redshift and stellar templates, as neither can reproduce both the magnitude drop between z' and Y and the blue spectral slope at longer wavelengths. The J-band detection is below the 5σ limit of the data and hence there is a large uncertainty in the extremely blue $Y - J = -0.5$ colour (bluer than predicted by our range of models; see Fig. 2.2). The candidate is formally undetected in the current K_s and H-band imaging which leads to a large uncertainty on these data points in the SED fitting. However, when a smaller $1.2''$ diameter aperture is used, marginal detections produce a flat spectral shape as seen in the dwarf-star SED fit figure. A faint detection in the z'-band is consistent with the $z_{\rm phot} = 7.04^{+0.10}_{-0.08}$ within the errors, although the detection here is best fitted with inclusion of a strong Lyα line of $EW_0 = 110$ Å at the very red end of the Subaru z'-band filter at $z_{\rm phot} = 7.20$. Fig. 2.4 shows a detection in the IRAC 3.6 μm image consistent with a flat SED extending from the near-infrared data, but the 4.5 μm image appears to have a negative hole at the position of our object. The implied stellar mass of 218467 is the lowest of the four robust candidates, indicating that it may be underestimated as a result of the potentially spurious lack of 4.5 μm flux. Alternatively, the implied blue 3.6μm - 4.5μm slope could indicate the presence of strong nebular emission lines.

Finally, object 61432 has a flat near-infrared spectral slope and has a strong spectral break, with only a marginal detection in the z'-band. The somewhat red 3.6μm - 4.5μm colour might appear difficult to reconcile with a high-redshift SED as illustrated in Fig. 2.3, but the error bars are large and neither a late-type dwarf star nor a low-redshift galaxy provide remotely acceptable solutions. As with the first object above (object 277912) allowance for a possible contribution from Lyman-α emission in the SED fitting does not change the photometric redshift, with zero Lyman-α emission remaining the preferred option.

2.4.2 Category 2 - Robust/Contaminant

The three candidates that make up category 2 are all still consistent with being at high redshift, and the $z > 6.5$ galaxy solution is still formally preferred. However, with the current data we cannot exclude the possibility that these objects could be either at low redshift or galactic dwarf stars.

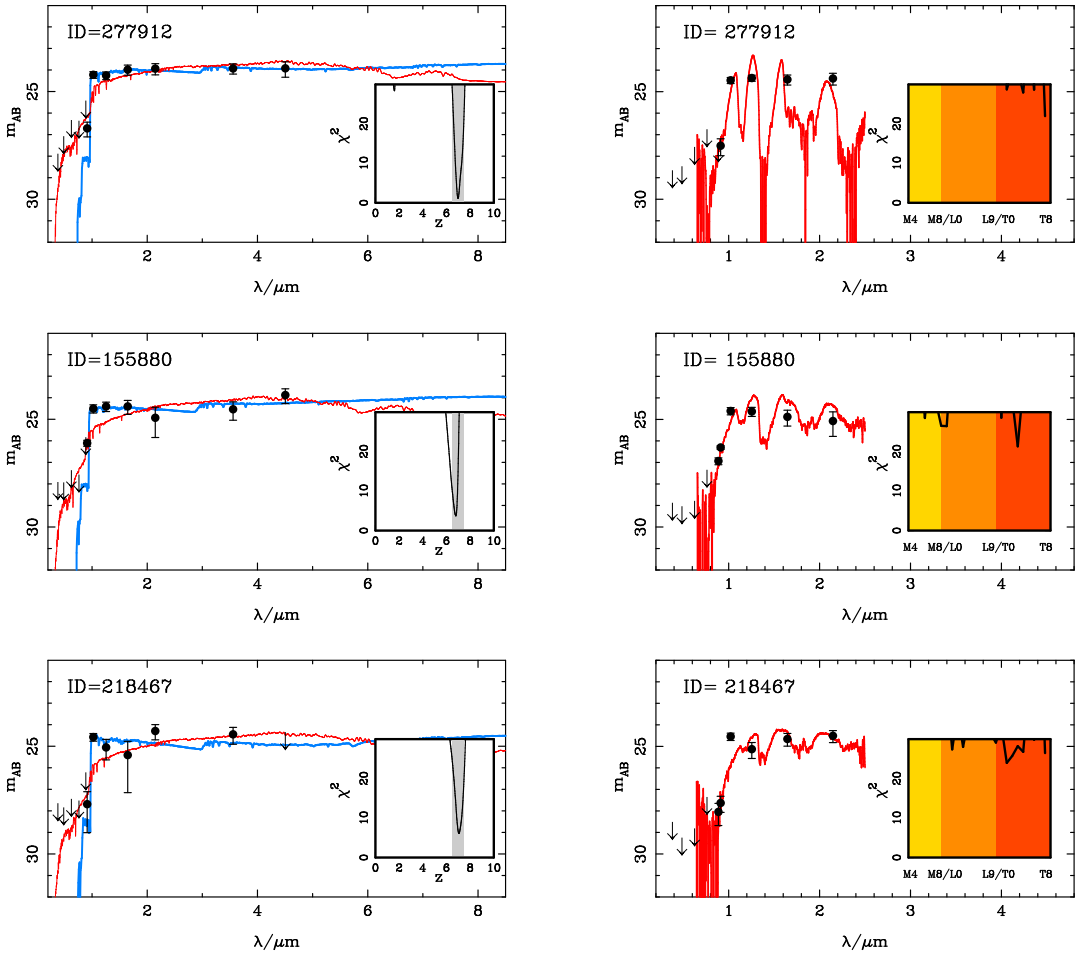

Figure 2.5 *SED fits for each member of the final sample of ten high-redshift galaxies. Where the candidate has a non-detection (below the 1σ level) in a given band, that point has been plotted with an arrow where the tip represents the 1σ limiting depth. The best-fitting high-redshift galaxy template (without Lyα) is shown in blue in the left hand panel, with the best-fitting alternative low-redshift template shown in red. The inset shows the redshift-χ^2 distribution produced in the fitting process, where the redshift range $6.5 < z < 7.5$ targeted in this study is highlighted in grey. The best-fitting low-redshift galaxy templates have a redshift around $z \simeq 1.2 - 1.6$, due to the fact that a 4000Å/Balmer break in the model galaxy spectra can sometimes reproduce the observed spectral break at $\sim 1\mu$m if the data have insufficient dynamic range. For each object the best-fitting stellar template is shown in the right-hand panel, where photometry measured in a 1.2″ diameter aperture has been used. The inset for the dwarf-star plots shows the χ^2 distribution versus stellar type, with effective temperature decreasing from M4 through to T8. The resulting best-fit photometric redshift, stellar type and derived parameters are detailed in Table 2.3.*

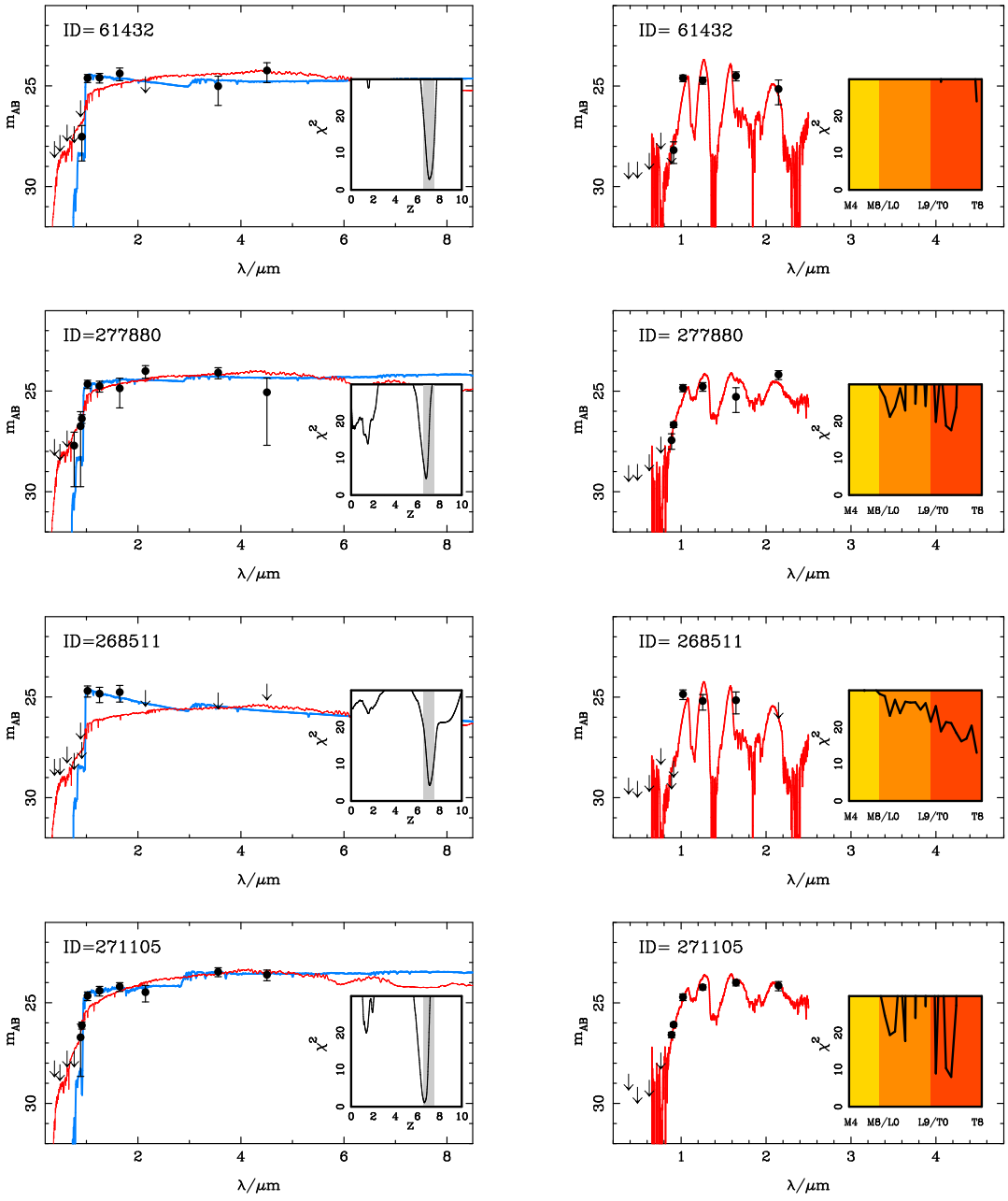

Figure 2.5 *Continued.*

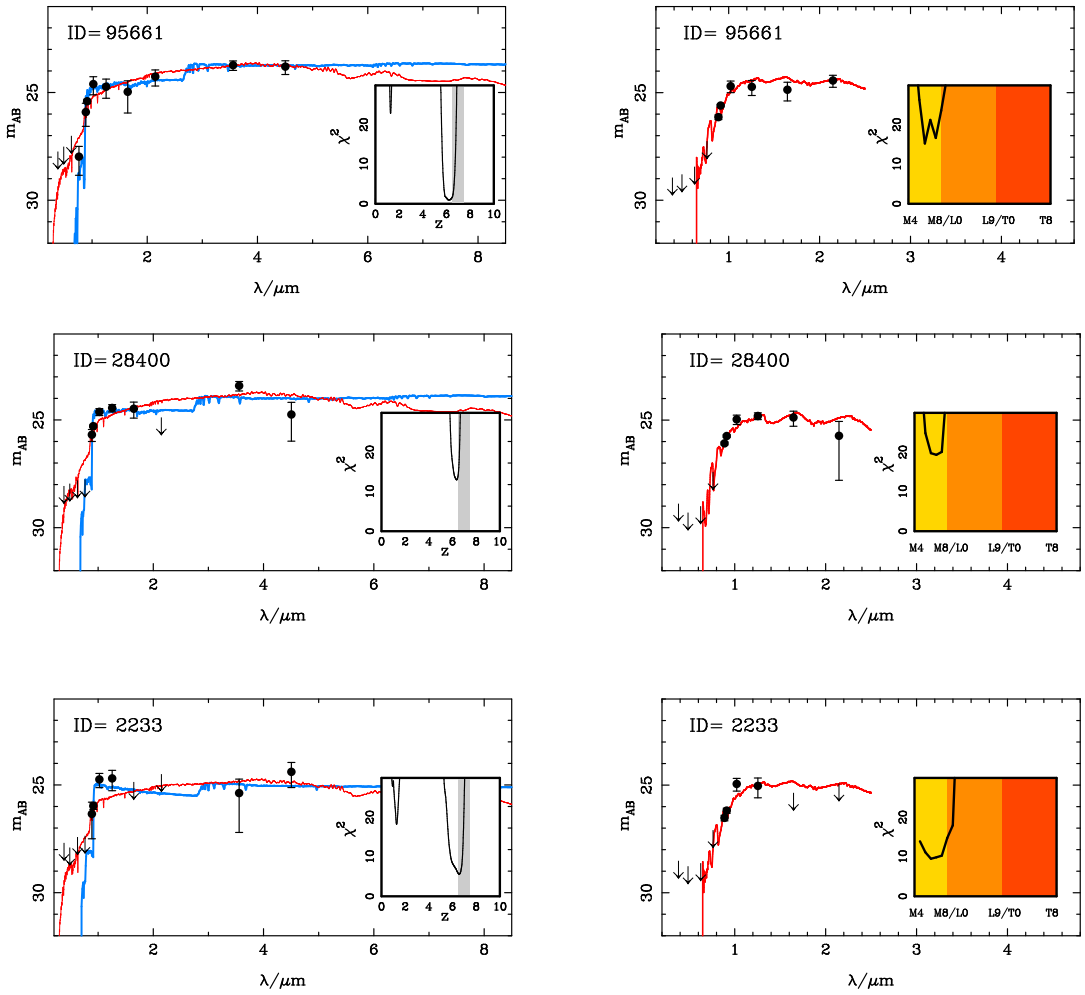

Figure 2.5 *Continued.*

Table 2.3 *Results from SED fitting of the ten $z > 6.5$ galaxy candidates. The photometric redshift for the high-redshift solution is given, along with the raw $\chi^2_{\rm gal}$, for fitted galaxy templates with or without a contribution from Lyα line emission. The dust-extinction (A_V) and metallicity (Z) values given in columns 4 and 5 are taken from the best-fitting model across all star-formation histories considered (but without Lyα). For the fits involving Lyα we give simply the inferred photometric redshift and the rest-frame equivalent width (EW_0) of the Lyα line as selected by the best-fitting model. By definition, the $\chi^2_{\rm gal}$ values for the Lyα fits are either the same as, or lower than the $\chi^2_{\rm gal}$ values given for the continuum-only fits as listed in column 3, while the photometric redshifts inferred from the Lyα fits are (inevitably) either the same as, or greater than those given in column 2. Note that as a result of including the IRAC photometry in the final stages of SED fitting, the χ^2 values here can exceed the $\chi^2 < 11.3$ condition stated in Section 2.3.2. Columns 9 and 10 give the key information for the best-fitting dwarf-star SED fits (note that, because of the different number of degrees of freedom, the values of $\chi^2_{\rm stellar}$ cannot be directly compared with the corresponding values for the galaxy fits). Finally, in the last 5 columns we give derived physical parameters for these objects without Lyα in the fitting. For stellar mass (M_*) we simply quote the range of possible stellar masses as calculated from tau, constant or burst star-formation models, while the tabulated star formation rate (SFR) and specific SFR (sSFR) are calculated from the best-fitting constant star-formation model. The A_V value for the best-fitting constant star-formation model is also presented, where the most extreme SFRs are inevitably coupled with the larger dust-reddening values (see the discussion in Section 2.6). The final column gives the SFR estimated directly from the (observed) rest-frame UV luminosity (i.e. assuming zero dust extinction), using the Madau, Pozzetti, & Dickinson (1998) prescription (dividing by a factor of 1.8 to convert from a Salpeter to a Chabrier IMF).*

	No Lyα				With Lyα			Stars		Constant SFH				
ID	$z_{\rm gal}$	$\chi^2_{\rm gal}$	A_V	Z	$z_{\rm gal}$	$\chi^2_{\rm gal}$	EW_0	Stellar	$\chi^2_{\rm stellar}$	M_*	SFR	A_V	sSFR	$\rm SFR_{UV}$
			mag	$\rm Z_\odot$			Å	Type		$10^9\rm M_\odot$	$\rm M_\odot yr^{-1}$	mag	$\rm Gyr^{-1}$	$\rm M_\odot yr^{-1}$
277912	$6.97^{+0.06}_{-0.07}$	1.1	0.7	1.0	6.97	1.1	0	T8	21.9	4.1 - 8.1	330	0.7	34.2	44
155880	$6.78^{+0.06}_{-0.09}$	3.7	0.5	0.2	6.98	2.8	40	T3	21.3	3.5 - 5.1	110	0.5	11.4	32
218467	$7.04^{+0.10}_{-0.08}$	6.1	0.0	1.0	7.20	4.9	110	T1	23.9	1.6 - 2.0	53	0.2	5.7	31
61432	$7.07^{+0.14}_{-0.10}$	2.8	0.2	0.2	7.07	2.8	0	T8	23.9	1.8 - 2.7	52	0.2	5.5	31
Stack	$6.98^{+0.05}_{-0.05}$	2.6	0.3	1.0	7.12	1.5	40	T3	37.9	3.0 - 4.0	98	0.4	32.7	32
277880	$6.77^{+0.07}_{-0.08}$	4.5	0.8	1.0	6.77	4.5	0	T3	17.5	2.8 - 7.1	280	0.8	29.7	26
268511	$7.09^{+0.12}_{-0.10}$	4.2	0.0	0.2	7.22	3.9	50	T8	13.0	0.4 - 1.2	41	0.0	4.8	28
271105	$6.62^{+0.13}_{-0.11}$	1.1	0.0	1.0	6.97	0.8	70	T3	8.0	8.3 - 22.4	830	1.2	83.7	26
95661	$6.13^{+0.38}_{-0.27}$	1.0	0.0	1.0	6.13	1.0	0	M6	15.2	13.2 - 24.5	69	0.5	6.6	25
28400	$6.34^{+0.11}_{-0.19}$	13.0	0.0	1.0	6.65	11.5	70	M7	19.3	8.7 - 15.1	39	0.2	3.8	26
2233	$6.56^{+0.14}_{-0.23}$	5.6	0.0	0.2	7.03	4.3	150	M6	9.5	2.3 - 5.9	15	0.0	1.6	25

The best-fitting SED for object 277880 is a galaxy at $z_{\rm phot} = 6.77^{+0.07}_{-0.08}$. However, because of a strong z'-band detection in combination with a relatively red spectral-slope through the near-infrared bands, the low-redshift solution at $z = 2.0$ cannot be completely excluded. A stellar fit of type T3, although not as good as that of the high-redshift galaxy SED fit, cannot be completely excluded either. However, the flat $Y - J$ colour is hard to reproduce with either a low-redshift galaxy or dwarf-star fit, and so the $z > 6.5$ galaxy solution is still favoured for 277880. Allowance for a possible contribution from Lyman-α emission in the SED fitting does not change the photometric redshift, with zero Lyman-α emission remaining the preferred option.

For object 268511, the SED fitting again indicates that the high-redshift solution is the best fit, with the strong $z' - Y > 2.6$ break resulting in $z_{\rm phot} = 7.07^{+0.12}_{-0.10}$ and excluding all stellar fits except for the reddest T-dwarfs. Inspection of the postage-stamps for this object, however, shows that it is only clearly seen by eye in the Y-band where it is compact, and therefore it could be a transient object or a T8 star. In this case, allowance for a possible contribution from Lyman-α emission in the SED fitting raises the photometric redshift to $z_{\rm phot} = 7.22$, with an implied Lyman-α rest-frame equivalent width of $EW_0 = 50$ Å.

Finally, 271105 has a best fitting high-redshift SED with $z_{\rm phot} = 6.62^{+0.13}_{-0.11}$, with a higher-redshift solution ($z_{\rm phot} = 6.97$) possible with the introduction of Lyα emission with $EW_0 = 70$ Å. A clear detection in the z'-band does, however, allow the stellar fit for a T3 dwarf to recreate the spectral break. However, the red $J-3.6\mu$m colour of 271105 is inconsistent with a T-dwarf star (the object is well detected and unconfused in all near-infrared bands). Hence, although we cannot rule a stellar solution, it still seems highly likely that 271105 is indeed a high-redshift galaxy.

2.4.3 Category 3 - Insecure

The final three candidates all have good SED fits to a high-redshift galaxy template, with photometric redshifts $z < 7.0$ due to clear z'-band detections. However, for these objects an M-dwarf stellar fit cannot be completely excluded, and some of the photometric redshift estimates suggest a redshift just below $z = 6.5$. For both these reasons we classify these objects as insecure $z > 6.5$ galaxies.

Object 95661 has a high-redshift galaxy fit with $z_{\rm phot} = 6.13^{+0.38}_{-0.27}$, and so still has some probability of being at $z > 6.5$ (although here the introduction of Lyα emission does not increase the inferred redshift). A dwarf star of type M6 can also reproduce the flat

near-infrared photometry as well as the spectral break, and so cannot be excluded.

Object 28400 has a high-redshift galaxy fit with $z_{\rm phot} = 6.34^{+0.11}_{-0.19}$ but in this case is actually better fitted with the inclusion of a Lyα emission line with $EW_0 = 70\,$Å increasing the inferred redshift above the $z = 6.5$ threshold to $z_{\rm phot} = 6.65$. The IRAC photometry shows a bright detection in the 3.6 μm image but nothing in the 4.5 μm data despite the similar depth, implying a break of at least 3.6μm - 4.5μm < -1.4 (taking the 2σ limit for 4.5 μm). A possible explanation would be an M-dwarf star which can produce this blue colour within the error bars as shown in Fig. 2.3. One alternative explanation for the blue 3.6μm - 4.5μm colour would be nebular emission.

Finally, object 2233 has a clear z'-band detection, but is weak in Y+ J and the other infrared bands. The high-redshift galaxy fit is comparable in quality to that of a M6 star and the weak near-infrared photometry allows the inclusion of a Lyα line of $EW_0 = 150\,$Å which raises the photometric redshift to $z_{\rm phot} = 7.03$.

2.5 Comparison with Previous Studies

Several other ground-based studies have attempted to determine, or at least place a meaningful limit on the very bright end of the galaxy UV luminosity function at $z \sim 7$, using deep near-infrared photometry and colour cuts to attempt to exclude low-redshift galaxies and cool galactic dwarf-star contaminants.

2.5.1 Capak et al. (2011)

Of particular relevance to this thesis is previous work within the COSMOS field undertaken by Capak et al. (2011). They utilised the deepest multi-wavelength data over the full COSMOS $2\,\mathrm{deg}^2$ field available at the time, in particular optical data from Subaru including the i^+ and z^+-bands, near-infrared data in the J-band from UKIRT/WFCAM and H, K_s imaging from CFHT/WIRCam (Bielby et al., 2012; McCracken et al., 2010). Galaxy candidates were selected in the K_s-band with a 5σ cut in the J and K_s bands of 23.7 mag ($3''$ diameter aperture) applied along with the colour conditions $z' - J \geq 1.5$, $K_s - 4.5\mu m > 0$ and $J - K_s > 0$. They found three objects consistent with being at $z > 7$ as defined by their colour-colour criterion, and presented follow-up spectroscopy which, along with SED fitting, resulted in the rejection of one object (C2 below) as most likely lying at much lower redshift. Since the near-infrared data from UltraVISTA extends to around one magnitude deeper than that exploited by Capak et al. (2011) in the J-band (with improved seeing) and also provides Y-band imaging that greatly improves the separation of contaminant populations (as described previously), we have extracted new photometry for all three of these objects and undertaken SED fitting in the same manner as described above for our own, new deeper sample of objects. Since none of the Capak et al. (2011) candidates actually made it into the sample described above, it should not be a surprise that, as described below, we fail to confirm that they lie at $z > 6.5$.

The first object presented by Capak et al. (2011), hereafter C1, in fact lies just outside the area of overlapping deep data utilised in this thesis and, as a consequence, the CFHTLS and new deeper Subaru z'-band imaging is unavailable. However, C1 is still within the $1.5\,\mathrm{deg}^2$ of the UltraVISTA imaging that extends beyond the central $\sim 1\,\mathrm{deg}^2$ area, as seen in Fig. 2.1. With the deeper near-infrared data, most importantly the Y-band, we obtained photometry for this object to check the consistency of the photometric redshift calculated in Capak et al. (2011). Near-infrared photometry was measured within a

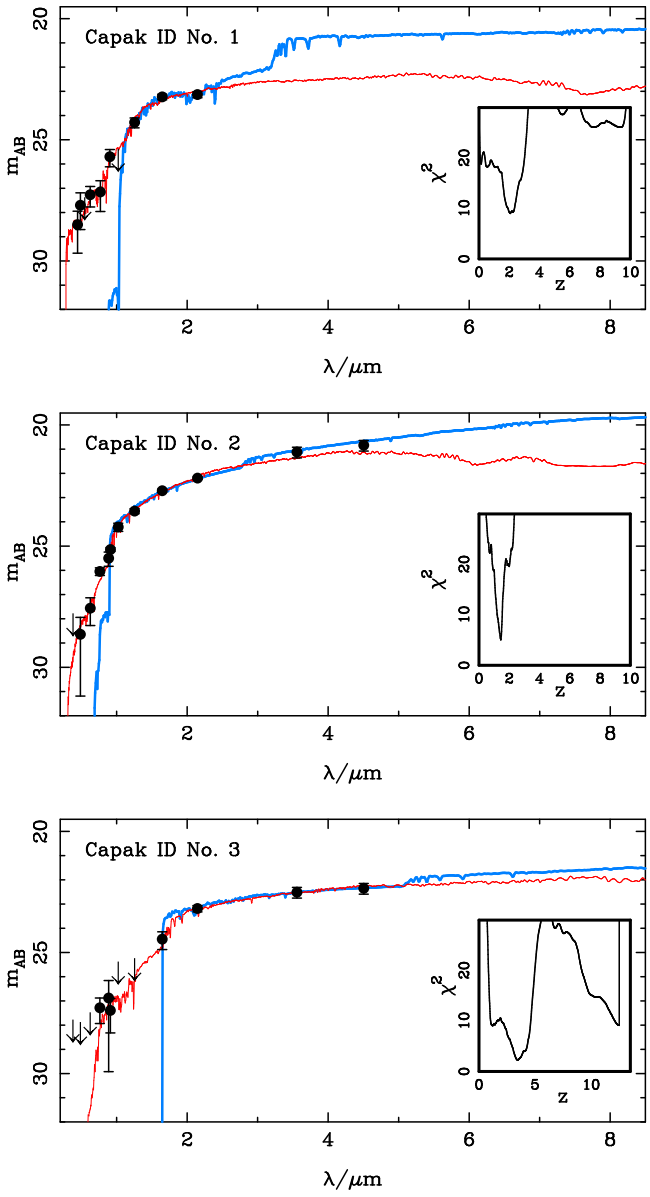

Figure 2.6 *SED fits for the three $z > 7$ galaxy candidates from Capak et al. (2011) using our revised photometry from the deeper UltraVISTA near-infrared imaging and the new z'-band Subaru imaging. The UltraVISTA data extends to around one magnitude deeper in the J-band that the previous imaging available in the COSMOS field. In addition, it provides previously unavailable deep Y-band imaging, invaluable for removing low-redshift galaxy contaminants and dwarf stars. The blue line shows the best fitting high-redshift model (with $z > 4$) and the red line shows the best low-redshift fit, where the photometric redshift and χ^2 values for these two solutions are Capak1: $z_{\rm phot} = 2.1(7.6)$, $\chi^2 = 9.0(26.0)$, Capak2: $z_{\rm phot} = 1.4(6.9)$, $\chi^2 = 5.0(42.2)$ and Capak3: $z_{\rm phot} = 3.4(12.6)$, $\chi^2 = 2.2(9.1)$. We have extended the redshift range of the Capak3 fit above to display the high-redshift model solution at $z \sim 13$, which although being a formally acceptable fit has an implied star-formation rate and stellar mass that make it unrealistic at this extreme redshift. Hence, with our new photometry it can be seen that none of these objects has a robust high-redshift fit, but rather all lie in the redshift range $z \simeq 1.5 - 3.5$.*

$2''$ diameter aperture using SEXTRACTOR in dual-image mode with selection in the K_s-band, where the candidate was brightest. For the optical bands, cutouts from the COSMOS website in the B_J, g^+, V_J, r^+, i^+ and z^+-bands were extracted and the magnitudes (measured using GAIA) and errors (taken from the 5σ limits presented in Capak et al. 2011) were included in the SED fitting analysis. We find C1 to be undetected in Y, and to have $J = 24.4 \pm 0.2$, $H = 23.3 \pm 0.1$ and $K_s = 23.2 \pm 0.1$ (within a $2''$ aperture with a correction to 84% enclosed flux). These values can be compared to the Capak et al. (2011) magnitudes of $J = 23.21 \pm 0.05$, $H = 23.09 \pm 0.12$ and $K_s = 22.14 \pm 0.02$ within a $3''$ aperture. The large differences in photometry cannot be explained by aperture corrections, as the $3''$ aperture used by Capak et al. (2011) was predicted to enclose 80% of the flux in the PSF-matched J, H, K_s imaging, implying the new magnitudes should be slightly brighter or comparable. An offset in photometry between the WIRCam and UltraVISTA data has been identified in the UltraVISTA data release documentation (see also McCracken et al. 2012), implying that the UltraVISTA data is 0.15 mag fainter than the previous imaging, which is thought to be a problem with the COSMOS data rather than with VISTA; however this effect still cannot explain the change in the observed near-infrared colours. The IRAC imaging of C1 is highly-confused with a nearby object and so no attempt was made to measure this by either ourselves or by Capak et al. (2011). The large companion object is a low-redshift interloper at $z_{\rm phot} = 0.35$ from the COSMOS catalogue, which may have affected the accuracy of the $3''$ photometry. Our SED analysis of C1, with the fit shown in Fig. 2.6, yields no acceptable high-redshift solution, but rather reveals this object to be a red galaxy at $z_{\rm phot} \simeq 2.1$.

The second object, C2, was already identified by Capak et al. (2011) as a likely low-redshift interloper at $z_{\rm phot} = 1.59$, which we here confirm with our SED fit to the UltraVISTA data shown in the second panel of Fig. 2.6. This galaxy candidate was selected in our own preliminary catalogue, but excluded at a relatively early stage as a low-redshift galaxy because of the clear i-band detection.

Surprisingly, the third object, C3, was not selected in our analysis despite the claim by Capak et al. (2011) that it has $J = 23.1 \pm 0.1$. Visual inspection of the UltraVISTA J-band image of this object in fact reveals little, if any, evidence of detectable flux, however the object is real as it is clearly visible in the K_s-band. Accordingly, photometry from a K_s-band selected catalogue for the object was collected and the SED fit performed which, as shown in the third panel of Fig. 2.6, reveals the galaxy to lie at $z \simeq 3.5$.

This analysis therefore highlights the power of the new deeper and better-quality

UltraVISTA data over the previously available near-infrared data in the COSMOS field, and confirms that the new objects uncovered here from the Y+ J UltraVISTA imaging are the brightest credible $z > 6.5$ galaxy candidates in this area of sky.

2.5.2 Salvato et al. (2011)

Another particularly relevant high-redshift candidate within the field is the object CID-2550 identified by Salvato et al. (2011), that they claim could potentially be the highest redshift X-ray-selected source found to date. By SED fitting to the optical and near-IR counterpart to a Chandra X-ray source (from the Chandra-COSMOS catalogue), they found a best fit photometric redshift of $z_{\rm phot} \sim 6.84$. The previous magnitudes of this object CID-2550 are $i \approx 26.6, z = 25.4, J = 23.6, H = 23.8, K = 23.0$ with the object becoming brighter still in the Spitzer channels. However, despite the extremely bright J-band magnitude reported by Salvato et al. (2011), CID-2550 was not present in our final sample. CID-2550 is present in our original $Y + J$ selected catalogue as you would expect, but was immediately excluded as it is unexpectedly below the 5σ-limit in the detection image (with $Y + J = 26.9$). Inspection of the UltraVISTA imaging and associated datasets shows the candidate to be clearly detected in the H and K_s-bands, with faint detections in the i, z', Y and J-bands. As the object is brightest in the K_s-band we used K_s-band selected magnitudes and performed SED fitting as for our own candidates. Figure 2.7 shows our best fit to this object at $z_{\rm phot} = 2.6$, where the decrease in the photometric redshift compared to the previous determination by Salvato et al. (2011) is a consequence of the reduced J-band magnitude and the inclusion of the Y-band, along with reduced errors throughout the near-IR that show the spectrum to be gradually rising rather than exhibiting a sudden break in the photometry. Given that the candidate is an X-ray source, we conclude that it is most likely a dusty active galactic nucleus at a lower redshift of $z_{\rm phot} = 2.6$.

2.5.3 Hsieh et al. (2012)

Hsieh et al. (2012) recently reported a search for z_{850}-dropout galaxies within the Extended Chandra Deep Field South (ECDFS), with objects detected in J-band data obtained as part of the Taiwan ECDFS Near-Infrared Survey (TENIS). Boxes in colour-colour space were used to select high-redshift galaxies, in particular the *Spitzer* IRAC channels were introduced in an attempt to eliminate low-redshift galaxy and dwarf-star contaminants. One candidate high-redshift galaxy with $J = 25.12 \pm 0.23$

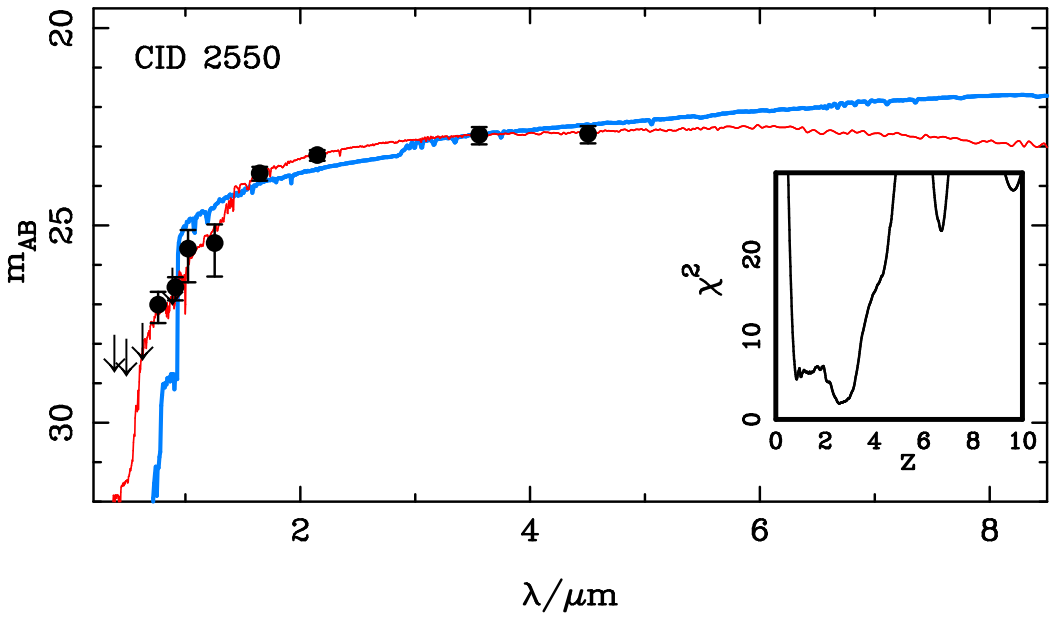

Figure 2.7 *SED fit for the candidate $z \sim 6.84$ X-ray-selected source from Salvato et al. (2011) using our revised photometry. The blue line shows the best fitting high-redshift model ($z_{\rm phot} = 6.7, \chi^2 = 22.9$) and the red line shows the best low-redshift fit ($z_{\rm phot} = 2.6, \chi^2 = 1.9$). Due to the improved near-infrared photometry, which shows the candidate to have a gradually rising SED rather than presenting a strong break, we conclude that the object is in-fact a lower redshift, dusty interloper.*

(total magnitude), TENIS-ZD1, was selected from the $0.25\,\mathrm{deg}^2$ surveyed, with a weighted photometric redshift of $z_{\mathrm{phot}} = 7.822^{+1.095}_{-0.725}$. The very large errors on the derived photometric redshift are a consequence of the proposed Lyman-break occurring between two widely-separated filters, the z_{850}- and J-band, due to the unfortunate lack of Y-band imaging. It is this lack of Y-band imaging which also makes it hard to exclude dwarf-star contaminants using the techniques discussed above (Fig. 2.2a), leading Hsieh et al. (2012) to rely on the IRAC colours in an attempt to achieve this.

The infrared colours of dwarf star contaminants utilised by Hsieh et al. (2012) were calculated from the AMES-dusty dwarf star models (Allard et al., 2001). However, with the advent of recent cool dwarf-star photometry by *Spitzer* from Patten et al. (2006) and Kirkpatrick et al. (2011) it is now clear that these models are inadequate. Specifically, while the largest observed colour over the spectral break of $z' - J \sim 3.5$ (see Fig. 2.2) agrees with the AMES-dusty model, where $z - J \sim 3$, the 3.6μm - 5.8μm colour, which is proposed by Hsieh et al. (2012) as the best way to discriminate between dwarf stars and galaxies, is underestimated by the model by over a magnitude. The results of Kirkpatrick et al. (2011) in particular, who observed mainly T-dwarf stars, show that dwarf stars can be significantly redder than predicted in the AMES-dusty model, with 3.6μm - 5.8μm $\simeq 0.5$ perfectly possible.

Despite these concerns, the 3.6μm - 5.8μm colour of TENIS-ZD1 reported by Hsieh et al. (2012) is still redder than observed in the coolest T-dwarf stars to date, albeit now by only $\simeq 2\sigma$. However, it also exceeds the predictions of high-redshift galaxy templates with reddening up to $A_V \simeq 1.0$. Unfortunately, because Hsieh et al. (2012) have neglected to provide the position of their putative high-redshift galaxy, we cannot check the IRAC photometry, or indeed the photometry and claimed non-detections at any other wavelength, despite the fact that much of the key datasets are public. Our own SED fit to the photometry provided by Hsieh et al. (2012) supports the high-redshift solution (which they derived using the EAZY code; Brammer et al. 2008), but we note that the extreme redshift which results is largely a consequence of the arguably surprisingly bright magnitude reported at 5.8 μm, while exclusion of the low-redshift alternative solution depends critically on the error ascribed to the single J-band data point (in the absence of any Y-band imaging of appropriate depth). Given that we cannot make our own photometric measurements for this object, it is difficult to comment further on the validity or otherwise of this proposed $z = 7 - 8$ galaxy. What we can say is that, given our own results, it would not seem unreasonable to detect one galaxy at $z \simeq 7$ at $J \simeq 25$ in the ECDFS, but also that it is somewhat unexpected to see it detected in the two longest-wavelength IRAC bands, given that *none* of our own

UltraVISTA candidate objects are detected in the S-COSMOS 5.8 μm or 8 μm imaging. However, we note that the reported $5.8\,\mu$m and $8.0\,\mu$m magnitudes for TENIS-ZD1, of $m_{\rm AB} \sim 23.3$ and 23.6 respectively, are deeper than the S-COSMOS limits.

2.6 Discussion

2.6.1 Stacked photometry and physical properties

Creation and analysis of the four-object stack

An average stack was made from the postage-stamps of our four most robust $z > 6.5$ galaxy candidates as illustrated in Fig. 2.4. This was done both to create higher signal-to-noise photometry to better explore the implications of SED fitting, and also to double-check that no low-level i-band flux was present that might indicate contamination of our "robust" sample with objects at $z < 6.5$. Photometric measurements were made in the same way as for the individual candidates, using SExtractor in dual-image mode with selection in the $Y+J$ image. The resulting average photometry is included in Table 2.2, and the best-fitting SED is shown in Fig. 2.8, where the variation in the rest-frame UV photometry observed in the four individual galaxies averages to produce a relatively flat UV slope, as discussed further below. The derived photometric redshift for the stack is $z = 6.98 \pm 0.05$, and the colour across the Lyman-break is $z' - Y = 2.5 \pm 0.2$, consistent with the marginal detection in the z'-band postage-stamp seen in Fig. 2.4, and yielding an extremely secure Lyman break. As detailed in Table 2.3, allowing the SED fitting to also include a contribution from Lyman-α emission causes the estimated redshift of the stack to rise to $z = 7.12$, with the best fit implying a rest-frame Lyman-α equivalent width of $EW_0 \simeq 40$ Å.

Extinction and star-formation rates

The best-fitting SED to the four-object stack is based on a tau-model with a characteristic star-formation timescale $\tau = 50\,{\rm Myr}$, with solar metallicity and moderate reddening of $A_V = 0.3$ mag. This is somewhat lower than the value of $A_V = 0.75$ derived at $z \simeq 6$ by Willott et al. (2013) from a stack of 23 $z \simeq 6$ galaxies with $z' \simeq 25.0$.

However, we caution that dust reddening is, of course, degenerate with age/metallicity, and may also be exaggerated in single-component fits such as those utilised here, as

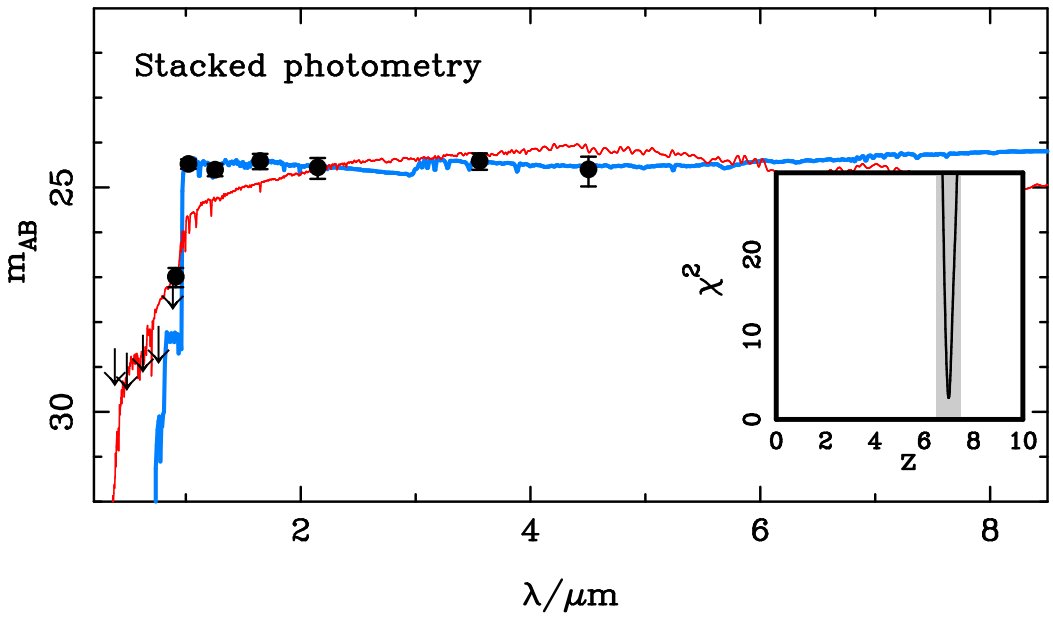

Figure 2.8 *The best SED fit to the average photometry produced from a stack of our four most robust $z \simeq 7$ galaxy candidates as shown in Fig. 2.4 and described in Section 2.4.1. The best-fitting photometric redshift for the stack is $z = 6.98 \pm 0.05$, rising to $z = 7.12$ with allowance for a contribution from Lyman-α emission (see Table 2.3). The best fitting low-redshift model ($z \simeq 1.5$) is shown as the red curve, which clearly cannot reproduce the large spectral break and flat near-IR colours of the stack photometry.*

there is evidence that a two-component star-formation history may better reproduce the combination of fairly blue UV continuum (as displayed by this stack - see below) and (relatively) red UV-to-optical colour seen in the SEDs of many $z \simeq 7$ galaxies (Curtis-Lake et al., 2013). The uncertainty in derived A_V is important to bear in mind when considering the SFRs and sSFRs of these galaxies because, as can be seen from columns 12 and 13 in Table 2.3, the galaxies with the most extreme inferred SFRs all have correspondingly high values of A_V. It is for this reason that we have also judged it helpful, in the final column of Table 2.3, to provide an alternative estimate of SFR, based simply on the Madau et al. (1998) conversion from UV flux density, assuming zero dust extinction.

The SFR of the stack derived from the best-fitting SED assuming a constant SFH is $98\,\mathrm{M_{\odot}yr^{-1}}$ or, if no dust extinction is assumed (i.e. using the Madau et al. 1998 prescription), the $\mathrm{SFR} = 32\,\mathrm{M_{\odot}yr^{-1}}$. From Table 2.3 it can be seen that, with zero dust, the SFRs of the individual galaxies lie in the range $25 - 50\,\mathrm{M_{\odot}yr^{-1}}$, but that adopting the best-fitting SED models can yield values as high as several hundred $\mathrm{M_{\odot}yr^{-1}}$, as a result of best-fitting values of A_V reaching as high as unity (although the single object with $A_V > 1$ is not from our 'robust' sample of objects).

UV slopes

An estimate of the UV continuum spectral slope, β ($f_{\lambda} \propto \lambda^{\beta}$), can be derived from the stacked near-infrared photometry in a number of ways. Following Bouwens et al. (2010) and Dunlop et al. (2012), a simple estimate of β can be derived from the $J - H$ colour (deliberately avoiding the Y-band which could be contaminated by Lyα emission). This yields a highly uncertain value of $\beta = -1.1 \pm 0.9$, but the availability of the K_s photometry enables a more accurate estimate based on power-law fitting to the J, H, K_s photometry which gives $\beta = -2.0 \pm 0.2$ (where the error is obtained from Monte Carlo simulations where the photometry is varied randomly according to the derived errors). Including the Y-band photometry as well (i.e. fitting to Y, J, H, K_s) yields a slightly bluer value $\beta = -2.16 \pm 0.18$, but this could potentially be affected by Lyα emission and is, in any case, still clearly consistent with $\beta \simeq -2$. We thus adopt $\beta = -2.0 \pm 0.2$ as the best estimate of β for the four-object stack, and note that this is perfectly consistent with the value deduced by Dunlop et al. (2012) and McLure et al. (2011) for the most luminous of the $z \simeq 7$ galaxies uncovered by the *HST* WFC3/IR surveys to date (albeit these are $\gtrsim 1.5$ mag less luminous than those considered here). Our result is also consistent with the value obtained by Finkelstein et al. (2012) who

found $\beta = -2.04^{+0.17}_{-0.27}$ for a sample of lower-luminosity galaxies with $L > 0.75L^*$ at $z = 7$, with a weak trend to redder colours with increasing luminosity. However, our result is significantly lower than the value of β derived at $z \simeq 6$ by Willott et al. (2013), who inferred a significantly redder value of $\beta = -1.44 \pm 0.10$ from their stacked Y, J, H, K_s photometry.

Stellar masses and specific star-formation rates

The stellar mass derived from the SED fitting of the stacked photometry is $M_* = 4 \times 10^9 \mathrm{M}_\odot$, which can be compared with the value found by Willott et al. (2013) of $M_* \simeq 10^{10} \mathrm{M}_\odot$ for bright galaxies at $z = 6$ (although the results are consistent within the errors); we note that the galaxy detected by Hsieh et al. (2012), if really at $z_{phot} \sim 7.8$, has a substantially larger inferred stellar mass of $M_* = 3.2 \times 10^{10}\,\mathrm{M}_\odot$.

Based on the best-fitting model, the specific SFR (sSFR) of the stack is then $\simeq 30\,\mathrm{Gyr}^{-1}$, falling to $\simeq 8\,\mathrm{Gyr}^{-1}$ if zero dust extinction is assumed. Clearly both these values (and indeed the values inferred from Table 2.3 for most of the individual objects) are higher than the average value of $\simeq 2-4\,\mathrm{Gyr}^{-1}$ generally reported for studies of fainter Lyman-break galaxies at these redshifts (e.g. González et al. 2010), although they lie within the range of values found for individual objects by McLure et al. (2011). However it is probably premature to over-interpret these values as they could be biased high for potentially two reasons. First, if there really is a significant range in sSFR at a given stellar mass, then since the UltraVISTA data has only just reached the depth required to select genuine $z \simeq 7$ galaxies, it is likely that those galaxies detected on the basis of their rest-frame UV flux will be biased towards high values of sSFR. Second, even if the intrinsic range in sSFR is small, photometric errors will conspire to yield a systematic over-estimate of the rest-frame UV luminosities of our candidates, a point which is also important for the estimation of number density as a function of magnitude (as discussed further below).

2.6.2 Luminosity Function

A full analysis of the implications of the new, luminous $z \simeq 7$ galaxies reported here for the form and evolution of the UV galaxy LF is deferred to the next Chapter (where we will be armed with a larger sample, and will have processed the required suite of detailed mock-data simulations). Nevertheless it is still instructive to briefly consider how our results compare with expectations based on existing determinations of the galaxy UV

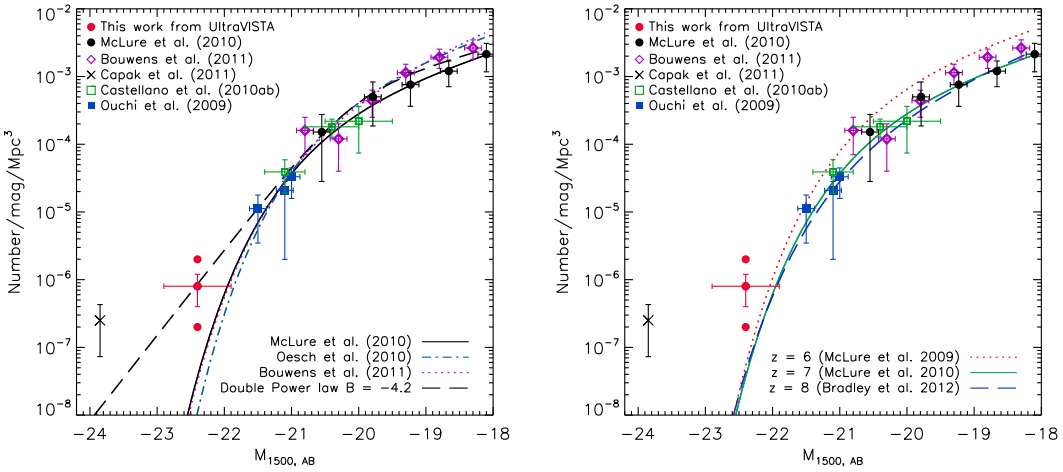

Figure 2.9 *The left-hand panel shows the $z = 7$ galaxy UV ($\simeq 1500$Å) LF with data shown from McLure et al. (2010), Bouwens et al. (2011b), Castellano et al. (2010a,b) and Ouchi et al. (2009a) overplotted on the best-fitting Schechter functions derived by Bouwens et al. (2011b), Oesch et al. (2010b) and McLure et al. (2010) (note the LFs derived by Ouchi et al. (2009) and McLure et al. (2010) are essentially identical). The estimated data-point from our new UltraVISTA study is shown in red, with Poissonian errors on the number density, with the upper, central and lower point given by ten, four or only one candidate in our sample being a confirmed as a $z > 6.5$ galaxy. A double power-law curve is also included for comparison, where the faint-end slope is matched to that of McLure et al. (2011) and at the bright end we adopt $B = -4.2$ (see Section 2.6 for parameterisation). In the right-hand plot we show the same data, but this time compare with the the $z = 6, 7, 8$ LFs from McLure et al. (2009), McLure et al. (2010) and Bradley et al. (2012) respectively (see text for further details and discussion).*

LF at these early times. However, we caution that the LF parameters calculated below rely on an approximate estimate of the survey volume and should be considered a preliminary result.

In the left-hand panel of Fig. 2.9 we illustrate how our results measure up against currently-published determinations of the UV galaxy LF at $z \simeq 7$ as reported by Ouchi et al. (2009a), McLure et al. (2010), Oesch et al. (2010b) and Bouwens et al. (2011b). As can be seen from this plot, despite the continuing (important) debate over the faint-end slope (see Dunlop 2012), these independent determinations of the $z \simeq 7$ LF are in generally good agreement, especially between the break luminosity at $M^{*}_{1500} \simeq -20$ and $M^{*}_{1500} \simeq -21$, the brightest luminosity effectively sampled by the pre-existing ground-based data (in fact the McLure et al. (2010) and Ouchi et al. (2009) LFs are so similar that only one can be usefully plotted). This agreement also appears to extend out to the luminosity region probed here by UltraVISTA, at $M^{*}_{1500} < -22$, but it is important to stress that this is largely a result of the common assumption of a Schechter form, and that these curves are simply extrapolations beyond the range of the pre-existing data.

To locate our new results on this plot we have adopted the J-band magnitude of the stack (i.e. the average J-band magnitude of our four most robust candidates), corrected to total magnitude, to calculate the rest-frame UV absolute magnitude at 1500Å, $M_{1500} = -22.5$. We have then conducted a set of simulations and find that our selection criteria, based on the Y+J image, implies that incompleteness and flux-boosting virtually cancel each other in this magnitude regime, and that a relatively modest flux-boosting correction of only $\simeq 0.1$ mag is merited. This leads to a data-point in Fig. 2.9 plotted at $M_{1500} = -22.4$, at a comoving number density based on the discovery of four galaxies within our estimated comoving survey volume of $5 \times 10^{6}\mathrm{Mpc}^{3}$, based on our effective survey area of 0.9 deg^{2} (excluding the area unavailable for galaxy selection due to diffraction halos/spikes from bright stars) and assuming that our selection function is effectively unity over the redshift range $z \simeq 6.5 - 7.2$. The size of the bin in M_{1500} was chosen to be 1 mag to indicate the range of the observed J-band measurements for our four most secure galaxies (as seen in Table 2.2), while the error bar in density is based purely on the Poisson noise. Finally, to indicate possible extremes, we also show where this data-point would lie in the unlikely circumstance that all ten of the objects presented here are truly at $z > 6.5$, or alternatively, if only one high-redshift galaxy were to be confirmed.

It is clear from this plot that, while our results are much less extreme than would be implied from the results of Capak et al. (2011), nevertheless our discovery of four robust $z \simeq 7$ galaxies at $M_{1500} \simeq -22.4$ yields a somewhat higher number density than

would be anticipated on the basis of simply extrapolating the existing LFs. For example, the McLure et al. (2010) LF predicts only $\simeq 0.8$ galaxies with $J < 25$ in our survey volume.

Given the small-number statistics, and the potential for cosmic variance (although with the low sample size available here, Poisson noise dominates that from cosmic variance), it would be premature to suggest that our results contradict the steep exponential fall-off at the bright end of the LF implied by the current Schechter-function fits to the $z \simeq 7$ LF. However, it also important to stress that, as is clear from Fig. 2.9, our results are certainly not in conflict with the existing *data* at this redshift, and would in fact lie naturally on a power-law extrapolation from the data at $M^*_{1500} \simeq -21$. To illustrate this we have plotted a simple double power-law LF through the data, with the functional form:

$$\phi(M) = \frac{\phi^*}{10^{0.4(A+1)(M-M^*)} + 10^{0.4(B+1)(M-M^*)}}. \quad (2.1)$$

We set ϕ^*, M^* and the faint end slope, A ($\equiv \alpha$), to the values determined in the Schechter-function fit by McLure et al. (2010), and have simply set the value of the bright-end slope, B, to make the function pass through our data-point ($B = -4.2$). Even without a detailed analysis it is obvious that this functional form provides a good description of all the available data, indicating that it may be premature to conclude that the LF at $z \simeq 7$ is best described by a Schechter function.

Finally, in the second panel of Fig. 2.9, we show the same $z \simeq 7$ data points, but here we plot the best-fitting galaxy UV LFs at $z \simeq 6$ (McLure et al. 2009; Willott et al 2013), $z \simeq 7$ (McLure et al. 2010) and $z \simeq 8$ (Bradley et al. 2012). This figure demonstrates that there is in fact currently very little (if any) significant evidence for evolution in the *bright* end of the galaxy LF in the redshift range $z \simeq 6 - 8$. We note that the only other work directly probing the galaxy LF at $M_{1500} < -22$ at these epochs is the study at $z \simeq 6$ by Willott et al. (2013), who exploited $\simeq 4\,\mathrm{deg}^2$ of ground-based CFHT imaging to search for $z \simeq 6$ galaxies brighter than $M_{1350} \simeq -21.5$. Willott et al. (2013) found 40 galaxies, many with $M_{1350} < -22$, but relatively few with $M_{1350} < -22.5$. Thus, even at $z \simeq 6$ the basic statistics at $M_{UV} < -22.5$ remain poor, but nevertheless a maximum likelihood fit to the $z \simeq 6$ LF led Willott et al. (2013) to conclude in favour of the steep exponential cutoff implied by the Schechter-function fit of McLure et al. (2009). However, the near-infrared data analysed by Willott et al. (2013) are somewhat inhomogeneous, of inadequate depth to detect the $z \simeq 6$ galaxies in J-band in two of the four survey fields, and lack the Y-band data which, ideally, would enable determination

of M_{1500} free from corrections due to IGM extinction (which can impact on the z'-band at these redshifts). Moreover, in the sample reported by Willott et al. (2013) the COSMOS field alone contains two $z \simeq 6$ galaxies with J-band magnitudes brighter than the most luminous galaxy candidate (as based on the z-band mag) reported from the full 4 deg^2 survey. We conclude that the form of the bright-end of the LF is still open to debate at both $z \simeq 6$ and $z \simeq 7$. At $z = 8$, Bradley et al. (2012) have also claimed to find no evidence for an excess of sources at the bright-end. However, due to the (relatively) small effective field size of the current BoRG survey, the galaxies detected are at $L < 2L^*$ (the galaxies presented here are $\simeq 9L^*$) and so the constraints on the very bright-end of the $z \simeq 8$ LF remain weak. The final UltraVISTA imaging is designed to improve our knowledge of the bright end of the galaxy UV LF at $z \simeq 8$ as well as at $z \simeq 7$.

2.7 Conclusion

We have exploited the new, deep, near-infrared UltraVISTA imaging of the COSMOS field, in tandem with deep optical and mid-infrared imaging, to conduct a new search for luminous galaxies at redshifts $z \simeq 7$. The unique multi-wavelength dataset provided by VISTA, CFHT, Subaru, *HST* and *Spitzer* over a common area of $\simeq 1$ deg^2 has allowed us to select galaxy candidates at redshifts $z > 6.5$ by searching first for UltraVISTA $Y+J$-detected (< 25 mag) objects which are *undetected* in the CFHT and *HST* optical data.

This sample was then refined using a photometric redshift fitting code, enabling the rejection of lower-redshift galaxy contaminants, and cool galactic M, L, T dwarf stars; brown-dwarf contamination is a much more serious problem for wide-area ground-based surveys than for deeper/narrower *HST* WFC3/IR surveys, and so we have taken great care to utilise the full multi-wavelength dataset (fitting the latest stellar templates), including IRAC colours, to minimise dwarf-star contamination.

The final result of this process is a small sample of (at most) 10 credible galaxy candidates at $z > 6.5$ (from over 200,000 galaxies detected in the year-one UltraVISTA data). The first four of these objects appear to be robust galaxies at $z > 6.5$, and fitting to their stacked spectral energy distribution yields $z_{phot} = 6.98 \pm 0.05$ with a stellar mass $M_* \simeq 5 \times 10^9\,\mathrm{M}_\odot$ and rest-frame UV spectral slope $\beta \simeq -2.0 \pm 0.2$ (where $f_\lambda \propto \lambda^\beta$). The next three are also good candidates for $z > 6.5$ galaxies, but the possibility that they are low redshift interlopers or dwarf stars cannot be excluded. Our final subset of

three additional candidates is afflicted not only by potential dwarf-star contamination, but also contains objects likely to lie at redshifts just below $z = 6.5$.

We have also been able to demonstrate that the three even-brighter $z \gtrsim 7$ galaxy candidates reported in the COSMOS field by Capak et al. (2011) are in fact all lower-redshift galaxies at $z \simeq 1.5 - 3.5$. Consequently the new $z \simeq 7$ galaxies reported here are the first credible $z \simeq 7$ Lyman-break galaxies discovered in the COSMOS field and, as the most UV-luminous discovered to date at these redshifts, are prime targets for deep follow-up spectroscopy. We have investigated the physical properties of these galaxies as inferred from the broad-band photometry, and have discussed the uncertainties in, and implications of their estimated star-formation rates and stellar masses. Finally, we have considered only briefly the implications of the inferred number density of these "bright" galaxies for the form of the galaxy luminosity function at these early epochs, deferring a full re-analysis of the $z \simeq 7$ UV luminosity function to the next Chapter (when we expect to be armed with a larger sample of objects).

CHAPTER 3

The bright end of the galaxy luminosity function at $z \simeq 7$

3.1 Introduction

Theoretically, the form and redshift dependence of the LF contains important information on the key physical processes that govern early galaxy formation and subsequent evolution. To match the observed luminosity and mass functions at $z = 0$, simulations of the build-up of galaxies require that, at some stage, the growth of galaxies in the most massive dark-matter haloes be suppressed by some mechanism, such as feedback from a central AGN. In effect, the challenge is to match the steep exponential decline of the galaxy stellar mass (and luminosity) functions at high mass/luminosity, as parameterised through the Schechter function described above. Interestingly, recent studies of the stellar mass function of *star-forming galaxies* have now shown that the characteristic mass above which this steep decline sets in appears to be essentially independent of redshift out to $z \simeq 3$ (e.g. Ilbert et al., 2013). This has led some authors to infer the presence of a characteristic "quenching mass", i.e. a stellar mass above which a galaxy is likely to have its star-formation activity strongly suppressed by some physical mechanism. As discussed in Peng et al. (2010), current data indicate that the quenching mass above which galaxies rapidly cease forming stars and leave the "main-sequence" of star-forming galaxies is $M_{\star} \sim 10^{10.2}\,\mathrm{M}_{\odot}$. If this mass quenching, whatever its physical origin, really does set in at a physical threshold which is independent of redshift, then we might reasonably expect the form of the galaxy UV LF to start to diverge from a simple Schechter function at very early epochs (when very few galaxies will have grown to the relevant stellar mass). The ability to test such key ideas, and potentially better constrain the (still unclear) physical origin of "mass quenching", provides additional strong motivation for determining the form of the bright end of the galaxy LF at the highest redshifts.

Further interest in the detailed properties of $z \simeq 7$ galaxies has been generated by the

follow-up *HST* and Atacama Large Millimeter/Submillimeter Array imaging of the spectroscopically confirmed Lyman-α emitter (LAE) at $z = 6.595$ (Ouchi et al., 2013), nicknamed 'Himiko', that was first discovered by Ouchi et al. (2009b). When observed at ground-based resolution this galaxy appears as a single bright extended source with $\mathrm{m_{AB}} \simeq 25$ (at $\lambda \simeq 1\mu$m). However *HST*/WFC3 imaging reveals the galaxy to be an apparent triple merger system, where each component has roughly the characteristic luminosity L^*. Although an extreme galaxy, Himiko illustrates the potential for detailed study of rare and bright $z \simeq 7$ galaxies that can only be efficiently detected in ground-based narrow- or broad-band survey fields.

Here we extend the work presented in Bowler et al. (2012) using the second data release (DR2) of UltraVISTA, which provides deeper imaging in the Y, J, H and K_s-filters, in strips covering approximately half of the full 1.5 deg^2 of the UltraVISTA DR1 data (McCracken et al., 2012). The improved photometry over 70% of the field searched in Bowler et al. (2012) allows us to check the previous candidates and hence validate our selection methodology. We also incorporate the UKIDSS Ultra Deep Survey (UDS), which has a comparable depth and area of J, H and K-band imaging to the UltraVISTA DR2. By combining the deep near-infrared survey data with the optical and mid-infrared data currently available in the UltraVISTA and UDS fields, we have assembled the widest area (1.65 deg^2) of imaging available for the robust selection of $z \simeq 7$ Lyman-break galaxies.

We begin with a summary of the multiwavelength data utilised here from the UltraVISTA and UDS fields in Section 3.2, followed by the details of our candidate selection in Section 3.3. The resulting sample of galaxies is presented in Section 3.4, with physical properties derived from our SED fitting analysis in Section 3.7. In Section 3.8 we investigate the sizes of the galaxies in our sample, including an analysis of *HST* imaging of four galaxies in our sample that lie within the region of the UltraVISTA field imaged as part of the CANDELS programme. We calculate the binned luminosity function for our sample in Section 3.9, where we also carefully consider the potential effect of gravitational lensing. We discuss our results and compare them to previous work at $z = 5$ and $z = 6$ in Section 3.10, which also includes a prediction of the level of contamination of our sample by high-redshift quasars. The astrophysical implications of our results are considered further in Section 3.11, and our conclusions are summarised in Section 3.12.

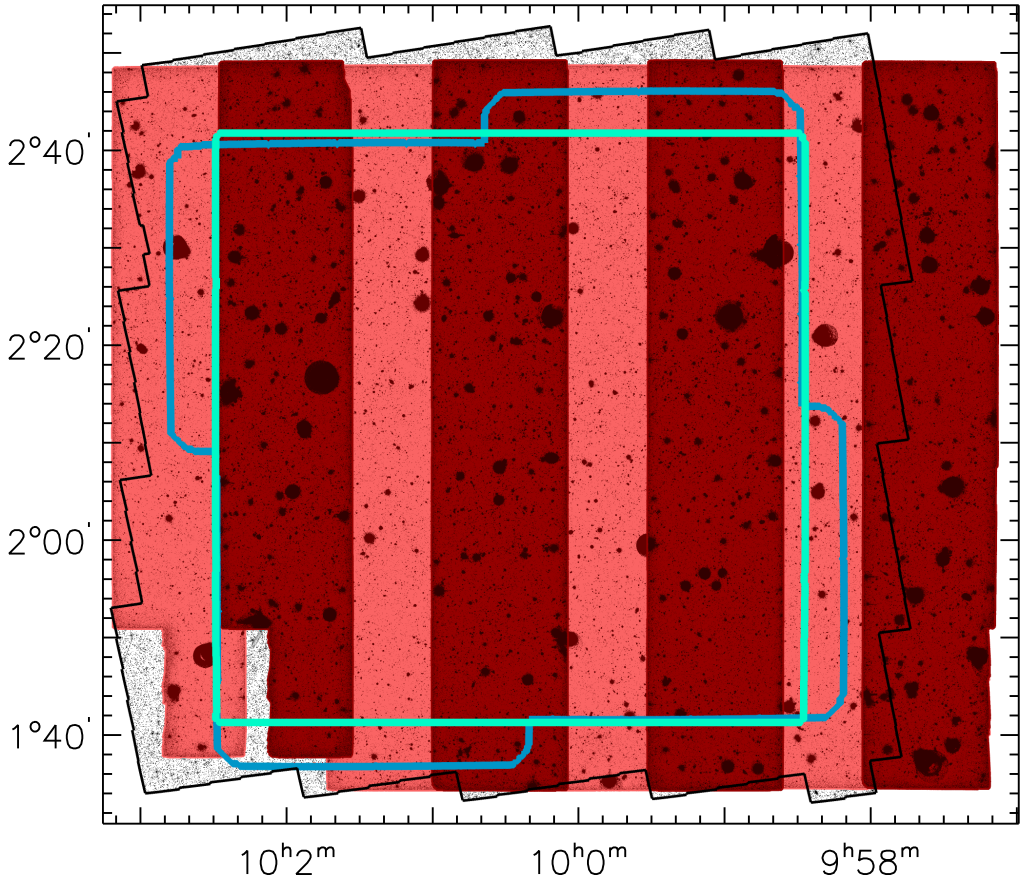

Figure 3.1 *The footprint of the UltraVISTA/COSMOS field showing the key multiwavelength data used here. The large red rectangle shows the year-one 1.5 deg^2 of near-infrared imaging from UltraVISTA DR1, with the deeper strips comprising the second data release shown in dark red. The Subaru z'-band mosaic, formed from four individual Suprime-Cam pointings, is indicated by the blue outline, and the 2 deg^2 of* HST/*ACS I_{814}-band imaging from the COSMOS survey is shown as the large jagged outline. The overlap with the DR2 strips in dark red and the central green square, which is the* $1\,\mathrm{deg}^2$ *area of a single pointing of CFHT/MegaCam, defines the* $\simeq 0.7\,\mathrm{deg}^2$ *area searched in this study.*

3.2 Data

The two multiwavelength survey fields analysed in this thesis contain a wealth of observations from X-ray to radio wavelengths. In the following section we describe the specific datasets utilised here for the selection of $z > 6.5$ galaxies, most importantly the near-infrared data from the UltraVISTA DR2 and UDS DR10. The coverage maps of the different wavelength data are shown in Figs. 3.1 and 3.2, and a summary of the available broad- and narrow-band filters utilised to image each field can be found in Table 3.1. The final area of overlapping multiwavelength imaging over the two fields, excluding large stellar diffraction haloes that were masked, comprised 1.65 deg^2, with 0.62 deg^2 from the UltraVISTA 'ultra-deep' survey, 0.29 deg^2 from the UltraVISTA 'deep' component and 0.74 deg^2 in the UDS field.

3.2.1 The COSMOS/UltraVISTA field

UltraVISTA near-infrared imaging

The analysis presented in this chapter relies on the first and second data releases of the ongoing UltraVISTA survey[1], which consists of Y, J, H and K_s imaging with the Visible and Infrared Camera (VIRCAM) on the VISTA telescope within the Cosmological Evolution Survey (COSMOS) field. The first data release, described in detail by McCracken et al. (2012), provided near-infrared imaging over the maximum area of the programme covering 1.5 deg^2. DR2 provides deeper data in strips that cover $\sim$70% of the the full field as shown in Fig. 3.1. Integration times for the DR2 Y, J, H and K_s bands range from 29-82 hours per pixel, compared with 11-14 hours per pixel from DR1. Throughout this chapter we refer to the DR2 imaging within the strips as the 'ultra-deep' part of the survey, and the DR1 imaging over the full field as the 'deep' part.

Auxiliary optical and mid-infrared imaging

The auxiliary data used in this chapter is described in full by Bowler et al. (2012) (and Chapter 2), but here we briefly describe the key datasets that are shown in Fig. 3.1. The UltraVISTA survey lies within the multiwavelength imaging taken as

[1] `http://www.eso.org/sci/observing/phase3/data_releases/`

part of the COSMOS survey (Scoville et al., 2007b), which covers a total of 2 deg^2 on the sky. Specifically we use optical imaging from the CFHTLS T0006 data release, which defines the maximal area of our search centred on RA $10^{\rm h}00^{\rm m}28^{\rm s}.00$, Dec. $+2^\circ12'30''$, with additional deep z'-band data from Subaru Suprime-Cam. Mid-infrared imaging over the COSMOS field by *Spitzer*/IRAC exists from two programmes; the *Spitzer* Extended Deep Survey (SEDS; Ashby et al., 2013) and the *Spitzer* Large Area Survey with Hyper-Suprime-Cam (SPLASH, PI: Capak). The SPLASH data consist of 438 individual exposures in the 3.6μm and 4.5μm bands, available as calibrated Level-2 files on the *Spitzer* Legacy Archive. We created a mosaic of the SPLASH images by first background subtracting the frames using SExtractor with a large background mesh size, before combining the frames using the software package Swarp. The SEDS data was also background subtracted and incorporated into the SPLASH mosaic using Swarp. The photometric and astrometric accuracy was confirmed by comparing to the shallower *Spitzer*/IRAC imaging across the field from the S-COSMOS survey (Sanders et al., 2007). Finally the field is also covered to single-orbit depth in the I_{814}-band by the *HST* Advanced Camera for Surveys (ACS; Koekemoer et al., 2007; Scoville et al., 2007a; Massey et al., 2010).

Data processing and consistency

All images were resampled to the pixel grid of the CFHTLS data (0.186-arcsec/pixel) using the IRAF package SREGISTER, once the astrometric solution had been matched to that of the UltraVISTA Y-band image using the IRAF package CCMAP.

Zeropoints of the full set of multiwavelength imaging were checked by inspecting the colours of flat-spectrum objects defined by the colour bridging the central band. For example, a sample of objects was extracted with aperture corrected flat $z' - J$ colours (e.g. $|z' - J| < 0.05$), and the $z' - Y$ colours of these objects were examined with the expectation that they should also be close to zero. The optical bands were found to have zeropoint offsets of < 0.05 mag, however when comparing the DR1 UltraVISTA data utilised in Bowler et al. (2012) to the optical imaging we found the Y-band magnitudes to be brighter than expected by 0.06 mag. The re-reduction of the full 1.5 deg^2 field encompassing the strips for the second data release, which included improved Y-band calibrations, entirely compensates for this observed colour difference in the DR1. Hence, when comparing the depths of the full-field of imaging in Table 3.1 and the magnitudes of the 10 objects selected in Bowler et al. (2012) in Section 3.5.3, note that there are small changes in the Y-band photometry as a result

of this zeropoint change. The zeropoints of the individual Subaru z'-band tiles were also adjusted slightly ($\Delta \mathrm{m} \simeq 0.04$) to be consistent with the single pointing of z-band imaging from CFHT/MegaCam.

3.2.2 The UKIDSS Ultra Deep Survey field

UKIRT and VISTA near-infrared imaging

In this study, we use the 10th data release (DR10) of near-infrared imaging in the UDS field, from the UKIRT Infrared Deep Sky Survey (UKIDSS; Lawrence et al., 2007). The UKIDSS UDS consists of deep imaging ($m_{\mathrm{AB}} \sim 25$, 5σ, see Table 3.1) in the J, H and K-bands over a total area of 0.8 deg^2 centred on RA $02^{\mathrm{h}}17^{\mathrm{m}}48^{\mathrm{s}}$, Dec. $-05°05'57''$(J2000). Data release 10 was made public in January 2013 and is available on the WFCAM science archive[2].

The UDS field lies within the *XMM-Newton* large-scale structure field, where there exists Y-band imaging from the VISTA Deep Extragalactic Observations survey (VIDEO; Jarvis et al., 2013) as can be seen in Fig. 3.2. The VIDEO survey is a public survey with VISTA that aims to cover 12 deg^2 in the Z, Y, J, H and K_s-bands over three separate fields. Imaging in the Y-band is key for the robust selection of $z \simeq 7$ galaxies in the UltraVISTA and UDS datasets, as the filter straddles the position of the spectral break and hence can separate genuine high-redshift galaxies from dwarf stars and low-redshift galaxy contaminants that can have identical, red, $z' - J$ colours. Furthermore, the presence of cross-talk artefacts (described further in Section 3.3.3) in the UKIRT J, H and K imaging, makes the presence of a detection in a bluer band independent from the UKIRT data an essential condition for confirming the reality of the high-redshift candidates. When compared to the UltraVISTA Y-band imaging however, the current release of the VISTA VIDEO data is substantially shallower by 1 mag (see Table 3.1), which reduces the capabilities of the data for selecting $z \sim 7$ sources and makes the selection function for the UDS field different to the UltraVISTA field.

Auxiliary optical and mid-infrared imaging

Optical imaging over the field was provided by the Subaru Suprime-Cam as part of the Subaru/*XMM-Newton* Deep Survey (SXDS; Furusawa et al., 2008). We also

[2] `http://surveys.roe.ac.uk/wsa/`

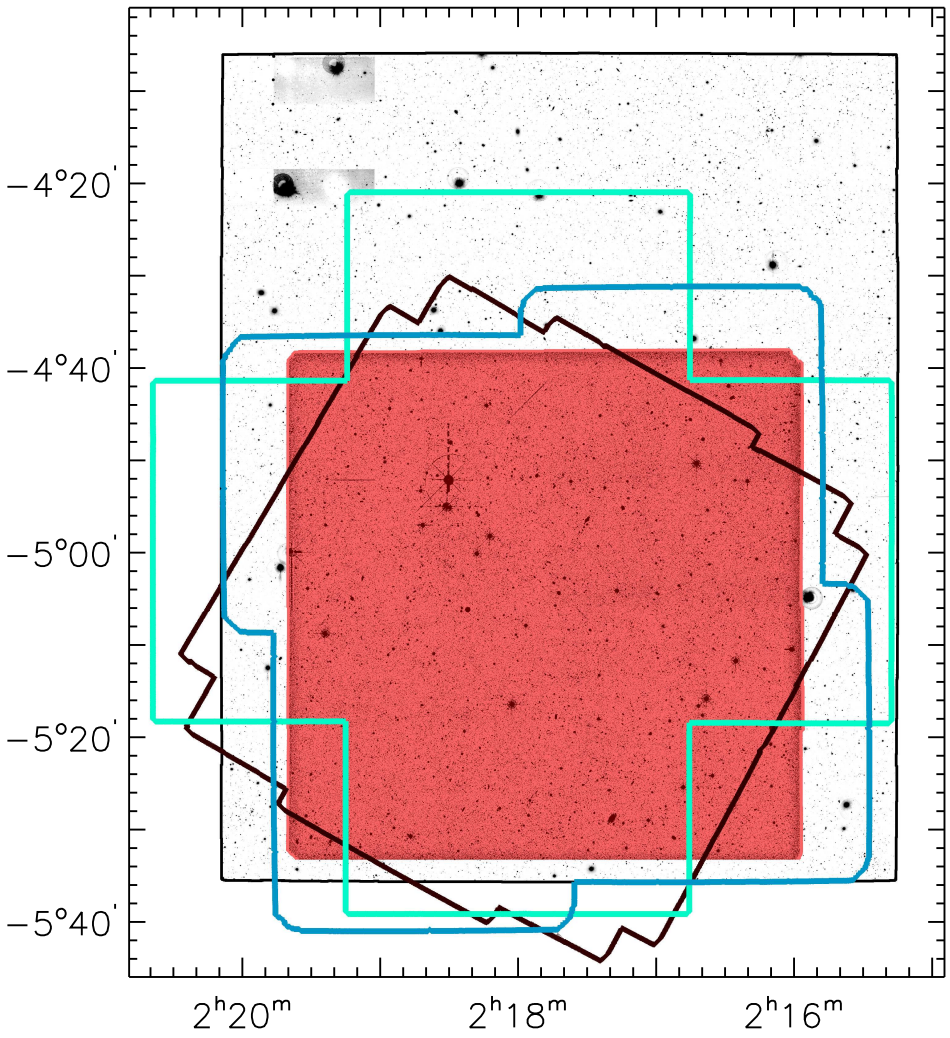

Figure 3.2 *The footprint of the UDS field, showing the UKIRT near-infrared data as the red square sitting within the large rectangle of Y-band imaging from the VISTA VIDEO survey. Data from Subaru Suprime-Cam are shown as the green and blue outlines, where the blue outline defines a z'-band mosaic of four pointings as in Fig. 3.1. The green cross-shaped outline shows the B, V, R, i and z'-imaging from the original Subaru programme (Furusawa et al., 2008), where the mosaic is formed from five separate pointings. Finally, the footprint of* Spitzer *data from SpUDS is shown as the black diamond. The total area of overlapping Subaru optical and UKIRT near-infrared imaging is $\simeq 0.8$ deg^2.*

obtained additional z'-band data in four Suprime-Cam pointings, each with $8-15$ hrs of integration time (Furusawa et al. in preparation). The astrometry of the individual tiles was matched to that of the UKIRT J-band image using the IRAF package CCMAP. The tiles were background subtracted using SExtractor (Bertin & Arnouts, 1996) and combined into a mosaic with the software SWARP (Bertin et al., 2002), where overlapping regions were combined with the WEIGHTED keyword, using weight maps produced by SExtractor. Finally, a science image on the pixel scale of the binned UKIRT imaging (0.2684-arcsec/pixel) was created from the mosaic (on the native Subaru pixel size of 0.202-arcsec/pixel) using the IRAF package SREGISTER.

In addition to the broad-band filters presented above, we also included data taken with the $NB921$ filter on the Subaru Suprime-Cam in our analysis (Sobral et al., 2012). The $NB921$ filter is positioned to the red side of the Subaru Suprime-Cam z'-band filter and hence allows better constraints on the photometric redshift for objects at $6.5 < z < 7.0$. The individual Suprime-Cam tiles were combined into a mosaic covering the full UDS field using the same method as for the z'-band mosaic described above.

The UDS field is covered by *Spitzer*/IRAC data from the *Spitzer* UKIDSS Ultra Deep Survey (SpUDS) programme (PI Dunlop), which has comparable depth to S-COSMOS (see Table 3.1) with an integration time per pointing of 1200 seconds. The central ~ 600 arcmin^2 of the UDS field is covered by deeper *Spitzer* imaging from SEDS, and we used a mosaic that included both the SpUDS and SEDS data for our analysis[3], taking into account the varying depths across the field using local depths.

Data processing and consistency

All images were mapped onto the astrometric solution and pixel grid of the binned UKIRT J-band imaging, with a pixel scale of 0.2684 arcsec/pixel. Consistency within < 0.05 mag was found between the zeropoints, with the exception being the VISTA VIDEO Y-band image which we found to be ~ 0.1 mag brighter than predicted from the sample of objects with flat $z'-J$ colours. We also observed an identical offset when comparing magnitudes with the Very Large Telescope/HAWK-I Y-band imaging in the field (Fontana et al. in preparation). Hence we shifted the zeropoint of the VIDEO imaging to produce fainter magnitudes by 0.1 mag, with the expectation that future reduction of the data will largely correct this offset with improved calibration, as was the case with the UltraVISTA Y-band data.

[3] http://www.cfa.harvard.edu/SEDS/data.html

3.2.3 Image depths

The careful determination of imaging depths across all bands is crucial to obtain accurate errors for use in the SED fitting analysis, and also in making appropriate preliminary magnitude cuts in the selection process. However, defining global limiting depths for data over degree-scale fields in the optical and near-infrared becomes problematic, as the combined pointings may have different integration times and seeing. Therefore, we obtained local depths over each image from the clipped median absolute deviation of the 200 closest apertures to each point. Apertures were placed randomly on the blank regions of the images that had been background subtracted using SExtractor, where blank regions were defined using the segmentation map of each image. The medians of the local depths for the imaging utilised here are presented in Table 3.1, within the 1.8-arcsec diameter circular aperture used for the photometry in this chapter.

3.2.4 Determination of the enclosed flux

We expect the high-redshift galaxies detected here to be close to unresolved in the available ground-based imaging, which typically has seeing of 0.8 arcsec (see Section 3.8). However, the variations in seeing throughout the multiwavelength data, along with potential variations across each individual mosaic, result in a different fraction of the enclosed flux in a given fixed circular aperture, which must be corrected for to ensure accurate colours and magnitudes. To extract a point spread function (PSF) for each image, we selected stars using the BzK-diagram (uzK-diagram for the UltraVISTA dataset) as defined in Daddi et al. (2004). For each star we extracted a postage-stamp from a background-subtracted image, before centring using the centroid coordinates from SExtractor. In a range of magnitude bins, these stars were then further background-subtracted and normalised, and a median was taken to form a high signal-to-noise PSF. The curve of growth was then measured on the stack for each magnitude bin (typically from $\mathrm{m_{AB}} = 18 - 25$, $\Delta \mathrm{m} = 1.0$), and the curves were visually inspected to exclude bins where the stars were saturated and to identify any possible trend with magnitude. Enclosed flux values in a 1.8-arcsec diameter aperture were typically 80% across the optical to near-infrared data, with the exception of the Y and J-band imaging from VISTA VIRCAM which has extended wings (as noted in McCracken et al., 2012) and hence encloses only $\sim$70%. For the IRAC imaging, the enclosed flux values quoted in the *Spitzer*/IRAC handbook were used.

Table 3.1 *The median 5σ limiting magnitudes for the relevant optical and near-infrared data used in this study, obtained from the median of local depths calculated from apertures placed in blank regions of each image (see Section 3.2.3 for more details). All ground-based magnitudes were calculated within the 1.8-arcsec diameter circular aperture used for photometry here. For the* HST*/ACS I_{814} depth, we used a 0.6-arcsec diameter aperture and the IRAC $3.6\,\mu$m and $4.5\,\mu$m values were calculated in a 2.8-arcsec diameter aperture. We present the depths of the near-infrared data from UltraVISTA separately for the 'ultra-deep' and 'deep' parts of the survey. Note that the depths for the 'deep' part shown here are ~ 0.4 mags deeper than the results from the original data release presented in Bowler et al. (2012) and McCracken et al. (2012). This is a result of improvements in the photometric calibration of the VISTA data, the smaller apertures used (1.8-arcsec diameter as opposed to 2-arcsec results presented previously) and an improved global depth derived from the local depths.*

COSMOS/UltraVISTA				UKIDSS UDS		
Filter	$m_{5\sigma,AB}$ deep	$m_{5\sigma,AB}$ ultra-deep	Source	Filter	$m_{5\sigma,AB}$	Source
u^*	27.2		CFHT/MegaCam	B	27.9	Subaru/Suprime-Cam
g	27.3		CFHT/MegaCam	V	27.6	Subaru/Suprime-Cam
r	27.0		CFHT/MegaCam	R	27.3	Subaru/Suprime-Cam
i	26.7		CFHT/MegaCam	i	27.2	Subaru/Suprime-Cam
I_{814}	26.7		*HST*/ACS			
z	25.5		CFHT/MegaCam			
z'	26.7		Subaru/Suprime-Cam	z'	26.5	Subaru/Suprime-Cam
				$NB921$	26.1	Subaru/Suprime-Cam
Y	25.1	25.8	UltraVISTA	Y	24.8	VISTA VIDEO
J	24.9	25.3	UltraVISTA	J	25.7	UKIRT/WFCAM
$Y+J$	25.3	25.9	UltraVISTA			
H	24.6	24.9	UltraVISTA	H	25.1	UKIRT/WFCAM
K_s	24.1	25.0	UltraVISTA	K	25.3	UKIRT/WFCAM
J_{125}		26.8	*HST*/WFC3	J_{125}	26.9	*HST*/WFC3
H_{160}		27.0	*HST*/WFC3	H_{160}	27.0	*HST*/WFC3
3.6µm	25.3		*Spitzer*/SPLASH	3.6µm	24.4, 25.2	*Spitzer*/SpUDS, SEDS
4.5µm	25.1		*Spitzer*/SPLASH	4.5µm	24.2, 25.0	*Spitzer*/SpUDS, SEDS

3.3 Candidate Selection

3.3.1 Initial detection and photometry

The primary catalogues for the UltraVISTA and UDS fields were created using SExtractor v2.8.6 (Bertin & Arnouts, 1996), run in the dual-image mode to create multiwavelength catalogues. The UltraVISTA catalogue was selected as in Bowler et al. (2012) in a $Y+J$ inverse-variance weighted stack, with additional objects included from Y and J-selected catalogues to ensure we are sensitive to very blue and red spectra up to $z = 7.5$. In the UDS field, where the J-band imaging is substantially deeper than the Y-band, we combined Y and J-band selected catalogues to form a master catalogue rather than creating a $Y + J$ stacked image. Magnitudes were measured in circular apertures of diameter 1.8-arcsec to deliver high signal-to-noise whilst ensuring that the measurements are robust against any astrometric differences between bands (typically $< 0.1''$). We also simultaneously created catalogues with photometry measured in 1.2-arcsec diameter circular apertures, which were used for SED fitting of stellar templates with the aim of increasing the signal-to-noise for true point sources.

The *Spitzer*/IRAC measurements were made in 2.8-arcsec diameter circular apertures, using images that had been background subtracted using a large filter size by SExtractor. The majority of our high-redshift candidates presented in the next section are isolated and hence the large aperture photometry is sufficiently accurate. However, when the photometry is confused, we have excluded the 3.6μm and 4.5μm bands from the SED fitting process. We have flagged confused and hence unreliable IRAC magnitudes (which translate into unreliable stellar mass estimates) in Tables 3.2, 3.3 and 3.6.

3.3.2 UltraVISTA DR2 selection

The initial catalogue for the UltraVISTA dataset consisted of 278916 objects within the $\simeq$ 0.7 deg^2 'ultra-deep' part of UltraVISTA imaging that overlaps with the multiwavelength auxiliary data shown in Fig. 3.1. We then required that an object be detected at greater than 5σ significance in either the Y or J-bands, where the 5σ limit here was taken as the median local depth from the deepest of the three strips (Y = 25.8, $J = 25.4$ mag, 5σ, 1.8-arcsec diameter circular aperture). Using our local depth estimates to compensate for the large diffraction halos around stars in

the CFHT/Mega-Cam imaging, we then required the candidate to be undetected in the u^*gri-bands at the 2σ-level. These optical non-detection requirements will inevitably result in a minority of real $z \simeq 7$ candidates being rejected at this stage (e.g. a true optical dropout galaxy has a probability of ~ 0.04 of being excluded here, assuming Gaussian distributed random noise). The number of objects lost at this stage is small however, and such a cut is standard practice to reduce the number of candidates for further analysis. The incompleteness of our sample as a result of these significance cuts, was carefully simulated using injection/recovery simulations, and folded into our LF analysis (see Section 3.9.1). The result of the described cuts was a sample of 1188 galaxy candidates, which was further reduced to 589 candidates with the removal of artefacts in the UltraVISTA imaging close to the area of missing data (seen in Fig. 3.1) and in the haloes/diffraction spikes produced by bright stars.

3.3.3 UKIDSS/UDS selection

The raw catalogue from the UDS dataset consisted of 248191 objects over the full area of J, H and K-band imaging shown in Fig. 3.2. We then applied the initial criteria that the candidates must be brighter than the 5σ-level in the J-band and undetected at 2σ-significance in the i-band, leaving 24797 sources. The available Y-band imaging in the UDS field is of insufficient depth to be competitive with the UltraVISTA Y-band imaging for the selection of galaxies, however it is essential to remove potential 'cross-talk' artefacts that occur only within the UKIRT imaging and hence can closely mimic a z-dropout LBG at $z \geq 7$. Cross-talk appears at constant pixel separation from all objects in the UKIRT/WFCAM imaging, which is 128 pixels on the native 0.4-arcsec/pixel scale (51.2-arcsec), and can appear many multiples of this distance away from the source object. Although the brightest occurrences are easily distinguishable from real objects by their 'doughnut' appearance, for fainter objects or artefacts a large distance away from the source, it can be very difficult if not impossible to distinguish cross-talk from a high-redshift galaxy. Hence, we apply the condition that candidates must be brighter than the 2σ-level in the VISTA VIDEO Y-band, and clearly visible in either the Y-image or the z'-band imaging, to ensure a detection in data obtained from independent telescopes. By further insisting that the objects must lie within the region of overlapping Subaru optical and UKIRT near-infrared data (see Fig. 3.2), and are further than 100 pixels from the edge of the UKIRT imaging, where the signal-to-noise drops significantly, we remove the majority of objects leaving only 202.

3.3.4 Visual inspection

In the final step before photometric redshift fitting, the candidates were visually inspected in the z', Y and J-images to remove obvious artefacts such as diffraction spikes, remaining cross-talk in the case of the UDS, and sources within the bright haloes around stars in the VISTA imaging. The i-band images were also inspected, and objects with any detection here (that may have escaped the 2σ-level cut applied above) were removed as indicative of galaxies at $z < 6.5$. The final samples containing the remaining high-redshift candidates for SED fitting consisted of 400 galaxies in the UltraVISTA data and 36 in the UDS field (where the lower number of objects remaining in the UDS is due to the additional Y-band detection requirement). All near-infrared photometry was corrected to a constant enclosed flux level of 84% (the enclosed flux in a 1.8-arcsec diameter aperture for the UltraVISTA CFTHLS z-band imaging), using the enclosed flux values derived for each image as described in Section 3.2.4. The 1σ-errors on the photometry were calculated from the nearest 200 blank apertures to each object, using the method described in Section 3.2.3.

Table 3.2 *The photometry for the sources in our final UltraVISTA and UDS samples is presented in the upper and lower sections of the table respectively. The magnitudes presented here were based on 1.8-arcsec diameter circular apertures except for the* Spitzer*/IRAC channels where 2.8-arcsec diameter circular apertures were used. The photometry has been corrected to the 84% enclosed flux level using the appropriate point-source correction. Where the flux is below 2σ significance, as defined by the local depth derived for each object, we replaced the magnitude with the limiting 2σ magnitude. The errors displayed were derived from the median absolute deviation of the fluxes from the closest 200 blank sky apertures. The presence of a dagger symbol in the right-hand column indicates that the [*$3.6\mu\mathrm{m}$*] and [*$4.5\mu\mathrm{m}$*] photometry is confused, and the number corresponds to the Bowler et al. (2012) galaxies with the order consistent with table 2 in Bowler et al. (2012). The 'Himiko' galaxy from Ouchi et al. (2013) referenced in the text is marked with an 'H'.*

ID	RA	DEC	z'	$NB921$	Y	J	H	K	$3.6\mu\mathrm{m}$	$4.5\mu\mathrm{m}$	B12
136380	09:59:15.89	+02:07:32.0	> 27.9	-	$25.5^{+0.2}_{-0.1}$	$25.3^{+0.3}_{-0.2}$	$25.1^{+0.3}_{-0.2}$	$25.6^{+0.4}_{-0.3}$	> 25.5	> 25.3	
28495	10:00:28.13	+01:47:54.4	> 28.1	-	$25.4^{+0.2}_{-0.2}$	$25.1^{+0.2}_{-0.2}$	$25.0^{+0.3}_{-0.2}$	$25.2^{+0.3}_{-0.2}$	$24.8^{+0.3}_{-0.3}$	$24.2^{+0.2}_{-0.2}$	
268511	10:00:02.35	+02:35:52.4	> 27.6		$25.0^{+0.3}_{-0.2}$	$25.0^{+0.5}_{-0.3}$	$25.4^{+0.6}_{-0.4}$	> 25.0	> 25.6	> 25.2	6
268037	09:59:20.69	+02:31:12.4	> 27.6	-	$25.1^{+0.2}_{-0.2}$	$25.5^{+0.4}_{-0.3}$	> 25.6	$24.9^{+0.2}_{-0.2}$	> 25.5	> 25.2	
65666	10:01:40.69	+01:54:52.5	> 27.6	-	$24.9^{+0.2}_{-0.1}$	$24.7^{+0.2}_{-0.2}$	$24.6^{+0.3}_{-0.2}$	$24.8^{+0.3}_{-0.2}$	> 25.1	$24.6^{+0.3}_{-0.2}$	4
211127	10:00:23.77	+02:20:37.0	> 27.6	-	$25.1^{+0.2}_{-0.2}$	$25.3^{+0.3}_{-0.2}$	> 25.8	$25.3^{+0.4}_{-0.3}$	$24.6^{+0.2}_{-0.2}$	$23.9^{+0.2}_{-0.2}$	†
137559	10:02:02.55	+02:07:42.0	> 27.5	-	$25.4^{+0.2}_{-0.1}$	$25.6^{+0.4}_{-0.3}$	$25.5^{+0.6}_{-0.4}$	$26.1^{+0.7}_{-0.4}$	> 25.3	> 25.1	
282894	10:00:30.49	+02:33:46.3	> 27.7	-	$25.5^{+0.3}_{-0.2}$	$25.8^{+0.6}_{-0.4}$	> 25.9	$25.5^{+0.6}_{-0.4}$	$25.0^{+0.4}_{-0.3}$	$24.7^{+0.3}_{-0.2}$	
238225	10:01:52.31	+02:25:42.3	> 27.6	-	$25.0^{+0.2}_{-0.2}$	$25.0^{+0.2}_{-0.2}$	$25.0^{+0.3}_{-0.2}$	$24.9^{+0.3}_{-0.2}$	$24.7^{+0.3}_{-0.2}$	> 25.2	3
305036	10:00:46.79	+02:35:52.9	> 27.7	-	$25.3^{+0.1}_{-0.1}$	$25.2^{+0.2}_{-0.2}$	$24.9^{+0.3}_{-0.3}$	$25.1^{+0.4}_{-0.3}$	$23.9^{+0.2}_{-0.2}$	$23.9^{+0.2}_{-0.2}$	†
35327	10:01:46.18	+01:49:07.7	$27.5^{+0.5}_{-0.4}$	-	$25.3^{+0.2}_{-0.2}$	$25.8^{+0.5}_{-0.3}$	$25.7^{+0.7}_{-0.4}$	> 25.5	> 25.3	> 25.3	
304416	10:00:43.37	+02:37:51.6	$26.6^{+0.3}_{-0.2}$	-	$24.3^{+0.1}_{-0.1}$	$24.2^{+0.1}_{-0.1}$	$24.1^{+0.1}_{-0.1}$	$24.2^{+0.1}_{-0.1}$	$23.4^{+0.2}_{-0.2}$	$23.4^{+0.2}_{-0.2}$	1†
185070	10:00:30.19	+02:15:59.8	$27.4^{+0.4}_{-0.3}$	-	$25.4^{+0.2}_{-0.1}$	$25.3^{+0.2}_{-0.2}$	$25.5^{+0.6}_{-0.4}$	$25.1^{+0.2}_{-0.2}$	$23.7^{+0.2}_{-0.2}$	$24.7^{+0.3}_{-0.2}$	†
169850	10:02:06.48	+02:13:24.2	$26.1^{+0.1}_{-0.1}$	-	$24.5^{+0.1}_{-0.1}$	$24.5^{+0.1}_{-0.1}$	$24.6^{+0.2}_{-0.2}$	$24.6^{+0.2}_{-0.2}$	> 25.1	> 25.1	2
304384	10:01:36.86	+02:37:49.2	$26.4^{+0.3}_{-0.2}$	-	$25.0^{+0.4}_{-0.3}$	$24.6^{+0.2}_{-0.2}$	$24.9^{+0.4}_{-0.3}$	$24.8^{+0.4}_{-0.3}$	$24.6^{+0.3}_{-0.2}$	$24.7^{+0.3}_{-0.3}$	5†

279127	10:01:58.50	+02:33:08.5	$26.1^{+0.1}_{-0.1}$	-	$24.8^{+0.1}_{-0.1}$	$24.6^{+0.2}_{-0.1}$	$25.4^{+0.5}_{-0.3}$	$25.5^{+0.5}_{-0.3}$	$25.3^{+0.6}_{-0.4}$	$25.0^{+0.4}_{-0.3}$	
170216	10:02:03.82	+02:13:25.1	$26.8^{+0.3}_{-0.3}$	-	$25.5^{+0.3}_{-0.2}$	$26.0^{+0.6}_{-0.4}$	> 25.6	$25.4^{+0.4}_{-0.3}$	> 25.1	> 25.0	
104600	10:00:42.13	+02:01:57.1	$26.3^{+0.2}_{-0.1}$	-	$25.0^{+0.2}_{-0.1}$	$25.0^{+0.2}_{-0.2}$	$24.7^{+0.2}_{-0.2}$	$25.4^{+0.4}_{-0.3}$	$23.5^{+0.2}_{-0.2}$	$23.6^{+0.2}_{-0.2}$	†
268576	10:00:23.39	+02:31:14.8	$26.8^{+0.3}_{-0.2}$	-	$25.5^{+0.3}_{-0.2}$	$25.6^{+0.3}_{-0.3}$	> 25.8	$25.9^{+0.6}_{-0.4}$	$24.4^{+0.2}_{-0.2}$	> 25.5	
2103	10:01:43.13	+01:42:55.0	$26.1^{+0.2}_{-0.1}$	-	$25.1^{+0.2}_{-0.2}$	$25.3^{+0.4}_{-0.3}$	> 25.3	$24.9^{+0.4}_{-0.3}$	$24.8^{+0.4}_{-0.3}$	> 25.4	
179680	09:58:39.76	+02:15:03.3	$26.0^{+0.2}_{-0.2}$	-	$25.0^{+0.2}_{-0.2}$	$24.9^{+0.2}_{-0.2}$	$24.8^{+0.3}_{-0.2}$	$24.6^{+0.3}_{-0.2}$	$24.0^{+0.2}_{-0.2}$	$24.5^{+0.2}_{-0.2}$	†
18463	09:58:49.36	+01:46:02.1	$26.3^{+0.2}_{-0.1}$	-	$25.4^{+0.1}_{-0.1}$	> 26.0	> 25.8	$25.9^{+0.7}_{-0.4}$	$24.8^{+0.3}_{-0.2}$	$24.7^{+0.3}_{-0.2}$	†
122368	10:01:53.46	+02:04:59.9	$26.5^{+0.3}_{-0.2}$	-	$25.5^{+0.2}_{-0.2}$	> 26.2	> 25.9	> 25.8	$24.9^{+0.5}_{-0.3}$	> 25.0	
583226	10:00:46.89	+01:58:46.9	$26.4^{+0.2}_{-0.2}$	-	$25.5^{+0.2}_{-0.2}$	$25.7^{+0.6}_{-0.4}$	$25.2^{+0.5}_{-0.3}$	$25.6^{+0.7}_{-0.4}$	$24.5^{+0.2}_{-0.2}$	> 25.4	
82871	10:01:43.04	+01:58:01.1	$25.9^{+0.1}_{-0.1}$	-	$25.1^{+0.1}_{-0.1}$	$25.6^{+0.3}_{-0.2}$	$25.4^{+0.3}_{-0.3}$	$25.2^{+0.4}_{-0.3}$	$25.0^{+0.4}_{-0.3}$	> 25.2	
68240	09:59:16.85	+01:55:22.1	$25.4^{+0.1}_{-0.1}$	-	$24.7^{+0.1}_{-0.1}$	$24.6^{+0.2}_{-0.1}$	$24.9^{+0.3}_{-0.2}$	$24.7^{+0.2}_{-0.2}$	$23.7^{+0.2}_{-0.2}$	$24.0^{+0.2}_{-0.2}$	
271028	10:00:45.17	+02:31:40.2	$25.9^{+0.1}_{-0.1}$	-	$25.5^{+0.2}_{-0.1}$	$25.2^{+0.3}_{-0.3}$	$25.3^{+0.6}_{-0.4}$	$25.4^{+0.3}_{-0.2}$	$24.3^{+0.2}_{-0.2}$	$24.7^{+0.3}_{-0.2}$	†
30425	10:00:58.01	+01:48:15.3	$25.2^{+0.1}_{-0.1}$	-	$24.8^{+0.2}_{-0.1}$	$24.6^{+0.1}_{-0.1}$	$25.0^{+0.4}_{-0.3}$	$25.1^{+0.4}_{-0.3}$	$23.5^{+0.2}_{-0.2}$	$24.9^{+0.6}_{-0.4}$	9
234429	09:58:36.65	+02:24:56.4	$25.7^{+0.3}_{-0.2}$	-	$25.3^{+0.3}_{-0.3}$	> 25.6	> 25.4	> 25.2	> 25.2	> 25.3	
328993	10:01:35.33	+02:38:46.3	$25.6^{+0.1}_{-0.1}$	-	$25.4^{+0.5}_{-0.3}$	$25.5^{+0.5}_{-0.3}$	> 25.4	> 25.4	$24.2^{+0.2}_{-0.2}$	$24.1^{+0.2}_{-0.2}$	
35314	02:19:09.49	-05:23:20.6	$26.7^{+0.2}_{-0.2}$	> 26.8	$25.2^{+0.5}_{-0.3}$	$25.1^{+0.2}_{-0.1}$	$25.3^{+0.3}_{-0.3}$	$25.5^{+0.2}_{-0.2}$	$25.3^{+0.5}_{-0.4}$	> 24.7	
118717	02:18:11.50	-05:00:59.4	$26.8^{+0.6}_{-0.4}$	$26.5^{+0.4}_{-0.3}$	$25.0^{+0.5}_{-0.3}$	$25.3^{+0.2}_{-0.2}$	$25.3^{+0.3}_{-0.3}$	$25.0^{+0.2}_{-0.2}$	$23.8^{+0.2}_{-0.1}$	$23.6^{+0.2}_{-0.2}$	†
88759	02:17:57.58	-05:08:44.8	$25.8^{+0.1}_{-0.1}$	$24.0^{+0.1}_{-0.1}$	$25.5^{+0.7}_{-0.4}$	$25.1^{+0.1}_{-0.1}$	$25.5^{+0.4}_{-0.3}$	$24.9^{+0.2}_{-0.1}$	$23.9^{+0.2}_{-0.2}$	$24.7^{+0.7}_{-0.4}$	H
87995	02:18:50.86	-05:08:57.8	$26.3^{+0.2}_{-0.1}$	$25.6^{+0.1}_{-0.1}$	$25.0^{+0.5}_{-0.3}$	$25.3^{+0.2}_{-0.1}$	$25.3^{+0.3}_{-0.2}$	$25.3^{+0.3}_{-0.2}$	$24.9^{+0.5}_{-0.3}$	$24.8^{+0.6}_{-0.4}$	†

3.3.5 Photometric redshift analysis

The final step in selecting our sample of $z \sim 7$ galaxies involves fitting the available multiwavelength data points using a photometric redshift fitting routine. By incorporating optical, near- and mid-infrared photometry, we can select good high-redshift galaxy candidates and identify possible low-redshift galaxy interlopers (where the Balmer or 4000Å break is confused with the Lyman-break) or galactic dwarf stars whose spectrum peaks in the near-infrared.

We fitted Bruzual & Charlot (2003) models assuming a Chabrier (2003) initial-mass function, using the Le Phare photometric redshift code (Arnouts et al., 1999; Ilbert et al., 2006)[4]. At each redshift, stellar populations were constrained to be older than 10 Myr and younger than the age of the Universe. We fitted models with an exponentially-decreasing star-formation history with a characteristic timescale, $50\,\mathrm{Myr} \leq \tau \leq 10\,\mathrm{Gyr}$, for two metallicities ($Z = 1/5\,\mathrm{Z}_{\odot}$ and $\mathrm{Z}_{\odot}$). Note that a constant star-formation and burst model can be closely reproduced by the longest and shortest age τ models respectively. Internal dust reddening was calculated using the Calzetti et al. (2000) attenuation law, and parameterised by values of the rest-frame V-band attenuation in the range $0.0 \leq A_V \leq 4.0$. Absorption by the intergalactic medium was applied using the prescription of Madau (1995).

The presence of a Lyman-α emission line within the spectrum can significantly alter the photometric redshift derived (up to $\Delta z \sim 0.5$) when fitting to broad-band photometry, and hence can cause genuine galaxies at $z \geq 6.5$ to be excluded from our sample. In addition to the models described above, we also separately fitted templates where Lyman-α emission was added to the full template set, with rest-frame equivalent width in the range $0.0 \leq EW_0 \leq 240\,$Å. The continuum level was estimated from the mean value of the continuum in the wavelength range $\lambda = 1250-1300\,$Å before the reddening was applied.

Contamination by cool galactic stars can be a significant problem when using ground-based data for high-redshift studies (Dunlop, 2013), particularly when there is insufficient wavelength sampling of the SED around the predicted Lyman-break. To ascertain how well our galaxy candidates could be described by stellar templates, we fitted the reference stellar spectra from the SpeX library[5] with spectral types from M4 to T8. The dwarf spectra do not extend to the wavelengths of the *Spitzer*/IRAC bands and so these were excluded during the fitting processes, although they can be taken into

[4] `http://www.cfht.hawaii.edu/~arnouts/lephare.html`
[5] `http://pono.ucsd.edu/~adam/browndwarfs/spexprism/`

account in the selection via the mid-IR colours (see Bowler et al. 2012).

Using the redshift-χ^2 distributions from our photometric redshift fitting procedure, we required an acceptable fit above z = 6 (determined by $\chi^2 < 10$ and 11.3 for the UDS and UltraVISTA respectively, which corresponds to 2σ significance given the degrees of freedom in the fitting). In an effort to remove low-redshift contaminants from the sample we also excluded all objects that had a low-redshift solution ($z < 4.5$) within $\Delta\chi^2 = 4$ of the high-redshift ($z > 6$) solution. Here the $\Delta\chi^2 = 4$ value gives the 2σ (~ 95 percent) confidence level for one degree of freedom, the redshift, as we have marginalised over all other parameters[6]. In the final stage of selection we performed careful visual checks of a stack of the optical bands blueward of the z'-band to ensure there was no residual optical flux that would imply a lower redshift solution. These further steps resulted in samples of 53 and 18 remaining candidates in the UltraVISTA and UDS datasets respectively.

Armed with a reduced sample of candidates that were acceptable as $z > 6$ objects, we performed further SED fitting including Lyα-emission and stellar templates. We also included photometry measured in the $NB921$ filter for candidates within the UDS field, as the narrow-band sits half-way through the z'-band filter and, with or without allowing for Lyα emission in the SED, allows a more precise determination of the photometric redshift. At this stage we also fitted to the photometry including the IRAC bands at 3.6μm and 4.5μm, to exclude dusty low-redshift solutions which have SEDs that rise rapidly to longer wavelengths, and also to obtain a more accurate estimate of the galaxy masses. We compared the fits with and without the inclusion of the IRAC data to ensure objects were not excluded due to nebular emission lines being present in the spectra (see Section 3.7.2 for further discussion), although in practice the IRAC imaging is sufficiently shallow compared to the near-infrared data that the unusual IRAC colours indicative of nebular emission, affect the χ^2 values derived from stellar only SED models very little (see Fig. 3.3). The results of careful consideration of the SED fits, along with final visual identification and removal of subtle near-infrared artefacts, resulted in the sample of 34 galaxies presented in the next section.

The strength of our selection methodology is demonstrated by the confirmation, using the deeper near-infrared imaging analysed in this work, of 9 of the 10 candidates we originally selected from the first data release of the UltraVISTA dataset in Bowler et al. (2012) as high-redshift galaxies (see Section 3.5.3). Furthermore, in the UDS dataset we have independently selected the brightest $z = 6.6$ LAE in the field, which was

[6]A useful guide and reference for the appropriate $\Delta\chi^2$ for a given number of degrees of freedom can be found in Press et al. (1992).

initially found using narrow-band imaging (where it is > 1 mag brighter than in the continuum bands that we use for selection) by Ouchi et al. (2008).

3.4 Candidate galaxies

The observed photometry for the final sample of 34 galaxies in the UltraVISTA and UDS fields is presented in Table 3.2 and the photometric redshifts and best-fitting parameters, such as the rest-frame equivalent width for Lyα and the dust attenuation, are presented in Table 3.3. In Figure 3.3 we present postage-stamp images of each candidate and the best-fitting galaxy and star SEDs. All the following tables, SED fits and postage-stamps show the candidates ordered by best-fitting photometric redshift without Lyα emission included in the fitting, where candidates have been split by field. With the goal of including all potential $z > 6.5$ galaxies, in the following tables we have included galaxy candidates that have best fitting photometric redshifts in the range $6.5 < z < 7.5$ only with the inclusion of Lyα emission in the SED, in addition to the galaxies that do not require Lyα to be robustly at $z > 6.5$. The presence of the spectroscopically confirmed galaxy 'Himiko' at z = 6.595 in the sample motivates this inclusive approach, as without the inclusion of Lyα in the SED, the galaxy would have been excluded from the sample on the basis of a best fitting photometric redshift of $z = 6.38^{+0.03}_{-0.05}$.

Table 3.3 *The best-fitting photometric redshift and model parameters for the DR2 UltraVISTA and UDS samples are presented in the upper and lower sections of the table respectively. Where the IRAC photometry is considered confused with a nearby object we exclude the [*$3.6\mu\mathrm{m}$*] and [*$4.5\mu\mathrm{m}$*] bands from the fitting procedure, and present the resulting* χ^2 *value labelled with a dagger to illustrate that there are different degrees of freedom, and hence acceptable* χ^2 *values, for these objects. We order the galaxies by the best-fitting photometric redshift in column 2. Columns 7-10 of the table show the redshift,* χ^2*-value, rest-frame equivalent width and* A_V *value when we introduce the possibility of Ly*α*-emission in the fits. The candidate labelled 'H' is Himiko, which has an extremely bright* $NB921$ *flux that can only be well-fitted with models including Ly*α *emission, hence the unacceptable* χ^2 *value for continuum-only fitting seen in column three. The best-fitting stellar template, where we fit spectral types M4−T8, is given in column 11 with the* χ^2 *in column 12. Missing FWHM values correspond to objects unselected by* SExtractor *in that band. In the final column, we flag the candidates from Bowler et al. (2012).*

	No Lyα				With Lyα					Star	FWHM				
ID	z	χ^2	A_V /mag	Z /$Z_\odot$	z	χ^2	EW_0 /Å	A_V /mag	Z /$Z_\odot$	Stellar Type	χ^2	z'	Y	J	B12
												/arcsec			
136380	$7.21^{+0.10}_{-0.21}$	1.7	0.0	1.0	7.24	1.6	10	0.0	1.0	T3	17.2	-	1.0	1.3	
28495	$7.19^{+0.10}_{-0.14}$	3.5	0.1	1.0	7.69	1.7	180	0.0	1.0	T1	23.2	-	2.1	2.2	
268511	$7.12^{+0.14}_{-0.11}$	2.6	0.0	0.2	7.25	2.2	80	0.0	0.2	T8	9.2	1.7	1.4	0.5	6
268037	$7.07^{+0.14}_{-0.12}$	9.5	0.2	1.0	7.55	8.6	200	0.3	1.0	T8	22.5	-	2.0	0.7	
65666	$7.04^{+0.16}_{-0.11}$	5.5	0.4	1.0	7.04	5.5	0	0.4	1.0	T4	25.0	1.7	1.1	1.6	4
211127	$7.03^{+0.12}_{-0.11}$	$3.2^\dagger$	0.0	0.2	7.20	2.4	160	0.0	0.2	T8	29.0	-	1.5	1.1	
137559	$7.03^{+0.14}_{-0.16}$	1.9	0.0	0.2	7.15	1.8	60	0.0	0.2	T8	9.8	-	1.7	-	
282894	$7.01^{+0.14}_{-0.15}$	8.5	0.0	0.2	7.31	6.6	240	0.4	0.2	T8	12.5	-	1.6	0.7	
238225	$6.98^{+0.12}_{-0.12}$	3.1	0.5	1.0	7.01	3.0	10	0.5	1.0	T3	23.2	1.0	1.0	1.6	3
305036	$6.95^{+0.23}_{-0.22}$	$0.7^\dagger$	0.0	1.0	7.04	0.7	40	0.0	1.0	T3	11.6	-	-	-	
35327	$6.88^{+0.10}_{-0.13}$	1.5	0.0	0.2	7.05	0.8	100	0.0	0.2	T8	19.0	-	1.5	-	
304416	$6.85^{+0.09}_{-0.10}$	$2.4^\dagger$	0.0	1.0	6.85	2.4	0	0.0	1.0	T3	27.2	-	1.7	1.9	1

185070	$6.77^{+0.14}_{-0.19}$	$1.1^{\dagger}$	0.1	0.2	7.01	1.1	90	0.2	0.2	T2	32.0	-	1.3	1.3	
169850	$6.70^{+0.05}_{-0.06}$	4.6	0.2	1.0	6.86	4.4	50	0.2	1.0	M6	28.0	1.4	1.7	2.2	2
304384	$6.64^{+0.12}_{-0.22}$	$1.9^{\dagger}$	0.8	0.2	6.65	1.9	0	0.8	0.2	T3	6.3	1.3	1.1	1.7	5
279127	$6.59^{+0.05}_{-0.06}$	8.8	0.0	0.2	6.59	8.8	0	0.0	0.2	M6	25.9	2.6	2.8	1.9	
170216	$6.55^{+0.14}_{-0.17}$	2.5	0.2	1.0	6.95	1.6	200	0.5	1.0	M6	10.6	1.5	1.2	-	
104600	$6.54^{+0.07}_{-0.08}$	$10.1^{\dagger}$	0.4	1.0	6.54	10.1	0	0.4	1.0	M6	16.7	1.9	1.5	1.7	
268576	$6.51^{+0.14}_{-0.12}$	9.2	0.0	0.2	6.93	8.6	180	0.0	0.2	M6	13.4	1.4	1.4	1.2	
2103	$6.41^{+0.11}_{-0.12}$	7.0	0.0	1.0	6.90	6.3	240	0.6	1.0	M7	17.3	1.1	2.8	1.3	
179680	$6.40^{+0.16}_{-0.26}$	$3.7^{\dagger}$	0.4	0.2	6.93	3.0	240	1.0	0.2	M6	20.3	1.6	1.0	0.9	
18463	$6.38^{+0.07}_{-0.10}$	$7.3^{\dagger}$	0.0	0.2	6.71	6.1	170	0.0	0.2	M7	37.4	1.3	1.6	-	
122368	$6.36^{+0.14}_{-0.16}$	6.4	0.0	0.2	6.94	5.4	240	0.0	0.2	M7	19.5	1.8	1.7	-	
583226	$6.33^{+0.15}_{-0.16}$	5.0	0.0	1.0	6.66	4.7	140	0.0	1.0	M7	10.7	1.5	1.7	1.9	
82871	$6.31^{+0.09}_{-0.08}$	6.1	0.0	1.0	6.81	4.0	240	0.1	1.0	M7	29.3	1.0	1.1	1.0	
68240	$6.29^{+0.08}_{-0.10}$	3.7	0.0	0.2	6.71	3.1	200	0.0	0.2	M7	20.6	1.8	2.0	2.3	
271028	$6.21^{+0.10}_{-0.19}$	$0.5^{\dagger}$	0.7	1.0	6.50	0.3	110	0.8	0.2	M7	8.2	1.3	1.8	1.6	
30425	$6.20^{+0.10}_{-0.08}$	15.3	0.0	1.0	6.59	13.6	150	0.0	0.2	M7	31.9	1.3	2.1	1.3	9
234429	$6.11^{+0.22}_{-0.21}$	4.3	0.1	0.2	6.64	3.1	240	0.0	1.0	M7	16.1	1.1	0.0	-	
328993	$6.01^{+0.19}_{-0.21}$	0.9	0.5	0.2	6.58	0.1	240	0.1	1.0	M7	21.7	0.9	-	0.7	
35314	$6.69^{+0.10}_{-0.07}$	6.9	0.2	0.2	6.90	6.6	80	0.3	0.2	M6	18.7	2.0	-	1.1	
118717	$6.51^{+0.05}_{-0.08}$	$1.0^{\dagger}$	0.0	0.2	6.61	1.0	30	0.0	0.2	M9	6.8	0.9	-	1.4	
88759	$6.38^{+0.03}_{-0.05}$	55.8	0.0	1.0	6.52	12.7	150	0.1	1.0	M8	109.8	2.2	-	2.1	H
87995	$6.48^{+0.03}_{-0.23}$	$1.4^{\dagger}$	0.0	1.0	6.59	1.0	60	0.0	0.2	M8	29.5	0.8	-	1.3	

3.5 Images and SED fits

In this section we present postage-stamp images and the best-fitting galaxy and star SED fits for the galaxies in our sample. The 30 galaxies from the UltraVISTA field are shown in Fig. 3.3, followed by the four UDS galaxies in Fig. 3.4.

3.5.1 UltraVISTA DR2

From the 0.62 deg^2 of the 'ultra-deep' UltraVISTA DR2 data, we found 29 candidate $6.5 < z < 7.5$ galaxies. These candidates are listed in the upper part of Tables 3.2 and 3.3, and include seven of the eight candidates presented in Bowler et al. (2012) that lie within the regions of the image covered by the ultra-deep data. The table also includes a single object from Bowler et al. (2012) that lies outside the new ultra-deep UltraVISTA imaging we analyse here, but is confirmed as a high-redshift galaxy with the improved photometry now available (see further discussion in Section 3.5.3). Of the 29 candidates within the ultra-deep strips, 11 have best-fitting photometric redshifts at $z > 6.5$ only when Lyα-emission is included in the templates, although in some cases the candidate still has a reasonable probability of being at $z > 6.5$ with continuum-only fitting (as illustrated by the error bars presented and the χ^2 vs. redshift insets in the SED figures). The majority of the candidates are detected in the *Spitzer*/IRAC bands; in the cases where the photometry was contaminated by nearby lower-redshift objects we have excluded these bands from the fitting procedure and flagged the object in Tables 3.2, 3.3 and 3.6. When excluding probable galactic stars from the sample based on the stellar template fitting, the size information obtained from the full-width at half-maximum (FWHM) measurement described in Section 3.8 was taken into account. Candidates excluded as stars were retained for size comparisons with the final sample as shown in Fig. 3.7.

3.5.2 UDS

Within the 0.74 deg^2 of overlapping optical and near-infrared imaging in the UDS field, we found four candidates for galaxies at $z > 6.5$ as listed in the lower section of Tables 3.2 and 3.3. Of the four candidate $z > 6.5$ galaxies, two have best-fitting models at $z > 6.5$ only when the fitting allows Lyα emission, one of which is the previously identified and spectroscopically confirmed galaxy 'Himiko' (Ouchi et al.,

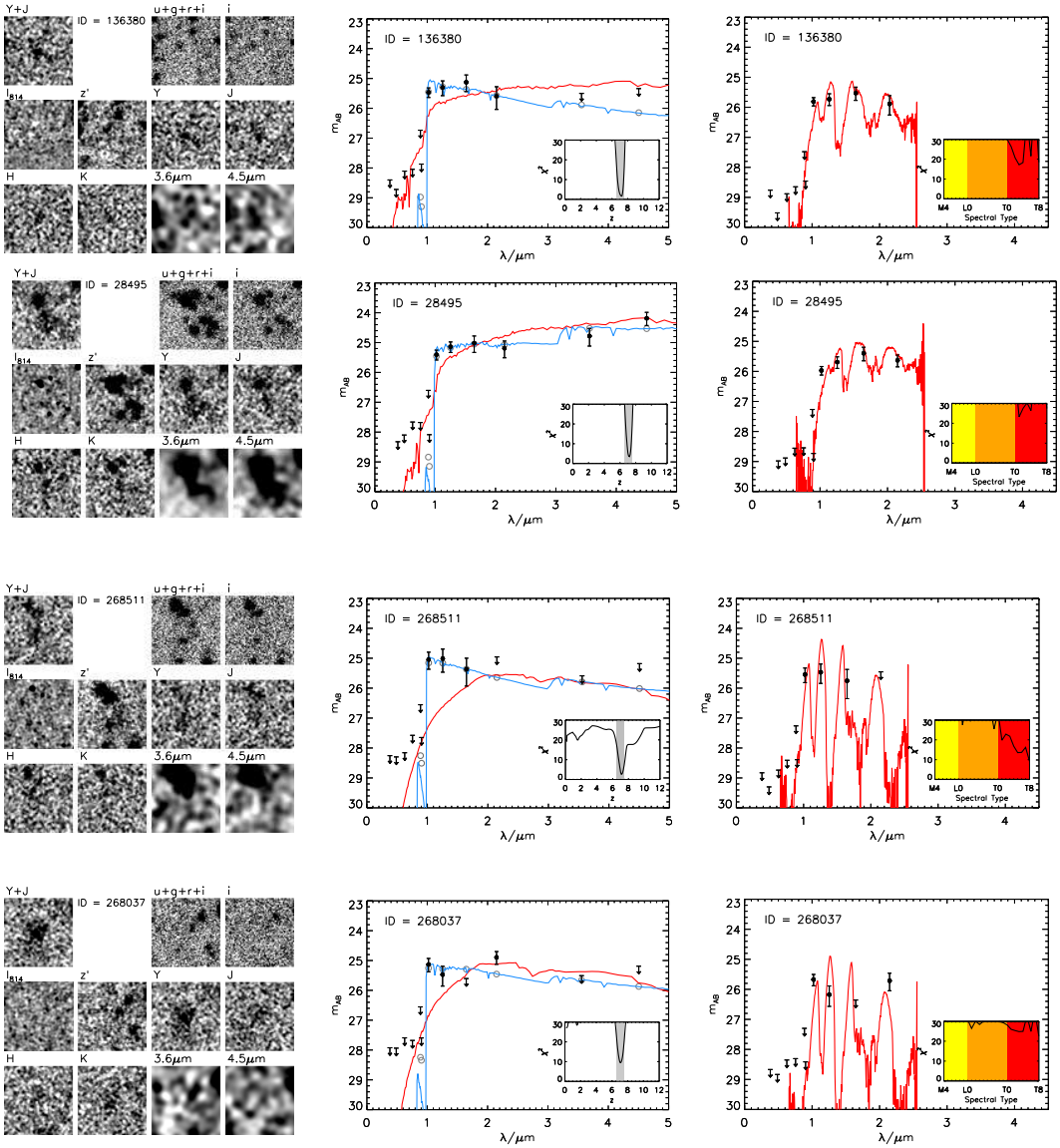

Figure 3.3 *Postage-stamp images and galaxy and star SED fits to the 30 galaxies from the UltaVISTA field. The stamps shown to the left are* 10×10*-arcsec, with the grey scale determined from saturating all pixels that exceed* 3σ *from the background. The measured photometry and errors are shown as the black points, with the grey circles showing the predicted photometry from the best-fitting high-redshift model. In the central plots, the best fitting low-redshift (*$z < 4.5$*) and high-redshift solutions are shown as the red and blue lines respectively. On the right, the best-fitting stellar templates are presented, where here the photometry was measured in smaller 1.2-arcsec diameter apertures. The insets on each plot show the chi-squared distribution as a function of redshift or stellar type, with the grey band on the redshift-*χ^2 *plot showing the range of redshifts covered by our sample (*$6.5 < z < 7.5$*).*

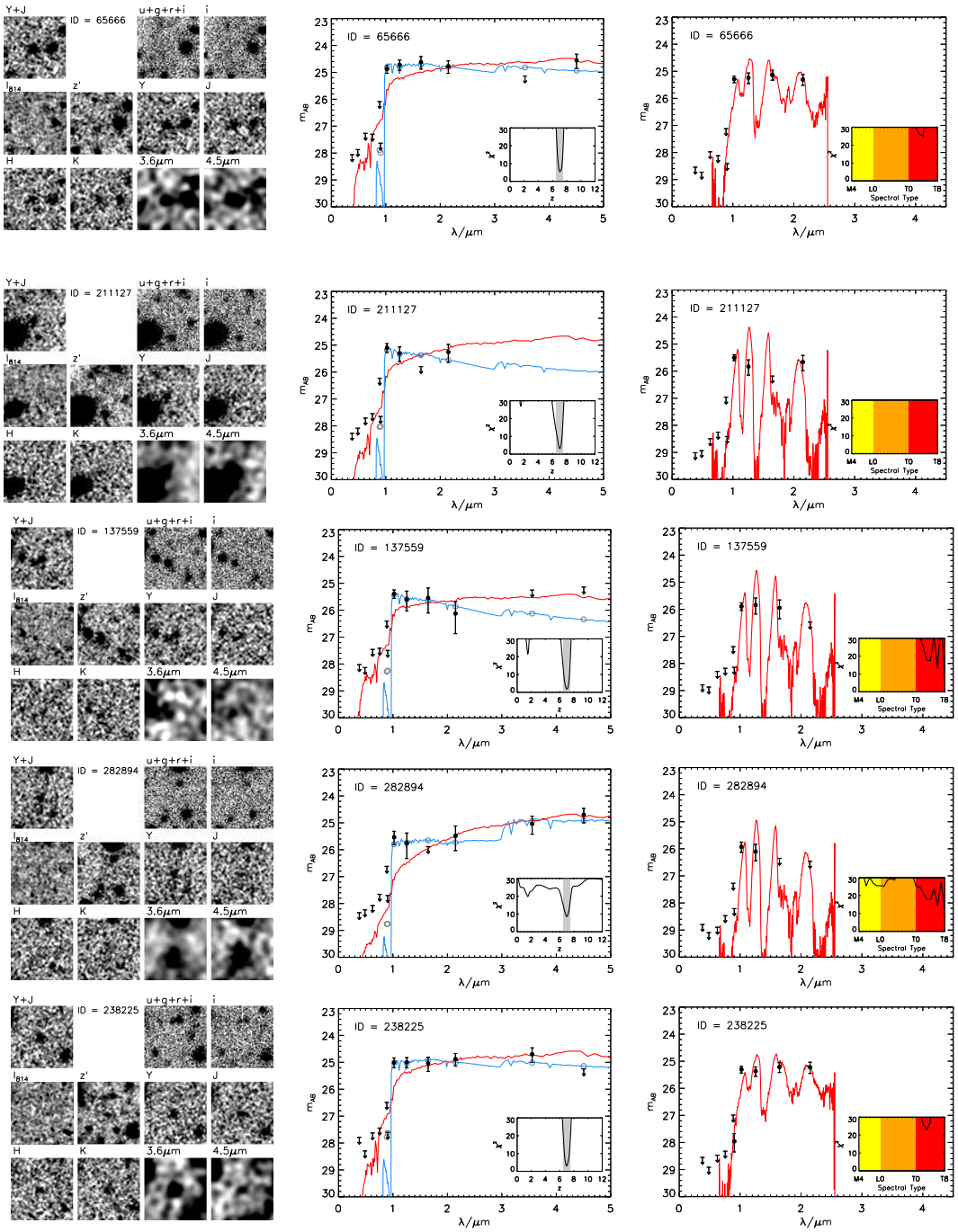

Figure 3.3 *Continued.*

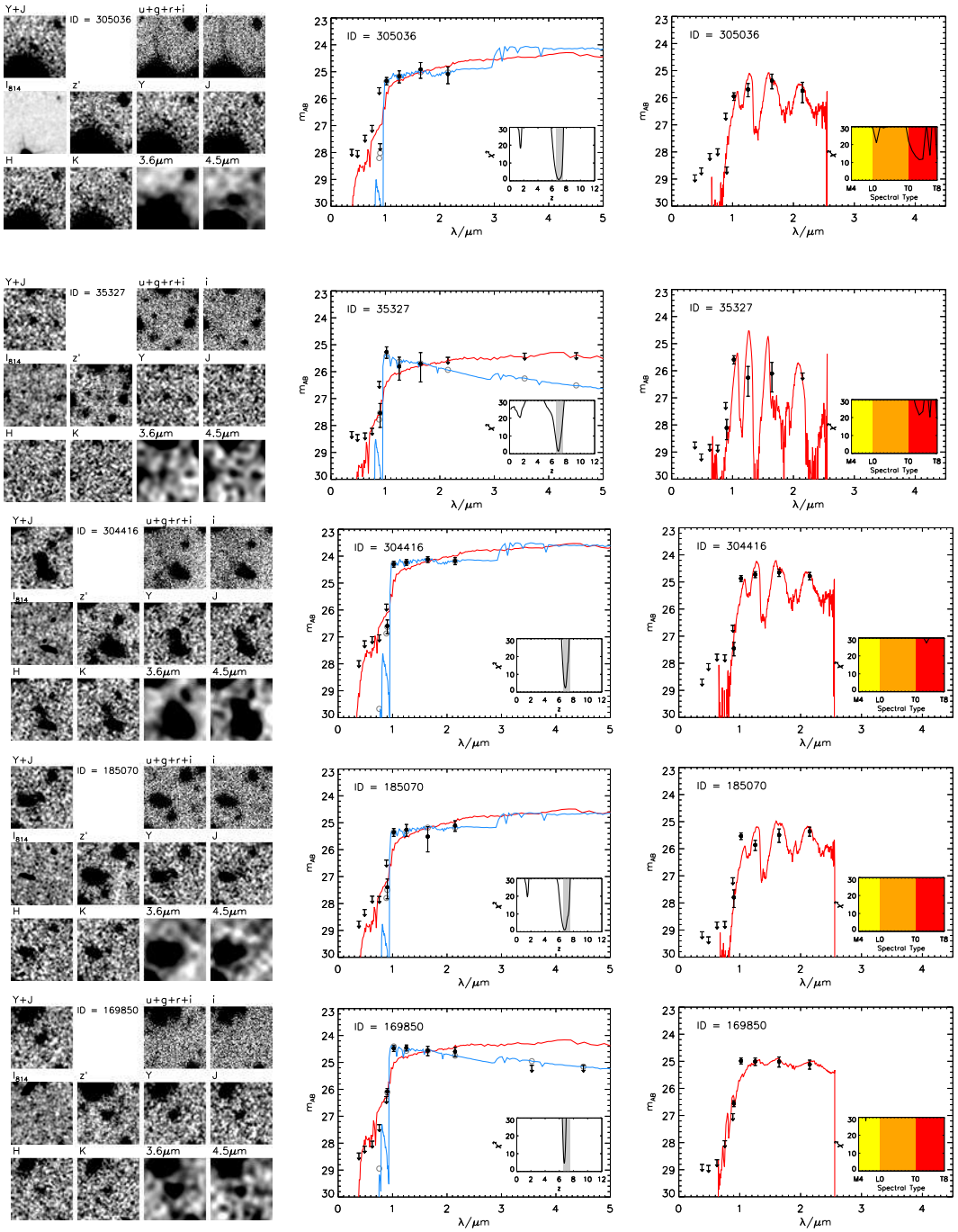

Figure 3.3 *Continued.*

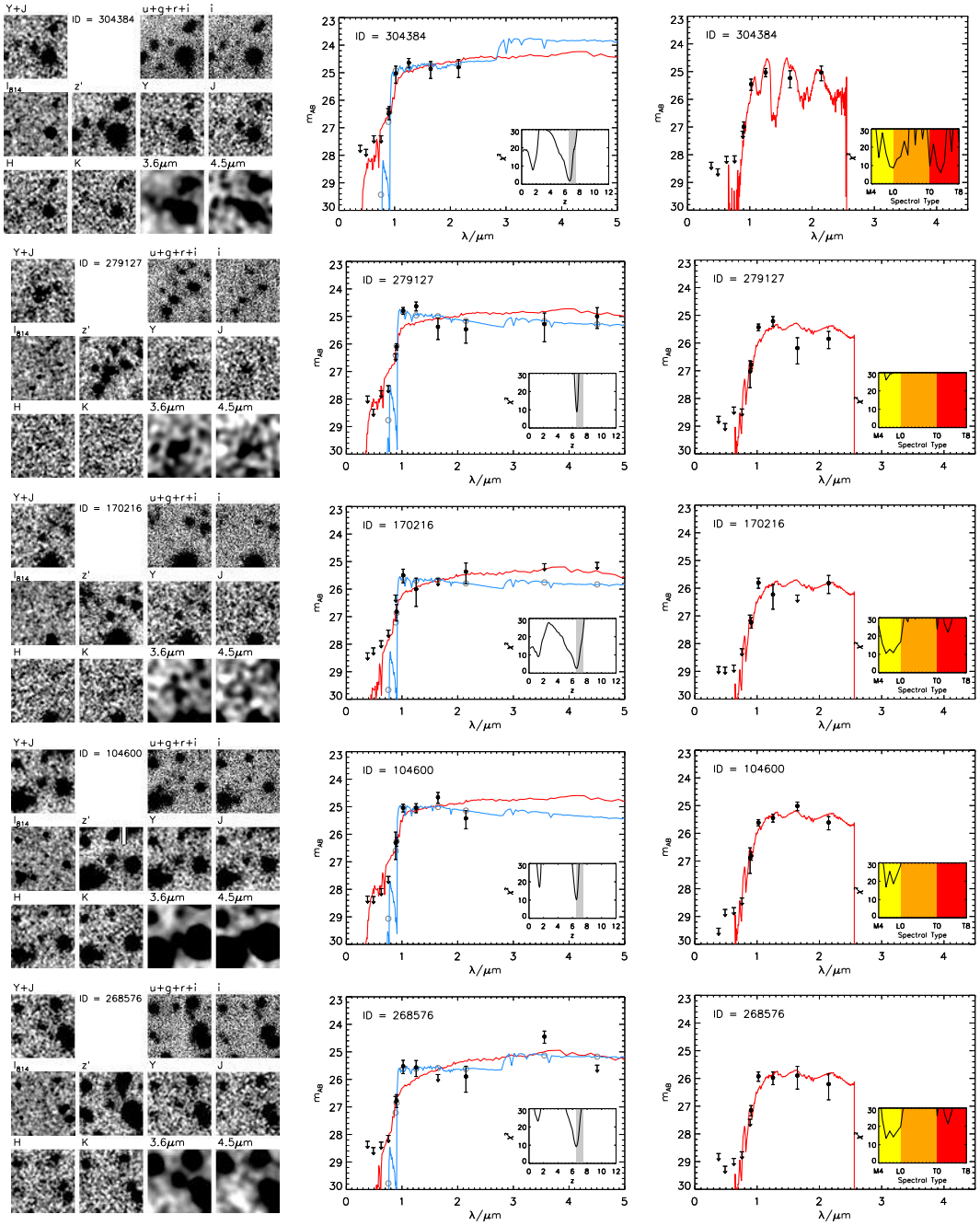

Figure 3.3 *Continued.*

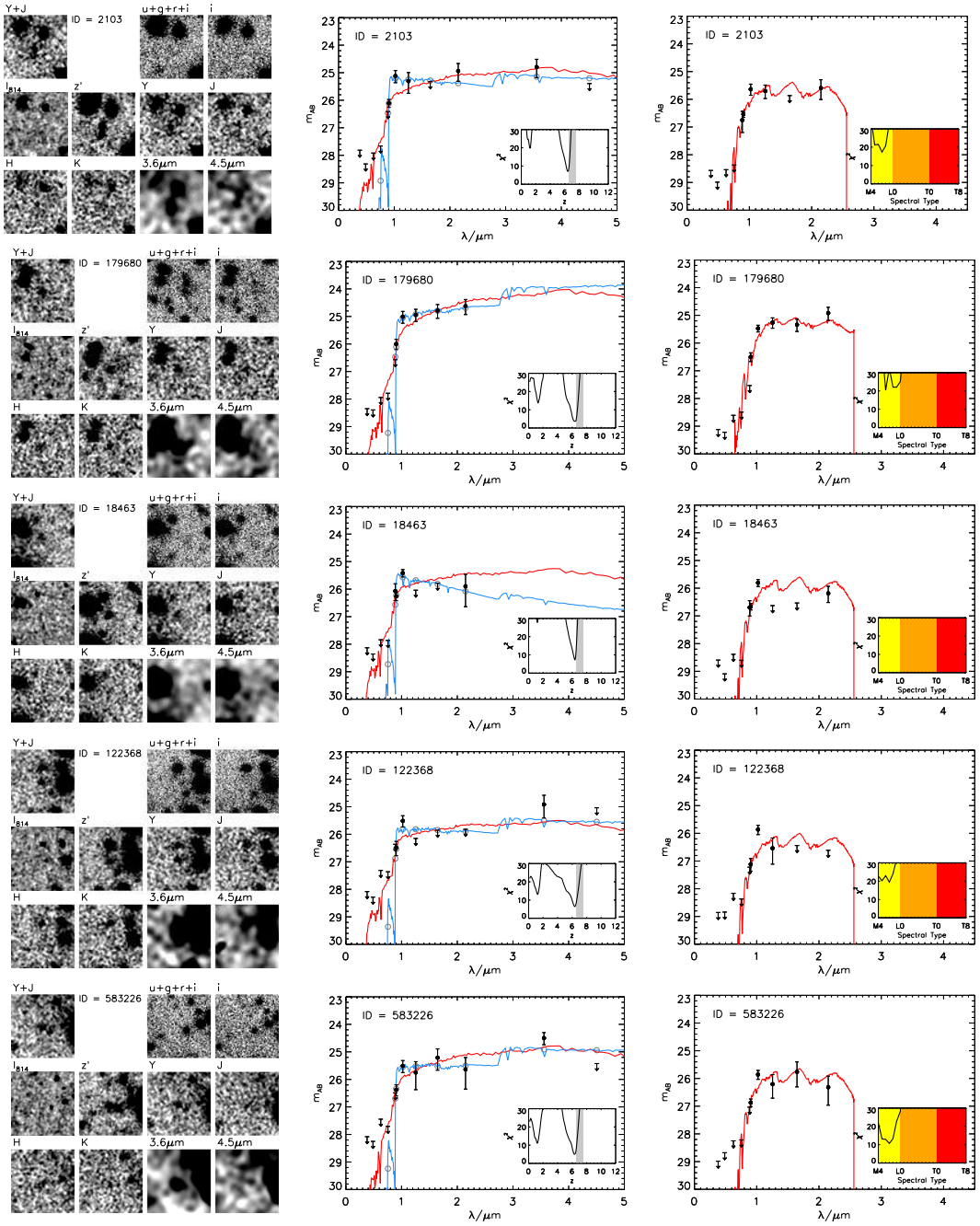

Figure 3.3 *Continued.*

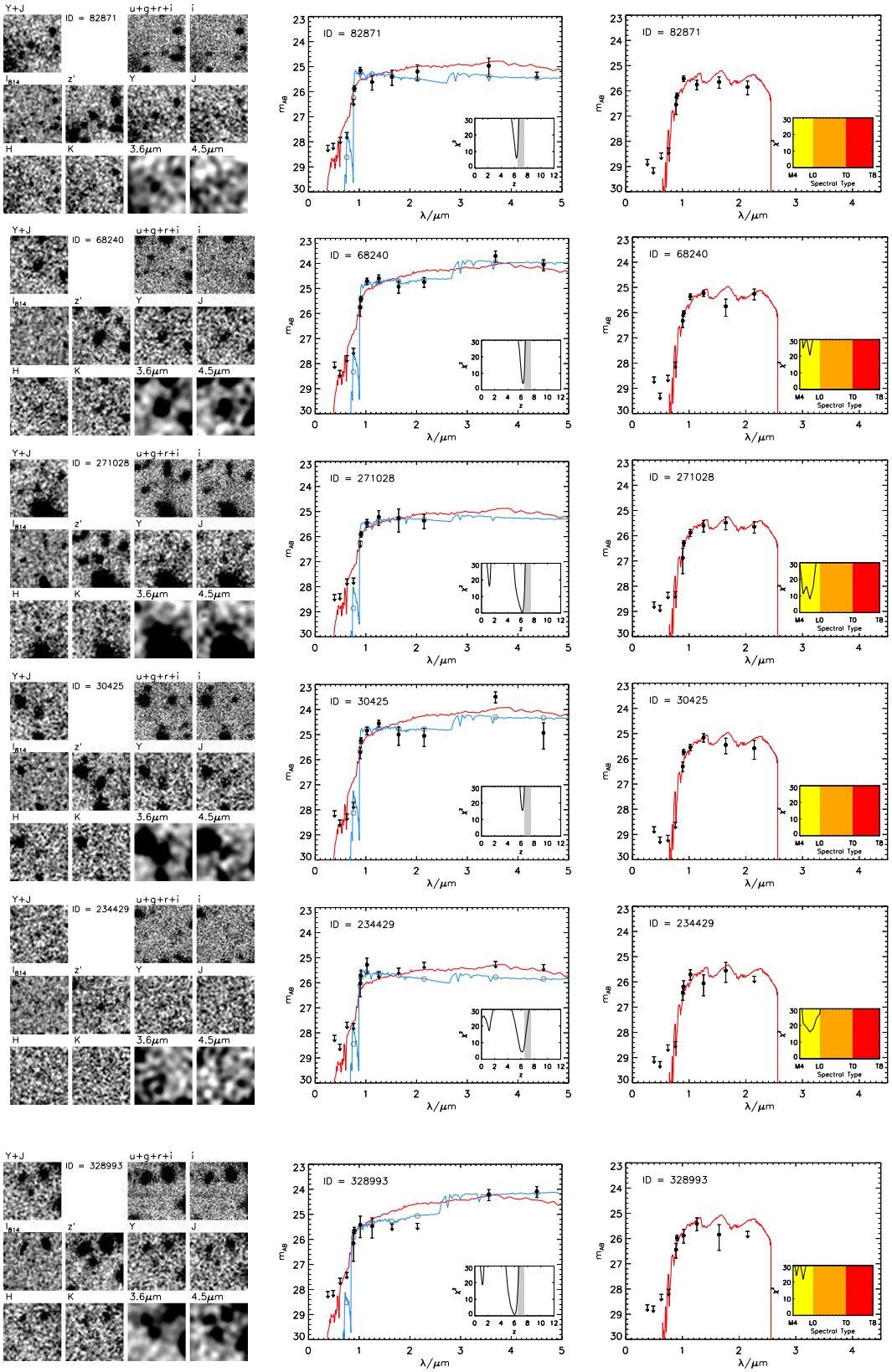

Figure 3.3 *Continued.*

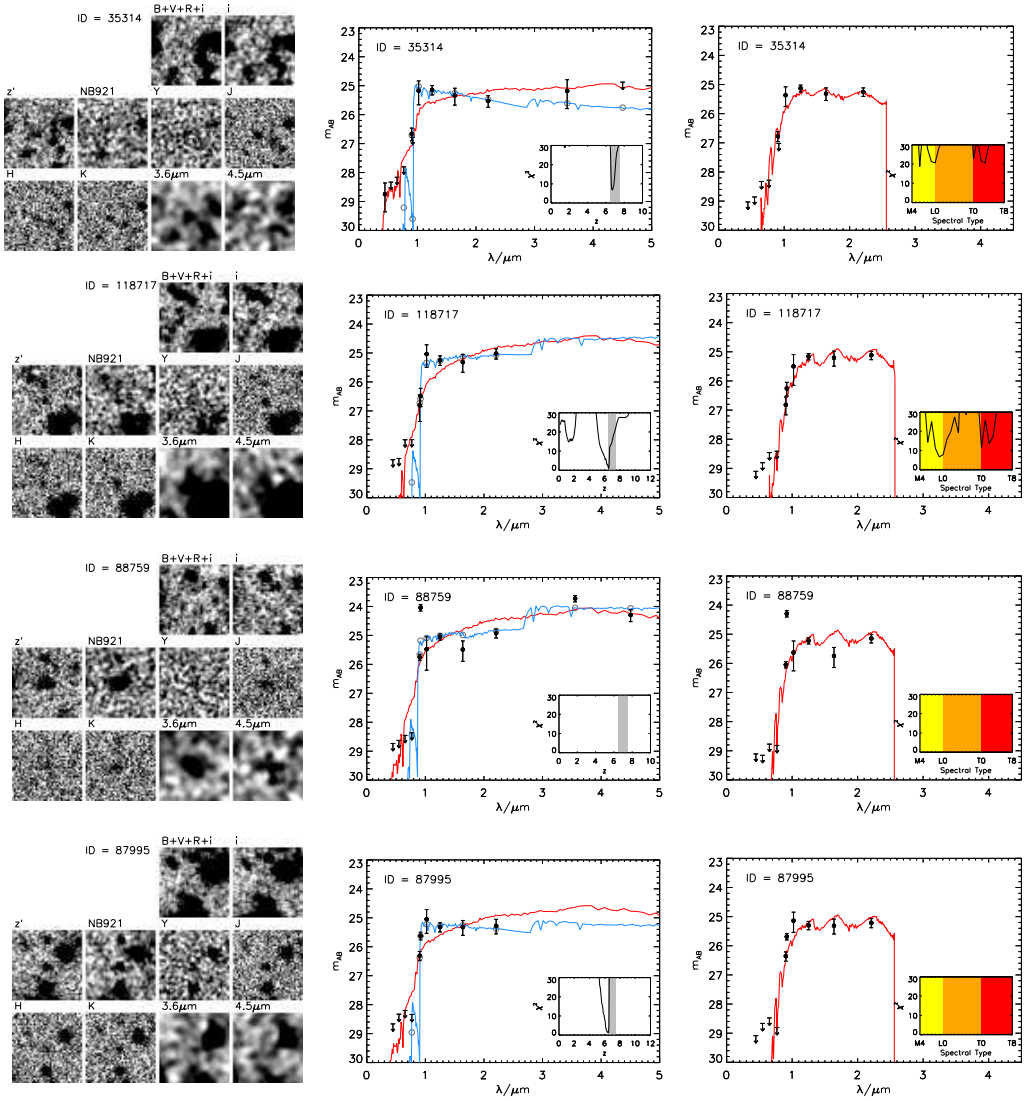

Figure 3.4 *Postage-stamp images and galaxy and star SED fits to the four galaxies from the UDS field. See the caption of Fig. 3.3 for details.*

2013) at z = 6.595. For Himiko, we find a best-fitting photometric redshift of $z = 6.52$ when including the narrow-band $NB921$ photometry and allowing for Lyα emission in the fits, and a value of $z = 6.38^{+0.03}_{-0.05}$ with continuum-only fits. The slightly lower redshift compared to that found spectroscopically for Himiko ($z = 6.52$ vs. $z = 6.595$), is a result of the exact redshift being very sensitive to the calibration between the z' and the $NB921$, as the strength of any line emission must be able to reproduce the $z' - NB921$ colour observed. The effect is compounded by the slightly longer-wavelength peak of the Lyα line compared with the central wavelength of the narrow-band filter, which is optimised to select LAEs with $z = 6.56 \pm 0.05$. We find a best-fitting $EW_0 = 160 \pm 60$Å for Himiko, which although large compared to that found spectroscopically (~ 80Å), is consistent with the original estimate from the broad- and narrow-band photometry made by Ouchi et al. (2009a) of $EW_0 = 100^{+302}_{-43}$Å.

3.5.3 Bowler et al. (2012) candidates revisited

In Bowler et al. (2012) we presented ten candidate $6.5 < z < 7.5$ galaxies in the first year 'deep' component of the UltraVISTA survey, within the full 1 deg^2 of overlapping data shown in Fig. 3.1. Using the new reductions of the full field that contain the DR2 imaging, we obtained improved photometry and photometric redshifts for all ten galaxies. Although only eight of the original ten candidates lie within the ultra-deep strips, the imaging available for the remaining two objects includes more exposures in the DR2 release than those utilised in Bowler et al. (2012), and improvements in the calibration and pipeline has resulted in deeper data by up to 0.35 mag in the case of the H-band. The depth improvements in the Y- and J-bands over the full area are moderate however (< 0.1 mag) and hence we do not repeat the selection process over the full 1 deg^2 here. The improved photometry shown in Table 3.4 was taken from the $Y + J$ selected catalogue created as part of the selection process described in Section 3.3.1. When comparing the photometry between DR1 and DR2, the Y-band magnitudes are fainter by $\gtrsim 0.1$ mag, a consequence of the zeropoint shifts in the data reduction process in part, with the remaining magnitude offset a likely result of the use of smaller apertures here (1.8-arcsec diameter vs. 2.0-arcsec) on resolved galaxies (see Section 3.8) .

The four candidates in the top 'robust' category are all confirmed as high-redshift galaxies by the new imaging, which forms effectively an independent check of the photometry given the difference in integration times between DR1 and DR2. Comparing the best-fitting parameters, all four have lower best-fitting redshifts by

$\Delta z \leq 0.1$. Inspection of the magnitudes and SED plots between the DR1 and DR2 data indicates that the shift in best-fitting redshift is a consequence of the drop in Y and J-band magnitudes closer in-line with the z'-band photometry, requiring the Lyman-break to additionally fill the z'-band to reproduce the now bluer $z' - Y$ colour. The stellar fits for these candidates get worse for three of the four 'robust' candidates, with the χ^2 value for object ID 218462 only marginally decreasing from $\chi^2 = 23.9$ to $\chi^2 = 23.2$.

Of the four out of six further candidates from Bowler et al. (2012) that lie in the deep strips, two are present in our final sample (277880 and 28400) with consistent photometry and resulting photometric redshift results as presented. The weakest candidate from Bowler et al. (2012), with ID 2233, was not present in the new $Y + J$ selected catalogue. Visual inspection shows 2233 to be faint in the near-infrared imaging, but bright and elongated in the z'-band. There is a tentative detection in the smoothed i-band image suggesting, when coupled with the photometric redshift analysis, that this object is likely at a slightly lower redshift of $6.0 < z < 6.5$. The remaining candidate (271105), which had the lowest χ^2 value for the stellar fits in Bowler et al. (2012), is best fitted as a star, with the characteristic 'hook' in the SED clearly seen in Fig. 3.5.

Only two of the original ten candidates (268511 and 95661) do not lie within the deep strips, however we remeasured the photometry using the improved data reductions of the full field. Candidate 95661 was included in the Bowler et al. (2012) sample as a result of the large errors on the photometric redshift of $z = 6.13^{+0.38}_{-0.27}$, but is now excluded from our new sample as a $z < 6.5$ galaxy with best-fitting photometric redshift of $z = 6.25^{+0.10}_{-0.13}$. Finally, object 268511 remains a good $z > 6.5$ LBG candidate, although as it is effectively only detected in the Y-band there is still the possibility of it being a transient. Hence, we include candidate 268511 in the final sample as our only candidate from the region of the full 1 deg^2 of overlapping multiwavelength imaging not covered by the ultra-deep DR2 imaging.

In conclusion, of the ten candidate $z > 6.5$ galaxies presented previously in Bowler et al. (2012), all four of the 'robust' candidates are reconfirmed here. Two of the three 'insecure/contaminant' galaxies are still present in the sample, with the third candidate being excluded as a star based on the improved photometry. Only one of the three 'insecure' candidates is retained in our final $z \simeq 7$ sample, with the two excluded galaxies now confirmed to lie at a slightly lower redshift in the range $6.0 < z < 6.5$. We present the improved photometry and derived SED properties for all ten candidates in the Appendix, along with the SED fits and postage-stamp images of the three candidates

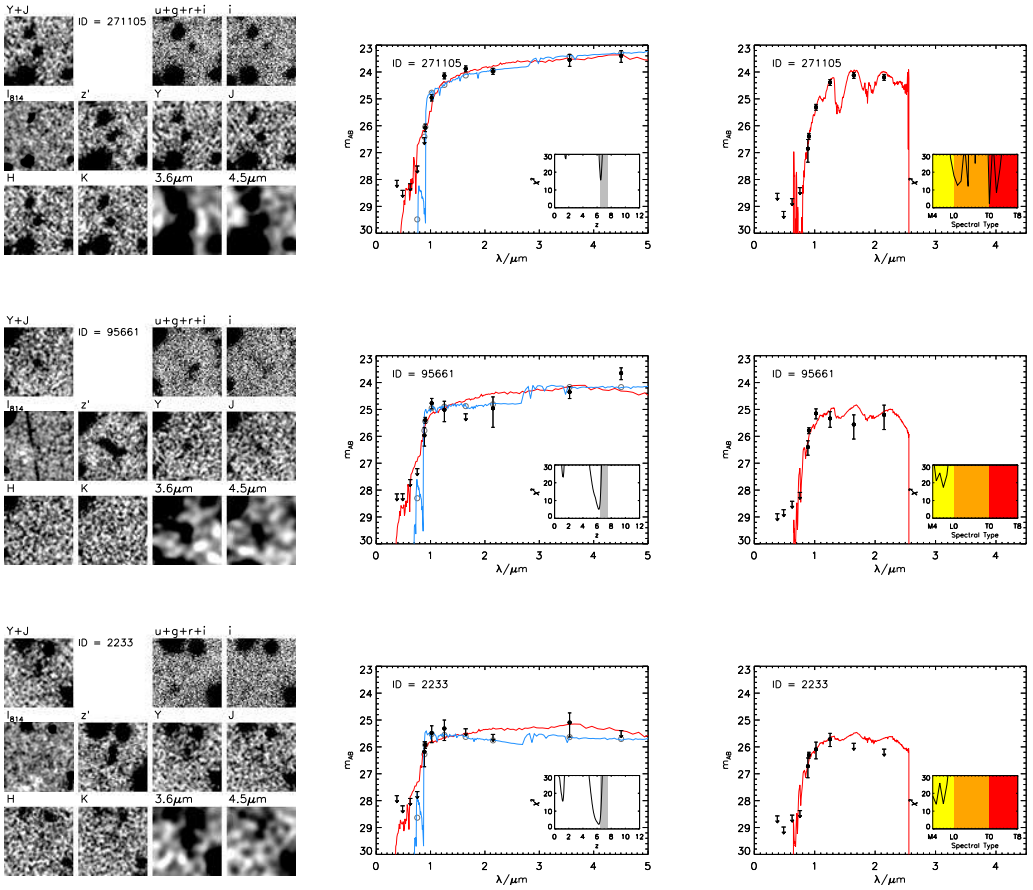

Figure 3.5 *Postage-stamp images, and galaxy and star SED fits for the three candidates from the Bowler et al. (2012) sample that are not present in our final sample. The details of the images and plots are described in the caption for Fig. 3.3. With the improved photometry, candidate 271105 is now best-fitted as a type-T0 dwarf star, showing the characteristic hook-like spectrum. The other candidates now have best-fitting photometric redshifts in the range* $6.0 < z < 6.5$.

from Bowler et al. (2012) that are not included in the final sample from this chapter.

3.6 Bowler et al. 2012 improved photometry and SED fitting analysis

Here we present improved photometry and SED fitting results for the 10 high-redshift galaxy candidates from Bowler et al. (2012), and 3.5 shows postage-stamp images and SED fits to the three Bowler et al. (2012) candidates that are not included in our new sample.

Table 3.4 *The DR2 UltraVISTA magnitudes for the ten galaxy candidates presented in Bowler et al. (2012). The magnitudes were measured in a 1.8-arcsec diameter circular aperture in all cases except the IRAC magnitudes which were measured in a 2.8-arcsec diameter circular aperture. All magnitudes have been corrected to the 84% enclosed flux level using appropriate point-source corrections, and the errors presented are determined from the local error method detailed in Section 3.2.3. The signal-to-noise of the detection is presented in brackets after each magnitude. Where an object was detected at less than 2σ significance, the magnitude is replaced with the 2σ local depth as an upper limit.*

ID	z'	Y	J	H	Ks	3.6μm	4.5μm
277912	$26.6^{+0.3}_{-0.2}$ (4)	$24.3^{+0.1}_{-0.1}$ (16)	$24.2^{+0.1}_{-0.1}$ (10)	$24.1^{+0.1}_{-0.1}$ (10)	$24.2^{+0.1}_{-0.1}$ (8)	$23.4^{+0.2}_{-0.2}$ (5)	$23.4^{+0.2}_{-0.2}$ (4)
155880	$26.1^{+0.1}_{-0.1}$ (9)	$24.5^{+0.1}_{-0.1}$ (11)	$24.5^{+0.1}_{-0.1}$ (10)	$24.6^{+0.2}_{-0.2}$ (6)	$24.6^{+0.2}_{-0.2}$ (6)	> 25.1 (1)	> 25.1 (0)
218467	> 27.6 (1)	$25.0^{+0.2}_{-0.2}$ (5)	$25.0^{+0.2}_{-0.2}$ (5)	$25.0^{+0.3}_{-0.2}$ (4)	$24.9^{+0.3}_{-0.2}$ (4)	$24.7^{+0.3}_{-0.2}$ (4)	> 25.2 (1)
61432	> 27.6 (1)	$24.9^{+0.2}_{-0.1}$ (7)	$24.7^{+0.2}_{-0.2}$ (5)	$24.6^{+0.3}_{-0.2}$ (4)	$24.8^{+0.3}_{-0.2}$ (4)	> 25.1 (0)	$24.6^{+0.3}_{-0.2}$ (4)
277880	$26.4^{+0.3}_{-0.2}$ (4)	$25.0^{+0.4}_{-0.3}$ (3)	$24.6^{+0.2}_{-0.2}$ (6)	$24.9^{+0.4}_{-0.3}$ (3)	$24.8^{+0.4}_{-0.3}$ (3)	$24.6^{+0.3}_{-0.2}$ (4)	$24.7^{+0.3}_{-0.3}$ (3)
268511	> 27.6 (0)	$25.0^{+0.3}_{-0.2}$ (3)	$25.0^{+0.5}_{-0.3}$ (2)	$25.4^{+0.6}_{-0.4}$ (2)	> 25.0 (0)	> 25.6 (1)	> 25.2 (1)
271105	$26.1^{+0.1}_{-0.1}$ (7)	$25.0^{+0.1}_{-0.1}$ (9)	$24.1^{+0.1}_{-0.1}$ (12)	$23.9^{+0.1}_{-0.1}$ (11)	$24.0^{+0.1}_{-0.1}$ (13)	$23.5^{+0.2}_{-0.2}$ (5)	$23.4^{+0.2}_{-0.2}$ (5)
95661	$25.4^{+0.1}_{-0.1}$ (15)	$24.8^{+0.2}_{-0.2}$ (5)	$25.0^{+0.4}_{-0.3}$ (2)	> 25.2 (1)	$25.0^{+0.7}_{-0.4}$ (2)	$24.4^{+0.2}_{-0.2}$ (5)	$23.6^{+0.2}_{-0.2}$ (5)
28400	$25.2^{+0.1}_{-0.1}$ (16)	$24.8^{+0.2}_{-0.1}$ (7)	$24.6^{+0.1}_{-0.1}$ (8)	$25.0^{+0.4}_{-0.3}$ (3)	$25.1^{+0.4}_{-0.3}$ (3)	$23.5^{+0.2}_{-0.2}$ (5)	$24.9^{+0.6}_{-0.4}$ (2)
2233	$25.9^{+0.1}_{-0.1}$ (9)	$25.5^{+0.4}_{-0.3}$ (3)	$25.3^{+0.4}_{-0.3}$ (2)	> 25.3 (0)	> 25.5 (1)	$25.1^{+0.5}_{-0.4}$ (2)	> 25.4 (0)

Table 3.5 *The best-fitting photometric redshift parameters and galaxies sizes derived from the improved UltraVISTA DR2 imaging of the ten galaxy candidates presented in Bowler et al. (2012). The photometric redshift is calculated by fitting to all available photometric bands including the IRAC* 3.6μm *and* 4.5μm *filters. The object 28400 has an unusually blue [*$3.6-4.5$*] colour and hence cannot be fitted well with our templates (that do not include potential nebular emission), and so this object has a large* χ^2*-value. Best-fitting redshifts with Ly*α *emission included are shown in the centre of the table; note that here we do not include the IRAC photometry. The FWHM values presented on the right-hand-side were calculated using* SExtractor*; missing values indicate that the object was not significantly detected in that band.*

	No Lyα				With Lyα					Star		FWHM		
ID	z	χ^2	A_V /mag	Z /$Z_\odot$	z	χ^2	EW_0 /Å	A_V /$Z_\odot$	Z	Stellar Type	χ^2	z'	Y /arcsec	J
277912	$6.85^{+0.08}_{-0.08}$	2.4	0.0	1.0	6.84	2.4	0	0.0	1.0	T3	27.2	-	1.7	1.9
155880	$6.70^{+0.05}_{-0.06}$	4.6	0.2	1.0	6.86	4.4	50	0.2	1.0	M6	28.0	1.4	1.7	2.2
218467	$6.98^{+0.12}_{-0.12}$	3.1	0.5	1.0	7.01	3.0	10	0.5	1.0	T3	23.2	1.0	1.0	1.6
61432	$7.04^{+0.16}_{-0.11}$	5.5	0.4	1.0	7.04	5.5	0	0.4	1.0	T4	25.0	1.7	1.1	1.6
277880	$6.67^{+0.11}_{-0.12}$	2.2	0.7	0.2	6.66	2.2	0	0.7	0.2	T3	6.3	1.3	1.1	1.7
268511	$7.12^{+0.14}_{-0.11}$	2.6	0.0	0.2	7.25	2.2	80	0.0	0.2	T8	9.2	1.7	1.4	0.5
271105	$6.51^{+0.05}_{-0.04}$	15.5	1.4	1.0	6.55	22.5	0	1.0	1.0	T0	2.4	1.6	1.1	0.9
95661	$6.25^{+0.10}_{-0.13}$	5.1	0.1	0.2	6.31	4.9	20	0.0	0.2	M7	17.4	2.7	0.8	1.8
28400	$6.20^{+0.10}_{-0.08}$	15.3	0.0	1.0	6.59	13.6	150	0.0	0.2	M7	31.9	1.3	2.1	1.3
2233	$6.24^{+0.12}_{-0.20}$	2.6	0.0	0.2	6.30	2.6	20	0.0	0.2	M5	13.9	1.4	2.8	-

3.7 Galaxy Properties

The extensive multiwavelength photometry available within the UltraVISTA and UDS fields allows an investigation of the physical properties of the galaxies, which further exploits the SED fitting analysis utilised in the selection of our sample. Here we present the derived physical properties including stellar masses, star-formation rates (SFRs) and specific star-formation rates (sSFRs). The section ends with an investigation into the rest-frame optical colours of the galaxies including the potential effects of nebular line emission.

Table 3.6 *The physical properties of the galaxies in our $z \simeq 7$ sample derived from the best-fitting SED models. The stellar mass, SFR and sSFR were determined from the best-fitting τ-model with the errors derived from the points with $\Delta\chi^2 = 1$ from the minimum χ^2 value, after minimising over all other variables. A sSFR of 100 Gyr^{-1} corresponds to the maximum attainable in the set of models we use, which always corresponds to an uncertain mass estimate. We also present the SFR$_{\rm UV}$ derived using the Madau, Pozzetti, & Dickinson (1998) prescription, which converts the observed rest-frame UV flux into a SFR directly. The absolute rest-frame UV magnitudes of our galaxies were measured on the best-fitting model (corrected to total magnitudes using a point-source correction) in the rest-frame, when observed through a top-hat filter of width $\Delta\lambda = 100$Å centred on 1500Å. Note that the absolute magnitudes presented here have not been corrected for gravitational lensing magnification, as discussed in Section 3.9.3. In the final two columns we present the rest-frame UV slope index β, calculated by fitting a power law to the measured $YJHK$ or JHK photometry. A missing value for β indicates that the object has large uncertainties in one or more bands and hence a secure value could not be obtained.*

ID	$\log(M_\star/\mathrm{M}_\odot)$	SFR /$\mathrm{M}_\odot\mathrm{yr}^{-1}$	sSFR /Gyr^{-1}	SFR$_{\rm UV}$ /$\mathrm{M}_\odot\mathrm{yr}^{-1}$	M_{1500} /mag	β_{YJHK}	β_{JHK}	B12
136380	$8.4^{+0.6}_{-0.1}$	27^{+22}_{-16}	100^{+0}_{-88}	19	-22.0	-2.4 ± 0.4	-2.4 ± 0.6	
28495	$10.1^{+0.1}_{-0.7}$	23^{+190}_{-15}	2^{+68}_{-1}	21	-22.1	-2.0 ± 0.4	-2.0 ± 0.5	
268511	$8.5^{+0.5}_{-0.1}$	31^{+9}_{-19}	100^{+0}_{-87}	20	-22.1	-3.5 ± 0.9	-3.9 ± 1.2	6
268037	$8.6^{+0.5}_{-0.2}$	43^{+29}_{-31}	100^{+0}_{-92}	18	-21.9	-1.8 ± 0.4	-0.8 ± 0.6	
65666	$9.2^{+0.4}_{-0.3}$	89^{+87}_{-72}	54^{+46}_{-49}	27	-22.4	-2.0 ± 0.3	-2.1 ± 0.5	4
211127	$8.8^{+1.3}_{-0.4}$	17^{+62}_{-11}	28^{+72}_{-27}	18	-21.9	-2.7 ± 0.5	-2.0 ± 0.8	†
137559	$8.4^{+0.9}_{-0.1}$	20^{+28}_{-14}	91^{+9}_{-86}	14	-21.7	-2.8 ± 0.6	-2.8 ± 0.4	
282894	$9.9^{+0.2}_{-0.3}$	8^{+25}_{-5}	$1^{+5}_{-0.5}$	12	-21.5	-2.8 ± 1.0	–	
238225	$9.0^{+0.6}_{-0.2}$	110^{+48}_{-98}	100^{+0}_{-98}	25	-22.3	-1.9 ± 0.4	-1.8 ± 0.5	3
305036	$10.4^{+0.6}_{-1.6}$	10^{+459}_{-8}	$0.4^{+100}_{-0.3}$	20	-22.1	-1.6 ± 0.3	-1.8 ± 0.6	†
35327	$8.3^{+0.8}_{-0.1}$	21^{+21}_{-14}	100^{+0}_{-95}	15	-21.7	-3.5 ± 1.1	-2.9 ± 1.1	
304416	$10.5^{+0.5}_{-1.0}$	26^{+560}_{-16}	$0.9^{+99}_{-0.7}$	47	-23.0	-1.9 ± 0.2	-1.9 ± 0.3	1†

185070	$10.5^{+0.2}_{-1.6}$	10^{+270}_{-9}	$0.3^{+100}_{-0.2}$	17	-21.9	-1.8 ± 0.3	-1.7 ± 0.5	†
169850	$8.9^{+0.2}_{-0.1}$	78^{+16}_{-38}	100^{+0}_{-69}	35	-22.7	-2.2 ± 0.2	-2.2 ± 0.3	2
304384	$9.4^{+1.4}_{-0.4}$	250^{+120}_{-250}	100^{+0}_{-100}	26	-22.3	-1.9 ± 0.4	-2.3 ± 0.6	5†
279127	$9.2^{+0.2}_{-0.6}$	21^{+54}_{-9}	12^{+88}_{-8}	25	-22.3	-2.8 ± 0.4	-3.8 ± 0.8	
170216	$9.0^{+0.7}_{-0.8}$	15^{+86}_{-12}	17^{+83}_{-15}	11	-21.4	-2.0 ± 0.6	-0.8 ± 1.2	
104600	$8.9^{+1.3}_{-0.2}$	74^{+84}_{-67}	100^{+0}_{-100}	20	-22.1	-2.2 ± 0.3	-2.4 ± 0.5	†
268576	$9.6^{+0.3}_{-0.2}$	4^{+15}_{-1}	$1^{+6}_{-0.6}$	12	-21.5	-2.5 ± 0.6	-2.7 ± 1.0	
2103	$9.4^{+0.3}_{-0.7}$	10^{+130}_{-4}	4^{+96}_{-2}	16	-21.8	-2.0 ± 0.6	-1.2 ± 0.9	
179680	$10.5^{+0.6}_{-1.5}$	22^{+610}_{-21}	$0.6^{+99}_{-0.5}$	20	-22.1	-1.5 ± 0.4	-1.5 ± 0.6	†
18463	$8.2^{+1.2}_{-0.1}$	17^{+11}_{-12}	100^{+0}_{-98}	12	-21.5	–	–	†
122368	$9.5^{+0.2}_{-0.7}$	7^{+7}_{-5}	2^{+9}_{-1}	9	-21.2	-4.1 ± 1.2	-2.5 ± 2.0	
583226	$9.8^{+0.2}_{-0.7}$	7^{+160}_{-5}	$1^{+99}_{-0.7}$	12	-21.5	-2.0 ± 0.5	-1.8 ± 0.8	
82871	$9.3^{+0.3}_{-0.7}$	11^{+76}_{-5}	5^{+95}_{-3}	15	-21.7	-2.3 ± 0.4	-1.3 ± 0.7	
68240	$10.0^{+0.3}_{-0.1}$	8^{+43}_{-3}	$0.8^{+4}_{-0.3}$	25	-22.3	-2.2 ± 0.3	-2.3 ± 0.5	
271028	$9.0^{+1.4}_{-0.3}$	97^{+140}_{-94}	100^{+0}_{-100}	12	-21.5	-1.9 ± 0.4	-2.2 ± 0.6	†
30425	$9.9^{+0.2}_{-0.6}$	12^{+229}_{-4}	$2^{+98}_{-0.7}$	22	-22.2	-2.2 ± 0.4	-3.0 ± 0.7	9
234429	$8.9^{+0.6}_{-0.8}$	9^{+62}_{-6}	12^{+88}_{-10}	10	-21.3	-3.4 ± 1.1	–	
328993	$10.3^{+0.1}_{-0.4}$	28^{+76}_{-25}	2^{+10}_{-1}	11	-21.4	-2.0 ± 0.7	-1.9 ± 1.1	
35314	$8.8^{+0.7}_{-0.4}$	35^{+47}_{-27}	62^{+38}_{-59}	20	-22.0	-2.5 ± 0.4	-2.6 ± 0.4	
118717	$10.2^{+0.6}_{-0.9}$	3^{+320}_{-1}	$0.2^{+100}_{-0.1}$	16	-21.8	-1.8 ± 0.4	-1.6 ± 0.4	†
88759	$10.3^{+-0.0}_{-0.3}$	17^{+2}_{-8}	$0.8^{+0.2}_{-0.7}$	21	-22.1	-1.8 ± 0.3	-1.9 ± 0.3	
87995	$10.0^{+0.5}_{-1.4}$	13^{+210}_{-10}	1^{+99}_{-1}	16	-21.8	-2.0 ± 0.5	-2.0 ± 0.5	†

3.7.1 Stellar populations

Stellar masses, SFRs and sSFRs

We present the stellar mass, SFR and sSFR for each object in the full sample in Table 3.6, derived from the range of τ-models we fitted to the photometry. Around half (19/34) of the galaxies in our sample have masses close to that found for fainter galaxies with $M_\star \sim 10^9 \mathrm{M}_\odot$ (McLure et al., 2011). However, as would be expected for our more luminous sample, the remaining 15 galaxies have significantly higher masses in the range $9.5 < \log(M_\star/\mathrm{M}_\odot) < 10.5$. We note however, that masses below $\log(M_\star/\mathrm{M}_\odot) = 9.5$ become increasingly uncertain, as they often arise from non-detections in the *Spitzer*/IRAC bands that correspond to the rest-frame optical part of the galaxy SED (and hence better trace the stellar mass of the galaxy). The majority of the galaxies have SFRs in the range $2 < \mathrm{SFR}/\mathrm{M}_\odot\mathrm{yr}^{-1} < 40$ from the best-fitting τ-model, which is consistent with the SFR determined directly from the UV luminosity via the Madau et al. (1998) formalism. For the 15 galaxies that have masses at $9.5 < \log(M_\star/\mathrm{M}_\odot) < 10.5$, we find a mean sSFR of 1.0 ± 0.1 Gyr^{-1} where the error quoted is the standard error on the mean. The errors on any individual measurement of the sSFR are large as a result of degeneracies in the SED fitting process, where in general a very young model with significant attenuation cannot be distinguished from an older model with little dust. Previous studies with less massive galaxies ($M_\star \sim 10^9 \mathrm{M}_\odot$) found higher values of sSFR than we find in our sample. For example, Smit et al. (2014) put a lower limit of sSFR > 4 Gyr^{-1} from a small sample of $z = 6.8$ lensed LBGs, which is consistent with the value of sSFR $\simeq 10$ Gyr^{-1} found by Stark et al. (2013). We do not include models with nebular emission lines in our SED fitting analysis, which can result in underestimated masses by a factor of $\simeq$2.4–4.4 (Stark et al., 2013), where the larger value assumes a continued evolution in the EW distribution of the contaminating lines beyond $z = 5$. Although correcting the masses of our sample by the factors derived by Stark et al. (2013) would bring our results into line with previous results, the inclusion of nebular emission lines into the SED models not only affects the resulting stellar mass estimate, but can result in younger ages and lower dust attenuation which subsequently affects the SFR estimate (de Barros et al., 2014). Curtis-Lake et al. (2013) found that sSFRs at $z \simeq 6$ were increased by a factor of at most two when nebular emission lines were included, and therefore it is likely that our sample shows a genuinely lower sSFR than lower-mass galaxies at $z \simeq 7$, with a sSFR $\lesssim 2$ Gyr^{-1}. The lower value of sSFR we find for our sample of $M_\star \sim 10^{10} \mathrm{M}_\odot$ galaxies is consistent with a galaxy formation model where star formation is most efficient in smaller galaxies

(e.g. Kauffmann et al., 2003).

From the subset of galaxies in our sample that have lower and hence more uncertain masses, there are several objects that have very low masses coupled with high best-fitting SFRs $\simeq 30 - 100\,\mathrm{M_{\odot}yr^{-1}}$ and hence extreme sSFR $\simeq 100\,\mathrm{Gyr^{-1}}$. Closer inspection of the best-fitting SEDs for these candidates show that they tend to have very blue SEDs and non-detections in the *Spitzer*/IRAC bands, which results in the SED fitting procedure fitting the youngest possible age (10 Myr) in an attempt to reproduce the steep spectral slope. While it is plausible that the extreme sSFRs observed could be genuine, resulting from a brief burst of star-formation in the galaxy, insufficient depth in the rest-frame optical region of the spectrum is more likely the cause of the large sSFRs. The near-infrared data available in the UltraVISTA and UDS fields is substantially deeper than the *Spitzer*/IRAC imaging, and the photometric errors on many of these galaxies are sufficiently large to allow a SED fit with a more moderate SFR and mass within the errors, as illustrated by the large uncertainties shown in Table 3.6.

With improved photometry for the Bowler et al. (2012) sample of galaxies, we find that the derived physical properties of the objects are more extreme in the analysis presented here. The high SFR and sSFR for several of the Bowler et al. (2012) objects are also a result of extremely young best-fitting ages as was the case for fainter galaxies described above, where the close-to-flat near-infrared photometry can typically be best-fitted using a model with a young age, high SFR and a large dust-attenuation. The coupling between high dust-attenuation and a low age in the best-fitting SEDs of these galaxies, is likely a consequence of degeneracies in the fitting process, where the currently available photometry could also be acceptably fit with a model including zero dust attenuation and a larger age.

By requiring zero dust attenuation using the Madau, Pozzetti, & Dickinson (1998) prescription we find more moderate values of the SFR, which then produce slightly lower sSFRs $\sim 10 - 60\,\mathrm{Gyr^{-1}}$. In the case of the top candidate in Bowler et al. (2012) which now has a more moderate SFR, further tension in the fitting was introduced in Bowler et al. (2012) by including confused IRAC photometry, which is excluded from the SED fitting procedure here.

Rest-frame UV slope

The rest-frame UV slope β was calculated for the galaxies in our sample by fitting a power law to the $YJHK$ or JHK photometry following the method of Rogers et al.

(2013). The error on the derived slope is reduced by including the Y-band. However, above $z = 6.8$ the Y-band is an unreliable continuum measure, due to the Lyman-break moving through the filter and potential contamination by Lyα-emission, and hence we quote the JHK value for comparison. The median values of $\beta = -2.1$ and $\beta = -2.0$ including the $YJHK$ and JHK bands respectively, are consistent with the value found for fainter galaxies at $z \sim 7$ using the same fitting method ($\beta = -2.1 \pm 0.2$; Rogers et al., 2013; Dunlop et al., 2013) and using the colours directly ($\beta = -2.33 \pm 0.33$; Bouwens et al., 2013). However, there is evidence that a colour-magnitude relation extends to $z = 7$ (Bouwens et al., 2013), and in which case we would expect the relatively luminous galaxies presented here to have redder rest-frame UV slopes on average. The relation derived by Bouwens et al. (2013) would predict an average $\beta = -1.6$ at $M_{\rm UV} \simeq -22$ and $\beta = -1.4$ at $M_{\rm UV} \simeq -23$. The β values for the faintest galaxies presented here at $M_{1500} > -22$ have large errors and exhibit a wide scatter, however the two brightest galaxies (304416 and 169850) that were originally selected in Bowler et al. (2012) are detected at $\sim 10\sigma$ in the near-infrared bands and have absolute magnitudes of $M_{1500} \sim -22.7$ (correcting for gravitational lensing as discussed in Section 3.9.3). Both candidates show bluer β values than predicted by the relation from Bouwens et al. (2013), with $\beta_{YJHK} = -1.9 \pm 0.2$ and $\beta_{YJHK} = -2.2 \pm 0.2$ respectively. However, the most recent results at $z = 5$ suggest that the bluest galaxies have a similar β at all luminosities, with an increased scatter to redder values with increasing luminosity, possibly as a result of greater dust attenuation or age spread (Rogers et al., 2014). The bluer values of β we find for the two brightest members of our sample are coupled with best-fitting models that show low values of dust extinction ($A_V = 0 - 0.2$), and therefore these galaxies could be extreme examples of the generally redder population of galaxies at $M_{1500} \simeq -22.5$. Our results contrast with Willott et al. (2013), who found a redder rest-frame UV slope of $\beta = -1.44 \pm 0.1$ in a stack of bright $M_{1350} \sim -22$ galaxies at $z = 6$, which was attributed to dust-reddening. Further imaging within the ultra-deep UltraVISTA survey regions over the next few years will allow more accurate β measurements for a larger sample of objects, and hence a meaningful constraint on the very bright-end of the colour-magnitude relation at $z \simeq 7$.

3.7.2 Nebular emission

There is growing evidence for the presence of nebular emission lines in the spectra of high-redshift galaxies (Stark et al., 2013; Smit et al., 2014). Aside from the physical repercussions for the star-formation environment at high redshift, the contamination

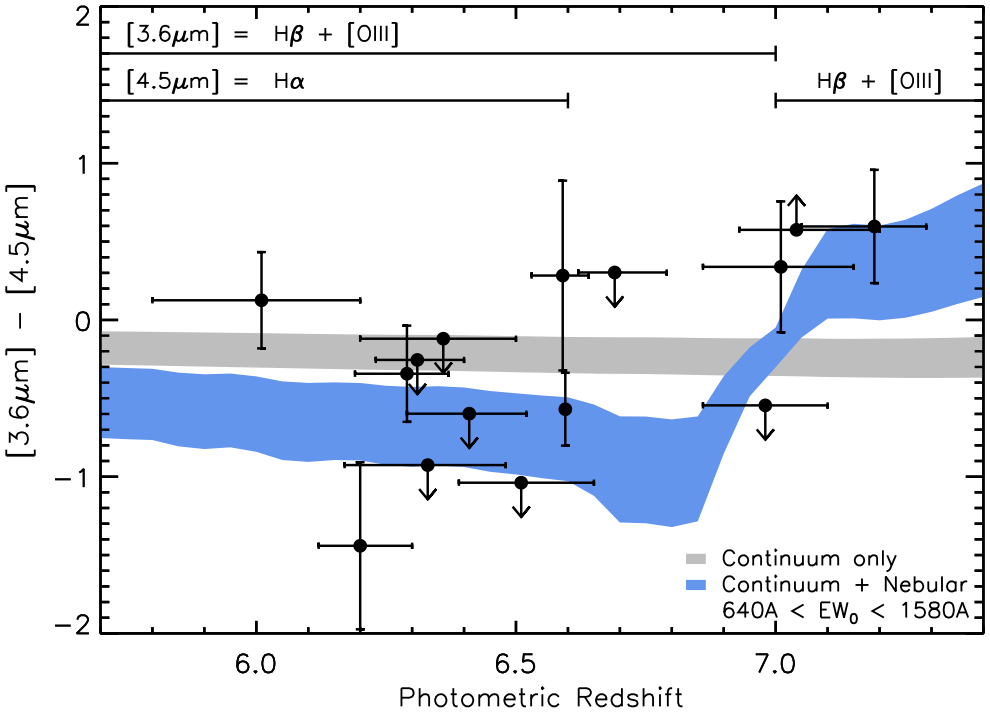

Figure 3.6 *The [3.6μm] − [4.5μm] colours plotted against photometric redshift for the UltraVISTA DR2 and UDS candidates. The grey and blue shaded regions represent the predicted [3.6μm] − [4.5μm] colours as a function of redshift as described in the text, for Bruzual & Charlot (2003) models with or without strong emission lines added respectively. Candidates with confused IRAC photometry, defined as when flux from a nearby object enters the 2.8-arcsec diameter circular aperture of the candidate, are not plotted here. If an object was not detected at greater than 2σ significance in either band then it has been excluded from the plot. Limit arrows represent objects that were undetected at less than 2σ significance in the appropriate band, and here the magnitude in the undetected band has been replaced by the locally-determined 2σ limiting depth for that object. The dominant emission lines present in each IRAC filter at that particular redshift are shown by the marks at the top of the plot. The data point at $z = 6.6$ with extremely small errors on the redshift is the spectroscopically-confirmed LAE Himiko.*

of the rest-frame optical photometry by nebular emission lines can increase the stellar mass estimate and hence artificially suppress the derived sSFR (Stark et al., 2013). In contrast to the majority of LBGs known, our candidates are sufficiently bright to be detected in the *Spitzer*/IRAC $[3.6\mu\mathrm{m}]$ and $[4.5\mu\mathrm{m}]$ -filters, and several galaxies within our sample show an unusual $[3.6\mu\mathrm{m}]-[4.5\mu\mathrm{m}]$ colour that cannot be reproduced by continuum fits for high or low-redshift galaxies. The $[3.6\mu\mathrm{m}]-[4.5\mu\mathrm{m}]$ colours of dwarf stars can reproduce such colours (see Figure 3 of Bowler et al., 2012), and the stellar locus in $[3.6\mu\mathrm{m}]-[4.5\mu\mathrm{m}]$ colour would roughly follow the predicted nebular emission curve. The dependence occurs because cooler T-dwarfs have extremely red spectra ($[3.6\mu\mathrm{m}]-[4.5\mu\mathrm{m}] \sim 0.0$–$2.0$) and hence become confused with higher redshift candidates, whereas the M and L dwarfs tend to have colours of $[3.6\mu\mathrm{m}]-[4.5\mu\mathrm{m}] \sim -0.5$ and best-fit galaxy redshifts of $z_{\mathrm{phot}} < 6.7$. However, we expect the degree of stellar contamination in our sample to be very low, as a result of our SED fitting analysis in combination with FWHM measurements (see Section 3.7) that can aid the exclusion of point sources for the candidates with the best (but still significantly worse that the high-redshift models) stellar fits.

For comparison with our observations, we predict the $[3.6\mu\mathrm{m}]-[4.5\mu\mathrm{m}]$ colours for continuum only and continuum + nebular emission by adding bright nebular emission lines to stellar continuum models. The underlying continuum was taken from a Bruzual & Charlot (2003) model with a constant SFH, Chabrier IMF, ages of either 10 or 100 Myr and metallicities of either $1/5\,\mathrm{Z}_{\odot}$ or $1/50\,\mathrm{Z}_{\odot}$. The model parameters were chosen to produce a range of plausible $[3.6\mu\mathrm{m}]-[4.5\mu\mathrm{m}]$ colours, while including the bluest values that could be exhibited by a realistic star-forming galaxy at high redshift in the absence of nebular emission lines. The expected colours for a given rest-frame equivalent width of Hβ and [OIII] combined were estimated assuming the Hβ to [OIII]λ4959, 5007 and Hβ to [OII]λ3727 ratios for a metallicity of $1/5\,\mathrm{Z}_{\odot}$ calculated by Anders & Alvensleben (2003), and assuming the Hα to Hβ ratio of 2.87 from Osterbrock & Ferland (2006). The combined EW_0 of Hβ to [OIII] λ4959, 5007 was chosen to be a minimum of 637 Å at $z = 6.8$, to correspond to the lower limit for the EW_0 of the mean $z = 7$ galaxy derived by Smit et al. (2014). An upper value for the EW_0 was taken to be 1582Å, the value derived from the four bluest galaxies in the Smit et al. (2014) sample. The EW_0 was allowed to evolve with redshift according to $EW(\mathrm{H}\beta + [\mathrm{OIII}]) \propto (1+z)^{1.8}$ which has been derived from lower-redshift results (Fumagalli et al., 2012). Although we did not calculate the relative line strengths using a full recombination analysis, our results closely mimic those presented in Wilkins et al. (2013) where the full analysis was undertaken.

Our observed $[3.6\mu\mathrm{m}] - [4.5\mu\mathrm{m}]$ colours plotted against the best-fitting photometric redshift (without Lyα emission included), along with the predicted colours from our models are shown in Fig. 3.6. We excluded candidates that had confused IRAC photometry, and those that were undetected at less than 2σ significance in both IRAC filters, resulting in 15 galaxies remaining. Around half of the galaxies with isolated IRAC detections are consistent with continuum-only models, while the remaining galaxies show deviations from the approximately flat colour and follow the predictions for continuum + nebular emission line models. de Barros et al. (2014) found that 65% of $z \sim 3-6$ galaxies showed signs of strong nebular emission lines, which would agree with our results that a fraction of our sample show IRAC colours consistent with no nebular contamination, assuming that the galaxies that are detected in the IRAC bands are representative of the population as a whole. Our results are also consistent with Smit et al. (2014), who found evidence for strong nebular emission in the majority of seven lensed galaxies around $z_{\mathrm{phot}} \simeq 6.7$. Future deconfusion analysis of the 'ultra-deep' imaging regions and spectroscopic confirmation of the candidates would allow tighter constraints on the prevalence and strength of nebular emission lines in the SEDs of bright $z \sim 7$ galaxies.

The presence of strong nebular emission lines in the SEDs of our galaxies could affect the best-fitting SED 'stellar-only' model that we determine and therefore the M_{1500} we derive. Although we do not explicitly fit with nebular emission lines in our SED fitting analysis, we do consider the SED fits both with and without the *Spitzer*/IRAC bands that could be contaminated by the nebular emission lines (see Figure 3.6). Crucially, the rest-frame UV slope from which we measure the M_{1500} of each galaxy, is predominantly constrained by the four near-infrared filters (Y, J, H and K) in both the UltraVISTA and UDS fields, and the data in the $[3.6\mu\mathrm{m}]$ and $[4.5\mu\mathrm{m}]$ filters is at least 0.5 mag shallower and therefore contributes significantly less weight to the resulting best-fitting model. As a simple check for how much nebular emission lines could affect our measured M_{1500}, we calculated the M_{1500} from fits that included and excluded the $[3.6\mu\mathrm{m}]$ and $[4.5\mu\mathrm{m}]$ data, and found no systematic difference between the derived M_{1500} values.

3.8 Galaxy Sizes

Lyman-break galaxies are known to be smaller at high redshift, with the median half-light radius for faint (0.1-1L^*) galaxies being $r_{1/2} < 1$ kpc at $z = 7$ (Oesch et al., 2010a; Huang et al., 2013). Confirmation of the existence of a clear size-magnitude relation (as observed at lower redshift) becomes challenging at $z > 6$, because of

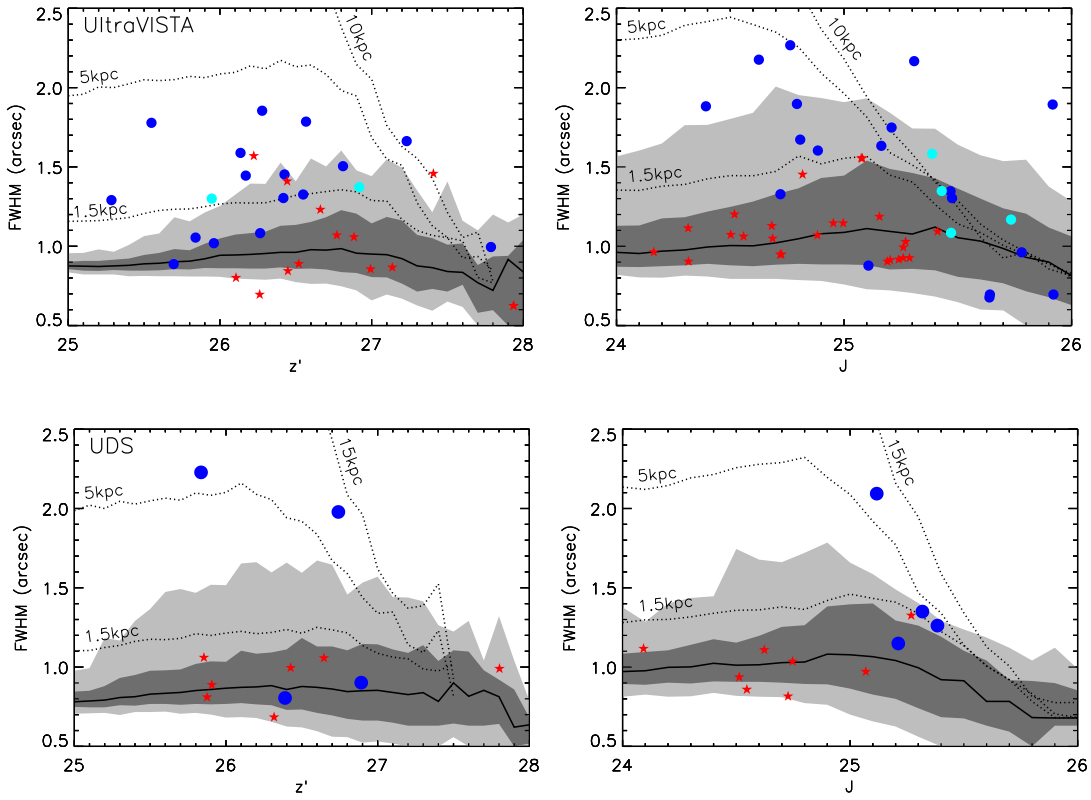

Figure 3.7 *The measured FWHM as a function of magnitude for the UltraVISTA and UDS galaxy samples in the top and bottom row respectively. Each column shows the results for the z' and J-bands, with the galaxy candidates presented as the blue circles. The four galaxies that lie within the COSMOS CANDELS imaging are shown as cyan circles. The magnitudes presented for the real and artificial sources are raw 1.8-arcsec diameter circular aperture values. The red stars show the FWHM of faint galactic dwarf stars, that were originally selected as high-redshift galaxy candidates but later excluded as stars based on the SED fitting analysis. The black curve shows the median value of recovered FWHM as it varies with the magnitude of injected point sources, and the dark and light grey bands show the 68% and 95% confidence intervals respectively. The dotted lines show the median value of recovered FWHM for Sersic profiles with $r_{1/2} = 1.5$, 5.0 and 10.0 or 15.0 kpc, that were convolved with the PSF and injected into the images.*

the restricted luminosity baseline over which sizes can be accurately measured. For example, the few tens of galaxies at $z > 7$ detected and measured in the HUDF by Oesch et al. (2010a) and more recently in the UDF12 dataset by Ono et al. (2013) typically have sizes at the limit of the resolution of *HST* (< 0.1 arcsec, which corresponds to a physical size of $d < 0.5$ kpc at $z = 7$). By incorporating the wider-area CANDELS data, Grazian et al. (2012) were able to determine a size-magnitude relation at $z = 7$ extending to $M_{\rm UV} \simeq -21$. An extrapolation of the size-magnitude relations of Oesch et al. (2010a) and Grazian et al. (2012) would predict $1.0 \lesssim r_{1/2} \lesssim 1.5$kpc for the bright galaxies detected here ($-22 \gtrsim M_{\rm UV} \gtrsim -23$ at $z = 7$). Converting the half-light radius into a full-width at half-maximum (FWHM) depends on the functional form of the surface-brightness profile; here we assume a Sersic profile with Sersic index $n = 1.5$ following Oesch et al. (2010a).

3.8.1 FWHM measurements

We measured the FWHM of the galaxies in the final UltraVISTA and UDS samples shown in Table 3.3 using SExtractor, where the value is calculated from a Gaussian fitted to the core photometry. Note that fitting a Gaussian to an extended Sersic profile causes an overestimate of the FWHM, and can be sensitive to the deblending procedure in SExtractor, which can cause nearby objects to be grouped and the resulting FWHM measurement to be larger than for the central object alone. The FWHM of the UltraVISTA and UDS galaxies in the z' and J-bands are shown in Fig. 3.7, along with the measured FWHM of simulated stars and galaxy profiles within each field. The Y-band imaging has poorer seeing than the J-band, and is of insufficient depth in the UDS image for FWHM measurements, and hence is not used. To simulate the range of sizes of recovered point spread functions (PSFs) and typical galaxy profiles, we injected and recovered simulated source profiles into the images. The PSF derived using the method described in Section 3.2.4, and Sersic galaxy profiles with a given $r_{1/2}$, were scaled to an input 1.8-arcsec circular aperture magnitude and injected into blank regions of the z' and J-band images. Simulated galaxy profiles were created with intrinsic $r_{1/2} = 1.5, 5.0, 10.0 \,{\rm and}\, 15.0$ kpc, and were then convolved with the PSF (modelled here as a Moffat function obtained by fitting to the stacked PSF). The injected images were then analysed using SExtractor, and the FWHM and aperture magnitude measurement was extracted for each recovered source, thus providing a consistent size measurement for comparison with our sample. In general, the recovered FWHM increases towards fainter magnitudes as a result of noise in the measurement, with the 68% and 95% confidence levels showing asymmetry as a result of the increased

probability of detection of a source that has been boosted in magnitude and size. As one would expect, the FWHM measurements become increasingly unreliable to fainter magnitudes, where the median FWHM turns over and starts to decrease as a result of the bias in selection; only sources that sit on a noise spike at such faint magnitudes will be detected and included.

Of the 30 galaxies in our final UltraVISTA sample, approximately two-thirds are consistent with having $r_{1/2} \geq 1.5$ kpc assuming a Sersic profile with $n = 1.5$. The z'-band imaging shows a clearer separation of the measured FWHM of galaxies in our sample and that from PSFs, due to the increased depth and better seeing available compared to the J-band imaging. Several of our brightest galaxies, including the brightest candidates from Bowler et al. (2012), are clearly resolved in the ground-based imaging, showing FWHM values that would suggest intrinsic sizes up to $r_{1/2} \sim 5$ kpc. Although the majority of the UltraVISTA galaxies are also consistent with being unresolved in the ground-based imaging, as shown by the 95% percentile displayed in Fig. 3.7, the distribution of FWHM values away from the locus of recovered genuine points sources suggests otherwise. Stellar contamination of the sample is strongly ruled out by the SED fitting, and given that the current known size-magnitude relation would predict a FWHM that is only just resolvable from the ground, it is entirely plausible that we would find unresolved galaxies with the available seeing. This point is reinforced in Section 3.8.2, where we analyse *HST* imaging of four galaxies in the UltraVISTA sample that are consistent with being a point source in the ground-based data (highlighted in cyan on Fig. 3.7), and find strong evidence that they have extended low surface brightness features.

From the final UDS sample of four galaxies, two appear resolved in the z'-band imaging (see Fig. 3.7), including the known extended z = 6.595 galaxy Himiko, which is the only UDS candidate to appear clearly resolved in the J-band imaging. Himiko has an extent of ~ 9 kpc in the continuum measured from higher resolution *HST* imaging, consistent with the FWHM measured here, and a diffuse Lyα halo greater than 17 kpc across. There are no sources in the UltraVISTA sample that have FWHM suggesting that they exceed 5 kpc in size, supporting the conclusion that Himiko is an extremely rare triple merger system and not a typical $\mathrm{m_{AB}} \sim 25$ galaxy at $z = 7$.

Our results agree with Willott et al. (2013), who found that around half of their bright $z \sim 25$ LBGs at $z = 6$ were resolved in the CFHTLS ground-based imaging which had a seeing of 0.85-arcsec. They found a median galaxy FWHM $= 1.1$-arcsec, which corresponded to an intrinsic FWHM = 0.35-arcsec or a $r_{1/2} = 2$ kpc. Willott et al. (2013) noted that, from high-resolution imaging of several members of their sample

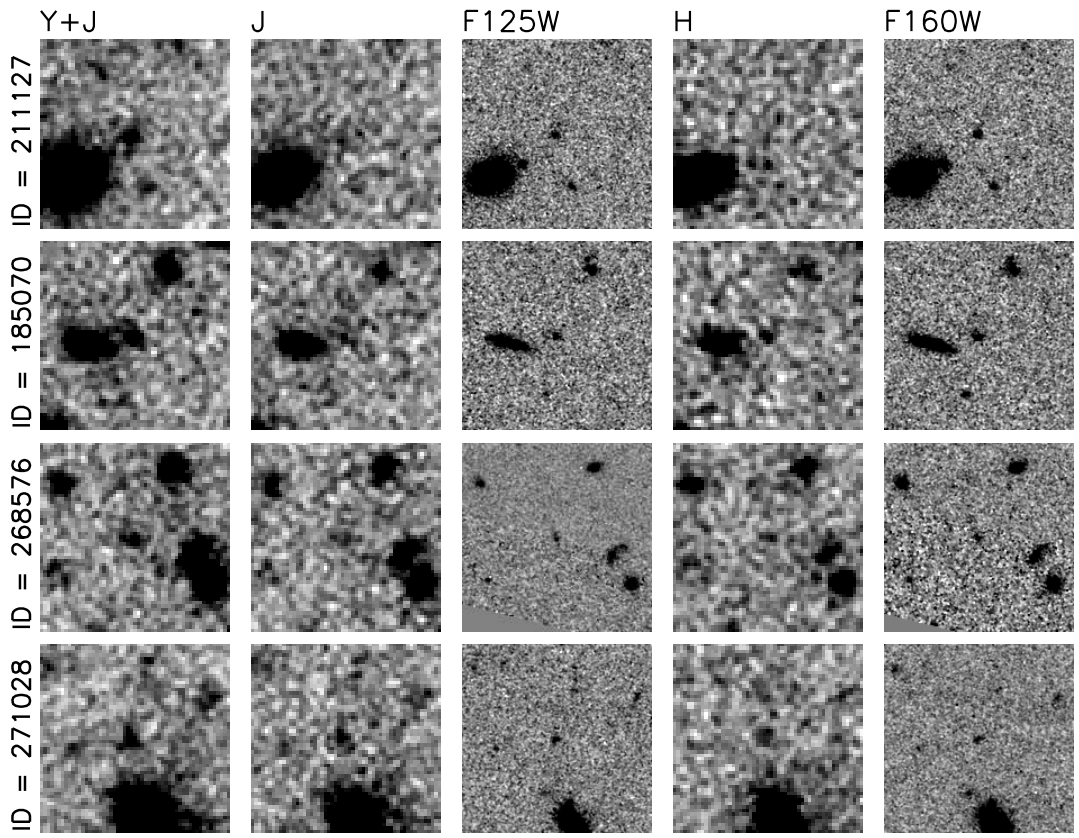

Figure 3.8 *Ground-based and* HST *postage-stamp near-infrared images of the four galaxy candidates that lie with the CANDELS COSMOS imaging. For each object the UltraVISTA $Y + J$ detection image is shown on the left, followed by the UltraVISTA J-band, WFC3 J_{125}, UltraVISTA H and WFC3 H_{160} stamps. Each stamp is 10 x 10 arcsec^2, with North to the top and East to the left. Three of the objects presented are fairly close to a low-redshift extended galaxy, however with the improved resolution provided by* HST *the objects are confirmed as clearly separate objects. Note that object 268576 lies near the edge of the WFC3 imaging, and hence the errors on the photometry and size measurements are correspondingly higher.*

with *HST*, many of the galaxies appeared clumpy and extended with features up to 6 kpc from the centre. Similarly, the two brightest z_{850}-drops presented in Ono et al. (2013) are formed of multiple components. These results suggest that mergers or interactions may be prevalent in bright galaxies at high redshift, although it is possible that these low surface brightness features are also present in fainter galaxies beyond the current detection limits.

3.8.2 HST imaging from CANDELS

Of the 30 candidates within the 1 deg^2 of UltraVISTA imaging, four lie within the 200 arcmin^2 of the CANDELS COSMOS field (Grogin et al., 2011) which lies close to the centre of the CFHTLS pointing that defines our maximal survey area, and hence in the left-central strip of the 'ultra-deep' UltraVISTA imaging. The CANDELS COSMOS field consists of a mosaic of 4×11 pointings of *HST*/WFC3 providing F125W (J_{125}) and F160W (H_{160}) imaging, and ACS imaging taken with the F606W (V_{606})and F814W (I_{814}) filters in the parallel observations (Koekemoer et al., 2011). In Fig. 3.8 we present postage-stamps of the four objects in the J_{125} and H_{160} images, with the corresponding VISTA J and H images for comparison. The measured photometry and FWHM values from SExtractor are shown in Table 3.7.

Of the four candidates we find in the UDS, the LAE Himiko lies within the 145 arcmin^2 of CANDELS UDS imaging. The detailed analysis of Himiko from the *HST* imaging was presented by Ouchi et al. (2013), who found the galaxy to consist of three components in an apparent triple-merger system. A triple-merger system is very rare at any redshift, and the UltraVISTA galaxies that lie within the CANDELS COSMOS imaging do not show any evidence of multiple components. The four galaxies in the CANDELS imaging however are fainter than Himiko, with absolute magnitudes in the range $-21.9 \leq M_{1500} \leq -21.5$ compared to $M_{1500} = -22.1$, and the brightest candidates presented here are comparably extended from the FWHM measurements in the ground-based imaging. Our sample includes galaxies brighter or comparable to the luminosity of Himiko, and hence follow-up with *HST* could determine how many of the most luminous $z = 7$ galaxies are in merger systems and would constrain the size-magnitude relation at the very bright end.

In the UltraVISTA imaging the four candidates, highlighted in Fig. 3.7, show FWHM that are consistent with being unresolved at ground-based resolution, with the exception of 271028 which appears marginally resolved in the z'-band imaging. The typical resolution of the *HST*/WFC3 J_{125} and H_{160} imaging in the CANDELS fields is 0.20 ± 0.01-arcsec (Koekemoer et al., 2011), and hence of the four candidates, three immediately appear resolved in the WFC3 data on the basis of the FWHM measurements. The brightest object in the WFC3 imaging, 211127, is close to being unresolved with a FWHM $= 0.22$ that only slightly exceeds the value expected for a point source. The remaining galaxies have larger FWHM in the range 0.3–0.5 arcsec, which is supported by the observed elongation of several galaxies in the images shown in Fig. 3.8. Note that object 268576 lies near the edge of the image and hence the size

Table 3.7 *The measured photometry and errors for the four $z \simeq 7$ galaxies in our sample that lie within the area of* HST *imaging provided by the CANDELS COSMOS survey. The measurements from the UltraVISTA J and H data were made in a 1.8-arcsec diameter circular aperture and corrected to the 80% enclosed flux level. The J_{125} and H_{160} photometry was measured in a 0.6-arcsec diameter circular aperture, which corresponds to 80% enclosed flux for a point source. The object ID 211127 appears barely resolved in the WFC3 imaging based on a measured FWHM close to the typical resolution of 0.20-arcsec, but as shown in Fig. 3.9, all four galaxies are clearly resolved in the* HST *imaging.*

ID	J	J_{125}	H	H_{160}	FWHM J /arcsec	FWHM J_{125} /arcsec	M_{1500}
211127	$25.4^{+0.3}_{-0.2}$	$25.6^{+0.1}_{-0.1}$	> 25.8	$25.6^{+0.1}_{-0.1}$	1.1	0.21	-21.9
185070	$25.3^{+0.2}_{-0.2}$	$25.7^{+0.1}_{-0.1}$	$25.6^{+0.6}_{-0.4}$	$25.6^{+0.1}_{-0.1}$	1.3	0.31	-21.9
268576	$25.6^{+0.3}_{-0.3}$	$25.7^{+0.1}_{-0.1}$	> 25.9	$26.0^{+0.1}_{-0.1}$	1.2	0.48	-21.5
271028	$25.3^{+0.3}_{-0.3}$	$25.8^{+0.1}_{-0.1}$	$25.3^{+0.6}_{-0.4}$	$26.0^{+0.1}_{-0.1}$	1.6	0.37	-21.5

and photometry measurements are subject to large uncertainties.

Photometry

When comparing the measured aperture magnitudes shown in Table 3.7, we find an offset between the photometry measured in the UltraVISTA J and *HST*/WFC3 J_{125} imaging which is inconsistent with the galaxies being point sources. Excluding object 268576 near the edge of the imaging, we find a mean offset of 0.4 mag between the raw 0.6-arcsec diameter aperture photometry measured on the J_{125} image (80% enclosed flux for a point source) and the 1.8-arsec diameter aperture photometry measured on the J-band image ($\sim 70\%$ enclosed flux) when corrected to match the enclosed flux level of the WFC3 imaging. Of course the most extended galaxies in the higher resolution *HST* imaging will similarly appear extended in the ground-based imaging, as we have shown the majority of the galaxies in our sample appear resolved in the z' and J-band data. However, because the circular apertures we used for photometry in the space- and ground-based data are designed to enclose around 70-80% of the flux of a point source, in the case of a resolved galaxy, more of the flux will spread beyond the aperture in the higher resolution *HST* imaging compared to the ground-based imaging where the seeing dominates over the intrinsic FWHM. We created model galaxy profiles to predict the magnitude offset we would expect between the VISTA and WFC3 imaging for an extended profile as compared to a point source. A magnitude offset of 0.4 mag could be reproduced if the simulated galaxy with an exponential profile (Sersic index $n = 1$) had a half-light radius of $r_{1/2} = 1$ kpc. Such a profile would result in 0.05 mag being lost from the ground-based aperture (increased to 0.1 mag for a profile with $r_{1/2} = 1.5$ kpc).

The ground-based imaging provides a closer measure of the true total flux of the galaxy than the results of using small apertures on higher resolution *HST* imaging, when the galaxy is assumed to be unresolved in both cases.

Finally, we measured the photometry for our sample using larger apertures, to empirically determine what the effect of assuming our galaxies are point sources in the ground-based imaging has on the total magnitudes derived. We used 3-arcsec diameter circular apertures (corrected to total assuming a point source) and two further magnitudes from SExtractor; the MAG_AUTO which returns an estimate of the total magnitude using Kron apertures and MAG_ISOCOR which uses isophotal apertures corrected to total using a Gaussian approximation to the galaxy profile. For the brightest objects, where Kron and isophotal magnitudes correspond to a sufficiently accurate total magnitude, we found an offset of ~ 0.1 mag compared with the total magnitude initially measured in a 1.8-arcsec aperture and then corrected to total, which is in agreement with that found for a simulated Sersic profile with $r_{1/2} = 1.5$ kpc as described above. Hence, from our ground-based imaging measurements, we expect at most a 0.1 mag brightening of our candidates to correct for missing flux beyond the apertures we use. In the case of the J_{125} and H_{160} imaging however, the offset is significantly larger and can result in an underestimation of the total magnitude of the galaxy by ~ 0.4 mag for photometry measured in a 0.6-arcsec diameter circular aperture.

Surface-brightness profiles

The surface-brightness profiles for the four galaxies in our sample that lie within the CANDELS COSMOS imaging are shown in Fig. 3.9. Each galaxy was normalised within the central circular aperture of radius 0.1 arcsec, and the normalised surface brightness was calculated in annuli of width 0.05 arcsec. We extracted several unsaturated stars from the imaging and computed the surface brightness for comparison with the galaxy candidates. The profiles show that the first three galaxies show compact cores, surrounded by extended emission that is observable to a maximum radius of 0.8-arcsec. For object 211127, which has a FWHM consistent with being a point source in the J_{125} image, the presence of extended emission further rules out a galactic dwarf star (which is strongly disfavoured from the SED fitting analysis). The compact cores observed for galaxies 211127 and 185070 are consistent with being unresolved in the *HST* imaging and could suggest a bulge component or active nucleus (further discussed in Section 3.10.3). The largest galaxy in our sample as measured by both the

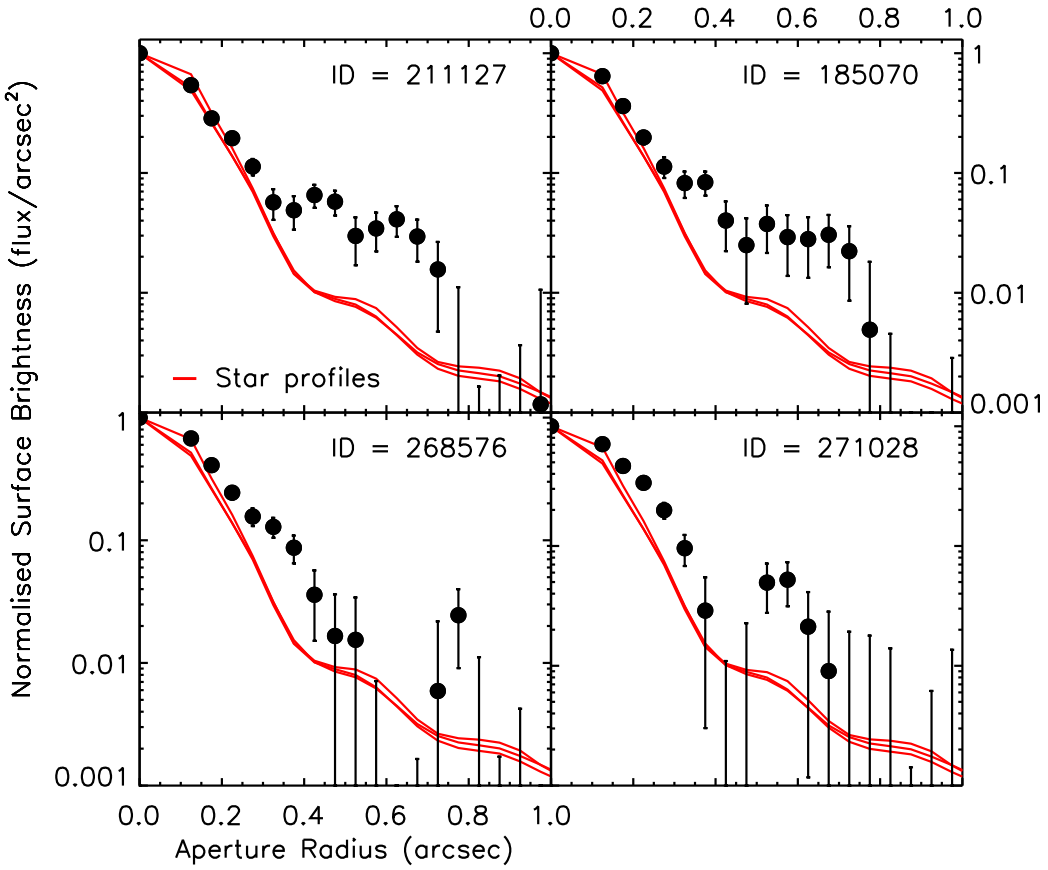

Figure 3.9 *The J_{125} surface-brightness profiles of the four galaxies in the UltraVISTA sample that lie within the CANDELS COSMOS* HST *imaging. Stellar profiles are shown for comparison (red lines), and all the galaxies and stars have been normalised to a peak flux of 1.0 in a 0.2-arcsec diameter aperture. All four galaxies show extended profiles.*

UltraVISTA J-band and J_{125} FWHM values, 271028, has a core that is significantly larger than the stellar point source surface brightness profile.

3.9 The Luminosity Function

The result of the analysis presented above is a sample of 34 $z \simeq 7$ galaxies with $M_{1500} \leq -21.2$, selected from the 1.65 deg^2 of imaging within the UltraVISTA and UDS fields. In this section we use our sample of galaxies to calculate the very bright end ($M_{1500} \simeq -22.5$) of the luminosity function at $z = 7$. Before we proceed to calculate the binned luminosity function points however, we must calculate how complete our selection process is and hence ascertain the true number density of sources our sample implies. At the bright end of the LF the use of realistic simulations becomes even more important, because the steeply-declining function can cause flux boosting of a significant number of galaxies into the sample from below the flux density limit of the data.

3.9.1 Completeness simulations

The sample of galaxies presented here will suffer incompleteness due to a combination of blending with foreground/background objects and photometric scattering which can shift galaxies over/below the detection threshold of the survey, as well as potentially changing the colours in such a way as to cause rejection as a contaminant. Hence, to calculate the LF accurately, the numbers of galaxies in each magnitude bin must be corrected for these effects.

We calculated the completeness of our two survey fields by injecting sources, assumed to be unresolved in ground-based imaging (see Section 3.8), that mimic high-redshift LBGs, and recovering them using the same method used for the selection of galaxies in this chapter. We first populated a grid of absolute magnitude vs. redshift space with steps of $\Delta M = 0.1$ and $\Delta z = 0.05$, assuming a linearly evolving Schechter function with redshift as described in McLure et al. (2009) and McLure et al. (2013). To determine the effect of a less steep functional form on the completeness corrections, we also ran simulations where a double power law was used to populate the input $M_{\rm UV} - z$ plane (see Section 3.9.2). When populating the input $M_{\rm UV} - z$ grid, the LF was integrated down to one magnitude fainter than the median 5σ-limit of each field (e.g. an apparent magnitude limit of $Y = 27$ for the UltraVISTA DR2 strips), to account for scattering

into the sample from below the magnitude limit of the survey. For each galaxy in the grid we randomly assigned a rest-frame UV slope β, drawing the value from a Gaussian distribution centred on $\beta = -2.0$ with a standard deviation of $\sigma = 0.2$. We then calculated the observed total magnitude in each band for a galaxy model with that β, $M_{\rm UV}$, and z combination, taking models from the Bruzual & Charlot (2003) library. To inject the galaxy into each band, the PSF (as determined using the method described in Section 3.2.4) was scaled to the apparent magnitude in each band and added into the images at a random position. For each survey field, we performed the simulation on 4 to 5 subsections to provide a representative result given the different depths of the individual mosaic panels and strips in the UltraVISTA and UDS imaging, while keeping computing time reasonable. We then ran SExtractor on the full optical and near-infrared images with the artificial sources injected, and selected objects from the resulting catalogues that passed the Y, J, or $Y + J$ cuts imposed on the genuine galaxy catalogues described in Section 3.3. A non-detection in the i-band was required, using local depths for the UltraVISTA ultra-deep data and global depths for candidates in the UDS to match our selection criterion used for the selection of real sources. Finally, SED fitting was performed and candidates were retained if the χ^2 value was acceptable, and no low-redshift solution had a χ^2 within $\Delta\chi^2 < 4$ from the minimum. In total we added 750000 artificial sources to each field through multiple runs of the simulation, with roughly $10000 - 50000$ candidates being retrieved depending on the functional form assumed for the input LF. The resulting completeness values were $\simeq 70 - 80\%$ for the two brighter LF bins we use, where the loss of input objects is dominated by the blending with foreground sources. For the faintest objects in our sample the completeness falls as low as $\simeq 50\%$, as a result of objects at the 5σ limit of the survey being scattered below the detection limit, coupled with up-scattered objects (that for the brighter magnitude bins helps to balance the loss of objects scattered to fainter magnitudes), having poorer SED fits and hence being more likely excluded as a high-redshift object.

3.9.2 The binned luminosity function

The luminosity function in a given absolute magnitude bin, $\Phi(M)$, derived from our data over the full redshift range of our survey ($6.5 < z < 7.5$) was estimated using the classic $1/V_{\rm max}$ method of Schmidt (1968):

$$\Phi(M) = \sum_{i=1}^{N} \frac{C(M_i, z_i)}{V_{{\rm max},i}} \tag{3.1}$$

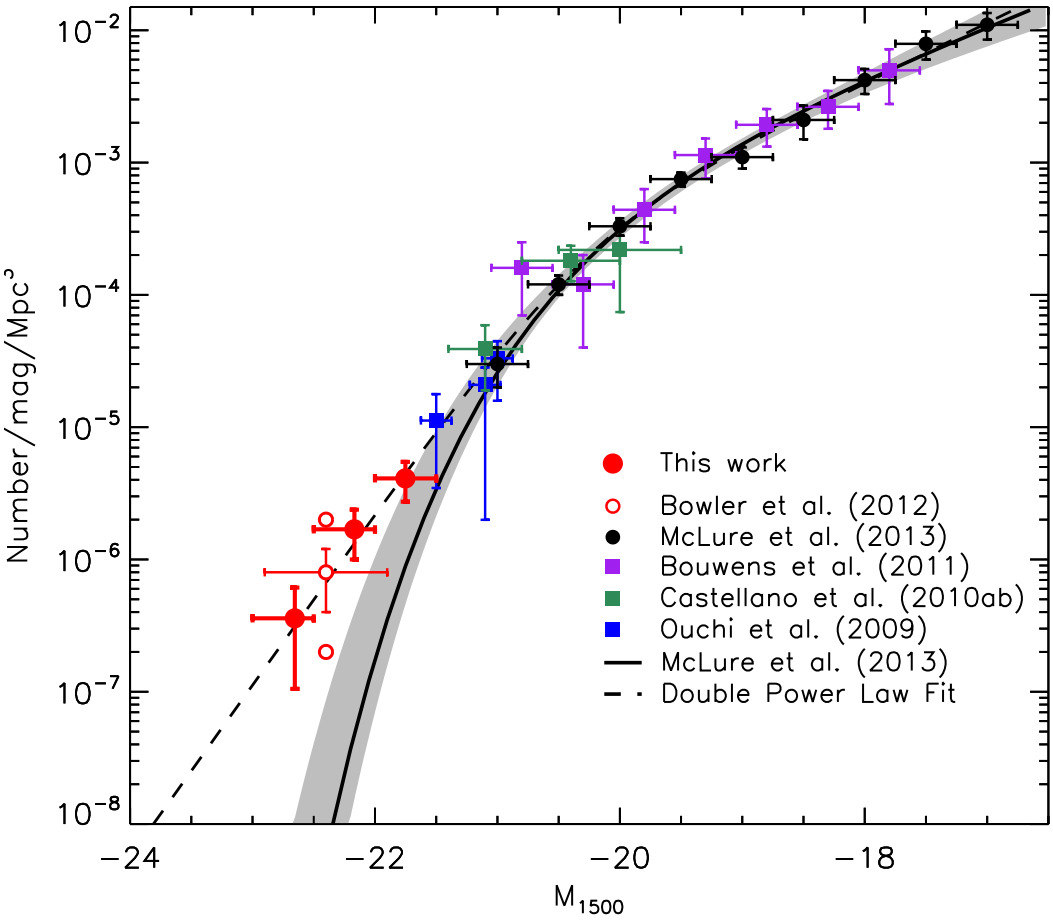

Figure 3.10 *The $z = 7$ UV (~ 1500Å) luminosity function. The results from our sample of galaxies from the UltraVISTA DR2 and UDS fields are shown as the red filled circles. The previous estimate calculated in Bowler et al. (2012) is shown as the open red circle, where the upper and lower circle represent the prediction if ten or one of the candidates were confirmed to be at $z > 6.5$. The best-fitting Schechter function at $z = 7$ from McLure et al. (2013) is plotted as the black line, and the best-fitting double power law is shown as the dashed line. By varying the Schechter function parameters ($M^\star$, $\phi^\star$ and α), a one-sigma confidence limit on the best-fitting LF can be obtained, and is shown as the grey shaded region. Data points determined by McLure et al. (2013) and Bouwens et al. (2011b) are shown extending to $M_{\rm UV} = -17$. The remaining data points were obtained from wider-area ground-based surveys by Ouchi et al. (2009a) and Castellano et al. (2010a,b).*

where the sum is over the N objects in the sample within the magnitude bin. In the simplest form, the luminosity function is found by summing $1/V_{\rm max}$ for all N galaxies in the bin, where $V_{\rm max}$ is the maximum volume the galaxy could occupy and still be included in the sample. The $V_{\rm max}$ was calculated by redshifting the best-fitting SED for each galaxy in the sample until it was fainter than the required Y and/or J-limit for detection in each field (with $z_{\rm max} \leq 7.5$), and summing the resulting volumes. The incompleteness is taken into account via the correction factor $C(M_i, z_i)$, which depends on the absolute magnitude and redshift of the galaxy.

When calculating the binned LF from our sample, we exclude the 0.29 deg^2 of shallower data within the UltraVISTA field not covered by the ultra-deep strips, as the volume is small compared with that from the UltraVISTA ultra-deep and UDS fields combined. The inclusion of the deep UltraVISTA field in the LF calculation leaves the fainter bins unchanged, as none of these objects could have been detected in the shallower data, and reduces the brightest bin by 18%. To be conservative in our LF estimation, galaxies were only included if the best-fitting photometric redshift without Lyα emission was in the range $6.5 < z < 7.5$. The absolute UV magnitude was calculated from the best-fitting SED to each galaxy (observed in the rest frame using a top-hat filter of width $\Delta\lambda = 100$Å centred on 1500Å), without any correction for dust attenuation. We chose three 0.5 magnitude wide bins centred on $M_{1500} = -22.75$, -22.25 and -21.75 to span the range of absolute magnitudes within our sample. The brighter bin at $M_{1500} = -22.75$ is occupied by two galaxies, the top two candidates presented in Bowler et al. (2012), and the fainter bins contain 6 and 9 galaxies respectively. We note that if all the galaxies listed in Table 3.3 were included (i.e. also those which require Lyα-emission in the SED to lie at $z > 6.5$) the faintest bins would rise by $\simeq 0.1$ dex.

To calculate the correction required for each galaxy due to the incompleteness of the survey, we compared the results when using an evolving Schechter function and several double power law functions. The exponential cut-off at the bright end of the Schechter function results in a significant number of galaxies being scattered into the sample from below the limit of the survey. The number of these scattered galaxies dominates over the intrinsic number of galaxies in the bin, resulting in a completeness value that exceeds one and a reduction in the final number density derived. However, even correcting the number density down as a result of scattering, we find an excess of galaxies above the Schechter function prediction, implying that the density of galaxies we find cannot be accounted for by such a function. One way to reconcile our results with a Schechter functional form, given that we find an excess of galaxies at $M_{1500} \lesssim$

-22.0, would be to assume that the characteristic magnitude, M^*, is brighter than the current determination of the $z = 7$ parameters (McLure et al., 2013; Schenker et al., 2013). However, the result of shifting M^* to a brighter value would bring the fit into conflict with the data points around the knee of the function, in particular the points from Ouchi et al. (2009a) and the brightest bin from McLure et al. (2013). Hence we proceed to calculate the completeness corrections assuming a shallower decline at the bright end of the LF as implied by our data, using a double power law (DPL). Our DPL function, which is the parameterisation commonly used to fit the quasar luminosity function (see Section 3.10.3), has the following functional form:

$$\phi(M) = \frac{\phi^*}{10^{0.4(\alpha+1)(M-M^*)} + 10^{0.4(\beta+1)(M-M^*)}}. \quad (3.2)$$

where ϕ^*, M^* and α are the normalisation, the characteristic magnitude and the faint-end slope in common with the Schechter function, and the bright-end slope is described by the power β. We carried out completeness simulations for DPL functions for bright-end slopes in the range $-4.6 \leq \beta \leq -4.0$. The results of the simulations are relatively insensitive to the steepness of the DPL function, with the results changing by less than 4% in the faintest bins and the brightest bin remaining unchanged. The data suggest a more moderate value of $\beta = -4.3$, which we use for our final results presented in Fig. 3.10 and Table 3.8.

Finally, if the underlying LF was a Schechter function, the absolute magnitude distribution should be dominated by galaxies at the limiting depth of the survey, however we find a more uniform distribution in the range $-22.5 < M_{\rm UV} < -21.5$. We calculate the probability of obtaining the absolute magnitude distribution we find by drawing a sample at random from the output of our simulations, and determining the number of times the distribution has the same number or more galaxies in the brighter 0.5 mag section of the $M_{1500} = -22.0$ bin as compared to the fainter section. For a Schechter function we find this distribution in only 3% of cases, whereas for the DPL we find this distribution in 18% of the samples drawn. The detection of two extremely bright $M_{1500} \simeq -22.7$ galaxies further supports our claim of a shallower functional form for the LF.

3.9.3 Gravitational lensing

Given that the galaxies in our sample are the brightest known to date at $z = 7$, we must consider the possibility that they are gravitationally lensed. There are two

Table 3.8 *The binned LF points at $z = 7$ derived from our combined UltraVISTA and UDS analysis. We use three 0.5 mag wide bins centred on $M_{1500} = -21.75, -22.25, -22.75$ and plot the point at the position of the mean completeness corrected absolute magnitude in that bin, which is displayed in the second column as $M_{1500,\mathrm{w}}$. The errors derived on the number density are the Poisson errors on the number counts.*

M_{1500} range /mag	$M_{1500,\mathrm{w}}$ /mag	ϕ /mag^{-1}Mpc^{-3}	ϕ_{upper} /mag^{-1}Mpc^{-3}	ϕ_{lower} /mag^{-1}Mpc^{-3}
$-21.5 < M < -22.0$	-21.75	4.10×10^{-6}	5.47×10^{-6}	2.73×10^{-6}
$-22.0 < M < -22.5$	-22.17	1.69×10^{-6}	2.38×10^{-6}	1.00×10^{-6}
$-22.5 < M < -23.0$	-22.66	3.59×10^{-7}	6.13×10^{-7}	1.05×10^{-7}

scenarios to consider, strong lensing by a lower-redshift galaxy directly along the line-of-sight of our candidate and moderate lensing by galaxies close to the line-of-sight. The first case is ruled out in our sample by the deep optical non-detections of our galaxies. The second case, of galaxies close to the line-of-sight causing moderate magnifications has been discussed before at $z = 5 - 6$ by McLure et al. (2006), who found a moderate magnification of < 0.1 mag for several candidates in their sample, and Willott et al. (2013) who concluded that the brightest candidate in their sample was lensed by ~ 0.25 mag. Following the method detailed in McLure et al. (2006), we calculated the magnification due to gravitational lensing from galaxies within 10-arcsec of each high-redshift galaxy. The velocity dispersion, σ_V, of each potential lensing galaxy was estimated using the Faber-Jackson relation for early-type galaxies from Bernardi et al. (2003), which gives a correlation between the absolute magnitude in the rest-frame i-band and σ_V at $z = 0$. The magnification can then be calculated by assuming the gravitational potential is an isothermal sphere. The absolute magnitude in the i-band was estimated from the nearest band to the redshifted i-band from a K-band selected SExtractor catalogue, where the total magnitude was estimated using MAG_AUTO. We assumed the redshift of the lensing galaxy from the COSMOS Photometric Redshift Catalogue (Ilbert et al., 2008) for the UltraVISTA sample, and the best-fitting photometric redshift for the UDS sample, where we found the z_{phot} using our photometric redshift fitting routine described in Section 3.3.5 using the K-band selected catalogue.

All of the 34 candidates within our sample have at least one low-redshift galaxy within 10 arcsec on the sky, and several galaxies have up to seven nearby low-redshift galaxies. The largest magnification comes from the closest galaxies as one would expect, with galaxies around 2.5-arcsec separation typically providing a magnification of 0.1 mag. Our selection procedure naturally removed genuine high-redshift galaxies in the wings

of low-redshift galaxies, with potentially high-magnification factors, as the foreground galaxy will contaminate the photometry of the candidate resulting in rejection. If the magnification factors from all of the galaxies within 10 arcsec of the high-redshift galaxy are combined, we find that galaxies in our sample can appear up to 0.3 mag brighter as a result of gravitational lensing. For example, the brightest galaxy in our sample at a measured $M_{1500} = -23.0$, has an estimated lensing boost of 0.3 mag as a result of multiple objects close to the line-of-sight. To present the most conservative estimate of the bright-end of the $z = 7$ LF, we demagnify all of the galaxies in our sample according to our estimate of the magnification, and use the corrected magnitudes in our derivation of the LF points. Furthermore, we present the LF points with a weighted central magnitude for each bin shown in Table 3.8, calculated from the mean completeness corrected absolute magnitude after demagnification.

3.9.4 UDF12 analysis

Before continuing to discuss the ground-based results derived from the UltraVISTA and UDS datasets, I will summarise the UDF12 imaging campaign which produced an improved determination of the faint end of the $z \simeq 7$–8 rest-frame UV LFs relevant for this work. The UDF12 program (PI Ellis), provided additional Y_{105}, J_{140} and H_{160} imaging within the UDF field, which when combined with the pre-existing UDF09 data results in the deepest near-infrared image in existence. The design of the program, with the particular filter and integration times chosen, was tailored to address the key science goals of the program, which were: i) the robust detection of a sample of $z \simeq 8$ galaxies, ii) the first secure samples of $z > 8.5$ galaxies and iii) improved SED fits of $z \simeq 7$ and 8 galaxies.

The UDF12 program reached depths of $m_{\rm AB} \simeq 30$ over 4.5 arcmin^2 (Koekemoer et al., 2013), confirming that the low-luminosity, early galaxies uncovered in the HUDF are compact (half-light radius, $r_{1/2} < 0.5$ kpc; Ono et al., 2013) and have similar colours to local star-forming galaxies (rest-frame UV slope $\beta_{\rm UV} \simeq -2$, where $F_\lambda \propto \lambda^\beta$; Dunlop et al., 2013). The detection of an increasing number of galaxies at $z = 6 - 8$, including the first sample of galaxies at $z > 9$ (Ellis et al., 2013; Oesch et al., 2013), within the UDF12 and other surveys (Zheng et al., 2012; Coe et al., 2013) has allowed the determination of the rest-frame UV luminosity function at high redshift. The extremely faint galaxies ($M_{\rm UV} > -17$) detected within the ultra-deep imaging of the UDF12 programme, have constrained the faint-end slope of the $z \simeq 7$ LF to be very steep with $\alpha = -1.9$ at $z = 7$ (McLure et al., 2013; Schenker et al., 2013). The slope of

the faint-end of the LF is key for ascertaining the role LBGs play in reionizing the Universe, as only by extrapolating the number densities of galaxies beyond the faintest galaxy detected even in the HUDF, can the ionising photon budget be met by early galaxies (Robertson et al., 2013; Salvaterra et al., 2011).

As part of the UDF12 collaboration, I developed my own independent WFC3/IR data reduction pipeline which I used primarily to reduce the BoRG pure-parallel imaging. The analysis of the BoRG dataset which I then performed resulted in a sample of bright galaxies which were used in the determination of the $z \simeq 8$ LF in McLure et al. (2013). My *HST*/WFC3 reduction pipeline also allowed an independent reduction of the UDF12 images themselves for comparison with the official reductions described in Koekemoer et al. (2013).

3.9.5 The BoRG dataset

One challenge when determining the $z \sim 8$ LF is selecting sufficient numbers of galaxies at the bright-end, given the small survey area of the UDF. The CANDELS program has improved the situation with near-infrared data over $800\,\mathrm{arcmin}^2$, however the subset of the survey that includes the necessary Y-band coverage stands at only $260\,\mathrm{arcmin}^2$ and is vulnerable to cosmic variance effects given the rarity of bright galaxies at $z > 7$. Here we incorporate data taken as part of the Brightest of the Reionizing Galaxies survey (BoRG, PID 11700 in Cycle 17, PID 12572 in Cycle 19; see Trenti et al., 2011, 2012). BoRG is a HST pure-parallel program, consisting of imaging in four filters from WFC3, designed to detect $z \sim 8$ Lyman-break galaxies as Y_{098} drop-out galaxies. Details of the observation strategy can be found in Trenti et al. (2011), however briefly, pure-parallel observations were obtained at multiple sightlines in the Y_{098} , J_{125}, H_{160} filters from WFC3/IR and one or both of V_{606} and V_{600}. The exposure times are carefully chosen to allow the detection of Y_{098} drop-out galaxies at $z \sim 8$ in colour space, from a large $Y_{098} - J_{125}$ colour and relatively flat rest-frame spectral slope inferred from the $J_{125} - H_{160}$ colour. The V-band imaging is designed to remove low-redshift contaminant galaxies, as a galaxy truly above $z > 6$ will contain no flux in any optical filter below the Lyman-break.

The complete BoRG dataset at time of writing consists of 69 independent fields, with further fields expected continually until the completion of Cycle 19. The reduced data for the first 29 fields presented in Trenti et al. (2011), hereafter the BoRG09 dataset, were obtained from the BoRG team. However, reduced data was not available for the additional 30 fields included in Bradley et al. (2012), hereafter the BoRG12 dataset,

and a subsequent 10 fields that were observed after submission of McLure et al. (2013); hence we produced our own reductions of these fields. The calibrated FLT files were obtained from the HST archive and background subtracted with SExtractor, before being combined with AstroDrizzle (Gonzaga, 2012). As a result of guide star acquisition errors introduced in the primary observations, the astrometric grid of these preliminary drizzled images could be offset by up to several arcseconds between different filters. The required shifts to the astrometric solutions were obtained by matching objects to the J_{125} -band image. These shifts were then applied to the original FLT files byway of modifying the WCS information stored in the FITS header, and finally AstroDrizzle was rerun to produce drizzled images directly on the same astrometric grid defined by the J_{125} observations. Within AstroDrizzle, the pixel size was set to 80mas to match the BoRG09 public reductions, and we used a large pix_frac = 0.9 when combining more than one exposure (pix_frac = 1.0 for a single exposure), to account for the lack of dithering in the observations where the primary observation was often spectroscopic. Inverse variance maps were produced directly from AstroDrizzle (final_wht_type = 'IVM') that include all background noise sources such as sky level and dark current, but not the Poisson errors from the objects themselves.

For subsequent depth analysis and object selection we use circular aperture diameters of 0.40″, 0.40″, 0.44″ and 0.50″ for the V, Y_{098} , J_{125} and H_{160} images respectively, where although the data quality of each BoRG field differs slightly, these apertures contain close to 70% of the flux of a point source, in agreement with the other *HST* data incorporated into the LF determinations of McLure et al. (2013).

The resulting BoRG dataset contains a diversity of exposure times ranging from 700-9500s in the J_{125} -filter in a contiguous pointing (resulting in typical depths of $m_{\rm AB} = 26.5$-28.1, 5σ, in a 0.44″-diameter circular aperture). The V and Y_{098} -band images have similar or slightly deeper depths (around 0.2 magnitudes) than the J_{125} -band detection image for a given field, and the H_{160} imaging is typically 0.6 magnitudes shallower than J_{125} , which motivates the choice of colour cut described below. For the analysis presented here, we only considered fields with a J_{125} -band depth deeper than 27.2 over a continuous area of a WFC3 pointing, hence imaging with multiple partially overlapping exposures were not used. The range of galactic latitudes of the pointings also resulted in the removal of several fields close to the plane of the galaxy or with a high density of stars. Our final sample of BoRG imaging consists of 41 fields, with a total area of 184 $\rm arcmin^2$.

Catalogues were produced using SExtractor in dual-image mode, with detection

in the J_{125} -band image, and $z \sim 8$ galaxy candidates were selected using colour-colour cuts analogous to those used in Bradley et al. (2012) with the distinction that here we use circular apertures for our depths and photometric measurements. Where an object is not detected above the 1σ limit in either Y_{098} or H_{160} , we set the magnitude here to be the 1σ-limit for the colour-cut selection, but use the original measured value in further SED fitting analysis. The colour-colour box defined in Bradley et al. (2012) requires that objects comply with the following significance and colour criterion:

- $SN_J > 5\sigma$
- $SN_H > 2.5\sigma$
- $SN_V < 1.5\sigma$
- Y_{098} -$J_{125} > 1.75$
- J_{125} - $H_{160} < 0.02 + 0.15((Y_{098}$ - J_{125} $) - 1.75)$.

The magnitudes were corrected for galactic dust extinction using the Schlegel et al. (1998) dust maps, although this is typically small and makes little difference to the near-IR colours. For the McLure et al. (2013) analysis, a sub-set of 41 BoRG fields (total area 180 arcmin^2) with 5σ detection limits in the range $J_{125} \geq 27.2$–27.9 ($0.44''$-diameter aperture), and which lie at high galactic latitude. The candidates were then analysed with a photometric redshift code, as used for the other fields, before being included in the luminosity function analysis. The reduced set of available filters for the BoRG candidates leads to higher errors in the photometric redshift, and therefore only the more secure candidates selected from BoRG brighter than $M_{\mathrm{UV}} \leq -20.5$ were included in the final analysis of the $z = 8$ luminosity function presented in McLure et al. (2013).

3.10 Discussion

The results of our LF analysis are shown in Fig. 3.10. Our results at bright magnitudes $M_{1500} < -21.5$ are clearly in tension with the best-fitting Schechter function fit to fainter galaxies, and therefore we also fit a DPL to our derived points and the fainter bins from McLure et al. (2013), with the parameterisation presented in Table 3.9. Early work presented in Bowler et al. (2012) indicated that there may be an excess of galaxies at the bright end of the $z = 7$ LF, which has been reproduced here with a confirmation of

the four brightest galaxies and the majority of the fainter candidates (see the discussion in Section 3.5.3 for more details). In particular, our two brightest bins contain our most secure candidates (with the two galaxies at $M_{1500} \sim -22.5$ now detected at $> 10\sigma$ significance) and therefore provide a strong challenge to the Schechter LF fitted to the fainter datapoints. The tension between the ground- and space-based observations could be compounded by the effect of missing flux from the use of small apertures and a point-source correction in the *HST* images. As discussed in Section 3.8, we find an offset of $\sim$0.4 mag between the total magnitudes (and therefore absolute magnitude) derived from the UltraVISTA imaging and *HST* CANDELS imaging, when the galaxies are treated as point sources. The size-magnitude relation would suggest that this effect is not a problem for the faintest and therefore smallest galaxies that population the LF, however around the knee of the function at $M_{1500} \simeq -21$, the absolute magnitudes of the galaxies could be underestimated. Other ground-based analyses support a shallower decline at the bright-end of the LF, with the brightest bin of Ouchi et al. (2009a) higher (but still consistent with) the best-fitting Schechter function.

Our derivation of the bright-end of the LF at $z = 7$ is not in conflict with the current sample of galaxies detected in the CANDELS survey, which in total provides ~ 800 arcmin^2 of imaging. Using the DPL fit to our data points at $z = 7$, we would predict ~ 4 galaxies at $M_{1500} < -21.5$ in the CANDELS wide survey. Finkelstein et al. (2013) has suggested that there may be an excess of $z \simeq 7$ high-SFR galaxies in the CANDELS Great Observatories Origins Deep Survey North (GOODS-N), where they found an unusually bright $z = 7.51$ LBG with $H_{160} = 25.6$ ($M_{\rm UV} = -21.2$). Ono et al. (2012) found one galaxy at $M_{\rm UV} = -21.8$ that lies within the CANDELS GOODS-N wide field, that was spectroscopically confirmed to be at $z = 7.21$. The LAE Himiko lies within the CANDELS UDS field ($M_{1500} = -22.1$) and of the four new galaxies we find in the CANDELS COSMOS field, two have photometric redshift at $z > 6.5$ and $M_{1500} < -21.5$. The above examples shows that there exist secure detections of $M_{1500} < -21.5$ LBGs at $z \simeq 7$ within the CANDELS fields, with a number in agreement with our predictions, and also illustrates the potential for follow-up observations of the brightest high-redshift galaxies as all the previously known $M_{1500} < -21.5$ examples have been spectroscopically confirmed.

We note here that when finished, the VISTA VIDEO survey (Jarvis et al., 2013) should provide the necessary Z and Y-band depth to search for extremely bright $z = 7$ LBGs over a total area of 12 deg^2, and therefore determine whether our DPL extrapolation holds to brighter magnitudes.

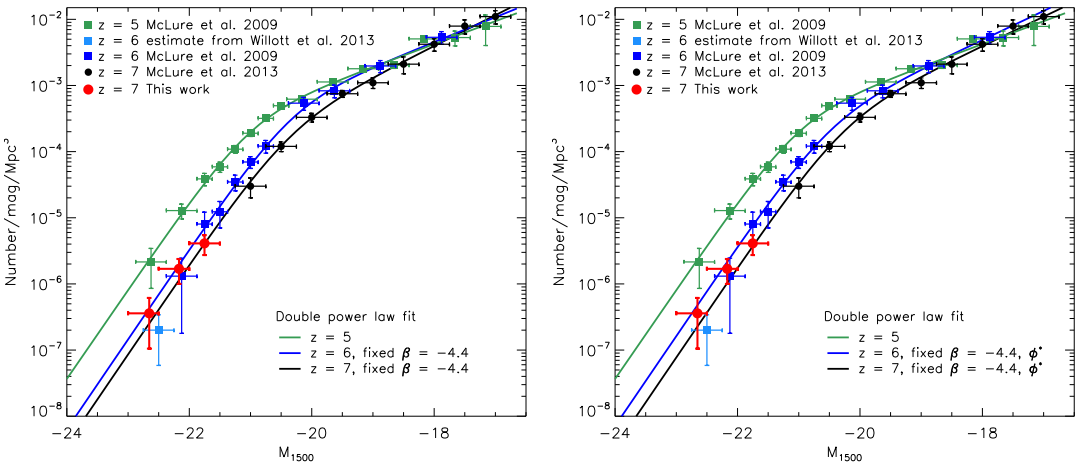

Figure 3.11 *The $z = 5$, $z = 6$ and $z = 7$ UV (~ 1500Å) luminosity function points with the best-fitting double power law fits. The filled red circles show our results for bright galaxies in UltraVISTA and the UDS at $z = 7$, and the black points show the results at $z = 7$ from McLure et al. (2013). At $z = 5$ and $z = 6$ we plot the results of McLure et al. (2009) that were obtained from a similar photometric redshift fitting approach to the work presented here. We estimate the number density of $M_{1500} = -22.5$ galaxies from the work of Willott et al. (2013) and plot this point in light blue. The left-hand panel shows DPL fits where the bright-end slope β has been fixed to the best-fitting value at $z = 5$, and the right-hand panel shows the results when both β and ϕ^* are fixed to the value at $z = 5$. The best-fitting parameters in each case are presented in Table 3.9.*

3.10.1 Comparison with $z = 5$ and $z = 6$ results

We present the best constraints available on the $z = 5$ and $z = 6$ LF in Fig. 3.11. In particular, the number density at the bright end has been determined by McLure et al. (2009) who exploited the DR8 release of near-infrared imaging within the UDS field to select a sample of LBGs at $z = 5$ and $z = 6$. For comparison with our results at $z = 7$, we fit DPLs to the binned LF points at $z = 5, 6$ and 7 from McLure et al. (2009, 2013) and this work using a simple χ^2-minimising routine and present the results in Table 3.9 and Fig. 3.11. At $z = 5$ we allow all the DPL parameters to be varied in the fitting procedure (ϕ^*, M^*, α and β), and for $z = 6$ and $z = 7$ we fix the value of the bright-end slope to the best-fitting value at $z = 5$ ($\beta = -4.4$). Fixing β ensures that we are not overly-fitting to the bright points that are affected by large Poisson errors and cosmic variance. We find that the reduced χ^2 values for the double power law fits are improved compared to a Schechter function, providing additional motivation for the choice of functional form. By alternately fixing ϕ^* and M^* we find that M^*-evolution

Table 3.9 *The best-fitting double power law parameters for the fits shown in Fig. 3.11 at $z = 5, 6$ and 7. The upper part of the table shows the results at $z = 7$ when all the DPL parameters are allowed to vary (shown in Fig. 3.10). The central section shows the results when fixing the value of $\beta = -4.4$ to the best-fitting value at $z = 5$, and the lower section shows the results with ϕ^* also fixed.*

z	ϕ^* /mag^{-1}Mpc^{-3}	M^* /mag	α	β
7.0	3.6×10^{-4}	-20.3	-2.1	-4.2
7.0	3.1×10^{-4}	-20.4	-2.2	-4.4
6.0	6.1×10^{-4}	-20.3	-1.9	-4.4
5.0	3.9×10^{-4}	-21.0	-1.9	-4.4
7.0	3.9×10^{-4}	-20.3	-2.1	-4.4
6.0	3.9×10^{-4}	-20.5	-2.1	-4.4
5.0	3.9×10^{-4}	-21.0	-1.9	-4.4

is preferred in the fitting procedure, supporting previous conclusions in favour of pure 'luminosity evolution' at $z = 5 - 7$, and we display the fits with ϕ^* fixed in Fig. 3.11. The results of McLure et al. (2009) around $M_{1500} \simeq -22$ are not in conflict with our high derived number density, and would support very little evolution in the bright-end of the LF between $z = 6$ and $z = 7$.

Our results however, appear in conflict with the brightest bin at $M_{1350} = -22.5$ from Willott et al. (2013), who used a step-wise maximum-likelihood analysis to conclude that there was an exponential cut-off at the bright-end of the $z = 6$ LF. From a sample of 40 i-dropout LBGs within a total area of 4 deg^2 from the four separate CFHT Legacy Survey fields, Willott et al. (2013) calculated a number density of $2.66^{+5.12}_{-1.75} \times 10^{-8}$ /mag/Mpc^3 at $M_{1350} = -22.5$, which, if unchanged at $z = 7$, would predict an order of magnitude fewer objects than we find in the UltraVISTA and UDS fields. On closer inspection of the sample obtained from the CFHTLS field however, there exist at least two candidates at $M_{1350} < -22.25$ that should be represented in the LF derivation, which would appear to contradict the space density calculated by Willott et al. (2013). Willott et al. (2013) note that they are unable to actually measure a volume density as low as $\sim 10^{-8}$ /mag/Mpc^3 from their dataset, and the anomalously low position of their brightest data-point could be an artefact of their chosen method of fitting the LF. Simply assuming the two brightest galaxies (WHM5 and WHM29) that occupy the $M_{1350} = -22.5$ bin could have been selected in the full survey volume of 10^7 Mpc^3, we estimate the measured value of the number density from the CFHTLS analysis and present this point in Fig. 3.11. The brightest bin from this work and Willott et al. (2013) both contain a small number of objects and hence are sensitive to Poisson

errors and cosmic variance, however within the errors, our determination of the bright-end of the $z = 7$ LF is not in conflict with that found at $z = 6$ by Willott et al. (2013), assuming our simple binned estimate for the bright bin at $M_{1350} = -22.5$. Finally, the best-fitting DPL we find at $z = 6$ would predict 4 galaxies in the brightest bin of the 4 deg^2 of data utilised by Willott et al. (2013), and hence our results are consistent within Poisson errors.

3.10.2 Cosmic variance

The derived LF can vary depending on the dimensions of the survey field observed, as a result of the underlying large-scale density fluctuations within the Universe. We find more galaxies within the UltraVISTA ultra-deep data than in the UDS field, which covers a similar area of sky. The interpretation is complicated, however, by the lower selection efficiency of the UDS dataset compared to UltraVISTA, as a result of the substantially shallower Y-band imaging in the field. Moreover, because we require that a candidate galaxy be detected at $> 2\sigma$ significance in the Y-band, our sample from the UDS field is significantly less complete for galaxies at $z > 6.8$ where the break starts to cut into the Y-band filter. We note that although all of the UltraVISTA candidates would be detected at the 2σ-level in the UDS Y-band, only the two brightest candidates would be detected at the 5σ level and hence likely included in the sample.

Cosmic variance affects the number counts of more massive and hence rarer galaxies more severely, however for small number counts the Poisson error can be more significant. We explore the sources of error on our observed number counts using the Cosmic Variance Calculator v1.02[7] (Trenti & Stiavelli, 2008), assuming a Sheth-Tormen halo mass function, σ_8 = 0.9 and a halo filling factor of 1.0. From the LF points derived from our sample, we estimated the true number of galaxies present in the UltraVISTA and UDS survey volumes for each 0.5 mag bin. Then, by inputting the completeness and survey dimensions, taking the UltraVISTA field to be a single rectangle with 0.65×1.0 deg^2 for simplicity, we can retrieve the error on the number counts and the relative contribution of Poisson noise and cosmic variance. For the brightest bin centred at $M_{1500} = -22.75$, we find the predicted number counts in each field to be $N = 1 \pm 1$ as one would expect from simple Poisson errors. The cosmic variance for such a small number of objects is dwarfed by the Poisson uncertainty, however it still contributes $\sim$ 10 % of the total error. Similarly, the central bin we calculate at $M = -22.25$ has a predicted number of 4 ± 3 galaxies in each field where

[7] `http://casa.colorado.edu/~trenti/CosmicVariance.html`

30% of the error is a result of cosmic variance. This prediction is consistent with the 5 galaxies we find in this magnitude range in the UltraVISTA ultra-deep imaging and 1 galaxy in the UDS. The faintest bin we calculate is very incomplete for the UDS field and so we do not compare the number counts between the two fields here. Therefore, we conclude that for our sample, the errors due to Poisson noise dominate over the cosmic variance, which contributes at most 30% of the total error on the number counts.

3.10.3 Contribution of faint $z = 7$ quasars

Around the peak of the quasar number density at $z = 3$, there is evidence that the very brightest end of the galaxy LF is contaminated by quasars (Bian et al., 2013). There are large uncertainties in the faint-end of the $z > 3$ quasar LF, and the faint-end of the $z = 7$ QLF is completely unknown due to a lack of datasets with the required depth over an adequate area on the sky for detection (see Willott et al., 2009). In Fig. 3.12, we compare the galaxy LF at $z = 7$ to the known QLF at $z = 5$ and $z = 6$ and the extrapolation of the $z = 7$ QLF beyond the absolute magnitude of the faintest quasar found at $z = 7$ with $M_{1700} = -25.5$ (Venemans et al., 2013). The bright-end of the QLF can be estimated from the four $z > 6.5$ quasars known, which includes one from the UKIDSS-LAS found by Mortlock et al. (2011) and three from the VISTA VIKING survey (Venemans et al., 2013). At $z = 6$, around ten quasars are known (Willott et al., 2009), however again the constraints on the faint-end slope are weak, illustrated by the large error bars on the faintest bin shown in Fig. 3.12 (with $\mathrm{M}_{1500} \sim -22$), which contains only one quasar.

To ascertain the level of contamination of our sample by quasars, we compare the number densities of bright LBGs at $z = 7$ to the predicted QLF at $z = 7$ by evolving the $z = 5$ QLF determined by McGreer et al. (2013) using the evolution model presented in their paper. A double power law form is typically used when fitting the QLF, as described in Section 3.9.2. When fitting a DPL to the data points, both McGreer et al. (2013) and Willott et al. (2009) fix the value of the faint-end slope, α, as a response to the large uncertainties in the faint-end determination. Lower redshift $z < 3$ results tend to favour $\alpha = -1.5$ (Croom et al., 2009), with a tenuous steepening observed with $\alpha \simeq -1.7$ to higher redshifts (Masters et al., 2012). McGreer et al. (2013) found a further steepening of the faint-end slope, with the best-fitting DPL with a fixed $\alpha = -1.8$ still under-predicting the number of faint quasars found. If the bright-end slope is instead fixed to $\beta = -4.0$, McGreer et al. (2013) found a best fitting model with a steeper $\alpha = -2.03^{+0.15}_{-0.14}$. Therefore, in Fig. 3.12 we plot the best fitting function with

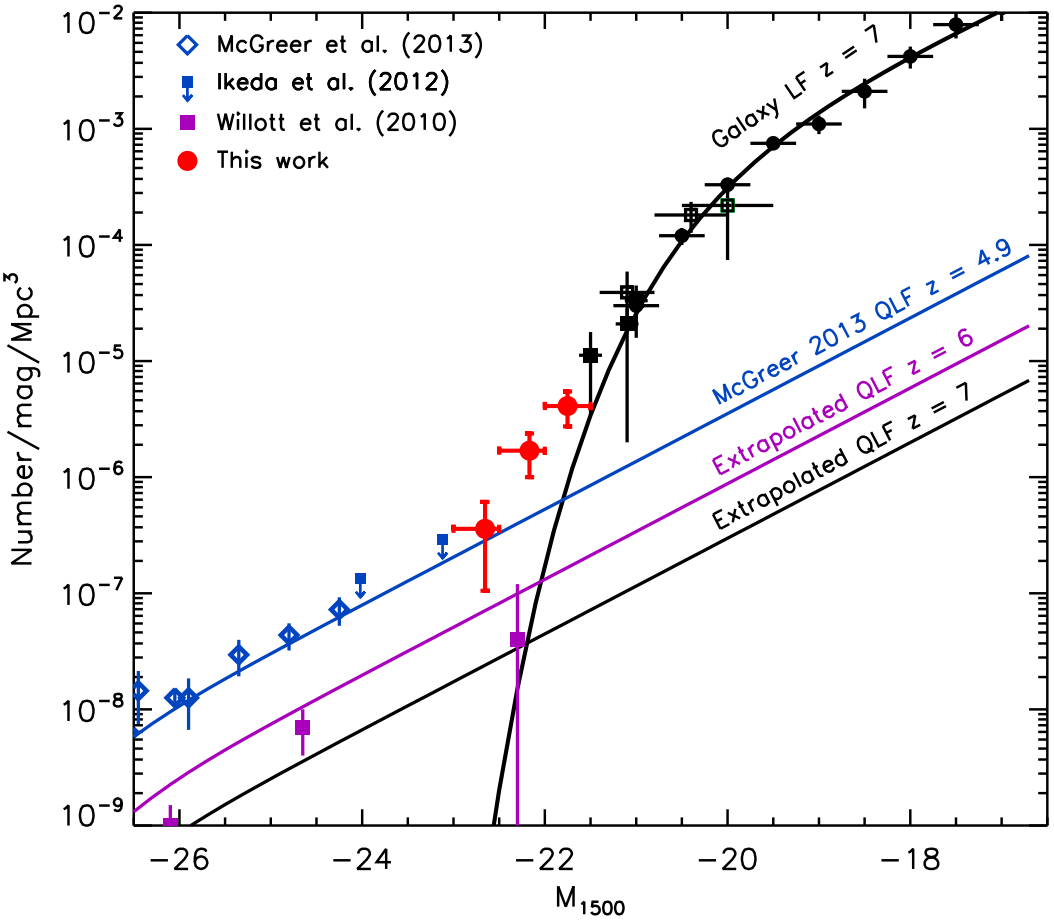

Figure 3.12 *The $z = 7$ galaxy LF from McLure et al. (2013) with the $z = 7$ data points from Fig. 3.10 shown in black and the data points determined from our analysis shown in red. The constraints on the $z = 5$ quasar LF from McGreer et al. (2013) are shown as the blue diamonds, with additional upper limits at fainter magnitudes from Ikeda et al. (2012), where we have shifted the data point at $M_{1500} = -23.0$ by 0.1 mag for clarity. Overplotted in blue is the best fitting double power law at $z = 5$ presented in McGreer et al. (2013). The purple squares show the constraints on the QLF at $z = 6$ from Willott et al. (2009). The QLF at $z = 6$ and $z = 7$ is estimated from evolving the $z = 5$ QLF shown using a LEDE evolution model for $\log(\phi^*)$ taken from McGreer et al. (2013), with fixed $\alpha = -2.03$ and $\mathrm{M}^* = -27.0$.*

$\alpha = -2.03$ from McGreer et al. (2013), to provide an upper limit on the number of faint $z = 5$ quasars.

The $z = 7$ LF parameters are predicted following the Luminosity Evolution Density Evolution (LEDE) model described in McGreer et al. (2013), using a fixed $\alpha = -2.03$ and $M_* = -27.0$. The model predicts that $\log(\phi^*)$ evolves linearly with redshift with gradient $k = \delta\log(\phi^*)/\delta z = -0.47$, derived from fitting to the measured parameters from $z = 2.2 - 4.9$ (Fan et al., 2001). The strength of the evolution when extended to higher redshift is supported by Venemans et al. (2013) at $z = 7$ who found $k = -0.49^{+0.28}_{-0.74}$. We display the data at $z = 6$ from Willott et al. (2009), overlayed with an extrapolated model using the same method as for the $z = 7$ model, again to show an upper limit on the expected number density of quasars here. As can be seen in Fig. 3.12, the LEDE model is consistent with the $z = 6$ LF from Willott et al. (2013) at least given the uncertainties at the faint end, although see the detailed discussions in McGreer et al. (2013). To estimate the number of quasars that could contaminate our sample, and assuming that the quasar SEDs are indistinguishable from the LBGs using the selection here, we integrate the QLF within the three LF points we calculated. We predict 0.3 quasars in the fainter bin at $M_{1500} = -21.75$, and 0.2 and 0.1 in the brighter bins at $M_{1500} = -22.25$ and $M_{1500} = -22.75$ respectively. Hence, from the analysis of the LF and QLF we conclude that contamination of our sample by quasars is minimal, a result obviously consistent with our finding that the vast majority of our $z \simeq 7$ objects are spatially resolved (see Section 3.8). However, given the large uncertainties in the faint-end slope of the QLF, the possibility of some low-level contamination is not completely ruled out. For example Willott et al. (2009) calculated an upper limit of two quasars per deg^2 in the UltraVISTA survey, when assuming the most extreme LF parameters from the range of acceptable fits to the QLF at $z = 6$. There is evidence that quasars may contaminate bright $z = 6$ LBG samples on the order of $\sim 10\%$, for example the sample of ten LBGs presented by McLure et al. (2009) and spectroscopically confirmed by (Curtis-Lake et al., 2012), included one Type I quasar identified by the broadened Lyα line (Willott et al., 2009).

Note that at high redshift, the observed QLFs only account for Type I unobscured quasars with both broad-line and narrow-line components, and there is evidence from X-ray surveys that unobscured quasars only account for 25% of the total number at $z = 4$ (Masters et al., 2012). If the ratio of Type I to Type II quasars persists to high-redshift, the results here are likely a lower limit on the number densities of quasars at $z = 7$.

The rest-frame UV colours of LBGs and quasars at high redshift are impossible to distinguish with the current photometric accuracy (Bian et al., 2013), and identical colour-colour cut selection criterion are often used for the selection of galaxies and quasars at $z > 5$ (Willott et al., 2009). Here, for completeness, we consider whether radio or X-ray emission could be detected from a quasar selected as a galaxy and included in our sample, with the data available in the COSMOS and UDS fields. The COSMOS field is imaged by the *Chandra*-COSMOS survey (Elvis et al., 2009), which has a limiting depth of 1.9×10^{-16} ergs/s/cm^2/Hz in the 0.5-2.0 keV channel and 7.3×10^{-16} ergs/s/cm^2/Hz in the 2-10 keV channel. In the radio, the COSMOS field is covered by the Very Large Array (VLA)-COSMOS survey (Schinnerer et al., 2010), with a sensitivity of $12\mu\mathrm{Jy}$ per beam. The UDS field has X-ray imaging from the Subaru/XMM-Newton deep survey Ueda et al. (2008), to depths of 6×10^{-16} ergs/s/cm^2/Hz in the 0.5-2.0 keV channel and 5×10^{-15} ergs/s/cm^2/Hz in the 2-10 keV channel.

We find no radio or X-ray counterparts for any of the galaxies within our sample, when comparing to the publicly available catalogues within each field derived from the datasets described above. We also perform a stack of the objects in the VLA-COSMOS imaging and again find no detection to a limit of $\sim 12\,\mu\,\mathrm{Jy}$ per beam. The average quasar SEDs from Shang et al. (2011) suggests that if one of our candidates was a typical radio-loud quasar, it would just be detectable in the X-ray and radio imaging (see Figure 6 of Ouchi et al., 2009b). Furthermore, a bright radio-loud quasar such as J1429+5447 at $z = 6.21$ (Willott et al., 2009; Frey et al., 2011), would be detected at high-significance in the available radio data. Therefore, although a non-detection in the radio and X-ray for the objects in our sample rules out the possibility that the majority of the objects have strong active nuclei, our sample could still contain $\simeq 1$ radio-quiet quasar. For comparison, the $z = 7.1$ quasar discovered by Mortlock et al. (2011), which is substantially brighter than our LBGs with $M_{\mathrm{UV}} = -26.6$, has been detected in the X-ray by Page et al. (2014) and Moretti et al. (2014) with fluxes of $5.7 \pm 1.2 \times 10^{-16}$ ergs/s/cm^2 and $9.3^{+1.6}_{-1.1} \times 10^{-16}$ ergs/s/cm^2 respectively in the 0.5-2.0 keV channel, but not in the radio with a 3σ upper limit of 23.1 $\mu\mathrm{Jy}$ per beam (Momjian et al., 2014).

3.11 Astrophysical Implications

As discussed in the introduction to this thesis, the Schechter functional form, with its steep exponential decline at high luminosity/mass, provides a good description of the galaxy LF and mass function (MF) observed at low redshift (Montero-Dorta & Prada, 2009). Moreover, recent work extending the study of the galaxy luminosity and stellar mass function out to higher redshift, indicate that a Schechter function (or double Schechter function) still provides a good description of the data out to at least $z \simeq 3$ (Ilbert et al., 2013; Muzzin et al., 2013). However, the results we have presented here suggest that this may not be the case at $z \simeq 7$.

It is thus worth briefly considering whether our derived $z = 7$ galaxy LF is physically reasonable, and what the inability of a Schechter function to reproduce the bright end of the LF might mean. As already discussed in Section 3.9, and shown in Fig. 3.10 one way to describe the apparent lack of a steep exponential decline at the bright end is to parameterise the LF as a double power-law fit, which well describes the full range of available data at $z \simeq 7$. However, the physical meaning of such a double power law is unclear, and moreover it is important to check that the number density of bright $z \simeq 7$ galaxies inferred from our study is not physically unreasonable given the expected number density of appropriate dark matter halos expected to exist at these early times.

We therefore conclude by showing, in Fig. 3.13, a comparison of the $z \simeq 7$ ΛCDM dark-matter halo mass function, scaled via a constant mass-to-light ratio, with our new observational determination of the $z \simeq 7$ galaxy LF. We produced the halo mass function using the code provided by Reed et al. (2007) using our chosen cosmology and $\sigma_8 = 0.9$ (the amplitude of the linear power spectrum on the scale of $8\,h^{-1}\mathrm{Mpc}^3$), but the basic results are not strongly influenced by the precise choice of code or parameters within current uncertainties. We then simply scaled the halo mass function into a UV luminosity function using a constant mass-to-light ratio, set by assuming that a galaxy with $M_{1500} = -22.4$ has a stellar mass of $M_* \simeq 10^{10}\mathrm{M}_\odot$ (as supported by our data) and a dark matter halo mass to stellar mass ratio of 30 (e.g. Behroozi et al., 2013b). As can be seen from Fig. 3.13, the result is a predicted LF which, without any additional shifting or fitting, does an excellent job of reproducing our new $z \simeq 7$ LF from the previously inferred break luminosity at $M_{1500} \simeq -20$ out to our brightest luminosity bin. Interestingly, over this range, it is evidently indistinguishable from our double power-law fit, confirming that it provides an excellent representation of the data. It is significantly shallower than the exponential decline shown by the pre-existing Schechter function fit, and only starts to deviate from the bright-end power law at very bright

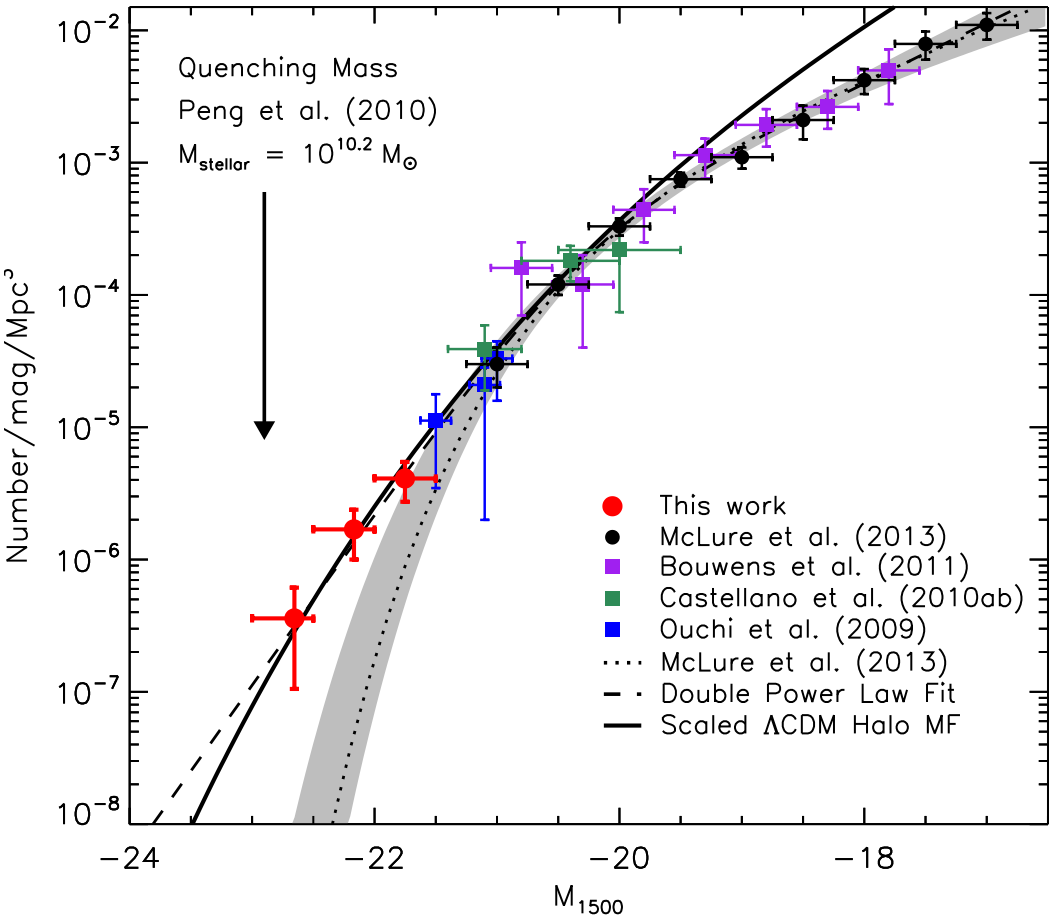

Figure 3.13 *The $z = 7$ UV (~ 1500Å) luminosity function showing a scaled ΛCDM halo mass function as described in the text (solid black line). The results from our sample of galaxies from the UltraVISTA DR2 and UDS fields are shown as the red filled circles. Data points from other studies are as described in the caption for Fig. 3.10 The best-fitting Schechter function at $z = 7$ from McLure et al. (2013) is plotted as the dotted black line, and the best-fitting double power law to our data points and those from McLure et al. (2013) is shown as the dashed line. The one-sigma confidence limit on the Schechter function parameters ($M^\star, \phi^\star$ and α) is shown as the grey shaded region. We highlight the quenching mass derived by Peng et al. (2010) with an arrow, after converting to a UV luminosity using the typical mass-to-light ratio displayed by our sample.*

magnitudes (thus suggesting that extrapolation of the double power law brightward of $M_{1500} \simeq -23$ will over-predict the number of extremely bright galaxies to be found in future wider area surveys).

This interesting result has a number of potentially important implications. First, it confirms that the number density of bright galaxies revealed in this study is not unreasonable. Neither is the inferred bright-end slope, as this essentially parallels the decline in the number density of appropriate-mass dark-matter halos. Second, it suggests that while the process (e.g. supernovae feedback) which limits star-formation in faint galaxies appears to be in operation at these early times (as evidenced from the difference between the slope of the halo mass function and the UV LF at faint magnitudes), the mechanism that limits high-mass galaxy growth may have yet to impact on the form of the LF at $z \simeq 7$, at least over the luminosity/mass range probed here. Perhaps this is because AGN have yet to grow to the masses and hence luminosities required to eject gas available for future star formation, and certainly there is little evidence for AGN within our galaxy sample (see Section 3.10). However, without over speculating we can at least say that, whatever the physical mechanism which ultimately limits the masses of star-forming galaxies, our results are certainly consistent with the redshift invariant 'mass quenching' argument proposed by Peng et al. (2010). Since the estimated masses of our brightest galaxies have only just reached a mass comparable to the proposed critical 'quenching mass' of $M_* = 10^{10.2}\mathrm{M}_{\odot}$, it is perhaps to be expected that the quenching of star-formation activity in galaxies which causes them to leave the 'main sequence' will only be revealed at lower redshifts and/or higher stellar masses than probed by the sample presented here.

Finally, we note that the above discussion implicitly attempts to relate our observational determination of the UV LF to the underlying mass function. The extent to which the form of the LF actually mirrors the form of the underlying stellar mass function of course remains unclear, and may only really be resolved at these extreme redshifts with the deep, high-resolution near-mid-infrared data anticipated from the James Webb Space Telescope.

3.12 Conclusions

We present the results of a new search for bright star-forming galaxies at $z > 6.5$ utilising the very latest data within the UltraVISTA and UKIDSS Ultra Deep Survey (UDS) fields. The $1.65\,\mathrm{deg}^2$ of available overlapping optical, near- and mid-infrared

data was analysed using a photometric redshift fitting method, which enables the identification of high-redshift galaxies and the rejection of contaminants such as low-redshift galaxies and galactic dwarf stars. In total we present 34 galaxies, 29 from within the ultra-deep UltraVISTA imaging, one from the deep UltraVISTA region, and four from the UDS field. With the improved photometry available, we reselect seven of the ten candidates presented in Bowler et al. (2012) as $6.5 < z < 7.5$ galaxies. Of the remaining original candidates, two are confirmed as galaxies at a slightly lower redshift of $6.0 < z < 6.5$ and the final candidate is now best fitted as a T-dwarf.

From the best-fitting model to the photometry of each galaxy we calculated the stellar mass, SFR and sSFR. Our sample contains some of the most massive galaxies at $z = 7$, with $M_\star \simeq 10^{10}\mathrm{M}_\odot$, which show a low sSFR compared to lower mass galaxies at $z = 7$, with an upper limit of sSFR $\lesssim 2$ Gyr^{-1}. We find no evidence for a redder rest-frame UV slope β for our sample (median $\beta_{JHK} = -2.0$), as would be expected by an extrapolation of the colour-magnitude relation at lower redshift to $z = 7$. We measure the sizes of the galaxies in our sample and find that although the majority are consistent with being uresolved in the ground-based imaging, a significant number have a larger FWHM suggesting $r_{1/2} \gtrsim 1.5$ kpc. For four galaxies that lie within *HST* imaging from the CANDELS COSMOS survey, we find an offset (~ 0.4 mag) between the total magnitudes when the object is assumed to be a point source in both the ground and space-based imaging. Inspection of surface-brightness profiles shows that the galaxies have an extended profile, which can lead to an underestimate of the galaxies total and therefore absolute magnitude when small apertures are used with the assumption of a point-source profile in *HST* imaging.

From our final sample we determine the form of the bright end of the rest-frame UV galaxy luminosity function (LF) at $z \simeq 7$. We use a $1/V_{\mathrm{max}}$ estimator to determine the binned LF points at $M_{1500} = -22.75, -22.25$ and -21.75, folding in the completeness of our selection methodology using injection and recovery simulations. In our determination of the LF, we take into account that some of our galaxies are gravitationally lensed by low-redshift galaxies along the line-of-sight, with a typical brightening of $0.1 - 0.3$ mag. We find that the bright end of the $z = 7$ LF does not decline as steeply as predicted by the Schechter function fitted to fainter data, and can be better described by a double power law. The possibility of significant contamination of our sample by high-redshift quasars can be excluded, with a predicted number of < 1 in the UltraVISTA and UDS imaging, calculated from an extrapolation of the $z = 5$ QLF to $z = 7$. From the observed UV LF at $z = 5$ and $z = 6$, we show that a DPL fit can provide a good description of the data and that the bright end of the LF at

$z = 6$ and $z = 7$ shows little evolution. Our results at the bright end of the LF mimic the prediction from the scaled dark matter halo MF, suggesting that the physical mechanism which inhibits star-formation activity in massive galaxies (for example AGN feedback) has yet to become efficient at $z \simeq 7$. The interpretation of our results agrees with the phenomenological model of Peng et al. (2010), which would suggest that the most massive $z \simeq 7$ galaxies in our sample have only just reached the critical "quenching mass" of $M_{\star} = 10^{10.2}\,\mathrm{M}_{\odot}$, above which star-formation activity is strongly suppressed.

CHAPTER 4

The galaxy luminosity function at $z \simeq 6$ and evidence for rapid evolution in the bright end from $z \simeq 7$ to 5

4.1 Introduction

Recent results from an analysis of $\sim 0.2\,\mathrm{deg}^2$ of *HST* imaging from the UDF and CANDELS surveys by Bouwens et al. (2014) at both $z \simeq 6$ and 7 appear to strongly contradict the LF calculated from ground-based results, an apparently surprising result as the inferred high density of bright objects should have been detected in the existing ground-based searches. Furthermore, the results from Bouwens et al. (2014) contradict previous work using a similar methodology (Bouwens et al., 2007), most noticeably at the bright-end, and hence further investigation with a wide-area and homogeneous dataset is warranted. The result of the high numbers of bright galaxies found by Bouwens et al. (2014) is effectively to fix the characteristic magnitude of the best-fitting Schechter functions to $M^* \simeq -21$ from $z = 3$–7, while instead invoking a strong evolution in the faint-end slope (α) and the overall normalisation. An approximately constant value of $M^* \simeq -21$ was also found by Finkelstein et al. (2014) using $\simeq 300\,\mathrm{arcmin}^2$ of data from the UDF and the Great Observatories Origins Deep Surveys (GOODS) North and South fields. The lack of luminosity evolution in the rest-frame UV LF at high-redshift from these recent studies starkly contrasts with the majority of results to date which have overwhelmingly favoured a strong luminosity-evolution (Bouwens et al., 2007, 2008, 2011a; McLure et al., 2009). Whether the observed evolution in the rest-frame UV LF from $z \simeq 7$ to $z \simeq 4$ occurs primarily as density or luminosity evolution depends critically on the combination of astrophysical process on the underlying evolution of the dark matter halo mass function (DMHMF). If the rest-frame UV luminosity of galaxies follows approximately the hierarchical assembly of the host dark matter haloes at high redshift then an evolution in the

characteristic luminosity would be expected (e.g. see figure 10 of Bouwens et al., 2008). However, the observed form of the rest-frame UV LF at $z < 5$ deviates from the power-law type form predicted for a simple conversion between mass and luminosity, and the implementation of astrophysical processes necessary to quench (e.g. feedback from accretion onto a black hole) or obscure (e.g. dust production) star-formation in the most massive haloes is required to bring the LFs into agreement (e.g. Bower et al., 2012; Cai et al., 2014). At $z \simeq 7$, Bowler et al. (2014) found evidence for a shallower drop-off in number density at the bright-end compared to the standard Schechter function fit, with a double power law (DPL) form preferred. The observed $z \simeq 7$ LF from Bowler et al. (2014) follows closely the form of the DMHMF, indicating that the onset of significant quenching or dust obscuration occurs at $z < 7$. A detailed analysis of the bright end of the $z \simeq 6$ LF is therefore essential to clarify the dominant form of the evolution of the rest-frame UV LF at high redshift, and to investigate how the functional form of the bright end changes as a result of the potential build-up of dust or the role of feedback in quenching the most massive galaxies.

In this work we follow the methodology of Bowler et al. (2012) and Bowler et al. (2014) to perform a search for bright $z \simeq 6$ star-forming galaxies within the UltraVISTA and UDS fields. These fields contain a wealth of multiwavelength imaging (including deep z'-band and near-infrared data essential for the secure selection of $z > 5$ galaxies) covering an area over eight times that analysed by Bouwens et al. (2014), and almost 20 times that utilised by Finkelstein et al. (2014). Recent improvements in the depth of imaging in both fields (e.g. $\gtrsim 1\,\mathrm{mag}$ deeper in the z' and/or Y, J, H and K bands) also allows us to directly compare to, and reassess, previous results at $z \simeq 6$ determined using these survey fields by McLure et al. (2009) and Willott et al. (2013).

This chapter is structured as follows. We start with a description of the UltraVISTA and UDS datasets in Section 4.2, followed by the details of our $z \simeq 6$ galaxy selection in Section 4.3. The potential contamination of our sample by dwarf stars is quantified in Section 4.4. Our sample of $z \sim 6$ LBGs is described in Section 4.5, where we compare our objects to previous $z = 6$ samples extracted from these survey fields by Willott et al. (2013) and McLure et al. (2009). We detail our determination of the rest-frame UV LF in Section 4.6 and present the results (including a comparison to previous studies) in Section 4.7. Finally, we investigate the form of the $z \simeq 6$ LF and the observed evolution from $z \simeq 5$–7 in Section 4.8, where we compare the observed evolution in the LF to the predictions from a range of theoretical models. We end with our conclusions in Section 4.9. All magnitudes are quoted in the AB system (Oke, 1974; Oke & Gunn, 1983) where $m_{\mathrm{AB}} = -2.5\log_{10}[F_{\nu}(\mathrm{Jy})/3631\,\mathrm{Jy}]$.

4.2 Data

The available optical/near-infrared imaging in the two extragalactic survey fields utilised here is summarised below, and further details of the data processing can be found in Bowler et al. (2012, 2014). Fig. 4.1 summarises the photometric bands used and illustrates the relative depths of the imaging (calculated in 1.8-arcsec diameter circular apertures). The search for galaxies at $z \simeq 6$ requires deep z'-band imaging for selection, and the UltraVISTA and UDS fields both benefit from deep Subaru z'-band imaging extending faint-ward of $m_{\rm AB} = 26$. The presence of imaging in filters long-ward of the Lyman-break, in the near-infrared at $z > 6$, allows the robust removal of contaminant populations such as Galactic brown dwarfs and dusty low-redshift galaxies, while deep optical imaging is necessary to accurately determine the redshift defined by the strong Lyman-break (which moves through the i-band filter at these redshifts).

4.2.1 UltraVISTA/COSMOS

The UltraVISTA near-infrared imaging essential for this work lies within the COSMOS field (Scoville et al., 2007a), which contains an abundance of multiwavelength imaging over 1–2 square degrees on the sky[1]. We obtained deep Subaru/SuprimeCam z'-band imaging of the central square degree of the field, which reaches a 5σ limit of $\mathrm{m_{AB}} = 26.6 - 26.8$ (1.8 arcsec diameter circular aperture) over four separate SuprimeCam pointings. The COSMOS field also contains one of four 'deep' fields (D2) imaged as part of the Canada-France-Hawaii Legacy Survey (CFHTLS), each corresponding to a single $1\,\mathrm{deg}^2$ pointing of CFHT/MegaCam. We use optical imaging in the u^*, g, r and i filters from the T0007 release of the CFHTLS. The near-infrared imaging from UltraVISTA provides data in the Y, J, H and K_s filters over a total of 1.5 square degrees of the COSMOS field. The UltraVISTA survey consists of a 'deep' component with depths of $\mathrm{m_{AB}} \sim 25$ over the full 1.5 square degrees (McCracken et al., 2012), superseded by the 'ultra-deep' imaging that covers $\sim 70\%$ of the full field in the form of four strips. Here we utilise the second data release (DR2) of UltraVISTA (McCracken et al., 2013), in which the 'ultra-deep' part has reached depths of $\mathrm{m_{AB}} = 25.8$ in the Y band (see table 1 of B14 and Fig. 4.1).

[1] `http://cosmos.astro.caltech.edu/`

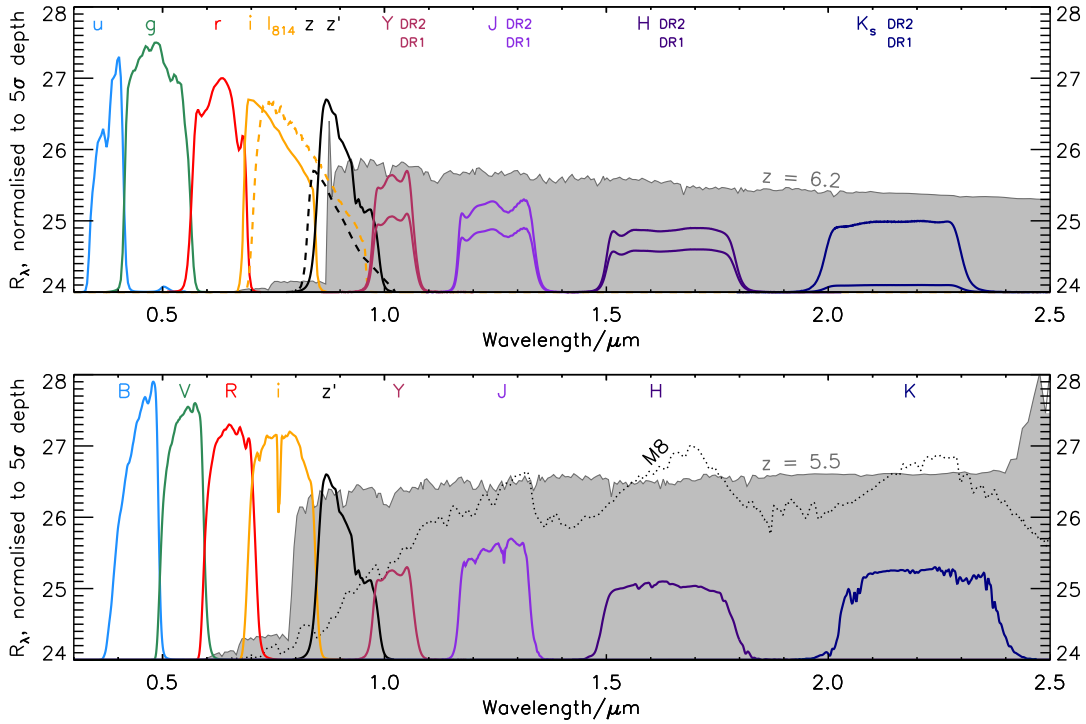

Figure 4.1 *The filter transmission curves for the filters used in this study in the UltraVISTA/COSMOS and UDS/SXDS fields are shown in the upper and low plot respectively. Each filter curve has been peak normalised to the median* 5σ *depth (calculated in* 1.8*-arcsec diameter circular apertures) and is shown as the response per unit wavelength. The upper and lower curves for the* Y*,* J*,* H *and* K_s *filters in the UltraVISTA/COSMOS field show the depths from the two epochs of imaging available. The deeper DR2 imaging exists over* $\sim$ 70 *percent of the UltraVISTA field with overlapping imaging from CFHTLS (for schematics see figures 1 and 2 of Bowler et al., 2014). In each plot an example redshifted galaxy SED from the Bruzual & Charlot (2003) library is shown, in flux per unit frequency, where the mean IGM absorption from Madau (1995) has been applied. The Lyman-break can clearly be seen at* $\sim 0.8\mu m$ *in each SED, with the Balmer break just visible in the lower plot. In the upper plot, a Lyman-*α *emission line of* $EW_0 = 10$*Å has been added to the SED, and the lower plot shows an example M-dwarf spectrum (dotted line).*

4.2.2 UKIDSS UDS/SXDS

The UKIDSS UDS field includes deep optical imaging taken as part of the Subaru *XMM-Newton* Deep Survey (SXDS) in the B, V, R, i and z' filters (Furusawa et al., 2008). Further to this public data, we obtained deep Subaru/SuprimeCam imaging in the z' band (see Bowler et al., 2014 for details) which reaches depths of $\mathrm{m_{AB}} = 26.5 - 26.7$ (1.8 arcsec diameter circular aperture) over four separate SuprimeCam pointings. The DR10 of the UKIDSS UDS (Lawrence et al., 2007) provides the key near-infrared imaging over the field in the J, H and K filters. Finally, we use the second data release of the VISTA Deep Extragalactic Observations survey (VIDEO; Jarvis et al., 2013), which has observed the UDS field in the Y band to a 5σ limiting depth of $\mathrm{m_{AB}} = 25.3$, extending $\simeq 0.5$ mag deeper than the previous imaging utilised in Bowler et al. (2014).

4.3 Candidate Selection

4.3.1 Catalogue production and initial cuts

Candidate high-redshift galaxies were selected from the deep Subaru z'-band imaging in the UltraVISTA/COSMOS and UDS/SXDS fields using SExtractor v2.8.6, with the fiducial photometry measured in 1.8 arcsec diameter circular apertures and multiwavelength catalogues produced using the 'dual-image' mode.

The full catalogues were first cut at a z'-band magnitude of 26.0 in the UltraVISTA DR2 ('ultra-deep') and UDS fields, and at 25.0 for the shallower UltraVISTA DR1 ('deep') regions, resulting in a minimum significance of 7σ in the shallowest Subaru/SuprimeCam tiles for each field, extending to $\sim 10\sigma$ in the deepest tiles. To ensure a non-detection in the bluest bands we removed any object with a detection at greater than 2σ significance in either the u or g band in the UltraVISTA field, or the B or V band in the UDS, using local depth estimates within the field. Local depths were calculated at each point in the images from the median absolute deviation (MAD) estimator (using $\sigma = 1.48 \times \mathrm{MAD}$) of the counts within the closest 200, randomly placed, blank apertures. For the purpose of SED fitting, we corrected all magnitudes to total assuming a point source correction. Many of the candidate high-redshift galaxies are resolved in the ground-based imaging (see Bowler et al., 2014), however the size is still dominated by the seeing of the images and therefore the point source correction dominates any colour difference due to intrinsic size variation between the bands.

4.3.2 Photometric redshift fitting

The final sample of $z \simeq 6$ galaxies was determined from SED fitting of Bruzual & Charlot (2003) models to the photometry, coupled with careful visual checks to remove artefacts and objects with low-level flux in the two bluest optical bands. Given the degeneracies between metallicity, age and dust reddening when using broad-band photometry, we fit our candidate galaxy photometry with a reduced set of model galaxy SEDs. The 'high-redshift' model set, designed to identify good high-redshift candidates, consisted of models with ages from 10 Myr to the age of the Universe at $z = 5$, $A_{\rm V} = 0.0$–2.0 and a single metallicity of $0.2\,{\rm Z}_{\odot}$ motivated by recent measurements of the metallicity in low-redshift LBG analogues (Stanway & Davies, 2014). The 'contaminant' model set was designed to provide red and dusty galaxy SEDs in the range $z = 1$–3, with strong Balmer or 4000Å breaks, and therefore we allow ages up to the present age of the Universe, $A_{\rm V} = 0.0$–6.0 and a single metallicity of $1.0\,{\rm Z}_{\odot}$. In addition to the suite of galaxy SEDs, we also fit standard stellar templates with types M4 to T8 (taken from the SpeX library [2]), as cool galactic brown dwarfs can mimic the colours of high-redshift LBGs with $z = 5 - 7$. We discuss and quantify potential brown dwarf contamination of our sample in Section 4.4.

For inclusion in our final $z \simeq 6$ galaxy sample, we required that the object had a best fitting SED at $5.5 < z < 6.5$ with an acceptable χ^2 (≤ 11.3), and a $\Delta\chi^2 > 4$ between the high-redshift solution and the next best-fitting $z < 5.5$ model. This step reduced the sample of several thousand objects that passed the magnitude cuts described above to a total sample of 335 objects, with 205, 3 and 127 objects from the UltraVISTA DR2 strips, DR1 and UDS respectively. The sample was then carefully visually checked to remove single-band detections (including z'-band CCD bleeds) and to identify false optical non-detections due to the negative haloes around stars in the CFHTLS and Subaru optical imaging, which resulted in the removal of a further 26 objects (15 in the UltraVISTA DR2 and 11 in the UDS). At this point we also removed the extreme LAE 'Himiko' from our UDS sample, because of the known spectroscopic redshift of $z = 6.595$, which places it outside our desired range. The result of the SED fitting and visual checks described was a sample of 309 objects (190, 3 and 116 in the UltraVISTA DR2, DR1 and UDS respectively) that are consistent with being $5.5 < z < 6.5$ LBGs. However, one final source of contamination must be considered, namely cool galactic brown dwarfs. The removal of candidates consistent with being a brown dwarf using the criterion described in detail in the next section, resulted in the removal of 37 and

[2] `http://pono.ucsd.edu/~adam/browndwarfs/spexprism/`

10 objects in the UltraVISTA DR2 and UDS samples respectively, producing a final sample of 266 galaxies with photometric redshifts in the range $5.5 < z < 6.5$.

4.4 Contamination by brown dwarfs

Cool galactic brown dwarfs (with spectral types M, L and T) have SEDs that peak in the near-infrared and drop steeply towards the optical bands (e.g. the M8 type dwarf shown in Fig. 4.1), potentially mimicking the colours of $z > 5$ galaxies. The number densities of dwarf stars begins to drop at $J > 25$ (Ryan et al., 2011) as the number counts of galaxies rapidly rise (e.g see Fig. 4.2), and therefore they are in practice a negligible contaminant for extremely deep, small area imaging programs such as the HUDF. In the search for the brightest high-redshift $z \simeq 6$ LBGs however, the number densities of dwarf stars can begin to dominate (see Fig. 4.2), and the high-redshift galaxy samples become increasingly susceptible to contamination by the relatively more numerous M- and L-type dwarf stars. The comparatively poor resolution of the ground-based imaging surveys utilised here compared to *HST* imaging, coupled with the small measured sizes of LBGs (Curtis-Lake et al., 2014; Ono et al., 2012), precludes any discrimination based on size, and hence we must carefully assess the available multiwavelength information to remove brown dwarfs from the $z \simeq 6$ sample. The UltraVISTA/COSMOS and UDS/SXDS fields utilised here contain the best deep optical to near-infrared photometric data available on the degree scale, and hence, as we show quantitatively in the following section, the removal of dwarf stars using SED fitting of standard spectral templates can be cleanly performed. The possibility of photometric scattering of stars (which are considerably more numerous than LBGs at $m_{\rm AB} \lesssim 25$) into our sample must be carefully considered however, and we use a simple model of the Galactic stellar distribution to estimate the likely number of contaminant stars in Section 4.4.2.

4.4.1 Injection and recovery simulations

We quantify the potential brown dwarf contamination of our sample by injecting and recovering synthetic dwarf star photometry into the UltraVISTA/COSMOS and UDS/SXDS images, passing the fake stars through an identical selection procedure as described above for our $5.5 < z < 6.5$ LBGs. Each standard spectral template for dwarf star types M4–T8 from the SpEX library was integrated through the appropriate

filters for the UltraVISTA/COSMOS and UDS/SXDS fields, scaled to a total z'-band magnitude in the range $m_{\rm AB} = 23$–26 and injected into the images using the model PSF (determined using the method described in Bowler et al., 2014) at a random position. As described further in Section 4.6.1, we used representative sub-sections of the full UltraVISTA and UDS mosaics to reduce computing time. If the object was recovered ($\sim 20\%$ of injected objects are lost due to blending with other sources), and passed the z'-band magnitude cut and the optical non-detection conditions (Section 4.3.1), the photometry was corrected to a total magnitude in each band and fitted with the galaxy and stellar spectral templates used in the LBG selection. The injected stellar photometry was then classified as an LBG contaminant if $\chi^2_{gal} < 11.3$ and $5.5 < z_{\rm phot} < 6.5$, following exactly our LBG selection procedure.

The resulting fraction of each stellar type classified as an LBG contaminant depended strongly on the assumed magnitude, with injected stars brighter than $z' \simeq 25$ rarely being classified as an LBG. We find that up to $\sim$ 10–20 per cent of the input dwarf stars with $z' = 25$–26 are classified as $5.5 < z < 6.5$ galaxies, depending on sub-type and field (where the differing relative depths of the imaging results in different vulnerabilities). The predicted number and redshift distribution of dwarf stars is discussed in the next section.

Crucially, the simulations show that the overwhelming majority ($> 95\%$) of injected stellar templates that are recovered as LBG candidates remain good stellar fits, and by imposing the condition that galaxy candidates must have a poor stellar fit with $\chi^2_\star > 10.0$, we can exclude these contaminants from our sample. A small number of genuine LBGs will also be excluded as a result of this criterion, however we account for the additional incompleteness of our sample when calculating the LF, by recreating this selection criterion in our galaxy injection and recovery simulations. By applying such a selection criterion, we remove 37 objects from the UltraVISTA DR2 sample, 0 from the DR1 and 10 from the UDS sample. In 4.1 we present the 47 objects that were excluded from the original sample as possible dwarf star contaminants based on a good stellar fit with $\chi^2_\star < 10.0$.

4.4.2 Number density model

Despite the apparent success of our stellar fitting method for removing dwarf stars masquerading as high-redshift LBGs, even a small contamination rate could be significant for the determination of the $z \simeq 6$ LF at the bright end (Fig. 4.2). Hence to constrain the likely contamination rate, an estimate of the number of each stellar type

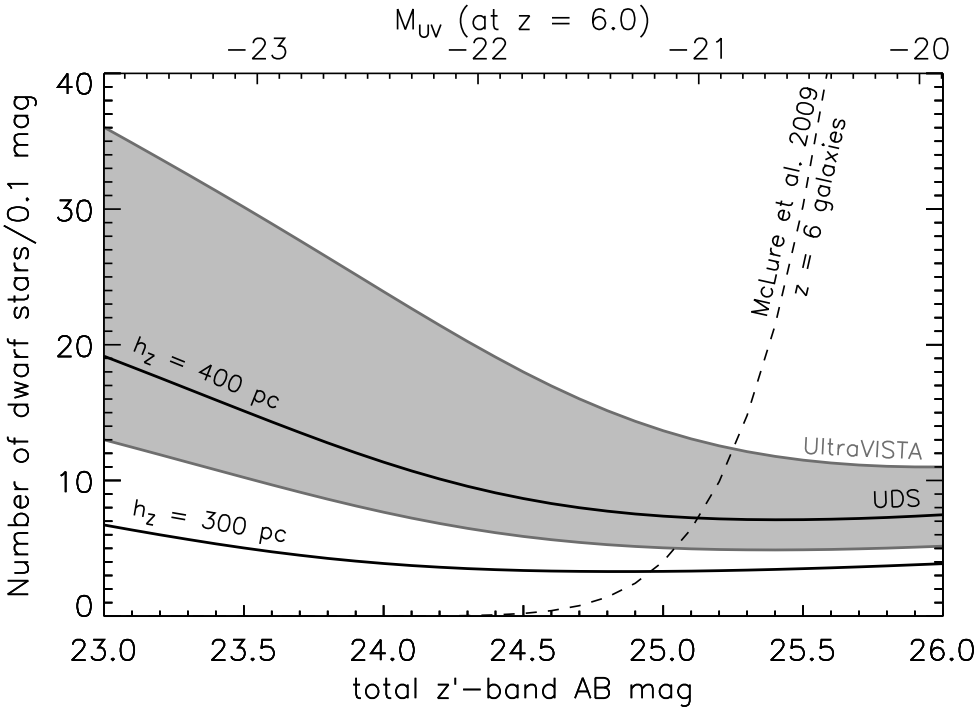

Figure 4.2 *The total number of dwarf stars (with spectral types M4–T8) predicted in the* $0.62\,deg^2$ *UltraVISTA/COSMOS DR2 field is shown as the grey shaded region, and the corresponding values for the* $0.74\,deg^2$ *UDS/SXDS field are shown as the black lines. The lower and upper curves for each field were calculated assuming a scale height of* $h_Z = 300\,\mathrm{pc}$ *and* $h_Z = 400\,\mathrm{pc}$ *respectively, using the exponential disk model of Caballero et al. (2008). The predicted number densities of* $z = 6$ *LBGs determined from the LF of McLure et al. (2009) is shown as the dashed line, for an example survey area of* $0.7\,deg^2$*. The upper axis shows as estimate of the absolute UV magnitude corresponding to the continuum magnitude on the lower axis, assuming the object is at* $z = 6$*.*

as a function of magnitude is required.

The dwarf stars relevant for high-redshift galaxy studies are typically distant objects in Galactic terms, e.g. an M4 dwarf star with observed magnitude $z' = 26$–24 probes the galaxy at a radius of 1.5–$4\,\mathrm{kpc}$ (or 250–600 pc for a T8 dwarf), and determining the scale height of the disk components is challenging. Previous searches for M, L and T-type stars have commonly assumed a single disk model (e.g. Holwerda et al., 2014; Ryan et al., 2011) to describe the observed number of stars, as the small samples of objects preclude a more complicated analysis. We follow such an approach using a single exponential disk model as described in Caballero et al. (2008). Here the number density of each dwarf star type s, as a function of galactic longitude and latitude (l, b) and heliocentric distance (d), is given by:

$$n_s = n_s(d=0)\,\mathrm{e}^{-\frac{R(d,l,b)-R_\odot}{h_\mathrm{R}}}\,\mathrm{e}^{-\frac{|Z_\odot+d\sin b|}{h_\mathrm{Z}}} \tag{4.1}$$

where $R_\odot$ and $Z_\odot$ denote the Galactocentric solar radius and height above the galactic disk, and h_R and h_Z are the radial scale length and scale height for the model. We use the approximations to Equation 4.1 outlined in Caballero et al. (2008) relevant for deep extragalactic survey fields, and predict the number density of each spectral type as a function of magnitude by integrating along a line-of-sight through the galactic disk. The local number densities and stellar absolute magnitudes (M_I) were taken from Caballero et al. (2008), converting the magnitudes from the Vega to AB system according to Frei & Gunn (1994). We then calculated the absolute z'-band magnitude from M_I using the $i-J$ colours from Caballero et al. (2008) and the standard spectral templates described in Section 4.3.2 to convert from M_J to M_z. We adopt the main parameters of the galactic thin disk model from Chen et al. (2001), with $Z_\odot = 27 \pm 4$pc, $R_\odot = 8600 \pm 200$pc and $h_\mathrm{R} = 2250 \pm 1000$ pc. The most relevant quantity for this study is the galactic vertical scale height, where we use two values at $h_\mathrm{Z} = 300\,\mathrm{pc}$ and $h_\mathrm{Z} = 400\,\mathrm{pc}$ to reflect the uncertainty in this quantity (Holwerda et al., 2014; Ryan et al., 2011; Pirzkal et al., 2009). Fig. 4.2 shows the predicted number of dwarf stars as a function of magnitude in the two fields. The analytic model shows that we expect more dwarf stars in the UltraVISTA/COSMOS field (galactic coordinates $b = 42.1$, $l = 236.8$) despite the smaller area covered (area of DR2 = 0.62 deg^2 vs. UDS = 0.74 deg^2), due to the line of sight intersecting with more of the galactic disk and being at a lower galactic latitude to the UDS/SXDS ($b = -60.0$, $l = 169.9$). The intersection of a pencil beam survey with this exponentially-declining distribution results in each dwarf star spectral type (which has a corresponding intrinsic absolute magnitude, $M_{J,\mathrm{AB}} \sim 9$–17 for spectral types M4–T8) having a peak in number density at an increasingly faint apparent magnitude,

with M-dwarfs peaking at $z' < 23$, L-dwarfs at $z' \simeq 25$ and T-dwarfs at $z' > 26$.

4.4.3 Predicted number of contaminant brown dwarfs

By combining the predicted number densities of dwarf stars illustrated in Fig. 4.2 with the probability of a given dwarf stellar type of a given magnitude passing the LBG selection criterion (from the simulations described in Section 4.4.1), we can predict the number of contaminant brown dwarfs expected in our $z \simeq 6$ sample. The expected redshift distribution for these stars can also be calculated and is shown in Fig. 4.3, assuming a vertical scale height of $h_{\rm Z} = 400$ pc to provide an upper limit on the number of objects. Within the UltraVISTA DR2 area we would predict a total of 2–7 dwarf stars with $h_{\rm Z} = 300$–400 pc, and in the UDS this drops to 0.1–0.4. Applying a $\chi^2_\star > 10.0$ condition to exclude objects with good stellar fits, the number of contaminant stars drops dramatically to 0.1–0.4 in UltraVISTA DR2 and 0.02-0.06 in the UDS samples as shown in the lower panel of Fig. 4.3. The predicted redshift distribution for the contaminant stars also illustrates the differences between the selection functions of the two fields. Most notably, the UDS field is more prone to contamination by late type dwarfs, such as L- and T-types, as a result of the deep optical imaging excluding early type M-dwarfs, and the shallower Y-band imaging making the separation of a sharp break and the gentle rise of a dwarf star through the z', Y and J filters difficult to distinguish. These late-type dwarves have higher photometric redshifts when identified as LBG candidates, and hence are excluded as part of our selection procedure for $5.5 < z < 6.5$ objects. The UltraVISTA/COSMOS field is more prone to contamination by M-dwarf stars, due to the shallower optical data available in the field. The lack of dwarf stars showing a best-fitting redshift in the range $5.7 < z_{\rm phot} < 6.1$ arises due to stellar templates being unable to reproduce the resulting large $i - z'$ colour produced from an LBG in this redshift range, this is clearly seen in the example SEDs shown in Fig 4.4. McLure et al. (2009) restricted the redshift range of their sample of $z \sim 6$ LBGs to the range $5.7 < z < 6.3$, which our simulations show is also a relatively clean dwarf star region.

In summary, our simulations would suggest a ~ 3 per cent contamination of our initial sample, which can be reduced to $\ll 1$ object by ensuring all galaxy candidates have a bad stellar fit (with $\chi_\star > 10.0$). Imposing a $\chi_\star > 10.0$ condition on our penultimate sample resulted in the removal of 37 and 10 objects from the UltraVISTA DR2 and UDS fields respectively, corresponding to ~ 20 per cent of the initial sample. Inspection of the χ^2 values for the stellar and galaxy fits for objects removed from the sample as

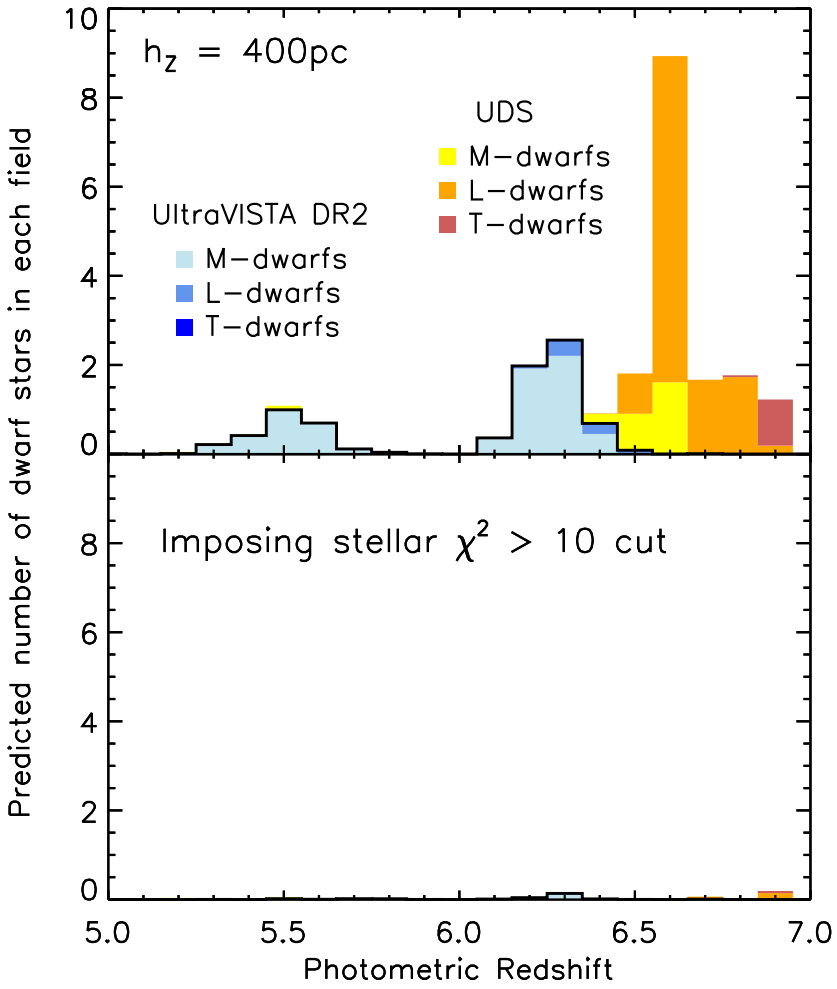

Figure 4.3 *The expected photometric redshift distribution of dwarf stars that are acceptable $z > 5$ LBG candidates in the UltraVISTA DR2 and UDS fields. The UltraVISTA DR2 results are shown as the blue histograms with a thick black outline, where each stellar type is highlighted in a different shade of blue, whereas the distribution for the UDS is shown in yellow and orange. A vertical scale height of $h_Z = 400$ pc is assumed to illustrate an upper limit on the number of potential stellar contaminants. The upper panel shows the predicted number of brown dwarfs in our sample when no attempt is made to remove objects with good stellar fits. By requiring that the objects have a poor stellar fit, with $\chi^2_\star > 10.0$, the expected number of contaminant brown dwarfs in the sample drops essentially to zero as shown in the lower panel.*

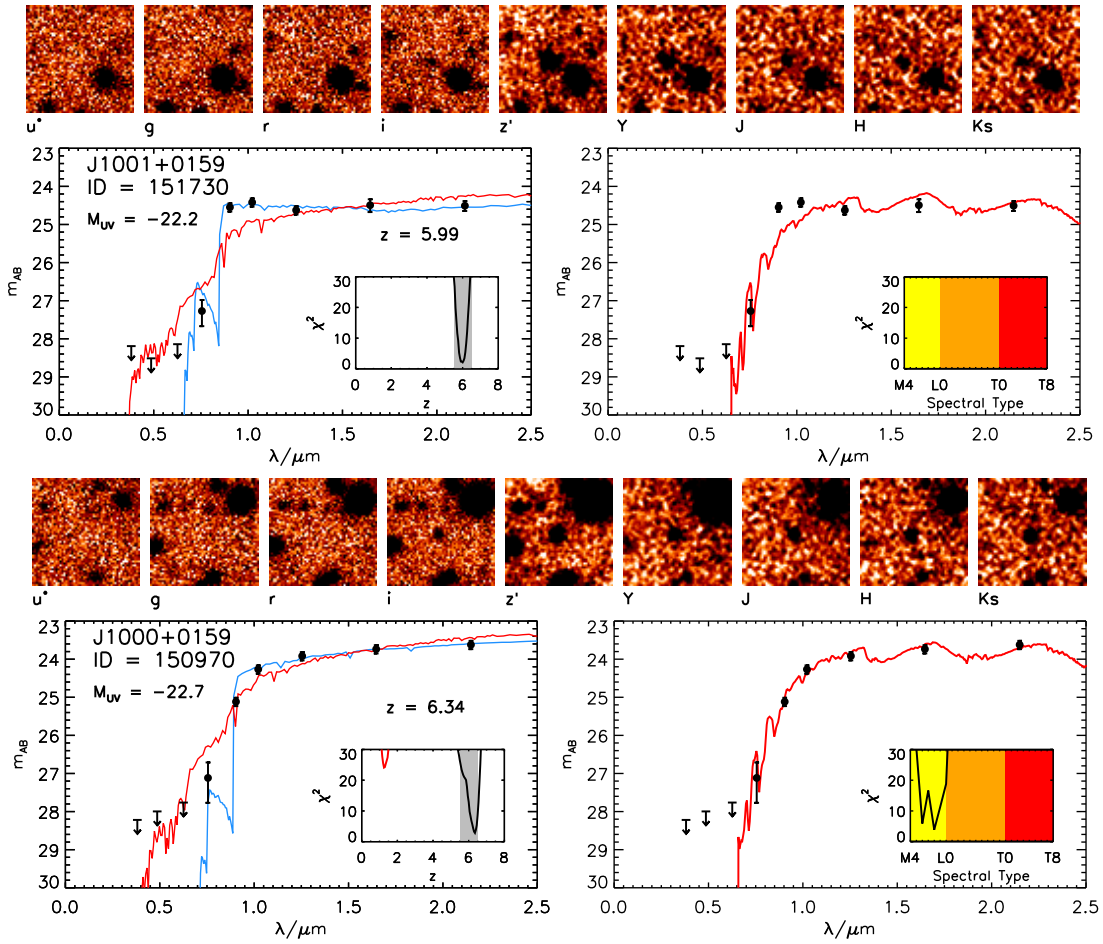

Figure 4.4 *SED fitting results and cut-out images of two objects from our penultimate sample of $z \simeq 6$ galaxies. For each object cut-outs (10-arcsec on the side) from the images are shown in the upper panels. The two plots show the observed photometry as the black points, with the best fitting high and low-redshift galaxy templates shown as the blue and red lines in the left-hand panel, and the best-fitting stellar template shown in the right-hand panel. The inset in each plot shows the distribution of χ^2 with either redshift or stellar spectral-type. The upper object at $z \simeq 6$ shows a clear break between the i and z'-bands that cannot be recreated by the low-redshift galaxy or stellar templates. The lower object however, is both a good stellar and high-redshift galaxy fit, illustrating the difficulty in removing stars in particular at $z > 6.3$ and $z < 5.7$, where the optical to near-infrared break appears more gradual. The lower object was removed from our final sample based on a good stellar fit (taken as $\chi^2_\star < 10.0$).*

potential stars (shown in Table 4.1), reveals that many of these objects are relatively poor stellar fits with $\chi^2_\star \sim 5$–9. Therefore we are likely excluding genuine galaxies by imposing such a cut, a hypothesis supported by the redshift distribution of our sample shown in Fig. 4.6, which after the imposition of a $\chi^2_\star > 10.0$ condition the distribution shows a deficit of objects at $5.5 < z < 5.7$ as compared to our expected distribution. The deficit is particularly obvious in the UDS field, and inspection of the $\chi^2_\star$ values for the objects classified as stars reveals that they are all > 5. This incompleteness is taken into account in our injection and recovery simulations, however to ensure that dwarf star contamination and our removal methodology has a minimum impact on our LF determination, we choose to restrict our redshift range to $5.7 < z < 6.3$ in the LF analysis. Such a redshift restriction also reduces the impact of the evolving LF on our analysis and makes the median redshift ($z_{\rm med} \simeq 5.9$) more in-line with previous determinations (McLure et al., 2009; Willott et al., 2013).

4.4.4 Thick disk and halo terms

Pirzkal et al. (2009) selected a sample of M-dwarf stars from within the Great Observatories Origins Deep Survey North and South fields (GOODS-N and GOODS-S) using slit less grism data from the Probing Evolution and Reionization Spectroscopically (PEARS) program, finding an average scale height of $h_{\rm thin} = 370^{+60}_{-65}$ pc for types M4–M9 when fitting a single thin disk model. However Pirzkal et al. (2009) note that they can better fit the number counts by including a thin disk and halo term, where the thin disk scale height is $h_{\rm thick} = 1000$ pc. The limiting depth of the Pirzkal et al. (2009) sample is $z = 25.0$ and therefore the constraints on the thick disk scale-height and the relative contributions of the thick disk and halo, compared to the thick disk, are fairly weak.

There is also a known discrepancy between the observed number counts between the North and South GOODS fields, with the GOODS-N fields found to contain 24% more stars (Pirzkal et al., 2009; Stanway et al., 2008a). However, it is unclear whether the boosted number counts applies to other fields particular for the late type dwarfs of interest to this study (Holwerda et al., 2014). Finally, using multiple independent sitelines through the Milky Way, Holwerda et al. (2014) found evidence for sub-structure in the Milky Way as traced by M-dwarfs on scales of ~ 4.5 arcmin^2 (the field-of-view of WFC3/IR on *HST*). Therefore, it is possible that there may be density fluctuations in the stellar disk in addition to the simple galaxy model we use here.

Table 4.1 *High-redshift galaxy candidates that were excluded based on a good fit to a stellar template (defined as $\chi^2_\star < 10.0$). Objects have been ordered by their best-fitting galaxy photometric redshift and separated by field (UltraVISTA/COSMOS DR2 in the upper part of the table, followed by objects in the UDS/SXDS). Note that the brightest object (S1) formally has a bad stellar fit, however this object is clearly stellar from inspection of the SED fit. The large $\chi^2_\star$ here is a result of the limited template set available and high-S/N photometry.*

ID	RA	Dec.	i	z'	Y	J	H	K	Star type	$\chi^2_{\rm star}$	$z_{\rm phot}$	$\chi^2_{\rm gal}$
S1	10:00:10.71	+02:06:37.1	$27.2^{+0.6}_{-0.4}$	$23.8^{+0.1}_{-0.1}$	$22.6^{+0.1}_{-0.1}$	$21.6^{+0.1}_{-0.1}$	$21.0^{+0.1}_{-0.1}$	$20.7^{+0.1}_{-0.1}$	L8	27.5	6.4	11.1
S2	10:00:23.90	+01:59:05.6	$27.1^{+0.7}_{-0.4}$	$25.1^{+0.1}_{-0.1}$	$24.3^{+0.1}_{-0.1}$	$23.9^{+0.1}_{-0.1}$	$23.7^{+0.1}_{-0.1}$	$23.6^{+0.1}_{-0.1}$	M8	3.9	6.3	2.9
S3	10:00:09.93	+02:22:07.2	> 27.0	$25.5^{+0.1}_{-0.1}$	$25.1^{+0.3}_{-0.2}$	$24.5^{+0.3}_{-0.3}$	$25.1^{+0.5}_{-0.4}$	> 25.5	M4	6.7	6.3	4.8
S4	10:02:14.87	+02:11:04.9	$26.8^{+0.4}_{-0.3}$	$24.9^{+0.1}_{-0.1}$	$24.2^{+0.1}_{-0.1}$	$23.9^{+0.1}_{-0.1}$	$24.0^{+0.1}_{-0.1}$	$23.7^{+0.1}_{-0.1}$	M7	9.0	6.2	4.9
S5	09:58:56.08	+02:35:08.1	> 27.3	$24.9^{+0.1}_{-0.1}$	$24.1^{+0.1}_{-0.1}$	$23.2^{+0.1}_{-0.1}$	$22.7^{+0.1}_{-0.1}$	$22.3^{+0.1}_{-0.1}$	L8	4.6	6.2	9.6
S6	09:58:42.41	+02:26:06.7	$26.9^{+0.5}_{-0.3}$	$24.8^{+0.1}_{-0.1}$	$24.3^{+0.1}_{-0.1}$	$23.9^{+0.1}_{-0.1}$	$24.0^{+0.2}_{-0.1}$	$23.9^{+0.1}_{-0.1}$	M7	7.0	6.2	5.4
S7	10:02:07.38	+02:25:44.1	> 27.4	$25.6^{+0.1}_{-0.1}$	$25.3^{+0.3}_{-0.2}$	$24.7^{+0.2}_{-0.2}$	$24.6^{+0.3}_{-0.2}$	$25.0^{+0.3}_{-0.2}$	M7	3.0	6.2	4.1
S8	10:02:02.78	+02:24:00.0	$27.1^{+0.7}_{-0.4}$	$25.0^{+0.1}_{-0.1}$	$24.5^{+0.2}_{-0.1}$	$24.4^{+0.1}_{-0.1}$	$24.1^{+0.2}_{-0.1}$	$24.4^{+0.2}_{-0.2}$	M7	6.5	6.2	3.5
S9	10:00:53.64	+02:09:45.5	> 27.9	$25.7^{+0.1}_{-0.1}$	$25.3^{+0.2}_{-0.2}$	$24.8^{+0.2}_{-0.2}$	$25.3^{+0.5}_{-0.3}$	$25.2^{+0.4}_{-0.3}$	M7	8.6	6.2	3.7
S10	10:00:45.18	+02:31:40.3	> 27.3	$25.6^{+0.1}_{-0.1}$	$25.1^{+0.1}_{-0.1}$	$25.1^{+0.4}_{-0.3}$	$25.1^{+0.6}_{-0.4}$	$25.1^{+0.3}_{-0.2}$	M7	9.7	6.2	0.1
S11	09:58:45.50	+02:23:24.7	> 27.6	$25.4^{+0.2}_{-0.1}$	$25.2^{+0.3}_{-0.2}$	$24.5^{+0.2}_{-0.2}$	$24.8^{+0.3}_{-0.3}$	$25.1^{+0.4}_{-0.3}$	M7	9.1	6.2	5.7
S12	09:58:45.02	+02:29:04.3	> 26.2	$25.7^{+0.2}_{-0.1}$	> 25.4	> 25.6	> 25.2	> 25.0	M4	5.6	5.9	1.2
S13	10:01:55.84	+02:37:51.9	> 27.7	$25.7^{+0.1}_{-0.1}$	$25.7^{+0.4}_{-0.3}$	$24.9^{+0.3}_{-0.2}$	$24.7^{+0.2}_{-0.2}$	$24.6^{+0.2}_{-0.2}$	M7	6.5	5.7	1.9
S14	09:59:29.41	+01:46:40.3	$27.4^{+0.7}_{-0.4}$	$25.4^{+0.1}_{-0.1}$	$25.1^{+0.3}_{-0.2}$	$25.1^{+0.4}_{-0.3}$	$25.1^{+0.5}_{-0.3}$	$25.1^{+0.5}_{-0.4}$	M5	9.4	5.7	1.1
S15	10:02:00.39	+02:23:52.3	> 27.1	$25.6^{+0.1}_{-0.1}$	$25.8^{+0.6}_{-0.4}$	$25.5^{+0.4}_{-0.3}$	> 25.7	> 25.5	M4	8.2	5.7	0.5
S16	09:58:53.79	+02:22:37.1	> 26.8	$25.2^{+0.1}_{-0.1}$	$24.9^{+0.2}_{-0.2}$	$24.6^{+0.2}_{-0.2}$	$24.3^{+0.2}_{-0.2}$	$24.2^{+0.1}_{-0.1}$	M5	5.9	5.7	0.5
S17	09:59:15.77	+01:51:06.2	> 27.5	$25.7^{+0.1}_{-0.1}$	$25.9^{+0.4}_{-0.3}$	$25.3^{+0.3}_{-0.2}$	$24.9^{+0.3}_{-0.3}$	$25.0^{+0.3}_{-0.3}$	M5	9.9	5.7	2.0

S18	09:59:07.45	+02:35:03.2	$27.0^{+0.4}_{-0.3}$	$25.3^{+0.1}_{-0.1}$	$25.0^{+0.2}_{-0.1}$	$24.9^{+0.2}_{-0.2}$	$24.3^{+0.2}_{-0.2}$	$24.8^{+0.2}_{-0.2}$	M5	9.0	5.7	6.2
S19	10:00:07.62	+02:21:25.0	$26.7^{+0.5}_{-0.3}$	$25.4^{+0.1}_{-0.1}$	$25.4^{+0.4}_{-0.3}$	> 25.2	> 25.1	> 25.3	M4	8.9	5.7	0.9
S20	10:02:18.39	+02:20:25.9	$26.9^{+0.4}_{-0.3}$	$25.2^{+0.1}_{-0.1}$	$24.8^{+0.2}_{-0.1}$	$24.6^{+0.2}_{-0.1}$	$24.4^{+0.2}_{-0.2}$	$24.6^{+0.2}_{-0.2}$	M5	3.4	5.7	6.0
S21	10:01:42.49	+02:38:24.0	$26.5^{+0.3}_{-0.2}$	$24.8^{+0.1}_{-0.1}$	$24.6^{+0.2}_{-0.2}$	$24.3^{+0.1}_{-0.1}$	$24.3^{+0.2}_{-0.2}$	$24.4^{+0.2}_{-0.2}$	M5	7.6	5.6	4.0
S22	10:01:47.42	+02:06:18.9	$27.0^{+0.6}_{-0.4}$	$25.5^{+0.1}_{-0.1}$	$25.6^{+0.2}_{-0.2}$	$25.2^{+0.3}_{-0.3}$	$25.4^{+0.6}_{-0.4}$	$25.4^{+0.4}_{-0.3}$	M4	8.3	5.6	1.0
S23	10:01:54.85	+02:33:33.4	$27.3^{+0.7}_{-0.4}$	$25.5^{+0.1}_{-0.1}$	$25.2^{+0.3}_{-0.2}$	$25.1^{+0.4}_{-0.3}$	$25.0^{+0.4}_{-0.3}$	$24.6^{+0.3}_{-0.2}$	M5	6.4	5.6	0.7
S24	09:58:44.72	+02:25:37.2	$27.1^{+0.5}_{-0.3}$	$25.6^{+0.2}_{-0.1}$	$25.5^{+0.3}_{-0.3}$	$25.4^{+0.4}_{-0.3}$	> 25.5	$25.4^{+0.4}_{-0.3}$	M4	5.5	5.6	0.6
S25	10:00:38.46	+01:56:22.3	$26.6^{+0.2}_{-0.2}$	$25.2^{+0.1}_{-0.1}$	$24.8^{+0.1}_{-0.1}$	$24.5^{+0.2}_{-0.1}$	$24.5^{+0.2}_{-0.2}$	$24.8^{+0.2}_{-0.2}$	M5	4.9	5.6	9.9
S26	09:58:41.39	+02:23:03.7	$26.9^{+0.3}_{-0.2}$	$25.4^{+0.1}_{-0.1}$	$25.2^{+0.3}_{-0.2}$	$25.5^{+0.7}_{-0.4}$	$25.1^{+0.4}_{-0.3}$	$25.2^{+0.4}_{-0.3}$	M4	7.7	5.5	1.6
S27	10:01:35.94	+02:23:03.3	$27.0^{+0.4}_{-0.3}$	$25.5^{+0.1}_{-0.1}$	$25.2^{+0.3}_{-0.3}$	$24.5^{+0.2}_{-0.2}$	$24.9^{+0.4}_{-0.3}$	> 25.1	M5	4.8	5.5	7.7
S28	10:02:15.54	+02:36:46.9	$26.8^{+0.3}_{-0.2}$	$25.7^{+0.1}_{-0.1}$	$25.4^{+0.2}_{-0.2}$	$25.8^{+0.6}_{-0.4}$	$25.1^{+0.7}_{-0.4}$	> 25.8	M4	7.5	5.5	5.2
S29	10:02:25.51	+02:33:32.1	$26.7^{+0.3}_{-0.2}$	$25.4^{+0.1}_{-0.1}$	$24.9^{+0.3}_{-0.2}$	$24.5^{+0.3}_{-0.2}$	$24.7^{+0.3}_{-0.2}$	> 25.3	M5	7.3	5.5	10.0
S30	10:02:21.87	+02:24:01.0	$26.7^{+0.4}_{-0.3}$	$25.3^{+0.1}_{-0.1}$	$25.2^{+0.4}_{-0.3}$	$25.4^{+0.7}_{-0.4}$	$25.1^{+0.5}_{-0.4}$	$24.7^{+0.3}_{-0.2}$	M4	7.7	5.5	1.8
S31	10:00:08.43	+02:20:49.1	$26.8^{+0.4}_{-0.3}$	$25.3^{+0.1}_{-0.1}$	$25.6^{+0.5}_{-0.3}$	$25.2^{+0.4}_{-0.3}$	$25.0^{+0.6}_{-0.4}$	$25.1^{+0.4}_{-0.3}$	M4	7.5	5.5	0.9
S32	10:02:05.41	+02:14:46.4	$26.9^{+0.5}_{-0.3}$	$25.5^{+0.1}_{-0.1}$	$25.5^{+0.3}_{-0.2}$	$25.0^{+0.2}_{-0.2}$	$25.3^{+0.6}_{-0.4}$	$25.1^{+0.3}_{-0.3}$	M4	5.6	5.5	2.1
S33	10:01:40.07	+02:11:51.1	$27.0^{+0.3}_{-0.3}$	$25.7^{+0.1}_{-0.1}$	$25.6^{+0.4}_{-0.3}$	$25.5^{+0.5}_{-0.4}$	> 25.4	> 25.6	M4	6.7	5.5	1.0
S34	10:02:22.64	+01:51:57.1	$26.7^{+0.4}_{-0.3}$	$25.5^{+0.2}_{-0.2}$	> 25.3	> 25.5	> 25.1	> 24.9	M4	4.8	5.5	1.5
S35	10:00:24.21	+02:39:07.2	$26.8^{+0.4}_{-0.3}$	$25.6^{+0.1}_{-0.1}$	$25.5^{+0.3}_{-0.2}$	$25.0^{+0.2}_{-0.2}$	> 25.6	> 25.6	M4	6.5	5.5	4.9
S36	10:01:33.84	+02:03:30.9	$26.7^{+0.5}_{-0.3}$	$25.7^{+0.1}_{-0.1}$	> 25.8	> 25.5	> 25.3	> 24.7	M4	7.8	5.5	2.2
S37	09:59:08.92	+01:50:50.7	$24.7^{+0.1}_{-0.1}$	$23.5^{+0.1}_{-0.1}$	$23.1^{+0.1}_{-0.1}$	$22.8^{+0.1}_{-0.1}$	$22.9^{+0.1}_{-0.1}$	$22.9^{+0.1}_{-0.1}$	M5	9.9	5.5	10.3
S38	02:18:01.62	-04:52:22.3	$27.4^{+0.4}_{-0.3}$	$25.4^{+0.1}_{-0.1}$	$24.6^{+0.2}_{-0.2}$	$24.1^{+0.1}_{-0.1}$	$24.2^{+0.1}_{-0.1}$	$24.0^{+0.1}_{-0.1}$	M8	6.8	6.4	6.1
S39	02:16:13.17	-04:51:40.5	$27.4^{+0.5}_{-0.3}$	$25.4^{+0.1}_{-0.1}$	$24.8^{+0.2}_{-0.2}$	$24.1^{+0.1}_{-0.1}$	$24.1^{+0.1}_{-0.1}$	$23.9^{+0.1}_{-0.1}$	M8	5.4	6.3	9.3
S40	02:19:36.16	-05:03:16.2	> 27.8	$25.5^{+0.1}_{-0.1}$	$24.9^{+0.2}_{-0.2}$	$23.8^{+0.1}_{-0.1}$	$23.7^{+0.1}_{-0.1}$	$23.2^{+0.1}_{-0.1}$	L4	7.9	6.3	11.0

S41	02:16:50.79	-05:28:44.5	$26.8^{+0.3}_{-0.2}$	$25.6^{+0.1}_{-0.1}$	$25.1^{+0.4}_{-0.3}$	$25.3^{+0.2}_{-0.1}$	$25.6^{+0.5}_{-0.3}$	$25.5^{+0.4}_{-0.3}$	M4	9.7	5.6	3.5
S42	02:17:40.34	-04:40:06.4	$26.5^{+0.1}_{-0.1}$	$25.1^{+0.1}_{-0.1}$	$25.0^{+0.3}_{-0.2}$	$24.6^{+0.1}_{-0.1}$	$24.5^{+0.2}_{-0.2}$	$24.4^{+0.1}_{-0.1}$	M5	8.2	5.6	1.3
S43	02:18:17.95	-05:25:47.9	$26.8^{+0.2}_{-0.2}$	$25.7^{+0.2}_{-0.1}$	> 25.6	$25.6^{+0.3}_{-0.3}$	> 25.6	$26.1^{+0.6}_{-0.4}$	M4	7.1	5.5	0.6
S44	02:17:06.25	-04:49:21.6	$26.7^{+0.2}_{-0.2}$	$25.6^{+0.1}_{-0.1}$	$25.6^{+0.5}_{-0.3}$	$25.7^{+0.3}_{-0.3}$	> 25.5	$25.8^{+0.6}_{-0.4}$	M4	9.5	5.5	0.3
S45	02:16:38.53	-05:02:08.2	$26.8^{+0.2}_{-0.2}$	$25.7^{+0.1}_{-0.1}$	$25.4^{+0.3}_{-0.2}$	$25.7^{+0.4}_{-0.3}$	$25.4^{+0.4}_{-0.3}$	$25.6^{+0.5}_{-0.3}$	M4	7.1	5.5	0.9
S46	02:19:09.36	-04:40:00.4	$26.3^{+0.1}_{-0.1}$	$25.2^{+0.1}_{-0.1}$	$25.5^{+0.5}_{-0.3}$	$25.0^{+0.2}_{-0.2}$	$24.9^{+0.3}_{-0.2}$	$25.2^{+0.3}_{-0.2}$	M4	8.1	5.5	2.2
S47	02:17:32.33	-04:39:36.4	$26.9^{+0.2}_{-0.2}$	$25.7^{+0.1}_{-0.1}$	$25.7^{+0.5}_{-0.3}$	$25.7^{+0.4}_{-0.3}$	$24.9^{+0.3}_{-0.2}$	$25.4^{+0.4}_{-0.3}$	M4	8.6	5.5	3.4

4.5 The sample

The final sample of $5.5 < z < 6.5$ galaxies consists of 266 objects, with 156, 3 and 107 coming from the the UltraVISTA/COSMOS DR2, DR1 and UDS/SXDS fields respectively. In the reduced redshift range $5.7 < z < 6.3$ used by McLure et al. (2009), we find 105, 2 and 70 objects in these fields. We postpone a full discussion of the SED properties and sizes of these objects to a future paper (Bowler et al. in prep), however the basic sample properties are discussed below.

4.5.1 Galaxy colours

Galaxies at $z \sim 6$ are typically selected as i-band dropout objects, and in Fig. 4.5 we show the $i - z'$ colour (which straddles the break at $z \simeq 5.8$) against the $z' - Y$ colour (which determines the rest-frame UV colour) of our sample of galaxies selected by their photometric redshift. Both the UltraVISTA/COSMOS and UDS/SXDS samples occupy a similar region of colour space, indicating no strong biases in the galaxy colours due to the different relative imaging depths. The colours of the objects can be reproduced by Bruzual & Charlot (2003) models with $A_V = 0.0$–0.5 within the errors, with no strong evidence for extremely red objects (to be compared with the stack of $z \sim 6$ galaxies found by Willott et al., 2013 which had a best-fitting $A_V = 0.75$, as discussed further in Section 4.5.5). We also show the colours of the possible dwarf stars excluded from our sample, along with the stellar locus as derived from stellar spectra compiled by Findlay et al. (2012). Several of these objects do lie on the stellar locus, however a considerable fraction are found with colours differing by up to $\simeq 0.5$ mag. The results of the injection and recovery simulations described in Section 4.4 showed that the majority of dwarf stars enter our LBG sample as a result of scattering of the photometry, hence a wide range of colours for potential dwarf stars is to be expected. The identification of potential stellar contaminants that would have identical colours to LBGs illustrates the power of using the full multiwavelength photometry, as several of the likely dwarf stars would be indistinguishable from LBGs based on a simple colour selection. Furthermore, Fig. 4.5 clearly shows that if a strict colour selection for $z \sim 6$ objects, designed to remove dwarf star candidates, was implemented, the true colour distribution of LBGs would have been biased to bluer objects.

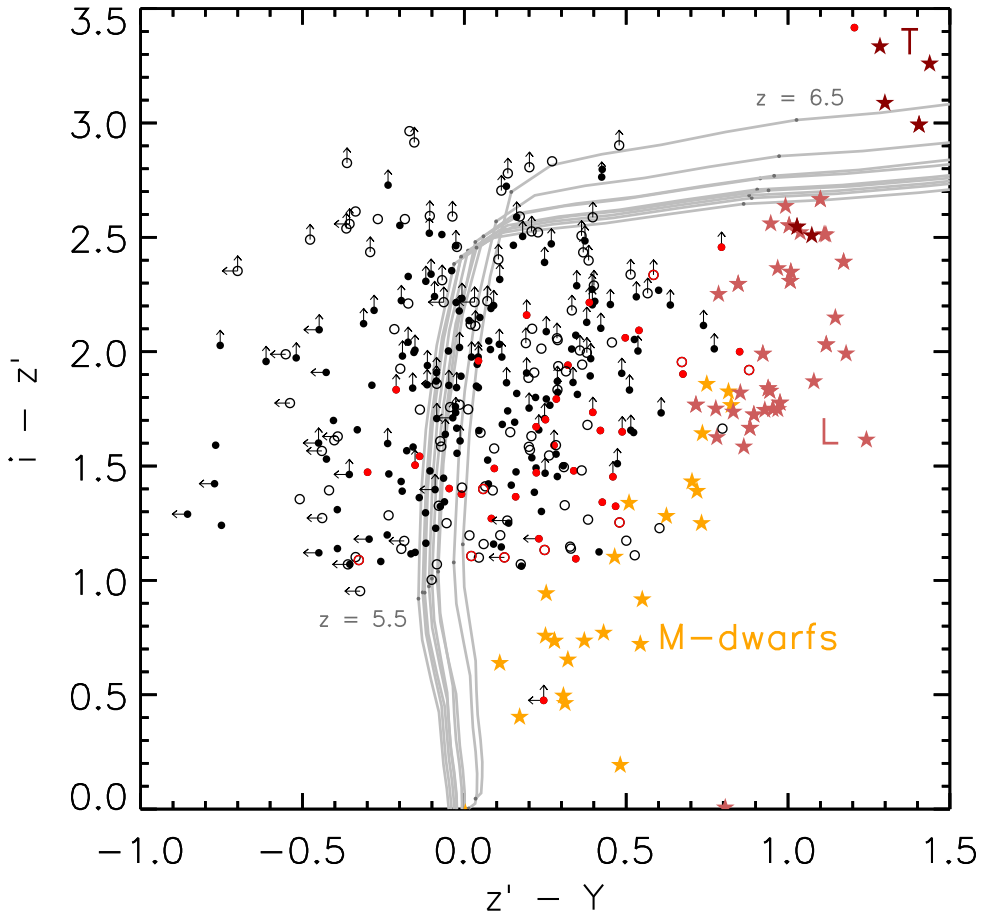

Figure 4.5 *The $z' - Y$ vs. $i - z'$ colours of the full $5.5 < z < 6.5$ sample. The colours derived from high-redshift galaxy SEDs (shown as grey tracks) and the colours of galactic dwarf stars (star symbols) are shown for comparison. The galaxy sample is shown as the black points, with the UltraVISTA/COSMOS and UDS/SXDS galaxies shown as the filled and open circles respectively. Objects that were excluded from these samples as possible brown dwarfs are shown as the red points. Error bars have been omitted for clarity but are typically $\sim 0.2 - 0.5$ mag, and where an object is detected at less than the 2σ-level in a given filter the magnitude here is set to the local 2σ depth, and we display the colour as a limit using an arrow. The M-, L- and T-dwarf star colours were calculated from spectra taken from the compilation of stellar spectra described in Findlay et al. (2012). High-redshift LBG colours taking from Bruzual & Charlot (2003) models are shown as the grey lines (constant star-formation history, $Z = 0.2\,Z_{\odot}$, $A_V = 0.0 - 0.5$, age = $50 - 500\,Myr$).*

4.5.2 Redshift, $M_{\rm UV}$ and $m_{\rm AB}$ distributions

In Fig. 4.6 we show the redshift distribution for our full sample of $5.5 < z < 6.5$ LBGs, and the $M_{\rm UV}$ and $m_{\rm AB}$ distributions in the restricted redshift range ($5.7 < z < 6.3$) to allow a direct comparison with our LF determination. In each panel, predicted distributions from the simulations described in Section 4.6.1 for an evolving LF model are shown. For each simulated distribution, the number of galaxies predicted by a linearly evolving model according to a Schechter function (derived from Bouwens et al. 2014 or McLure et al. 2009) or a DPL function (derived from Bowler et al. 2014) were injected into the images, and the resulting $z_{\rm phot}$, $M_{\rm UV}$ and $m_{\rm AB}$ histograms are displayed. The LF determinations of Bouwens et al. (2014) over-predicts the number of galaxies we should find by around a factor of two, whereas the LF determinations of McLure et al. (2009) and Bowler et al. (2014) show a better agreement with the final sample. Splitting the sample by field (middle and lower panel for the UltraVISTA/COSMOS and UDS/SXDS samples respectively) reveals an excess of galaxies in the UltraVISTA/COSMOS field as opposed to the McLure et al. (2009) and Bowler et al. (2014) models, which is present over a range of redshifts and absolute magnitudes. In both fields there exist more $M_{\rm UV} < -22.0$ galaxies than predicted by the Schechter function model of McLure et al. (2009).

The redshift distribution differs from the model prediction, with a flatter distribution than expected. Some of the flattening could be a result of too strictly removing galaxy candidates that have good stellar fits, which would cause a drop in the number of objects in the range $5.5 < z < 5.7$. However, the precise details of the form and evolution of the LF in the range $z = 5$–7 are not well constrained, and therefore the model predictions shown are rough estimates of the predicted distributions.

4.5.3 Cosmic variance between the fields

The galaxies in our sample are not uniformly spread between the UltraVISTA/COSMOS and UDS/SXDS fields. Given that the UltraVISTA DR2 region is only $\sim 84\,\%$ of the area of the UDS data, the discrepancy becomes more significant, with the ratio of the surface density between the UltraVISTA DR2 and the UDS $= 1.7$ (or 1.8 in the redshift range $5.7 < z < 6.3$). Here we compare the smaller DR2 region of the UltraVISTA field to the UDS, because they have similar depths in the near-infrared and were cut at an identical z'-band magnitude ($z' = 26.0$). The difference is present over a full range of redshifts and magnitudes as shown in Fig. 4.6. Correcting for the

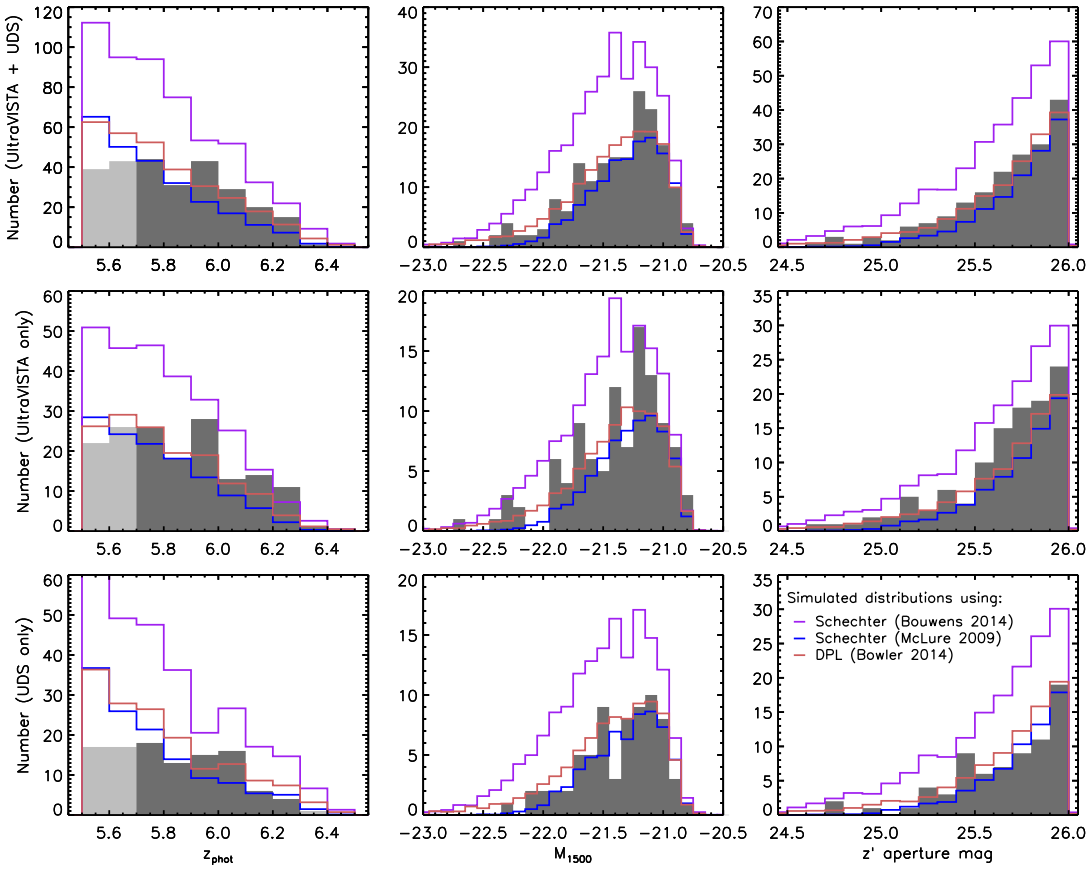

Figure 4.6 *The distributions of the $z \simeq 6$ galaxy sample with best-fitting photometric redshift, M_{1500} and observed z'-band aperture magnitude. The upper row of plots show the full sample, with the middle and lower rows showing the UltraVISTA/COSMOS and UDS/SXDS samples separately. The lines show the predicted distributions from the injection and recovery simulations described in Section 4.6.1, for evolving LF models derived from the Schechter function fits of McLure et al. (2009) and Bouwens et al. (2014) and the double power-law fits from Bowler et al. (2014) in blue, purple and orange respectively. In the $M_{\rm UV}$ and $m_{\rm AB}$ plots we show only the objects in the restricted redshift range $5.7 < z < 6.3$.*

different areas of the surveys and the different selection function, we find a surface density of 169 ± 13 or 95 ± 10 galaxies per deg^2 in the UltraVISTA/COSMOS and UDS/SXDS fields (Poisson errors). We calculated the predicted cosmic variance from the Cosmic Variance Calculator v1.02[3] (Trenti & Stiavelli, 2008) with a Sheth-Tormen halo MF, $\sigma_8 = 0.9$ and a unity halo filling factor. The result of the calculating was an expected cosmic variance on the average density of 132 ± 21 galaxies per deg^2. Hence the difference in number counts can just exceeds that expected due to the large scale structure variations over fields of this size.

The predicted number counts of brown dwarfs are higher in the UltraVISTA/COSMOS field as a result of the galactic coordinates, which if dwarf star contamination was significant, could produce a higher number of objects in our sample in this field. The simulations described in Section 4.4 show that dwarf stars can be effectively identified and removed using our stellar fitting procedure and furthermore, the expected redshift distribution of dwarf stars (shown in Fig. 4.3) does not match that observed in our sample. The strongest evidence for a genuine discrepancy between the number of objects between the two fields comes from considering the reduced redshift range, which cannot be dominated by stellar contamination due to the large $i - z'$ colour required. Restricting the redshift range of our sample to the dwarf star free region with $5.7 < z < 6.1$ results in 82, 2 and 61 objects in the UltraVISTA DR2, DR1 and UDS fields, producing a number density ratio of $= 1.6$.

We consider the possibility of gravitational lensing and further large scale structure effects that could be responsible for the field-to-field variance in Sections 4.6.4 and 4.7.2.

4.5.4 Overlap with previous studies

McLure et al. (2009) and Curtis-Lake et al. (2013)

The first search for $z \gtrsim 5$ galaxies using the UKIDSS UDS near-infrared imaging was undertaken by McLure et al. (2006), who found 9 massive $z \simeq 5$ galaxy candidates by combining the SXDS optical imaging with the J, H and K images from the UDS early data release. Using the subsequent release of the UKIDSS UDS imaging (DR1, which is ~ 1.5 mag shallower than the data utilised in this work), McLure et al. (2009) were able to calculate the bright-end of the LF at $z = 5$ and $z = 6$. In addition, the brightest

[3] `http://casa.colorado.edu/~trenti/CosmicVariance.html`

14 galaxies from the $z \simeq 6$ sample of McLure et al. (2009) in the range $6.0 < z < 6.5$ were targeted spectroscopically and the results were presented by Curtis-Lake et al. (2013) who detected Lyman-α emission in 11 of the objects. Comparing our sample of $z \simeq 6$ galaxies in the UDS, we find 8 of the 10 galaxies presented in Curtis-Lake et al. (2013). Inspection of our initial catalogues reveals that the two excluded objects, UUDS_J021922.01−045536.3 and UUDS_J021701.44−050309.4, were both removed because they are fainter than our imposed z'-band magnitude limit, with 1.8 arcsec aperture magnitudes of $z' = 26.2$ and $z' = 26.4$ respectively. The brightest object targeted by Curtis-Lake et al. (2013) was identified as a faint AGN based on the broad Lyα line (Willott et al., 2009). This object was excluded from our galaxy sample based on a $\chi^2 = 12.6$, which slightly exceeds our acceptable criterion. Closer inspection of the SED reveals that the poor galaxy fit is driven by an enhanced z'-band flux, as a result of strong Lyα emission at the very blueward edge of the z'-band filter (at $z = 6.01$), which contributes $\sim 70\%$ of the z'-band flux (Willott et al., 2009). The presence of strong Lyα emission sufficient to significantly change the redshift of a galaxy candidate in our sample is unlikely, as the space density of quasars is extremely low (e.g. one object in the full UDS area) and the most luminous LBGs exhibit significantly lower EWs ($EW_0 \ll 100$Å, Curtis-Lake et al., 2013; Stark et al., 2011).

Willott et al. (2013)

Using the $4\,\mathrm{deg}^2$ of multiwavelength imaging from the CFHTLS 'deep' component, Willott et al. (2013) found 40 i-band dropout galaxies at $z \sim 6$. The CFHTLS data consisted of u^*, g, r, i and z-band imaging in 4 separate MegaCam pointings, including the COSMOS field (D2) which is utilised in this work. Further near-infrared data from a variety of different observing programs in each field was also utilised for the selection of $z \simeq 6$ galaxies by Willott et al. (2013) where available. Willott et al. (2013) were sensitive to the very brightest $z \simeq 6$ galaxies, with a z-band magnitude limit of 25.3 (in a 2 arcsec diameter circular aperture), and the imposition of a strict $i - z > 2$ criterion resulted in a higher median redshift of the candidates with $z \gtrsim 5.8$ (see Fig. 4.5) . In our final $z \simeq 6$ sample we find 7 of the 15 galaxies presented in Willott et al. (2013) in the COSMOS/UltraVISTA field. One object was removed only in the final stage of potential star removal, where it was classified as a possible brown dwarf with $\chi^2_\star = 9.1$. Another object in the sample, WMH18, was not selected in our initial z'-band catalogue and inspection of the imaging shows that it is heavily blended with a low-redshift galaxy 3-arcsec away. The six further missing objects however, were initially selected in our sample but subsequently removed.

The removal of four of the objects (WMH11, WMH12, WMH19 and WMH21) is simply because they lie in the shallower DR1 region of UltraVISTA, where we applied a conservative magnitude limit of $z' < 25.0$. We nevertheless extracted the photometry for these objects and performed SED fitting as for our $z \simeq 6$ objects, finding that all the objects except WHM11 would indeed have been selected as high-redshift galaxies. WMH11 has low level flux in the optical bands and was excluded based on our local depth cuts in the u^* and g-bands.

Of the final two objects, WMH23 was also removed based on a marginal detection in the u^*-band, although the results of SED fitting of this object also show it to be a plausible high redshift candidate. We note here that occasionally genuine $z \simeq 6$ objects will be lost during our selection process as a result of our optical drop-out criterion; however this incompleteness is carefully simulated and included in our LF analysis. Finally, object WMH14 was excluded because it has a marginally unacceptable $\chi^2 = 12.6$, which exceeds our formal good fit criterion ($\chi^2 < 11.3$). Inspection of the imaging reveals the object to be close to a low-redshift companion, which is likely contaminating the photometry for this galaxy.

Two of the 15 objects presented in the $z \simeq 6$ sample from Willott et al. (2013) in the COSMOS field have spectroscopic confirmations, WMH13 at $z = 5.983$ and WMH15 at $z = 5.847$. Reassuringly we find $z_{\rm phot} = 5.92^{+0.13}_{-0.08}$ and $z_{\rm phot} = 5.99^{+0.09}_{-0.23}$ respectively.

In conclusion, we find good agreement with the bright sample of $z \simeq 6$ galaxies found in Willott et al. (2013) with 12 out of the 15 objects present being consistently classified as high-redshift galaxies here.

Bowler et al. (2014)

In Bowler et al. (2014), we presented a sample of $z \simeq 7$ LBGs found within the UltraVISTA/COSMOS and UDS/SXDS datasets utilised in this work. As part of the selection procedure, which was primarily aimed at finding $6.5 < z < 7.5$ galaxies, candidates with $z > 6$ were retained and presented if the presence of Lyα emission in the spectrum could shift the object into the primary redshift window. We therefore expect some overlap with the sample presented in Bowler et al. (2014). Taking the subset of the 34 objects presented in Bowler et al. (2014) that have $z' < 26.0$, we find 6 galaxies in the UltraVISTA field and 1 in the UDS (the spectroscopically confirmed LAE 'Himiko' at $z = 6.595$). Comparing to the $z \simeq 6$ sample, we find all 7 objects (Himiko was identified and removed from the final sample), with photometric redshifts

that agree within the errors. The full recovery of these objects in the present work is a strong vindication of our selection methodology, as the sample presented in Bowler et al. (2014) were selected in a different band (Y and J-band selected) and refined using a slightly different SED fitting analysis.

Narrow-band selected samples

In addition to the Subaru/SuprimeCam broad-band optical imaging, the UDS/SXDS field has also been the site of extensive narrow band photometric surveys with SuprimeCam. Narrow-band surveys select line emitters via a 'narrow-band excess', where the objects appears brighter in the narrow-band as compared to an encompassing broader band, with the sample refined to high-redshift galaxies using further broadband colour information across the putative Lyman break. Ouchi et al. (2005) selected $z = 5.7$ Lyman-α emitters (LAEs) from the $NB816$ imaging within the UDS, finding a total of 515 emitters with a surface density of $\Sigma = 0.14 \pm 0.01$ arcmin^{-2} (with an expected contamination rate of 30%). For comparison, we find a surface density of only 0.04 arcmin^{-2} in the UDS (0.07 arcmin^{-2} in the UltraVISTA DR2 field) over the full redshift range $5.5 < z < 6.5$. However, it is non-trivial to compare the two samples as narrow-band selection is based on an excess of flux over that from the broad band, and therefore selects objects that are fainter in the broad bands. Furthermore, the narrow band will select objects over a smaller redshift range ($z = 5.70 \pm 0.05$ for the $NB816$ filter) than that utilised in our study. The steep rise in number counts of objects to fainter z'-band magnitudes, coupled with the rise in prevalence of strong Lyman-α emission in fainter objects, implies that the narrow-band sample is probing a different M_{1500} range. An illustration of the different selection functions comes from a comparison between our sample and of Ouchi et al. (2005), who presented 16 spectra of narrow-band selected $z = 5.7$ LAE candidates that overlap with our smaller UKIDSS UDS region (see figure 2 of Bowler et al., 2014). The objects are targeted because they are the brightest narrow-band emitters and lie in two clusters of objects, however only 4 of these 16 objects are bright enough in the continuum to be selected in our initial catalogues (e.g. $z' < 26.0$). None of these 4 objects are present in the final UDS sample, with two objects being excluded based on optical detections; one has a close companion contaminating the aperture magnitude and the other is only marginally ($\Delta m = 0.01$) above the local 2σ depth in the B-band. Another object, with $z_{\rm spec} = 5.624$, was selected as a high-redshift object in our analysis, however was excluded from the final samples because of a best fitting $z_{\rm phot} = 5.39$. This galaxy is faint in the z'-band with $z' = 25.7$ aperture magnitude, and has a strong Lyα emission line with a total line flux

of $f = 2.5 \times 10^{-17}\mathrm{ergs}^{-1}\mathrm{cm}^{-2}$. The final object, with $z_{\mathrm{spec}} = 5.600$ was excluded as a high-redshift object by the SED fitting process (with $\chi^2 = 35.7$), and is instead a likely M-dwarf with $\chi_\star = 3.4$ for stellar type M7, illustrating the importance of having near-infrared photometry in the selection of $z \sim 5$–6 LBGs.

The majority of the narrow-band selection galaxies in the SXDS/UDS have been spectroscopically confirmed (Ouchi et al., 2010), however the spectra are not public. We do however, recover the extreme LAE Himiko in our sample with a best-fitting $z_{\mathrm{phot}} = 6.19$ compared to the spectroscopic redshift $z = 6.595$.

4.5.5 Rest-frame UV slope (β_{UV})

The rest-frame UV slope, β_{UV}, of each galaxy was measured by fitting a power law (parameterised as $F_\lambda \propto \lambda^{\beta_{\mathrm{UV}}}$) to the $YJHK$ photometry for each object. The z'-band was excluded from the fitting process as at $z \gtrsim 5.8$ the Lyman-break is moving through the filter and furthermore there could be contamination by Lyman-α emission. Our results for the sample of objects in the $5.7 < z < 6.3$ range are shown in Fig. 4.7, where the reduced redshift range was chosen to allow more direct comparison with the results of Willott et al. (2013). Using a subset of the 40 objects covered by sufficiently deep near-infrared data, Willott et al. (2013) was able to measure β_{UV} using an identical method, finding a mean value of $\beta_{\mathrm{UV}} = -1.38 \pm 0.2$, which is redder than that found for fainter galaxies which tend to exhibit $\beta_{\mathrm{UV}} \simeq -2.0$ (Dunlop et al., 2013; Rogers et al., 2013; Bouwens et al., 2013). We measured β_{UV} for the 7 objects from the Willott et al. (2013) that are present in our sample and highlight these objects as red points in Fig. 4.7. The deeper near-infrared imaging available in the UltraVISTA/COSMOS and UDS/SXDS fields utilised in this work make our determination of β_{UV} significantly more robust than that of Willott et al. (2013). Excluding the faintest object that has a poorly constrained β_{UV} value, we also find a mean $\beta_{\mathrm{UV}} = -1.4 \pm 0.2$ for the sub-set of the Willott et al. (2013) sample. Comparing our larger sample of galaxies to the colour-magnitude relation determined by Rogers et al. (2014) at $z = 5$, we find slightly bluer values with a mean $\beta_{\mathrm{UV}} = -1.8 \pm 0.1$ for the galaxies brighter than $M_{\mathrm{UV}} = -22.0$ (excluding the brightest objects which is discussed below).

The very brightest object in our sample lies within the UltraVISTA/COSMOS field and shows a particularly red slope ($\beta_{\mathrm{UV}} = -1.1 \pm 0.2$), in contrast to the bluer values ($\beta_{\mathrm{UV}} \simeq -2.0$) found for the very brightest $z \simeq 7$ galaxies (Bowler et al., 2014). Larger samples are clearly needed, however an increase in dust obscuration for the brightest objects in our sample is one theoretical process by which the number density at the

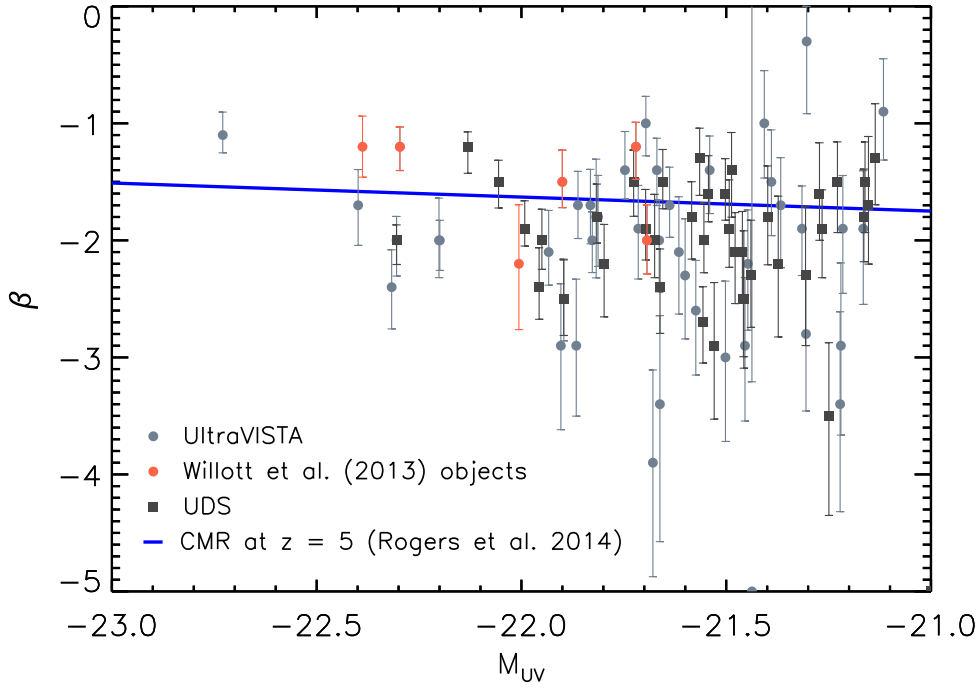

Figure 4.7 *The rest-frame UV slope (β) measured for our sample in the reduced redshift range $5.7 < z < 6.3$, plotted against absolute UV magnitude ($M_{\rm UV}$). The galaxies shown have a detection in the Y, J, H or K_s bands at greater than 5σ significance. Objects in the UltraVISTA/COSMOS field are shown as grey circles, with the galaxies previously detected by Willott et al. (2013) highlighted in red, and the objects in the UDS/SXDS field are shown as dark grey squares. The colour magnitude relation at $z \simeq 5$ determined by Rogers et al. (2014) is shown as the blue line.*

bright end of the rest-frame UV LF could be suppressed (e.g. see comparison with theoretical models in Section 4.8.3).

4.6 Determination of the LF

Using our sample of bright $z \simeq 6$ LBGs selected within the total $1.65\,\mathrm{deg}^2$ area of the combined UltraVISTA/COSMOS and UDS/SXDS fields, we are able to place the best constraints to date on the very bright end of the rest-frame UV luminosity function. The wide area of our survey allows us to probe the number densities of bright LBGs more securely than the CANDELS survey, which has a maximal area of $\sim 0.2\,\mathrm{deg}^2$ (the available filters vary between the 5 fields and hence not all fields are optimal for LBG selection), and the depth of the optical/near-infrared data in our study enables improvements over the previous ground-based studies of McLure et al. (2009) and Willott et al. (2013). The high signal-to-noise ratio of our galaxies ($> 7\sigma$ in the z'-

band) strongly reduces the occurrence of spurious detections, and the application of our careful SED fitting procedure can remove low-redshift interlopers and Galactic brown dwarfs. Our samples will, however, still suffer incompleteness from blending with foreground objects and from misidentification as dwarf stars or low-redshift galaxies at the faint end of our sample. In the following section we describe our injection and recovery simulations that quantify our completeness and we also consider the effect of gravitational lensing of our sample by galaxies close to the line-of-sight (lensing by clusters is considered in Section 4.7.2), which could potentially enhance our measured number of very bright objects.

4.6.1 Completeness simulations

We estimate the completeness of our sample following the methodology presented previously in McLure et al. (2009), McLure et al. (2013) and Bowler et al. (2014), by injecting synthetic $z = 5 - 7$ LBGs into the UltraVISTA/COSMOS and UDS/SXDS datasets, and attempting to recover them using an identical procedure as for the real $z = 6$ objects selected in this work. Photometric errors can scatter injected objects in magnitude and redshift, and therefore we inject galaxies from $z = 5$ to $z = 7$ and with magnitudes as faint as one magnitude below the z'-band cut we use for each field. Whereas the number of objects scattered out of a bin is symmetric, the number scattered into a given bin depends on the underlying luminosity function e.g. a Schechter function exponential decline will result in more objects up scattered into a given bin than a shallower function. Since we do not know a priori the form of the bright end of the LF, we calculate the incompleteness using a range of functional forms for the injected galaxy population and compare the results. In addition, the luminosity functions of LBGs are evolving with time, which must be taken into account and could potentially effect the derived parameters at each redshift (Muñoz & Loeb, 2008). In the Schechter function case, we assume the parameters from McLure et al. (2009) at $z = 5$ and McLure et al. (2013) at $z = 7$, with a simple linear evolution in all the Schechter parameters between these redshifts. We use an analogous approach for the DPL, using the fitted parameters from Bowler et al. (2014) with a fixed bright-end slope ($\beta = -4.4$). Using the evolving LFs, we then randomly populated an input $M_{\rm UV} - z$ plane, assigning each galaxy a rest-frame UV slope, $\beta_{\rm UV}$, drawn at random from a Gaussian distribution with mean $\beta_{\rm UV} = -1.8$ and standard deviation $\sigma = 0.3$, to mimic the slightly red $\beta_{\rm UV}$ and intrinsic scatter found for bright galaxies at $z = 5$ by Rogers et al. (2014). The objects were then selected using SExtractor and the high-redshift candidates extracted using the magnitude cuts and SED fitting analysis as described in Section 4.3.

We find that ~ 20 per cent of injected objects are not recovered due to blending by foreground images in the crowded optical bands. Of the objects that are recovered, we find a completeness of ~ 80 per cent, where objects here are lost either because they do not pass the optical drop-out criterion or because they were misclassified as a dwarf star or low-redshift galaxy contaminant.

4.6.2 The $1/V_{\rm max}$ estimator

We used the $1/V_{\rm max}$ estimator (Schmidt, 1968) to derive the LF, where the number density of objects in a given magnitude bin, $\phi(M)$, depends on the maximum volume ($V_{\rm max}$) each galaxy could have been selected in, modulated by a completeness correction factor (C) which accounts for galaxies missed in our selection procedure due to a combination of object blending and photometric scatter:

$$\phi(M) = \sum_{i=1}^{N} \frac{C(M_i, z_i)}{V_{{\rm max},i}} \tag{4.2}$$

Here the sum is over the N galaxies in the magnitude bin in question, where we chose magnitude bins of width $\Delta M = 0.25$–0.5 mag depending on the number of objects available. We present the derived rest-frame UV LF in Fig. 4.9, and in Table 4.2. The errors on the number densities are assumed to be Poissonian, however there is also an additional error in the derived number density resulting from the error in the completeness value. Hence, we include an estimate of this error by bootstrap resampling the galaxies within each bin. The Poisson error dominates in the bright bins, however the error in the completeness becomes comparable in the faintest bins.

4.6.3 The binned LF

We restrict the redshift range to $5.7 < z < 6.3$ to enable direct comparison to the work of McLure et al. (2009) and to ensure we are not influenced by any residual brown dwarf contamination or any incompleteness due to our dwarf star removal methodology. Our results are robust to the underlying function assumed in our completeness simulations, due to the high signal-to-noise of our galaxies which reduces the effect of up-scattering. We assume the DPL parameterisation an in Bowler et al. (2014) in the final LFs presented.

We determine the LF in the range $-22.625 < M_{\rm UV} < -21.125$, using 0.25 or 0.5

mag bins depending on the number of objects available. The faintest bin is defined by the point at which our observed absolute magnitude counts begin to drop, as shown in Fig. 4.6, indicating that our sample is becoming increasingly incomplete. The maximum volume available to our brightest objects is 7×10^6 Mpc^3 in the UltraVISTA DR2 and UDS fields combined, with an additional 1×10^6 Mpc^3 available for the brightest objects that could have been selected in the $0.29\,\mathrm{deg}^2$ of UltraVISTA DR1 imaging. Our LF results calculated following the described methodology are presented and discussed in Section 4.7.

4.6.4 Gravitational lensing by foreground galaxies

To determine whether the bright galaxies we find are only present in our sample as a result of 'moderate' gravitational lensing by foreground galaxies, we estimated the expected magnification due to galaxies along the line of sight to each $z \simeq 6$ object in our sample. Note that strong gravitational lensing by objects directly along the line of sight is ruled out by our deep optical non-detections. Following the approach presented in McLure et al. (2009) and Bowler et al. (2014), we estimated the magnification, μ, from foreground galaxies at a separation, θ, from our high-redshift galaxy as:

$$\mu = \frac{\theta}{\theta - \theta_{\mathrm{E}}} \tag{4.3}$$

using the singular isothermal sphere (SIS) approximation to describe the dark matter halo of each foreground galaxy. Here θ_{E} denotes the Einstein radius which depends on the velocity dispersion, σ_V, of the dark matter halo as:

$$\theta_{\mathrm{E}} = \frac{4\pi(\sigma_V/c)^2\, D_{LS}}{D_S} \tag{4.4}$$

in the SIS model, where D_{LS} denotes the luminosity distance from the lens object the the source and D_S denotes the luminosity distance to the source.

In each field we created a K-band (mass selected) catalogue using the MAG_AUTO from SExtractor as an estimate for the total magnitude of the foreground galaxies, which then allowed an estimate of the velocity dispersion of the dark matter halo from the i-band absolute magnitude using the Faber-Jackson relation from Bernardi et al. (2003). The photometric redshifts of the foreground K-band selected objects were calculated using the Le Phare code using 3-arcsec diameter circular aperture photometry following Ilbert et al. (2009, 2013). The Ilbert et al. (2009) SED template

set was used in the SED fitting process rather than the high and low-redshift model subsets utilised in our sample selection, to better represent the range of galaxies found at $z < 4$. We select galaxies based on an acceptable galaxy solution and a superior galaxy fit over that from stars (using the PICKLES library of stellar templates).

The resulting magnification distributions for our samples of objects in the UltraVISTA/COSMOS and UDS/SXDS fields are shown in Fig. 4.8, where we also plot the magnification against the z'-band magnitude of the galaxy. The magnification sums the contribution from all foreground galaxies closer than 10-arcsec to the high-redshift galaxy. We find that the majority of galaxies have some magnification of the order of ~ 0.1 mag, with several objects showing magnifications as large as ~ 0.6 mag. The inset plot of magnification against z'-band magnitude shows no evidence for the brightest objects having the largest magnification, which, if true, could influence the derived shape of the LF.

The magnification of the objects we derive could impact the measured LF, however we must determine if this magnification is unusual given that all astronomical imaging surveys show foreground objects close to the line of sight of the high-redshift galaxies observed. Hence, we calculated the expected magnification for random positions in the field. A minimum separation of 1-arcsec was applied when calculating the lensing at a given position, to exclude very high magnification of objects directly along the line of sight. The resulting distribution of magnification values, for a randomly drawn sample of 159 or 107 objects for the UltraVISTA/COSMOS and UDS/SXDS fields respectively, is shown in Fig. 4.8. The random distributions are very similar to those observed in our samples, indicating that modest gravitational lensing of our objects is not unusual for high-redshift sources in the field. We therefore do not correct the absolute magnitudes of our objects for this magnification when determining the LF.

We find a slight difference in the observed and predicted magnification distributions between the UltraVISTA/COSMOS and UDS/SXDS fields. The K-band data in the UDS/SXDS field is deeper than that in UltraVISTA/COSMOS ($m_{\rm AB} = 24.6$ as compared to $m_{\rm AB} = 24.2$), which would imply a higher surface density of sources in the UDS/SXDS field and hence a higher derived magnification. Inspection of the distribution of the number of sources within 10-arcsec radius of the sample of high-redshift galaxies shows that this is indeed the case, and the magnification distributions can be brought into closer agreement if we cut the UDS/SXDS catalogue at the same depth as the UltraVISTA/COSMOS data, which results in a shift in the peak of the magnification distribution faint-wards by ~ 0.05 mag. Any residual difference is likely due to the slightly different redshift distribution between the two fields, a result of large-

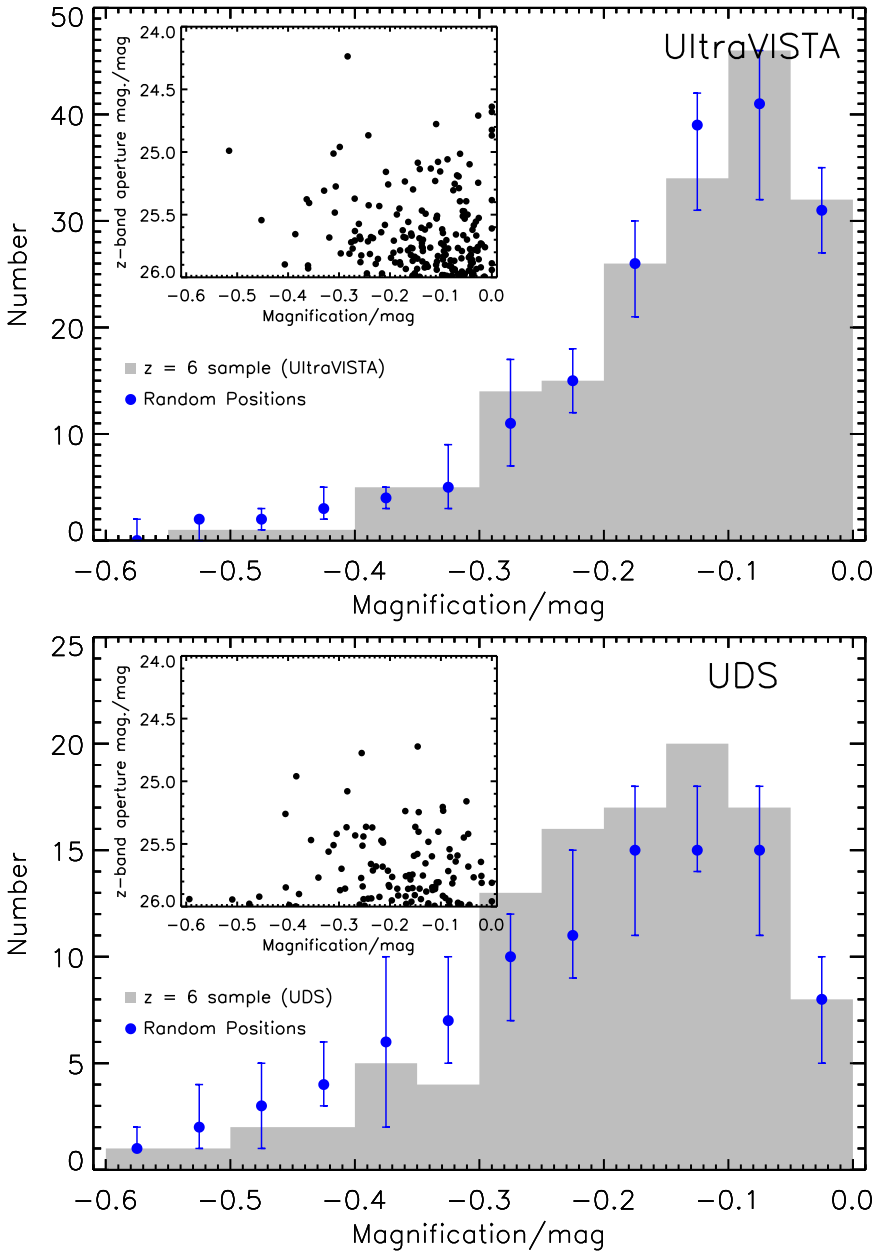

Figure 4.8 *The magnification distribution of the full $z \simeq 6$ sample due to gravitational lensing by the mass associated with foreground galaxies close to the line of sight. The observed magnification distribution is shown in grey, for the UltraVISTA/COSMOS and UDS/SXDS samples in the upper and lower plots respectively. The predicted magnification distribution for random positions in the field is shown as the blue points. The inset plot shows the gravitational magnification plotted against the z'-band magnitude for the sample.*

Table 4.2 *The binned rest-frame UV LF points at $z_{\rm med} \sim 5.9$ from this work, as shown in Fig. 4.9. The upper section of the table shows the results from the UltraVISTA/COSMOS and UDS/SXDS fields combined, with the middle and lower sections showing the results including only the UltraVISTA/COSMOS and UDS/SXDS fields respectively (e.g. the inset in Fig. 4.9). Columns 1 and 2 show the central $M_{\rm UV}$ of the bin and the width, where we calculate the M_{UV} by integrating the best-fitting SED through a top-hat filter centred on 1500Å with a width of 100Å. The weighted bin centre is shown in Column 3, given by the median completeness corrected M_{UV} of the galaxies in that bin. The number density is shown in Column 4 and the number of galaxies in each bin is shown in Column 5.*

$M_{\rm UV}$ /mag	$\Delta M_{\rm UV}$ /mag	$M_{\rm UV,w}$ /mag	ϕ /mag/Mpc^3	#
-22.625	0.500	-22.52	$1.16 \pm 0.67 \times 10^{-6}$	3
-22.125	0.500	-22.08	$5.98 \pm 1.64 \times 10^{-6}$	17
-21.750	0.250	-21.74	$1.90 \pm 0.41 \times 10^{-5}$	23
-21.500	0.250	-21.49	$3.92 \pm 0.70 \times 10^{-5}$	35
-21.250	0.250	-21.22	$9.14 \pm 1.39 \times 10^{-5}$	49
-22.625	0.500	-22.52	$2.20 \pm 1.27 \times 10^{-6}$	3
-22.125	0.500	-22.11	$7.60 \pm 2.92 \times 10^{-6}$	10
-21.750	0.250	-21.75	$2.92 \pm 0.76 \times 10^{-5}$	16
-21.500	0.250	-21.48	$4.76 \pm 1.17 \times 10^{-5}$	19
-21.250	0.250	-21.22	$1.34 \pm 0.25 \times 10^{-4}$	31
-22.125	0.500	-22.04	$4.54 \pm 1.74 \times 10^{-6}$	7
-21.625	0.500	-21.57	$2.15 \pm 0.47 \times 10^{-5}$	23
-21.250	0.250	-21.22	$5.54 \pm 1.45 \times 10^{-5}$	18

scale structure in the fields or the different relative depths in the multiwavelength images which can subtly bias the photometric redshifts. A thorough investigation of the true redshift distributions in the two fields is beyond the scope of this work, however we note that if we use the Ilbert et al. (2008) photometric redshifts in the UltraVISTA/COSMOS field we find a slightly different shape for the magnification distribution, which supports this hypothesis.

4.7 The luminosity function

In Fig. 4.9 and Table 4.2 we present our measured rest-frame UV LF at $z \simeq 6$. The binned LF points were derived from 177 luminous LBGs found within the combined UltraVISTA and UDS imaging, in the redshift range $5.7 < z_{\rm phot} < 6.3$.

The median redshift of the galaxies included in our LF determination is $z_{\rm med} = 5.9$. Comparing to previous determinations of the $z \simeq 6$ LF from a compilation of *HST* imaging from Bouwens et al. (2007, 2014), the larger area available from the combined UltraVISTA/COSMOS and UDS/SXDS fields allows us to more accurately probe lower space densities of objects (down to $\sim 1 \times 10^{-7}$ /mag/Mpc^3). Furthermore, the error bars on our brightest points show that we are able to probe the number densities of the brightest galaxies more accurately than the previous determinations using ground-based imaging surveys from Willott et al. (2013) and McLure et al. (2009).

The use of two independent fields in the present analysis also allows us to probe the cosmic variance and potential large-scale structure effects in the number counts of bright objects. Willott et al. (2013) pointed out an over-density of $z \simeq 6$ galaxies in the COSMOS/UltraVISTA (CFHTLS D2) field, an observation that we are able to confirm using $\times 10$ the number of LBGs. The inset plot in Fig. 4.9 shows our results at $z \simeq 6$ determined from the two fields separately. There is a clear excess of galaxies in the COSMOS/UltraVISTA survey as compared to the UDS/SXDS field, which is present over the full magnitude range probed. The discrepancy is most noticeable in our faintest bin at $M_{\rm UV} = -21.5$ where the number counts differ by a factor of $\gtrsim 2$. The discrepancy between the fields is also evident in the observed $M_{\rm UV}$ histograms in Fig. 4.6. We note that our faintest bin is our most uncertain, however if lensing by foreground structures (as discussed in Section 4.7.2) was a factor in the increased number counts in UltraVISTA/COSMOS then we would expect the largest difference at the faint end of our sample, due to the rapidly increasing number counts of objects faint ward of the limiting magnitude. Due to the cosmic variance in the faintest bin and the resulting uncertainty in the underlying LF here, we highlight this point in Fig 4.9 as an open circle and exclude it from the functional fitting in Section 4.8.1.

4.7.1 Comparison to previous work

Previous determinations of the $z \simeq 6$ rest-frame UV LF from McLure et al. (2009), Willott et al. (2013), Bouwens et al. (2007, 2014) and Finkelstein et al. (2014) are shown in Fig. 4.9, with the best-fitting Schechter functions from McLure et al. (2009) and Bouwens et al. (2014) also shown. The derived data points faint-ward of $M_{\rm UV} = -20.5$ show good agreement (with the exception of Finkelstein et al., 2014 in the range $-20.0 \gtrsim M_{\rm UV} \gtrsim -19.0$), although there is tension between the Schechter function fits derived by McLure et al. (2009) and Bouwens et al. (2014). At $M_{\rm UV} \lesssim -21$ however, large discrepancies between the determination of Bouwens et al. (2014) and

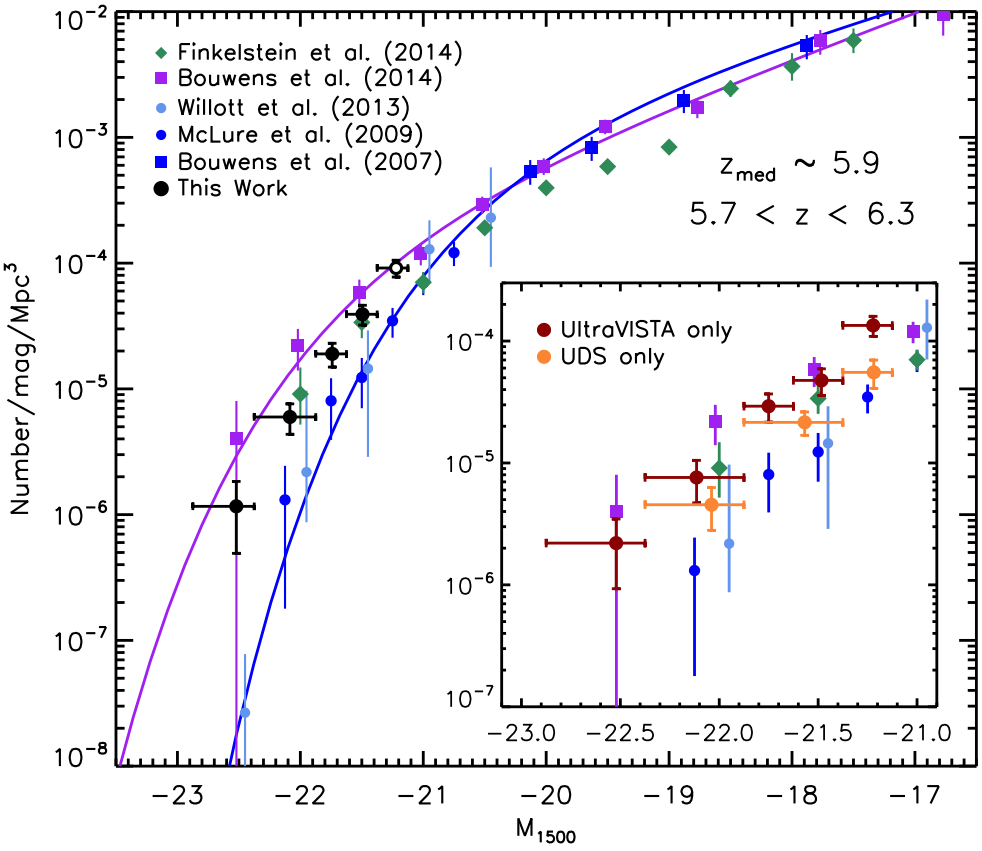

Figure 4.9 *The rest-frame UV LF at $z \simeq 6$, showing our results from the combined UltraVISTA/COSMOS and UDS/SXDS datasets as the black circles. The redshift range is restricted to $5.7 < z < 6.3$ as in McLure et al. (2009), which results in a median redshift of $z_{\rm med} \sim 5.9$. The inset plot shows our results from the UltraVISTA/COSMOS and UDS/SXDS fields separately as the red and orange points respectively. Here we have not corrected the absolute magnitudes for dust extinction. We have shifted the Willott et al. (2013) points by 0.05 mag faint-ward for clarity.*

the ground-based results of McLure et al. (2009) and Willott et al. (2013) become evident. Using our wide-area *and* deep dataset we find a $z \simeq 6$ LF that lies midway between the previous determinations.

McLure et al. (2009)

Using the DR1 of the UKIDSS UDS near-infared data in the UDS/SXDS field (Section 4.5.4), McLure et al. (2009) determined the $z \simeq 5$ and 6 LF following an analogous methodology to this work. Comparing our determination of the LF from the combined UltraVISTA/COSMOS and UDS/SXDS datasets to the results of McLure et al. (2009) however, we find a significantly higher number density of bright LBGs. The difference is further highlighted because the Schechter function fit of McLure et al. (2009) underestimates the brightest two binned points from their work. Considering our derived LF from the two fields separately (inset of Fig. 4.9) sheds light on the discrepancy, as the results from this work exclusively in the UDS/SXDS field are in-fact in fair agreement (within $\simeq 1\sigma$) with the data points of McLure et al. (2009). Overall there is still a lower number of objects found by McLure et al. (2009), which is likely due to the shallower near-infrared photometry available, resulting in a more conservative selection procedure being employed to ensure the removal of low-redshift interlopers or dwarf stars without secure near-infrared colours.

Willott et al. (2013)

The results of Willott et al. (2013), which were derived from 40 galaxies at $z \simeq 6$ found in the four CFHTLS fields (as described in Section 4.5.4), are in good agreement with those of McLure et al. (2009) and therefore fall below our determination. The four independent fields analysed should make the Willott et al. (2013) result more robust to the potentially large cosmic variance in the number counts of bright LBGs as found in this study. Furthermore, one of the CFHTLS fields analysed by Willott et al. (2013) overlaps with the UltraVISTA/COSMOS field, which we find to be over-dense compared to the UDS/SXDS, a result also corroborated by Willott et al. (2013) who found 15 galaxies in UltraVISTA/COSMOS as compared to ~ 8 in each of the three other fields. Willott et al. (2013) attributes the over density in UltraVISTA/COSMOS to be chance as a result of cosmic variance. We note that two of the four fields used only had shallow J-band data available (D3 and D4), and hence the number counts here are the most uncertain (8 and 9 objects respectively). Taking these uncertainties into

account, it remains possible that either UltraVISTA/COSMOS is over-dense *or* the true global number densities of these galaxies was not adequately probed by CFHTLS due to the inhomogenous datasets (e.g. the four CFHTLS fields should have had ~ 11.5 galaxies in each). Potential biases in the Willott et al. (2013) selection were highlighted in the rest-frame UV slope measurements for their sample discussed in Section 4.5.5.

The very brightest datapoint derived by Willott et al. (2013) at $M_{\rm UV} = -22.5$ is strongly in tension with our results. However, as discussed in Bowler et al. (2014), Willott et al. (2013) does not directly measure such a low space density, rather they infer $\phi(M)$ using a maximum likelihood approach. In Bowler et al. (2014) we estimated the space density of galaxies in the Willott et al. (2013) analysis at $M_{\rm UV} = -22.5$ using the brightest two objects presented (WHM5 and WHM29, neither of which is in the COSMOS/UltraVISTA field). The result ($\phi \simeq 2.0 \pm 1.4 \times 10^{-7}$ /mag/Mpc^3), is still in tension with our brightest point, but the larger sample of galaxies we find in the deeper z'-band and near-infrared imaging utilised here would suggest that our results are more reliable.

Bouwens et al. (2014)

Using a combination of the HUDF and two parallel fields, the Early Release Strip (ERS) and the CANDELS survey fields, Bouwens et al. (2014) selected a large sample of LBGs at $z \simeq 6$. The *HST* surveys used in the analysis covered a total of $0.2\,{\rm deg}^2$ on the sky. The LF determination derived from the full set of fields available is shown in Fig. 4.9 along with the best fitting Schechter function. The data points and the fit lie above our determination from the UltraVISTA/COSMOS and UDS/SXDS fields, and furthermore the simple evolving LF model we use assuming the Bouwens et al. (2014) LFs at $z = 5$ and $z = 6$ predicts approximately double the number of galaxies than we find in these fields (see Fig. 4.6). Due to the relatively small area of the fields used by Bouwens et al. (2014), the number of $z \simeq 6$ galaxies at $M_{\rm UV} \simeq -22.5$ is poorly constrained, however at $M_{\rm UV} = -22.0$ there is a clear tension with our results.

At the very bright end of the LF however, the small area probed by Bouwens et al. (2014) results in the samples being vulnerable to strong cosmic variance, as is evident from the distribution of the number counts of bright objects across the fields used (table 8 of Bouwens et al. 2014). Furthermore, the small number statistics result in a large Poisson error as demonstrated by the brightest point shown in Fig. 4.9. Hence, the results of Bouwens et al. (2014) cannot be relied upon in this magnitude regime ($M_{\rm UV} \lesssim -21$). The area, depth and homogeneity of the data-sets utilised in this work

enables a significantly improved determination of the bright-end of the LF at $z \simeq 6$ than can be provided by the combination of current and future *HST* surveys. Finally, for the Bouwens et al. (2014) results to be correct at the bright end of the LF we would expect to find roughly double the number of LBGs, which at $z' \sim 25.0$ would be detected at a significance of $> 20\sigma$.

Finkelstein et al. (2014)

From a combination of the UDF and parallels, the two GOODS fields and parallel imaging taken as part of the *Hubble* Frontier Fields program, Finkelstein et al. (2014) selected a sample of z =4–8 LBGs using a photometric redshift fitting methodology. In total, the area included was $\simeq 300\,\mathrm{arcmin}^2$, and the derived LF points are shown in Fig. 4.9. The results of Finkelstein et al. (2014) are in excellent agreement with our determination of the bright end of the LF, however they appear to diverge from the results of McLure et al. (2009) and Bouwens et al. (2014) at fainter magnitudes, and furthermore show a step at $M_{\mathrm{UV}} \simeq -19.0$. Although the Finkelstein et al. (2014) analysis used a sub-set of the larger area of imaging used by Bouwens et al. (2014), the results are in good agreement with the ground-based analysis presented here, and could indicate large over-densities in the additional fields incorporated by Bouwens et al. (2014) or contamination of the Bouwens et al. (2014) sample by brown dwarfs (see the discussion in Finkelstein et al. 2014).

4.7.2 The effect of large scale structure

As described in Section 4.5.3, we find a difference in the number counts of galaxies between the two field studied, with the UltraVISTA/COSMOS field containing $\simeq 1.8$ times the number of objects than the UDS/SXDS fields. Cosmic variance struggles to account for the difference and hence further investigation is warranted. The UltraVISTA/COSMOS field has been known to harbour an unusual richness of structure as measured by clustering analyses, particularly at $z \simeq 1$ (McCracken et al., 2007; Meneux et al., 2009; Skibba et al., 2014). We showed in Section 4.6.4 that the $z \simeq 6$ objects here show no evidence for 'excess' lensing by foreground galaxies as compared to a random position on the sky, and the UltraVISTA/COSMOS fields shows a similar predicted magnification distribution to the UDS/SXDS field. Such a calculation does not include gravitational lensing by galaxy clusters however, rather simply galaxy-galaxy lensing along the line of sight. A full analysis of the lensing cross-section for the

two fields is beyond the scope of this work, however a calculation of the magnification by the total matter in clusters can be made using the X-ray observations available in the fields. The UltraVISTA/COSMOS and UDS/SXDS fields have been observed to similar depths ($\simeq$ 2–3 $\times$ 10^{-15} $\mathrm{ergs\,cm^{-2}s^{-1}}$ at 0.5–2 keV) with *XMM-Newton*, and the X-ray bright clusters have been identified by Finoguenov et al. (2007) and Finoguenov et al. (2010) in each field respectively. From the X-ray luminosity we calculated the M_{200}[4] using the correlation presented by Rykoff et al. (2008). The magnification due to the total matter present in clusters was then calculated using the SIS approximation as described in Section 4.6.4, summing the contribution from the clusters at the position of each $z \simeq 6$ galaxy in our sample.

The cluster X-ray luminosity function reveals a higher density of X-ray luminous clusters in the UltraVISTA/COSMOS field compared to the UDS/SXDS (Finoguenov et al., 2010), and calculating the predicted magnification from the clusters using the simple method described shows that the difference in lensing magnification due to the increased number density of high mass clusters in UltraVISTA/COSMOS is of the order of ~ 0.05–0.1 mag. Although small, such a magnification could have a significant effect on the determination of the bright end of the LF due to the declining number counts, and could be the origin of the discrepancy we find close to the 5σ limit of our survey. Correcting our derived LF points by ~ 0.1 mag faint-ward would not impact on our conclusions described below, and would further strengthen the derived evolution in M^*.

Conversely, narrow-band studies of the UDS/SXDS field have revealed large voids in the distribution of $z = 5.7$ galaxies (Ouchi et al., 2005), with comoving sizes of the order 10–40 Mpc which corresponds to $\sim 4 - 17$ arcminutes on the sky (see figure 2 of Ouchi et al., 2005). Hence it remains possible that the LF derived from the UDS/SXDS field at $z \simeq 6$ is biased low as a result of these voids at $z = 5.7 \pm 0.1$.

The discovery of cosmic variance between degree-scale fields at $z \simeq 6$ in this work further highlights the necessity of using such large fields to robustly determine the number density of bright galaxies. A single CANDELS field, or even a collection, could be strongly influenced by this large-scale structure as a result of their small size. Given the potential structure, or lack of structure, in the COSMOS/UltraVISTA and UDS/SXDS fields discussed above, future work on additional fields will be required to shed light on the origin of the discrepancy between them.

[4]The mass enclosed within a sphere of radius R_{200}, which contains a density of $200\,\rho_{\mathrm{critical}}$ at that redshift.

Table 4.3 *The best-fitting parameters derived from fitting the observed $z \simeq 6$ LF. The results are shown for a Schechter function, double power law and Saunders function, which are displayed in Fig. 4.10. The errors are the one sigma errors on that parameter, marginalising over all other parameters.*

Function	ϕ^* /mag/Mpc^3	M^* /mag	α	β	σ
Schechter function	$4.6^{+2.7}_{-1.9} \times 10^{-4}$	$-20.84^{+0.20}_{-0.22}$	$-1.9^{+0.2}_{-0.2}$	–	–
Double power law	$1.9^{+1.4}_{-0.8} \times 10^{-4}$	$-21.17^{+0.27}_{-0.24}$	$-2.1^{+0.2}_{-0.2}$	$-5.0^{+0.5}_{-0.6}$	–
Saunders function	$3.6^{+9.4}_{-2.9} \times 10^{-4}$	$-20.79^{+1.09}_{-1.19}$	$-2.0^{+0.2}_{-0.2}$	–	$0.3^{+0.1}_{-0.1}$

4.8 Form and evolution of the UV LF

4.8.1 The functional form of the $z \simeq 6$ LF

The galaxy LF at high redshift has been commonly fitted with a Schechter function, with the resulting best-fitting parameters used to determine the dominant form of the evolution (Bouwens et al., 2012, 2014, 2007; McLure et al., 2013). A Schechter function has been shown to well describe the mass and luminosity functions at low redshift. At $z \simeq 7$ however, Bowler et al. (2014) showed that a double-power law provides a better description of the rest-frame UV LF, from measurements of the number of bright galaxies with $M_{UV} \lesssim -21.5$. A Schechter function in not used universally to fit luminosity functions. A broken power law or double power law has been shown to provide a better description of the LF of galaxies in groups (e.g. Tempel et al., 2014, 2009), the far-infrared galaxy luminosity functions (e.g. Soifer et al., 1987) and the LFs of quasars (e.g. McGreer et al., 2013). A shallower decline at the bright end of the LF than expected from a Schechter function has also been found in the NUV LF from the Wiggles survey (Jurek et al., 2013) and in the Hα LF (Gunawardhana et al., 2013).

There are no strong theoretical motivations for any one particular functional form of the LF, although any scatter in the mass-to-light ratio of galaxies will naturally lead to a shallower function when measuring the luminosity function (Salim & Lee, 2012). If the mass function is well described by a Schechter function, then one would expect any luminosity function measurement that directly traces the galaxy mass (e.g. the rest-frame optical) would also follow such a form (Bernhard et al., 2014). However, when the luminosity of the galaxies in question is measured from wavelength regimes that are dominated by recent star-formation and hence trace the SFR rather than the

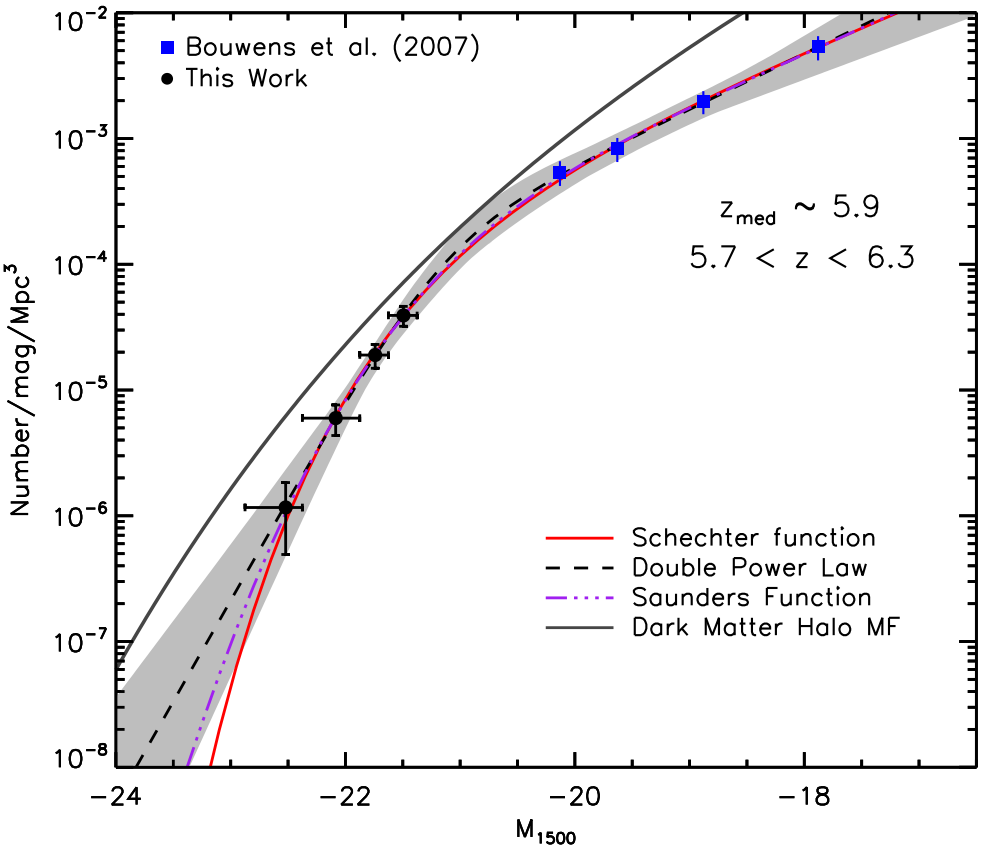

Figure 4.10 *The $z \simeq 6$ LF points from this work and Bouwens et al. (2007), with the best fitting Schechter (red solid line), double power law (black dashed line) and Saunders function (blue dot-dashed line) shown. The grey shaded region shows the one-sigma confidence interval on the double power law fit. The dark matter halo mass function, scaled as described in the text, is shown as the solid grey line.*

mass directly, then the shape of the observed LF will be convolved with the mass to SFR relation of the galaxies (Salim & Lee, 2012). The scatter in this relation tends to flatten the slope of the LF, resulting in a shallower function. Salim & Lee (2012) showed that a Saunders functional form, derived originally by Saunders et al., 1990 to model the $60\mu\mathrm{m}$ LF), where the bright-end of the LF declines as a log-normal, provides an improved fit to a LF that follows the SFR of the galaxies.

The bright end of the LF is the most sensitive to astrophysical effects such as dust obscuration and feedback mechanisms (we discuss theoretical predictions in Section 4.8.3), and crucially it is observations of the number density of rare and bright galaxies that place the tightest constraints on the position of the knee in the LF. The typical errors on the determination of the bright end of the LF at high redshift, and more severely the systematic difference between different studies, make a secure determination of the form of the LF challenging. We therefore investigate the functional form of the rest-frame UV LF using a sub-set of the observed LF points at $z \simeq 6$, using the determination from this work at $M_{\mathrm{UV}} \lesssim -21.5$ due to the superior depth and/or area of the combined UltraVISTA/COSMOS and UDS/SXDS fields utilised here when compared to previous studies. For the faint end of the LF we used the results derived by Bouwens et al. (2007) given the discrepancy we find with the Bouwens et al. (2014) results at $z \simeq 6$. We fit these determinations of the LF with a Schechter, DPL and Saunders functional form and show the resulting fits in Fig. 4.10. The double power law provides a slightly better fit to the data, even when corrected for the additional parameter available in the fitting. As can be seen from the best-fitting parameters shown in Table 4.3, the functional form assumed changes the derived characteristic magnitude M^*. Although there is clearly a change in slope of the LF at brighter magnitudes, the exact position of the 'break' is not clear from the current data and therefore depends strongly on the function assumed. The Saunders function also provides a good fit to the data, however the function poorly constrains the characteristic magnitude M^*. The uncertainty is a result of the parameter σ, which provides additional freedom in the shape of the bright end of the function. Hence we only present the results of fitting with the Schechter function and DPL in the next section.

In Bowler et al. (2014) we found good agreement between the observed rest-frame UV LF of galaxies at $z \simeq 7$ and the shape of the DMHMF when scaled using a constant mass to light ratio. Evolving the DMHMF according to the Reed et al. (2007) model, and using the same scaling as at $z \simeq 7$, we find the curve shown in Fig. 4.10. Again there is a good agreement between the simple LF predicted from the DMHMF, especially considering that the only evolution incorporated is due to dark matter halo build-up.

There is a clear deficit of galaxies at the faint end, as would be expected from models of supernova feedback which rapidly quench the star-formation in low-mass galaxies. In contrast to the results at $z \simeq 7$ from Bowler et al. (2014), the bright end of the rest-frame UV LF at $z \simeq 6$ shows a deficit of objects compared to the underlying halo distribution. Regardless of the exact scaling of the DMHMF into luminosity space, the comparison indicates that the bright-end slope of the LF is now steeper than the DMHMF at $z \simeq 6$. This interesting discovery, although tentative, could indicate that we are now observing the build-up of dust or the onset of AGN feedback in the brightest galaxies at $z \simeq 6$ as discussed further in Section 4.8.3.

4.8.2 Evolution of the LF from $z \simeq 5$–7

Comparing a subset of the observed rest-frame UV LF points from different studies in Fig. 4.11 clearly shows that there is strong evolution in the LF between $z \simeq 7$ and $z \simeq 5$. The constraints provided by this work at $z \simeq 6$ and the analogous work at $z \simeq 7$ presented in Bowler et al. (2014) allow the form and evolution of the bright end of the LF to be tightly constrained, and potential evolution of the functional form to be investigated. In addition to the studies described previously in the text, in the following section we also include the result at $z \simeq 5$ derived by van der Burg et al. (2010), who used the CFHTLS data to determine the $z = 3$–5 LF using a colour-colour selection. As can be seen in Fig. 4.11, the observed LFs from $z \simeq 5$ to $z \simeq 7$ show little evolution faint ward of $M_{\rm UV} \simeq -19.0$, however brighter than $M_{\rm UV} \simeq -20.0$ there is clear evolution in the number densities of galaxies, with LBGs at $z \simeq 7$ being an order of magnitude less numerous than $\simeq 5$ galaxies at the same luminosity. Determining the exact evolution of the LFs however is not straightforward, as although the general agreement with different studies is good, there are systematic differences between the results that are larger than the errors estimated by each individual study. Hence, the exact parameterisation of the LF derived from each analysis can disagree, for example at $z \simeq 5$ van der Burg et al. (2010) find a best-fitting characteristic magnitude $M^* = -20.93^{+0.10}_{-0.11}$ whereas the fit to the McLure et al. (2009) results give $M^* = -20.73 \pm 0.11$. We therefore only fit to a subset of the available rest-frame UV LF points from different studies as motivated below, however we display a large compilation of studies in Fig. 4.13 where the systematic errors are apparent.

To attempt to quantify the evolution of the bright end of the LF, we fit DPL and Schechter functions to the subset of derived rest-frame UV LF points from $z \simeq 5$–7 shown in Fig. 4.11. A simple χ^2 minimisation method was used, and the errors were

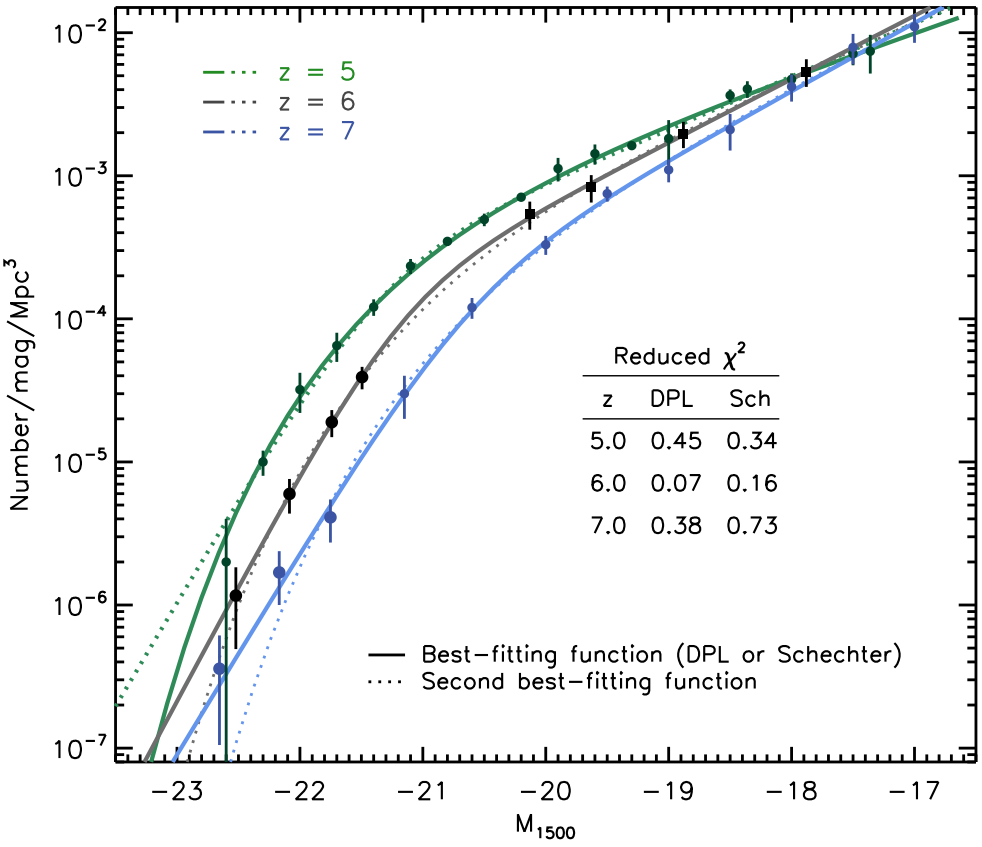

Figure 4.11 *The best-fitting DPL and Schechter function fits to a selection of observations of the rest-frame UV LF at $z = 5, 6$ and 7 (green, black and blue lines/points respectively). For each redshift, the best-fitting function is shown as the solid line and the second best fitting function is shown as a dotted line. The inset table shows the reduced χ^2 for each fit. At $z \simeq 5$ the fitted points are from van der Burg et al. (2010), Bouwens et al. (2014) and Finkelstein et al. (2014), and at $z \simeq 6$ the LF determination from this work is combined with the results from Bouwens et al. (2007). Finally, at $z \simeq 7$ we fit to the LF determined by Bowler et al. (2014) and McLure et al. (2013). The best fitting parameters are presented in Table 4.4.*

found as the value of the parameter which gives a $\Delta\chi^2 = 1.0$, minimised over all other parameters. We combine our results with those of Bouwens et al. (2007) at $z \simeq 6$, again excluding the Bouwens et al. (2014) points due to the uncertainties in the bright-end of the LF where the sample is sensitive to cosmic variance (see Section 4.5.4). At $z \simeq 5$ we choose to fit to the van der Burg et al. (2010) results at the bright-end, excluding the results of McLure et al. (2009) as they were based on a single field, and hence as we have found in this study at $z \simeq 6$, could be vulnerable to cosmic variance. The results of Bouwens et al. (2014) and Finkelstein et al. (2014), although excluded in the fitting process at $z \simeq 6$ and $z \simeq 7$, agree well at $z \simeq 5$ at faint magnitudes and hence we supplement the $z \simeq 5$ points from van der Burg et al. (2010) with their points faint-ward of $M_{\rm UV} = -19.0$. At $z \simeq 7$ we use the McLure et al. (2013) determination of the LF, which follows a similar methodology to this work. Bouwens et al. (2014) showed that the magnitudes of the brightest galaxies found by McLure et al. (2013) were underestimated by assuming a point-source correction when using small apertures, as these objects are marginally extended. We therefore boost the magnitudes of the points at $M_{\rm UV} = -21.0$ and $M_{\rm UV} = -20.5$ from the McLure et al. (2013) analysis by 0.15 and 0.1 mag respectively when fitting, to account for the underestimation of the magnitudes here. Uncertainties in the Bouwens et al. (2014) analysis at the bright-end of the $z \simeq 7$ LF (which we exclude from the fitting process) are evident in Fig. 4.13, where the implied number density of galaxies at $M_{\rm UV} = -21.86$ is comparable to that of $z \simeq 5$ galaxies at the same luminosity.

Fig. 4.11 shows the result of fitting a DPL and Schechter function to the observed LFs at $z = 5$–7, with the best-fitting function parameters presented in Table 4.4. The reduced χ^2 values for the fits are shown in Fig. 4.11, where it is evident that the current error bars available on the observed rest-frame UV LF result in an 'over-fitting' of the data with the multiple variable fit provided by the Schechter or DPL functions, resulting in $\chi^2_{\rm red} < 1$. Reassuringly, we recover the steep faint-end slopes found in previous studies (Bouwens et al., 2012; McLure et al., 2013; Schenker et al., 2013), showing that our measurement of α is not being strongly influenced by any tension in the fitting process. For the DPL fit, the recovered bright-end slope values are relatively uncertain at $z = 6$ and $z = 7$, however there is tentative evidence for a steepening of β from $z \simeq 7$ to $z \simeq 6$. At $z = 5$, the errors on β are much smaller, however as we have only fitted to the van der Burg et al. (2010) data the derived value and uncertainty does not include the systematic error between the van der Burg et al. (2010) and McLure et al. (2009) results (which can be seen in Fig. 4.13). Fitting the two studies separately we find $\beta = -4.8^{+0.4}_{-0.5}$ and $\beta = -4.4^{+0.3}_{-0.3}$ for the van der Burg et al. (2010) and McLure et al. (2009) respectively, and hence it remains possible that a further steepening of the bright-

end of the LF continues to $z = 5$ and this is not excluded by the data. Furthermore, at $z \simeq 5$, the Schechter function formally becomes the best-fitting function, demonstrating the steepening of the bright-end slope that is observed in the data.

Evolution in M^* from $z = 5$–7?

The evolution in the characteristic magnitude with redshift we measure by fitting DPL and Schechter functions to the data shown in Fig. 4.11 is shown in Fig. 4.12, along with other determinations from *HST* surveys (Finkelstein et al., 2014; Bouwens et al., 2014; Schmidt et al., 2014; McLure et al., 2013; Schenker et al., 2013; Oesch et al., 2012; Bouwens et al., 2007) and ground-based analyses (van der Burg et al., 2010; McLure et al., 2009). While the error bars at $z \simeq 6$ are large, at $z \simeq 5$ and $z \simeq 7$ the data we fit to more completely fills the available magnitude space and hence M^* is more securely defined. The functional form assumed changes the derived values, as can be seen from comparing the DPL and Schechter function results, with the DPL fit tending to produce brighter characteristic magnitudes, and hence the DPL results cannot be directly compared with the result from other studies that exclusively derive M^* using a Schechter function. Fig. 4.12 further illustrates the uncertainty in deriving the bright end of the LF from small fields such as those provided by the CANDELS survey, as the implied evolution from Bouwens et al. (2014) changes substantially depending on whether the full or a reduced set of the CANDELS fields are included. The effect of cosmic variance in degree-scale fields is also evident from the faint inferred M^* found in the potentially under-dense UDS/SXDS field by McLure et al. (2009).

In contrast to the work by Bouwens et al. (2014) and Finkelstein et al. (2014) we find an evolution in M^* between $z \simeq 5$ to $z \simeq 7$ of $\Delta M^* \simeq 0.4$–0.5 mag. Both Bouwens et al. (2014) and Finkelstein et al. (2014) found little evolution in the characteristic magnitude over the same redshift range, with both studies suggesting that $M^* \simeq -21.0$ provides a good fit until $z \simeq 7$. The results of fitting the $z \simeq 7$ rest-frame UV LF, including the results of this work, with both a DPL and a Schechter function show a best-fitting $M^* > -21.0$; a result which, when combined with the results found at $z \simeq 8$ by Bouwens et al. (2014), Schmidt et al. (2014), Schenker et al. (2013) and Oesch et al. (2012), suggest a smooth brightening of the characteristic magnitude from $z \simeq 8$ to $z \simeq 5$. Although the error bars on M^* are relatively large at $z \simeq 6$, they follow a smooth decline to the observed $M^* \simeq -20.5$ observed at $z \simeq 7$. Such an evolution, primarily in the characteristic magnitude of galaxies, is qualitatively to be expected from the hierarchical coalesce and growth of the underlying DMHMF. We caution, however,

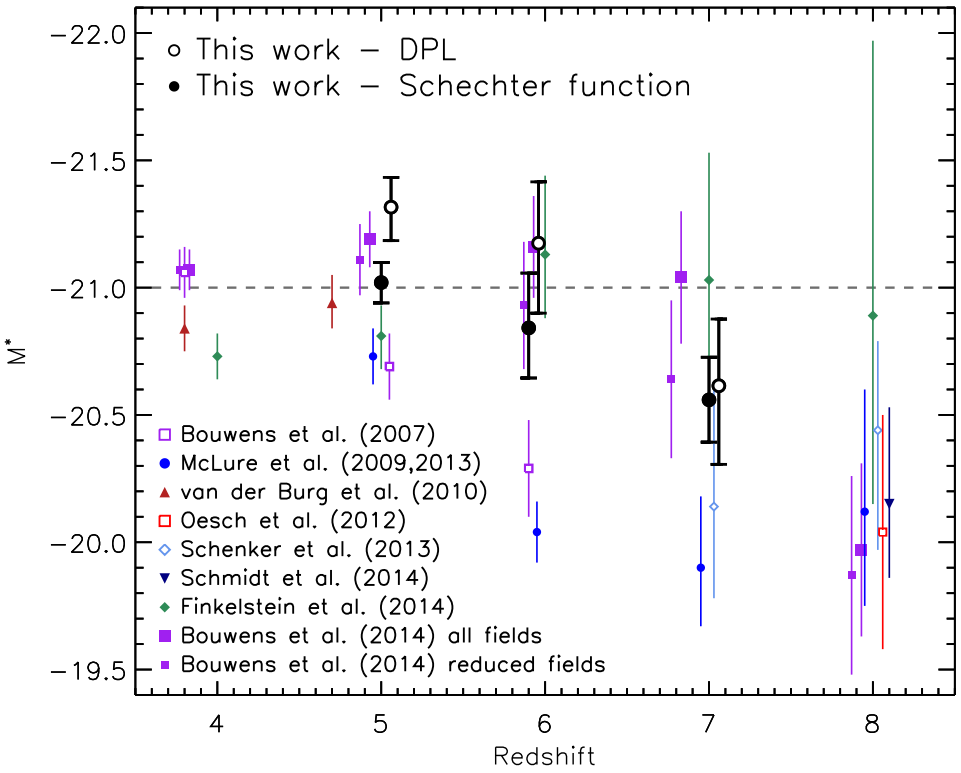

Figure 4.12 *The evolution in the characteristic magnitude derived from fitting a Schechter (circles) or DPL (open circles) to the $z \simeq 5$–7 data shown in Fig. 4.11. The results of primarily* HST *surveys from Finkelstein et al. (2014), Bouwens et al. (2014), Schmidt et al. (2014) McLure et al. (2013), Schenker et al. (2013) and Oesch et al. (2012) are shown, with additional results from wider-area ground-based imaging from van der Burg et al. (2010) and McLure et al. (2009). The constant characteristic magnitude of $M^* = -21.0$ proposed by Bouwens et al. (2014) and Finkelstein et al. (2014) is shown as a dashed line. For clarity, in some cases the plotted redshift of a point has been shifted by $\Delta z = 0.05 - 0.1$.*

Table 4.4 *The best-fitting DPL and Schechter function parameters derived from fitting the selection of observations of the rest-frame UV LF at $z \simeq 5$, 6 and 7 as described in the text and displayed in Fig. 4.11. The DPL results are shown in the upper part of the table, with the Schechter function fits below. Column 1 gives the approximate redshift, with the characteristic number density and absolute magnitude shown in Columns 2 and 3. The faint and bright-end slope (for the DPL) are displayed in Columns 4 and 5.*

z	ϕ^* /mag/Mpc^3	M^* /mag	α	β
5.0	$2.9^{+0.7}_{-0.5} \times 10^{-4}$	$-21.32^{+0.13}_{-0.12}$	$-1.9^{+0.1}_{-0.1}$	$-4.6^{+0.3}_{-0.3}$
6.0	$1.9^{+1.4}_{-0.8} \times 10^{-4}$	$-21.17^{+0.27}_{-0.24}$	$-2.1^{+0.2}_{-0.2}$	$-5.0^{+0.5}_{-0.6}$
7.0	$2.2^{+1.7}_{-0.9} \times 10^{-4}$	$-20.61^{+0.31}_{-0.26}$	$-2.2^{+0.1}_{-0.1}$	$-4.6^{+0.4}_{-0.5}$
5.0	$7.1^{+1.0}_{-0.9} \times 10^{-4}$	$-21.02^{+0.08}_{-0.08}$	$-1.7^{+0.1}_{-0.1}$	–
6.0	$4.6^{+2.7}_{-1.9} \times 10^{-4}$	$-20.84^{+0.20}_{-0.21}$	$-1.9^{+0.2}_{-0.1}$	–
7.0	$3.7^{+1.5}_{-1.1} \times 10^{-4}$	$-20.56^{+0.17}_{-0.17}$	$-2.1^{+0.1}_{-0.1}$	–

that condensing any evolution in the LF to a single parameter is very uncertain and may be missing subtleties in the form of the evolution as illustrated by the potential change in functional form from $z \simeq 7$ to $z \simeq 5$ hinted at in Fig. 4.11. The evolution we observe from $z = 5$–7 is occurring in only 400 Myr, and hence is apparently rapid evolution in the characteristic magnitude of LBGs in the first billion years of cosmic time. Improved constraints on the rest-frame UV LF around the apparent break magnitude from reconciling the current *HST* determinations, combined with future constraints on the form of the extreme bright-end of the LF from wider area imaging (e.g. VISTA VIDEO), will reduce the current errors on the determination of the form and evolution of the LF, and hence allow a more detailed comparison with the theoretical models described in the next Section.

4.8.3 Comparison to theory

In Fig. 4.13 we present a comparison of the latest observational data on the rest-frame UV galaxy LF at $z \simeq 5$, 6 and 7 (including the new results on the bright end presented here and in Bowler et al. 2014) with the predictions of several of the latest semi-analytic and hydrodynamical models of galaxy formation. This comparison is not completely fair, as some of the models have been (to some extent) tuned to explicitly match existing high-redshift data (generally at the faint end of UV LF, e.g. Dayal et al. 2014), while others have not been tuned at all (e.g. the First Billion

Years (FiBY) simulations; Paardekooper et al., 2013). Moreover some models include the effects of dust obscuration (e.g. the new Munich models of Henriques et al., 2014 and Clay et al. 2014, and the SPH simulations of Jaacks et al., 2012) while others have yet to implement any form of dust obscuration at these redshifts (e.g. the Illustris simulation predictions from Genel et al., 2014, and the semi-analytic results from Dayal et al., 2014). Instructively, the predictions of some models (e.g. Cai et al. 2014 and Paardekooper et al., 2013) were made available to us both with and without dust obscuration. Finally, it should be noted that several of the models do not cover large enough cosmological volumes for useful comparison with the very bright end as derived from the degree-scale ground-based surveys (e.g. Kimm & Cen 2013; Cen & Kimm 2014).

Despite these complications, some useful conclusions can still be drawn from this figure. First, it is clear that while most models do a reasonable job of reproducing the fainter end of the LF (with the sole exception of the revised Munich models; Clay et al. 2014), there is a general problem of over-predicting the bright end, even though the actual data produced by the work presented here indicate a shallower bright-end slope than would be inferred from a Schechter function fit to the fainter data. Second, with the possible exception of Dayal et al. (2014) (although this dust free model seems to start to struggle at $z \simeq 5$), those models which do provide a satisfactory fit to the LF over this large dynamic range include substantial dust obscuration. In particular, the model which performs 'best' in this comparison is the Cai et al. (2014) model after application of dust obscuration, but it can be seen that the impact of this dust obscuration is enormous, equivalent to either an average depression of UV luminosity by $A_{1500} \simeq 2\,\mathrm{mag}$ at a number density of $10^{-5}\,\mathrm{mag}^{-1}\mathrm{Mpc}^{-3}$, or a depression in observed number density by $\simeq 2$ orders of magnitude at $M_{1500} \simeq -22.5$.

Thus, while much attention has been focussed on the faint end of the high-redshift galaxy LF in recent years (quite reasonably, especially given the important implications for reionization; Robertson et al., 2013) it is clear that the full shape of the LF, extended to the brightest magnitudes through large-area ground-based surveys, has the potential to differentiate between alternative models of early galaxy formation and evolution. Moreover, while it currently remains unclear whether the shape of the bright end of the LF at $z \simeq 5-7$ is really driven by evolution in dust properties or by mass quenching (e.g. Peng et al., 2010), or early AGN feedback (or indeed by some other as yet poorly understood mechanism for regulating star formation), forthcoming observations have the potential to clarify and quite possibly resolve these issues. For example, pointed Atacama Large Millimetre Array (ALMA) follow-up of bright UV-selected galaxies

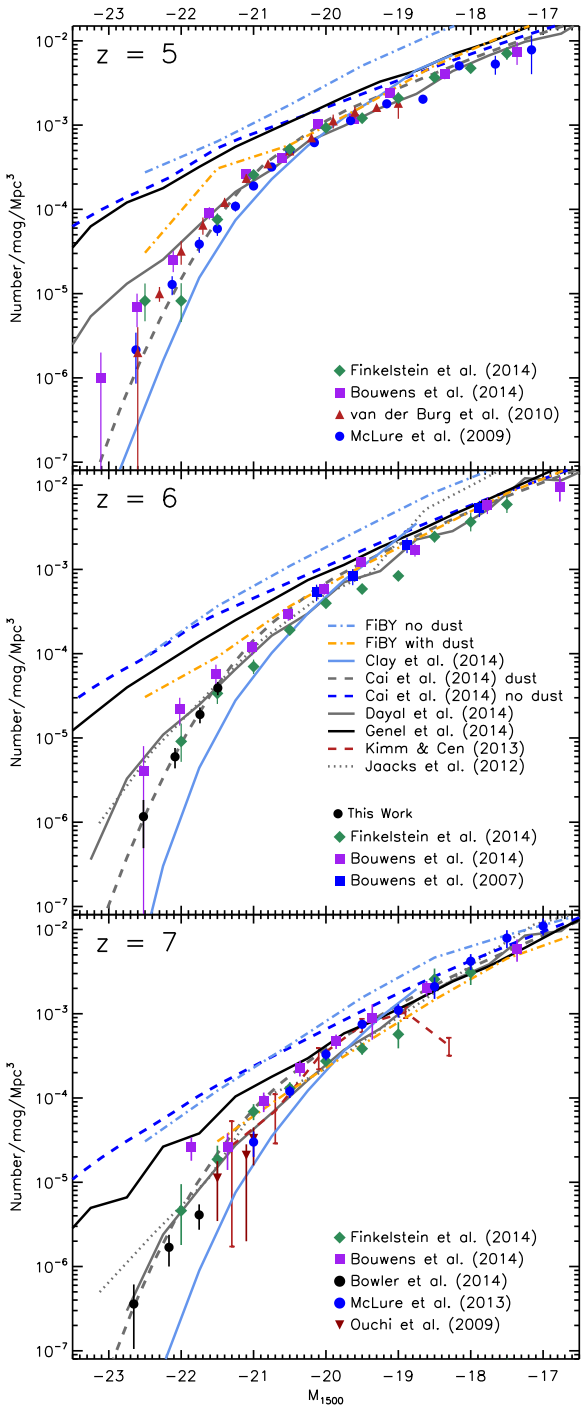

Figure 4.13 *A comparison of the latest observational data on the rest-frame UV galaxy LF at $z \simeq 5$, 6 and 7 (including the new results on the bright end presented here and in Bowler et al. 2014) with the predictions of several of the latest semi-analytic and hydrodynamical models of galaxy formation. The sources of the data points are indicated in each panel, with the various models references in the central ($z \simeq 6$) panel. The implications of this comparison are discussed in the text (Section 4.8.3) but in general it can be seen that most of the models struggle to reproduce the observations over the redshift range $z \simeq 5 - 7$ when faced with the large dynamic range now made possible by the combined ground-based and* HST *dataset.*

can address the prevalence of dust in such objects, while improved measurements of the stellar mass function at these early times (e.g. through improved deconfusion of deep *Spitzer* IRAC data, and ultimately with *JWST* observations) will provide another important reference point for comparison with theoretical predictions. At the same time, UltraVISTA DR3 (expected July 2015) should be deep enough to enable the work presented here at $z \simeq 6-7$ to be extended out to $z \simeq 8$ (with potentially useful constraints also at $z \simeq 9$), while wider-area surveys (e.g. with VISTA VIDEO at near-infrared wavelengths, and Subaru/Hyper-SuprimeCam at red optical wavelengths) culminating in the *Euclid* Deep Survey (Laureijs et al., 2011) should remove any remaining ambiguity over the shape of the bright end of the galaxy UV LF in the first billion years of cosmic history.

4.9 Conclusion

We have selected a sample of 266 star-forming galaxies at $z \simeq 6$ from the COSMOS/UltraVISTA and UDS/SXDS fields, which in total provide an area of $1.65\,\mathrm{deg}^2$ of deep multiwavelength imaging in the optical/near-infrared. The galaxies were selected using a full photometric redshift analysis, which allows the removal of low-redshift dusty galaxies and cool galactic brown dwarf stars. The main findings of our work are as follows.

- Using a simple thin disk galaxy model we find that the expected number of brown dwarf stars in each field greatly exceeds the number of LBGs at the bright-end ($m_{\mathrm{AB}} < 25$), however brown dwarfs can be well distinguished using fitting of stellar templates to the multiwavelength optical/near-infrared photometry.

- We measure the rest-frame UV slope of the galaxies in our sample, finding that the derived values follow the colour-magnitude relation found at $z \simeq 5$ by Rogers et al. (2014), and show a mean $\beta_{\mathrm{UV}} = -1.8 \pm 0.1$ at $M_{\mathrm{UV}} < -22.0$ in contrast to the redder slopes found by Willott et al. (2013).

- The number density of $z \simeq 6$ galaxies we find in the UltraVISTA/COSMOS fields exceeds that in the UDS/SXDS by a factor of ~ 1.8, a deviation that just exceeds that predicted from cosmic variance for fields of this size. We consider the effect of gravitational lensing of our objects by galaxies close to the line of sight, finding no evidence that the objects in our sample have preferential boosting over random positions in the field. X-ray observations of the two fields

indicate a higher number of bright clusters in the UltraVISTA/COSMOS field, and we find the UltraVISTA/COSMOS sample could be lensed by ~ 0.1 mag by the excess dark matter mass here. Narrow-band observations also find evidence that the UDS/SXDS contains large voids, which could further contribute to the cosmic variance observed between the fields.

- We calculate the rest-frame UV galaxy LF from the galaxies in our sample, using the restricted redshift range $5.7 < z < 6.3$ to compare directly with the work of McLure et al. (2009) and to ensure minimal contamination by brown dwarf stars. Our determination of the LF lies midway between previous determinations from *HST* surveys by Bouwens et al. (2014) and Finkelstein et al. (2014) and the ground-based analysis by McLure et al. (2009). The recent determination of the UV LF from Bouwens et al. (2014) over-predicts the expected number of LBGs in the fields we analyse by approximately a factor of two.

- By comparing the LF derived from the COSMOS/UltraVISTA and UDS/SXDS fields separately, we conclude that part of the discrepancy between the results of Bouwens et al. (2014) and McLure et al. (2009) at the bright end of the LF is a result of the UDS/SXDS (analysed by McLure et al., 2009) appearing under-dense at $z \simeq 6$. Our results show that cosmic variance on scales of $1\,\mathrm{deg}^2$ can be significant and therefore determining the bright-end of the LF from relatively small area datasets such as the 200 arcmin^2 CANDELS fields could be highly uncertain.

- We fit Schechter and DPL functions to the observed $z \simeq 6$ rest-frame UV LF, showing that the DPL is marginally preferred, although an exponential decline equally well describes the current data. The fits show that the bright-end slope of the LF at $z \simeq 6$ is likely steeper than that at $z \simeq 7$, suggesting the onset we may be observing the onset of feedback (e.g. from AGN) or the build-up of dust in the brightest LBGs.

- In contrast to Bouwens et al. (2014) and Finkelstein et al. (2014), we find evidence for a brightening of the characteristic magnitude, M^*, between $z \simeq 7$ and $z \simeq 5$ of $\simeq 0.4$–0.5 mag. Our results show that the evolution is well described as predominately luminosity evolution, where the star formation of the galaxies follows the hierarchical build-up of the underlying dark matter haloes.

- Finally, comparison of a collection of semi-analytical and hydrodynamical models to the observed rest-frame UV galaxy LF at $z \simeq 5$, 6 and 7 reveal that the models tend to over-predict the number density of bright galaxies and substantial

attenuation is required ($A_{1500} \simeq 1.5$–2.0) to bring the models into agreement with the data.

CHAPTER 5

Conclusions & Future Work

5.1 Conclusions

In this thesis, I have presented the results of a search for bright ($M_{\rm UV} \lesssim -21.0$) Lyman-break galaxies at $z = 6$–7 within two wide-area ground-based survey fields. An initial search was undertaken in the first data-release of the UltraVISTA survey, a 1.5 deg^2 imaging program in the near-infrared within the COSMOS field. The multiwavelength imaging available over the central degree square of the COSMOS field, from the CFHTLS, Subaru telescope and *Spitzer*/IRAC, allowed the secure selection of $z \simeq 7$ galaxies using an SED fitting analysis. I have shown the necessity of deep Y-band imaging for the secure selection of $z = 7$ galaxies, showing that the extremely bright candidates selected by Capak et al. (2011) found without Y-band imaging, are more consistent with low-redshift objects (as is the apparently highest redshift X-ray selected quasar found by Salvato et al. 2011). Both the Capak et al. (2011) and Salvato et al. (2011) samples were selected only using the $z - J$ colour as a proxy for the Lyman-break, which is insufficient to distinguish dwarf stars and low redshift red galaxies, particularly with poor near-infrared imaging depths. A subsequent search for $z \simeq 7$ LBGs was undertaken using the second data-release of the UltraVISTA imaging (DR2), which extends ~ 0.5–1 mag deeper over 70% of the previous utilised imaging. The UDS/SXDS field was also searched using the deep DR10 release of the J, H, K data from UKIDSS. Multiwavelength data from Subaru, particularly deep z'-band imaging, and Y-band imaging provided by the VISTA VIDEO survey, was essential in this field for clean selection of $z \simeq 7$ objects.

The first search for $z \simeq 7$ galaxies in the UltraVISTA DR1 imaging led to the selection of 10 credible objects, of which 4 were labelled robust to represent the difficulty in fitting stellar or low-redshift galaxy templates to the photometry. A stack of the four most robust objects showed no residual optical flux, which would be indicative of contamination of our sample by low-redshift interlopers, and showed a strong Lyman-break with $z - Y = 2.5 \pm 0.2$. Measuring the rest-frame UV slope of the stack showed

it to be similarly blue ($\beta = -2.0 \pm 0.2$) to fainter galaxies at the same redshift, and the galaxies had masses from SED fitting of around $5 \times 10^9\,\mathrm{M}_\odot$ and dust free SFRs of $25 - 50\,\mathrm{M}_\odot\mathrm{yr}^{-1}$. The number densities of galaxies found in the first year of data from UltraVISTA, from an approximation of the volume and absolute magnitude of the $z \simeq 7$ objects, was higher than expected from the extrapolation of the Schechter function fitted to fainter data. Although the derived number density of $M_{\mathrm{UV}} \sim -22.5$ galaxies was only a rough estimate, the results highlighted the lack of knowledge of the very bright-end of the LF, with the Schechter function extrapolations for $z = 6$–8 predicting little if no evolution brightwards of $M_{\mathrm{UV}} = -22.0$.

The second data-release of the UltraVISTA data, and the inclusion of the UDS field, resulted in a significantly improved dataset with which to search for $z \simeq 7$ galaxies, covering an area of $1.65\,\mathrm{deg}^2$ (split as $0.74\,\mathrm{deg}^2$ in the UDS, $0.69\,\mathrm{deg}^2$ in DR2 and $0.29\,\mathrm{deg}^2$ in DR1). Following a similar SED fitting analysis, including the removal of dwarf star candidates and likely low-redshift galaxies, resulted in a sample of 34 galaxies at $6.5 < z < 7.5$ from the two fields. The superior depth of the UltraVISTA DR2 Y-band imaging resulted in the majority of objects coming from these strips of deep imaging, with only 4 galaxies in the UDS field in total. As for the initial UltraVISTA DR1 sample, the possibility of Lyα emission in the SED was included in the fitting process and resulted in additional objects being included that could be at $z > 6.5$ *only with* a Lyα emission line. Of the ten galaxies presented from the initial UltraVISTA DR1 data, seven were present in the new sample with improved photometry, validating the selection methodology. The three remaining objects were either classified as slightly lower redshift ($6.0 < z < 6.5$) or one candidate was shown be a T-dwarf star, which was not unexpected from the original stellar fit to the DR1 photometry.

Instead of resorting to stacking the galaxies to obtain robust properties, the deeper near-infrared photometry from the UltraVISTA DR2 and UDS allowed measurements of the masses and rest-frame UV slopes on individual galaxies. The brightest galaxies showed masses of $M_* \sim 10^{10}\,\mathrm{M}_\odot$, making them some of the most massive known high-redshift galaxies, and the sSFRs of the brightest objects were found to be low (sSFR $< 2\,\mathrm{Gyr}^{-1}$) as compared to fainter objects at the same redshift. No evidence was found for redder rest-frame UV slopes, with a median $\beta = -2.0$ and the two brightest objects also showing similarly blue values. An analysis of the 3.6μm - 4.5μm colour of the sample, where the IRAC imaging was unconfused, showed tentative evidence for a strong contribution from nebular emission lines although the errors are large. Comparing the measured FWHM of the $z \simeq 7$ sample with those from recovered

point sources and Sersic profiles with different half-light radii, showed that some of the brightest objects are clearly resolved even in the ground-based imaging available. In-fact, two thirds of the sample showed evidence for a half-light radius larger than 1.5 kpc, which is the expected size from extrapolating the size-luminosity relation observed at fainter magnitudes. A detailed analysis of four members of the sample that had high-resolution imaging from *HST*/WFC3, taken as part of the CANDELS COSMOS program, revealed that the objects, although indistinguishable from a point-source in the ground-based data, are clearly resolved in the *HST* imaging and show extended wings in the surface brightness profile. A 0.4 mag offset was found between the derived total magnitude between the ground and space-based data, resulting from the use of small apertures on the *HST* imaging. This results in a larger fraction of the extended flux profile being lost as compared to aperture photometry performed on the seeing dominated ground-based imaging.

From the wider area provided by the addition of the UDS field combined with the deeper UltraVISTA DR2 strips, it was then possible to calculate the bright-end of the rest-frame UV LF at $z = 7$. Injection and recovery simulations were performed, to account for scattering of galaxies in and out of each magnitude bin and further to correct for true high-redshift objects lost as interlopers in the selection process (including optical cuts and SED fitting steps). The resulting volume of the survey was $\sim 1 \times 10^7\,\mathrm{Mpc}^3$, with galaxies of absolute UV magnitudes in the range $-22.7 < M_{\mathrm{UV}} < -21.2$. The results derived from the $1/V_{\mathrm{max}}$ LF estimator showed a clear excess of galaxies at the bright end of the rest-frame UV LF at $z = 7$, over that predicted by the extrapolated Schechter function fit to fainter data. An estimate of the magnification of the high-redshift galaxies by foreground galaxies close to the line of sight could not account for the excess of objects. Neither could contamination by $z = 7$ quasars, a result supported by a non-detection of any of the sample individually in the X-ray or radio, or in a radio stack. The derived UV LF from the UltraVISTA and UDS fields, although found to deviate from the Schechter function extrapolations, is not in conflict with the data at fainter magnitudes, and instead the observed UV LF can be well described by a double power law. By fitting DPL functions to the LF results at $z = 5$ and 6, there appeared to be little evidence for a Schechter function decline at the bright end from $z = 5$–7 given the data, and the DPL fits also well produce the steep faint-end slope and the evolution in the characteristic magnitude as found by other works. The power-law shape of the observed UV LF at $z \simeq 7$, as revealed by the results at the bright end presented in this thesis, matches well the shape of the underlying dark matter halo mass function when scaled by a realistic mass-to-light ratio. Such a power law shape, and the lack of a deficit from the scaled HMF, is consistent with a picture where the processes required

to quench SF in the brightest objects (e.g. AGN feedback) or obscuration by dust, has yet to come into effect by $z \simeq 7$.

In the final chapter of this thesis, I turned my attention towards $z \simeq 6$, utilising an identical dataset to the final $z \simeq 7$ work to place the strongest constraints to date on the bright-end of the rest-frame UV LF only $\simeq 200\,\mathrm{Myr}$ later. From the combined UltraVISTA DR2 and UDS data, I selected a sample of 266 LBGs in the redshift range $5.5 < z < 6.5$ using a photometric redshift fitting methodology as for the $z \simeq 7$ work. The issue of contamination of the sample by brown dwarfs was investigated quantitatively through injection and recovery simulations of standard brown dwarf SEDs, showing that contamination of the $z \simeq 6$ LBG sample by dwarf stars is expected to be $< 3\%$ without any measures to exclude them. The simulations showed that the expected contamination can be reduced to < 1 object by applying a $\chi^2_\star$ condition, which removes objects that have good fits to stellar spectra, and further restricting the redshift range to $5.7 < z < 6.3$. The final sample of objects showed rest-frame UV slopes that follow the $z = 5$ colour-magnitude relation derived by Rogers et al. (2014), and showed bluer slopes than the sample of $z \simeq 6$ galaxies found by Willott et al. (2013). The inferred number density of LBGs derived from the UltraVISTA DR2 and UDS fields were found to differ by a factor of $\simeq 1.4$, which can (just) be accounted for by to cosmic variance between degree-scale fields. The resulting rest-frame UV LF derived from the sample lies mid-way between previous determinations from Bouwens et al. (2014) and McLure et al. (2009), where the results from the UDS field are in fair agreement with the results from McLure et al. (2009) which were also derived from data within the UDS. The discrepancy between the results from the UltraVISTA and UDS fields could potentially be due to the UDS containing large voids as uncovered by Ouchi et al. (2005), and/or the UltraVISTA/COSMOS field being the site of large foreground structures that could impact the derived LF through gravitational lensing.

The determination of the rest-frame UV LF from the combined UltraVISTA DR2 and UDS fields provides the best constraints on the bright-end of the LF at $z \simeq 6$, where the two fields and superior depth data provide an advantage over ground-based works from McLure et al. (2009) and Willott et al. (2013), and the wide area in particular provides a more robust determination to that derived from $< 0.2\,\mathrm{deg}^2$ *HST* data (e.g. from CANDELS, UDF etc., Bouwens et al., 2014). The results, when combined with fainter data from *HST*, show that both a Schechter function and a DPL can provide good fits to the data at $z \simeq 6$, with an observed steepening in the bright-end slope from $z \simeq 7$. Fitting Schechter and DPL functions to data from $z = 7$ to $z = 5$ shows a brightening in the characteristic magnitude of the rest-frame UV LF, from $M_{\mathrm{UV}} \simeq -21.0$ at $z = 5$

to $M_{\rm UV} \simeq -20.6 \pm 0.2$ at $z = 7$ when taking the Schechter function results. When compared with theoretical simulations of the evolving rest-frame UV LF, the results are consistent with the evolution of the underlying DMHMF building up the mass and hence luminosity of galaxies with time, and the change in steepness of the bright-end slope could indicate that quenching mechanisms (e.g. AGN feedback) or obscuration by dust is coming into effect between $z \simeq 7$ and $z \simeq 5$. Future, both deeper and wider area imaging will be necessary to further pin down the form and evolution of the rest-frame UV LF at high-redshift, and comparisons with theoretical models will shed light on the astrophysics at work in these early massive and highly star-forming galaxies.

5.2 Future Work

5.2.1 The bright end of the rest-frame UV LF

As has been seen from my final chapter, there remain uncertainties in the bright end of the rest-frame UV LF from $z = 5$–7, due to relatively small numbers of galaxies in the brightest bins and the underlying cosmic variance between fields. In 2015, the third data release of the UltraVISTA survey will provide deeper Y, J, H, K_s imaging over the 'deep strips' of the full UltraVISTA/COSMOS field. The imaging will be ~ 0.5 mag deeper than that currently available, and hence as demonstrated on the $z \simeq 7$ LF shown in Fig. 5.1, will allow the ground-based determinations to extend faint-wards towards estimates derived from *HST* data. In particular, there is recent controversy at $z \simeq 7$ (and at $z \simeq 6$ as discussed in Chapter 4), with an analysis of a collection of *HST* imaging from the CANDELS and UDF datasets by Bouwens et al. (2014) appearing to predict significantly more galaxies at $M_{\rm UV} < -21.5$ than found in this thesis. The UltraVISTA DR3 release will be ideal for resolving the controversy and reconciling the results from the cosmic variance dominated CANDELS dataset and the shallower but wider area ground-based work.

The VISTA VIDEO survey will cover an area of $12\,{\rm deg}^2$ in the Y, J, H and K_s bands to predicted depths of 24.6, 24.5, 24.0, 23.5 respectively (Jarvis et al., 2013, 2-arcsec diameter circular aperture depths) and hence provides a wider-area, but shallower, dataset to compliment the UltraVISTA and UDS imaging for the selection of high-redshift galaxies. The imaging is over three fields, the *XMM*-Large Scale Structure (LSS) field, the ELIAS-S1 field and the Extended *Chandra* Deep Field South (ECDFS). The XMM-LSS field contains the UDS on one of the three tiles (VIDEO-XMM1)

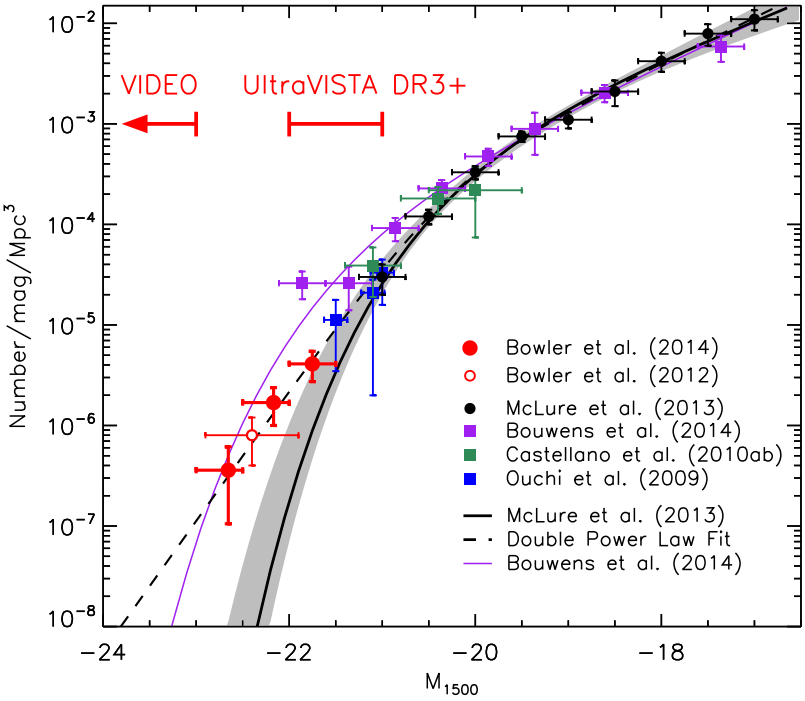

Figure 5.1 *The rest-frame UV LF at $z \simeq 7$ showing a compilation of previous works. The purple line shows the derived LF from Bouwens et al. (2014), which is most in conflict with the UltraVISTA + UDS results around $M_{\rm UV} \simeq -21.5$; the magnitude range to be probed by the UltraVISTA DR3 and future releases. At the very bright end, the VISTA VIDEO survey will be able to probe the number densities of extremely bright LBGs over $12\,{\rm deg}^2$ of imaging.*

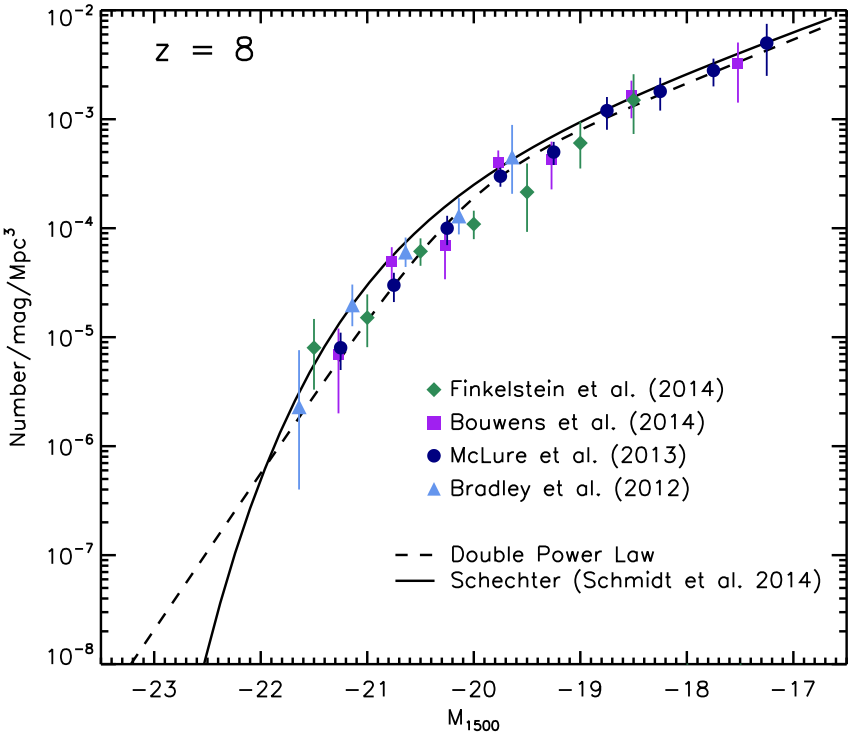

Figure 5.2 *A compilation of the observed $z \simeq 8$ rest-frame UV LF. The dashed line shows a double power law fit to the McLure et al. (2013) data, and the solid line shows the Schechter function fit derived by Schmidt et al. (2014).*

formed from the field of view of the VISTA VIRCAM, and upcoming deeper Y-band imaging here will be essential for exploiting the full depth of the UKIDSS UDS J, H, K data for the selection of $z \geq 7$ objects. The first field to be completed from the 5 year VIDEO survey is another of the three tiles from the XMM-LSS field (VIDEO-XMM3), which overlaps with optical imaging from the CFHTLS (D1 field). Particularly at $z \simeq 6$, the VIDEO-XMM3/CFHTLS D1 field will be ideal for investigating which of the UltraVISTA/COSMOS and UDS/SXDS fields are discrepant from the underlying LF, via an over- or under-density as discussed in Chapter 4. The VISTA VIDEO data probes a magnitude range where the galaxy number counts are falling while the quasar number counts are expected to be rising. Hence, detecting extremely rare and bright galaxy candidates from the wide area imaging, coupled with potential spectroscopic follow-up programs, could directly investigate the AGN–galaxy connection at high redshift.

At $z \simeq 8$, the best constraints to-date on the bright-end of the LF have come from the BoRG pure parallel and the CANDELS survey, as shown in Fig. 5.2. Constraints on the form of the LF are weak due to the restricted dynamic range of the observations, however the UltraVISTA DR3 and future releases will be able to probe significantly brighter ($M_{\rm UV} \lesssim -22.0$) and hence potentially distinguish between a shallower power

law decline and an exponential Schechter function at $z \simeq 8$.

5.2.2 The merger fraction, sizes and morphologies

High-resolution observations with *HST* have charted the growth of galaxies, showing that galaxies get progressively smaller to higher redshift, with the $z = 7$ - 8 galaxies in the UDF having half-light radii of $r_{1/2} < 0.5$ kpc (Ono et al., 2013; Oesch et al., 2010b). Furthermore, the existence of the size-luminosity/mass relation has now been confirmed up to $z \simeq 5$ (Law et al., 2012), suggesting an early onset to the key astrophysical processes thought to impact the relation, such as feedback and/or mergers. At the highest redshifts however, the existence of a size-luminosity relation is controversial. By using WFC3/IR imaging to determine the sizes and morphologies of $z = 6$ LBGs in the Subaru Deep Field, Jiang et al. (2013a) found little evidence for a size-luminosity relation over the magnitude range explored ($-22.0 < M_{\rm UV} < -19.0$). These results, however, seemingly contradict the results at $z \simeq 7$, where studies of the sizes of galaxies in the UDF (Ono et al., 2013; Oesch et al., 2010b) and CANDELS (Grazian et al., 2012) have shown evidence for a size-luminosity relation (see Fig. 5.3). Estimates of the sizes of the galaxies in the $z \simeq 7$ sample from the UltraVISTA and UDS fields, based on 0.8-arcsec FWHM ground-based imaging, are shown in Fig. 5.3. Frustratingly, these derived sizes demonstrate that the uncertainties on the current ground-based measurements are simply too large to constrain the size-luminosity relation. Furthermore, galaxies undergoing a merger are indistinguishable from intrinsically larger galaxies in the ground-based imaging (as shown in our simulated imaging in Fig. 5.3), a distinction that can only be made with high-resolution imaging with *HST*. CANDELS COSMOS imaging of three $z > 6.5$ galaxies in the sample tentatively indicates a flatter relation at $z \simeq 7$, however these galaxies are some of the faintest members of the sample with $M_{\rm UV} \sim -21.5$.

I have recently been awarded 17 orbits of *HST*/WFC3 time to obtain high-resolution follow-up imaging of the 17 brightest $z \simeq 7$ galaxies from the UltraVISTA and UDS sample. The Cycle 22 observations, scheduled for the coming year, will be taken in the J_{140} filter to ensure the highest possible S/N, and will provide a resolution of ~ 0.2 arcsec (FWHM) sufficient to determine the sizes of the galaxies and reveal any multiple component systems. The awarded *HST*/WFC3 imaging will extend the measurement of the size-luminosity relation through efficient targeted follow-up of robust LBGs with $-23.0 < M_{\rm UV} < -21.5$, which are bright enough (> 3 mag brighter than the Ono et al. (2013) sample) to provide robust size measurements from single-orbit *HST* imaging,

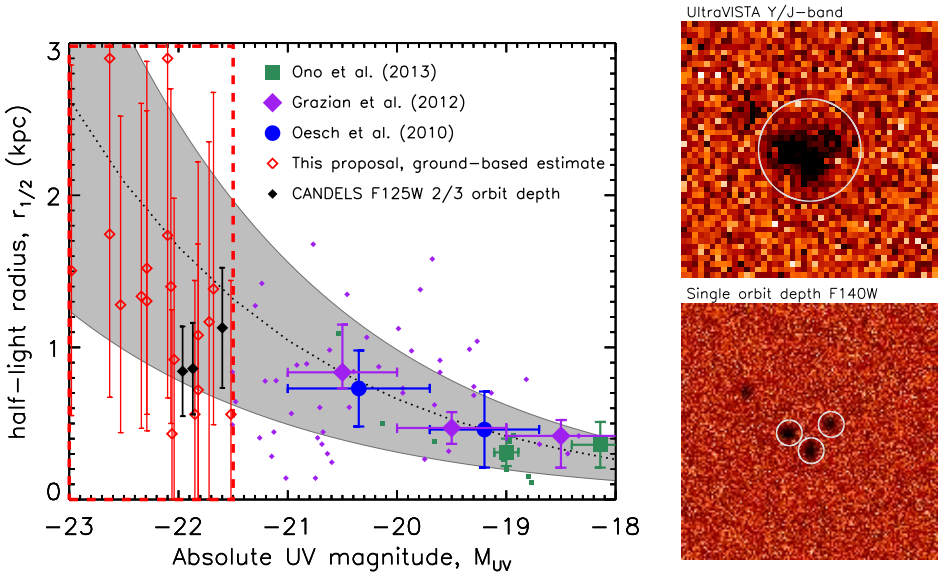

Figure 5.3 *The size-magnitude relation at $z = 7$, showing previous work from the UDF (Ono et al., 2013; Oesch et al., 2010b) and the wider area CANDELS fields (Grazian et al., 2012). Measurements from individual galaxies are shown as the small points, with the mode/median or stacked values shown as the larger points with errors. The best fitting size-luminosity relation from Grazian et al. (2012) is shown as the dotted line, and the grey shaded region shows the current level of uncertainty derived by Ono et al. (2013). Size estimates for the $z \simeq 7$ UltraVISTA + UDS sample at brighter magnitudes are shown as the red diamonds, derived from ground-based imaging. Black diamonds show the sizes derived for three of these objects that lie in the CANDELS COSMOS imaging, where sizes have been derived following the method of Oesch et al. (2010b). The images on the right-hand side show the simulated UltraVISTA and* HST *WFC3/IR images (including realistic noise) of the brightest galaxy at $z \simeq 7$ produced within the state-of-the-art 100 Mpc^3 simulation described by Dayal et al. (2013) and Maio et al. (2010).*

with no need for stacking.

As discussed in Section 1.5, there is evidence for an increasing merger rate with redshift, and tentative evidence that the trend continues to very high redshift, with the brightest galaxies at $z > 6$ being dominated by interacting systems (Ono et al., 2013; Jiang et al., 2013a; Willott et al., 2013; Oesch et al., 2010b). Due to the low surface density of extremely bright $z \simeq 7$ LBGs, few occur within the available deep high-resolution *HST* imaging surveys that are required for accurate size measurements. The exception is the LAE 'Himiko', which lies within the CANDELS UDS imaging (and also has targeted follow-up presented in Ouchi et al., 2013). Himiko is an extended source in the ground-based imaging used to detect it, with a FWHM $= 2.2$-arcsec, and the high-

resolution WFC3/IR reveals three distinct components each of $L \sim L^*$ in an apparent triple merger system. Rough estimates of the sizes of the $z \simeq 7$ galaxies presented in Chapter 3, based on the 0.8-arcsec full-width at half-maximum (FWHM) ground-based imaging, indicate that several of the brightest objects have inferred sizes comparable to that of Himiko, suggesting merger/multiple-component systems or intrinsically larger galaxies. The high-resolution *HST*/WFC3 data, which will provide a $S/N > 15$ for each galaxy, will provide the first measurement of the merger fraction at $z > 6$ in a uniquely bright sample of galaxies that cannot be investigated with current or future planned *HST* imaging surveys due to their rarity on the sky. The resulting measurement of the merger fraction will also be key for the secure determination of the form of the bright-end of the LF at $z \simeq 7$, as the measured decline of the bright-end slope will dramatically change if the brightest galaxies are in-fact collections of fainter objects.

5.2.3 Lyα emission and stellar populations

Spectroscopic follow-up campaigns of $4.5 < z < 7.5$ galaxies have shown, through careful simulations of the expected number of detected Lyα emission lines, a significant decline in the fraction of LBGs showing Lyα emission above $z = 6$ (e.g. Finkelstein et al., 2013; Ono et al., 2012; Stark et al., 2010, 2011). However these studies have been restricted to relatively faint galaxies with $M_{UV} > -21.75$ as a result of the small area HST surveys that are typically used to select the initial LBG sample. The fraction of bright $z \geq 5$ LBGs that show Lyman-α emission is unknown, and can only be determined with deep spectroscopic follow-up of samples of continuum selected objects which, because of their rarity on the sky, must be selected from degree-scale near-infrared survey fields. Such an approach has been successfully demonstrated at $z = 6$ by Curtis-Lake et al. (2012) who found a significantly higher fraction of objects showing Lyα than previous studies based on fainter galaxies (10 out of 14 objects), using observations of bright LBGs selected from the $0.7\,\mathrm{deg}^2$ UDS field using VLT/FORS2. The high spectroscopic confirmation rate ($\sim 70\%$) allowed detailed measurements of the ages and rest-frame UV properties of the sample (Curtis-Lake et al., 2013), and resulted in the discovery of the faintest known $z = 6$ quasar. Further evidence for a higher Lyα emitting fraction amongst the brightest $z > 5$ galaxies comes from studies comparing the rest-frame UV continuum luminosity functions of LBGs and LAEs. Jiang et al. (2013b) have shown that, while there is a drop in the number of continuum faint LAEs between $z = 5.7$ and $z = 6.6$, the bright-end of the rest-frame UV luminosity function of objects selected based on their Lyα emission closely resembles that of the LBGs. These results both indicate that unless there is another

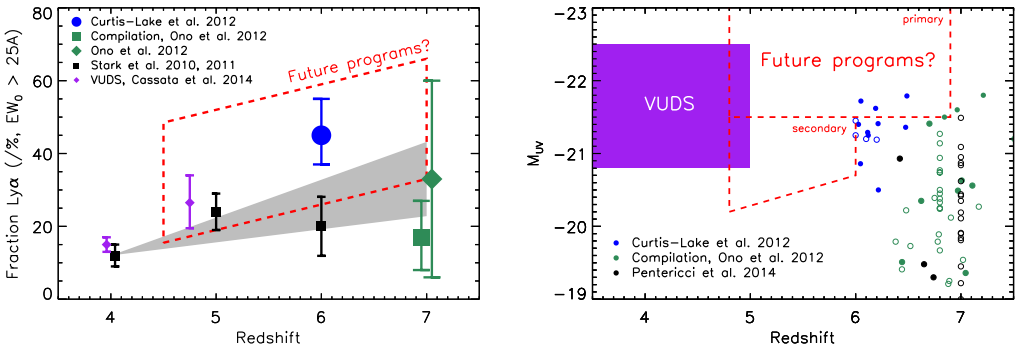

Figure 5.4 *The left hand plot shows the fraction of bright LBGs* ($-21.75 < M_{\rm UV} < -20.25$) *with observed Ly$\alpha$ of rest-frame EW exceeding* 25 Å*, as a function of redshift for several studies. The grey shaded region shows the evolution in the fraction with redshift, extrapolated to* $z = 7$*, as derived by Stark et al. (2011). At* $z = 7$ *the best constraints come from a compilation of results by Ono et al. (2012), shown by the green square. However, the samples compiled by Ono et al. were all selected using different methodology and the contamination fraction is uncertain. At* $z = 6$*, Curtis-Lake et al. (2012) found a high fraction of LAEs in their sample of very bright* ($M_{\rm UV} \sim -21.5$) *LBGs, selected analogously to our sample. The right-hand plot shows the redshift and absolute UV magnitude range of previous studies from VUDS (Cassata et al., 2014), Curtis-Lake et al. (2012), Pentericci et al. (2014) and a compilation of studies at* $z \simeq 7$ *from Ono et al. (2012). The points represent all objects targeted as part of the particular study (when this information is available), with the filled points showing the objects where Lyα was confirmed. In the case of the VUDS, the region highlighted represents where the survey has the ability to determine the fraction of LAEs, as the survey only contained* ~ 10 *objects at* $z > 5$*.*

factor governing the escape of Lyman-α photons from $z > 6$ galaxies, such as an increased neutral hydrogen fraction or dustier/more gas rich galaxies, we should expect a high spectroscopic completeness ($> 50\%$) even at $z \simeq 7$.

The current samples of spectroscopically targeted LBGs at high redshift, and the derived constraints on the fraction of galaxies showing Lyα emission is shown in Fig. 5.4. Spectroscopic follow-up of the brightest candidates presented in this thesis would probe a significantly brighter magnitude regime that previous studies, and the secure spectroscopic redshifts would allow detailed analysis of the physical properties of the galaxies, for example a measurement of the strength of nebular emission lines using the deep *Spitzer*/IRAC imaging from SPLASH. The detection of Lyα in a sample of extremely bright $z \simeq 6$–7 galaxies would make them ideal candidates for follow-up in the sub-mm with ALMA to attempt to detect the metallicity dependent CO ladder emission lines and [CII] 158μm. To date there have been a handful of bright $z > 6$

objects targeted with ALMA, with no detection of [CII], although deeper imaging is required to place strong limits on the inferred metallicity (Schaerer et al., 2014).

5.2.4 Future surveys and instruments

The form of the bright-end of the $z \simeq 5-8$ galaxy luminosity function has strong implications for the likely yield of upcoming wide-area optical/near-infrared surveys such as the 'deep' survey proposals for both *Euclid* and the Large Synoptic Survey Telescope (LSST). For example, the most comprehensive constraints on the very bright-end of the $z \simeq 8$ LF will come from the final data release of UltraVISTA, which has sufficient depth in the near-infrared bands to identify Y-dropout galaxies, hence providing the first strong prediction of the number densities of $z > 7$ galaxies detectable by *Euclid*. And whereas we would expect at most a few extremely bright $z \simeq 7$ galaxies within the VIDEO data, the Bowler et al. (2014) LF predicts hundreds of $M_{\rm UV} \lesssim -21.5$ galaxies in the planned 'deep' Euclid survey (~ 40 deg^2 to UltraVISTA depth). Finally, the sample of bright and star-forming galaxies at $z = 6-8$ from the UltraVISTA and UDS surveys will be ideal candidates for follow-up imaging and spectroscopy with the JWST and the next generation of extremely large telescopes.

Bibliography

Allard F., Hauschildt P. H., Alexander D. R., Tamanai A., Schweitzer A., 2001, ApJ, 556, 357

Anders P., Alvensleben U. F., 2003, A&A, 401, 1063

Arnouts S., Cristiani S., Moscardini L., Matarrese S., Lucchin F., Fontana A., Giallongo E., 1999, MNRAS, 310, 540

Ashby M. L. N. et al., 2013, ApJ, 769, 80

Becker G. D., Rauch M., Sargent W. L. W., 2007, ApJ, 662, 72

Beckwith S. V. W. et al., 2006, AJ, 132, 1729

Behroozi P. S., Wechsler R. H., Conroy C., 2013a, ApJ, 762, L31

Behroozi P. S., Wechsler R. H., Conroy C., 2013b, ApJ, 770, 57

Bernardi M. et al., 2003, AJ, 125, 1849

Bernhard E., Bethermin M., Sargent M., Buat V., Mullaney J. R., Pannella M., Heinis S., Daddi E., 2014, MNRAS, 442, 509

Bertin E., Arnouts S., 1996, A&AS, 117, 393

Bertin E., Mellier Y., Radovich M., Missonnier G., Didelon P., Morin B., 2002, ASP Conf. Proc., 281

Bian F. et al., 2013, ApJ, 774, 28

Bielby R. et al., 2012, A&A, 545, A23

Bouwens R. J., Illingworth G. D., Blakeslee J. P., Broadhurst T. J., Franx M., 2004, ApJ, 611, L1

Bouwens R. J., Illingworth G. D., Blakeslee J. P., Franx M., 2006, ApJ, 653, 53

Bouwens R. J., Illingworth G. D., Franx M., Ford H., 2007, ApJ, 670, 928

Bouwens R. J., Illingworth G. D., Franx M., Ford H., 2008, ApJ, 686, 230

Bouwens R. J. et al., 2011a, Nat, 469, 504

Bouwens R. J. et al., 2011b, ApJ, 737, 90

Bouwens R. J. et al., 2013, preprint (arXiv:1306.2950)

Bouwens R. J. et al., 2014, preprint (arXiv:1403.4295)

Bouwens R. J. et al., 2012, ApJ, 752, L5

Bouwens R. J. et al., 2010, ApJ, 708, L69

Bower R. G., Benson A. J., Crain R. A., 2012, MNRAS, 422, 2816

Bowler R. A. A. et al., 2015, preprint (arXiv:1411.2976)

Bowler R. A. A. et al., 2012, MNRAS, 426, 2772

Bowler R. A. A. et al., 2014, MNRAS, 440, 2810

Bradley L. D. et al., 2012, ApJ, 760, 108

Bromm V., 2013, Reports on progress in physics. Physical Society (Great Britain), 76, 112901

Bruzual G., Charlot S., 2003, MNRAS, 344, 1000

Bunker A. J. et al., 2010, MNRAS, 409, 855

Burningham B. et al., 2010, MNRAS, 406, 1885

Caballero J. A., Burgasser A. J., Klement R., 2008, A&A, 488, 181

Cai Z.-Y., Lapi A., Bressan A., De Zotti G., Negrello M., Danese L., 2014, ApJ, 785, 65

Calzetti D., Armus L., Bohlin R. C., Kinney A. L., Koornneef J., Storchi-Bergmann T., 2000, ApJ, 533, 682

Capak P. et al., 2007, ApJS, 172, 99

Capak P. et al., 2011, ApJ, 730, 68

Cappellari M. et al., 2012, Nat, 484, 485

Caruana J., Bunker A. J., Wilkins S. M., Stanway E. R., Lorenzoni S., Jarvis M. J., Ebert H., 2014, MNRAS, 443, 2831

Cassata P. et al., 2014, preprint (arXiv:1403.3693)

Castellano M. et al., 2010a, A&A, 511, A20

Castellano M. et al., 2010b, A&A, 524, A28

Cen R., Kimm T., 2014, ApJ, 782, 32

Chabrier G., 2003, PASP, 115, 763

Chen B. et al., 2001, ApJ, 553, 184

Coe D. et al., 2013, ApJ, 762, 32

Conroy C., 2013, ARA&A, 51, 393

Conselice C. J., 2014, ARA&A, 52, 291

Croom S. M. et al., 2009, MNRAS, 399, 1755

Curtis-Lake E. et al., 2014, preprint (arXiv:1409.1832)

Curtis-Lake E. et al., 2013, MNRAS, 429, 302

Curtis-Lake E. et al., 2012, MNRAS, 422, 1425

Daddi E., Cimatti A., Renzini A., Fontana A., Mignoli M., Pozzetti L., Tozzi P., Zamorani G., 2004, ApJ, 617, 746

Daddi E. et al., 2007, ApJ, 670, 156

Dalton G. B. et al., 2006, Proc. SPIE, 6269, 30

Davé R., Oppenheimer B. D., Finlator K., 2011, MNRAS, 415, 11

Dayal P., Dunlop J. S., Maio U., Ciardi B., 2013, MNRAS, 434, 1486

Dayal P., Ferrara A., Dunlop J. S., Pacucci F., 2014, MNRAS, 445, 2545

de Barros S., Schaerer D., Stark D. P., 2014, A&A, 563, A81

Dijkstra M., Wyithe S., Haiman Z., Mesinger A., Pentericci L., 2014, MNRAS, 440, 3309

Draine B. T., Hensley B., 2012, ApJ, 757, 103

Duncan K. et al., 2014, MNRAS, 444, 2960

Dunlop J. S., 2013, ASSL, 396, 223

Dunlop J. S., Cirasuolo M., McLure R. J., 2007, MNRAS, 376, 1054

Dunlop J. S., McLure R. J., Robertson B. E., Ellis R. S., Stark D. P., Cirasuolo M., de Ravel L., 2012, MNRAS, 420, 901

Dunlop J. S. et al., 2013, MNRAS, 432, 3520

Elbaz D. et al., 2007, A&A, 468, 33

Ellis R. S. et al., 2013, ApJ, 763, L2

Elvis M. et al., 2009, ApJS, 184, 158

Emerson J. P., Sutherland W. J., 2010, Proc. SPIE, 7733, 4

Erb D. K. et al., 2014, ApJ, 795, 33

Fan X. et al., 2006, AJ, 132, 117

Fan X. et al., 2001, AJ, 121, 54

Findlay J. R., Sutherland W. J., Venemans B. P., Reylé C., Robin A. C., Bonfield D. G., Bruce V. A., Jarvis M. J., 2012, MNRAS, 419, 3354

Finkelstein S. L. et al., 2013, Nat, 502, 524

Finkelstein S. L., Papovich C., Giavalisco M., Reddy N. A., Ferguson H. C., Koekemoer A. M., Dickinson M., 2010, ApJ, 719, 1250

Finkelstein S. L. et al., 2012, ApJ, 758, 93

Finkelstein S. L. et al., 2014, preprint (arXiv:1410.5439)

Finlator K., Oppenheimer B. D., Davé R., 2011, MNRAS, 410, 1703

Finoguenov A. et al., 2007, ApJS, 172, 182

Finoguenov A. et al., 2010, MNRAS, 403, 2063

Frei Z., Gunn J. E., 1994, AJ, 108, 1476

Frey S., Paragi Z., Gurvits L. I., Gabányi K. E., Cseh D., 2011, A&A, 531, L5

Fumagalli M. et al., 2012, ApJ, 757, L22

Furusawa H. et al., 2008, ApJS, 176, 1

Genel S. et al., 2014, MNRAS, 445, 175

Gonzaga S., 2012, The DrizzlePac Handbook

González V., Bouwens R., Illingworth G., Labbé I., Oesch P., Franx M., Magee D., 2014, ApJ, 781, 34

González V., Labbé I., Bouwens R. J., Illingworth G., Franx M., Kriek M., 2011, ApJ, 735, L34

González V., Labbé I., Bouwens R. J., Illingworth G., Franx M., Kriek M., Brammer G. B., 2010, ApJ, 713, 115

Grazian A. et al., 2012, A&A, 547, A51

Grogin N. A. et al., 2011, ApJS, 197, 35

Gunawardhana M. L. P. et al., 2013, MNRAS, 433, 2764

Gunn J. E., Peterson B. A., 1965, ApJ, 142, 1633

Hammer D. M., Hornschemeier A. E., Salim S., Smith R., Jenkins L., Mobasher B., Miller N., Ferguson H., 2012, ApJ, 745, 177

Henriques B., White S., Thomas P., Angulo R., Guo Q., Lemson G., Springel V., Overzier R., 2014, preprint (arXiv:1410.0365)

Herrera-Camus R. et al., 2014, preprint (arXiv:1409.7123)

Hogg D. W., Baldry I. K., Blanton M. R., Eisenstein D. J., 2002, eprint arXiv:astro-ph/0210394

Holwerda B. W. et al., 2014, ApJ, 788, 77

Hsieh B., Wang W., Yan H., Lin L., Karoji H., Lim J., Ho P. T. P., Tsai C., 2012, ApJ, 749, 88

Huang K.-H., Ferguson H. C., Ravindranath S., Su J., 2013, ApJ, 765, 68

Hutter A., Dayal P., Partl A. M., Muller V., 2014, MNRAS, 441, 2861

Ikeda H. et al., 2012, ApJ, 756, 160

Ilbert O. et al., 2006, A&A, 457, 841

Ilbert O. et al., 2009, ApJ, 690, 1236

Ilbert O. et al., 2013, A&A, 556, A55

Ilbert O. et al., 2008, ASP Conf. Ser., 399

Jaacks J., Choi J.-H., Nagamine K., Thompson R., Varghese S., 2012, MNRAS, 420, 1606

Jarvis M. J. et al., 2013, MNRAS, 428, 1281

Jiang L. et al., 2013a, ApJ, 773, 153

Jiang L. et al., 2013b, ApJ, 772, 99

Jurek R. J. et al., 2013, MNRAS, 434, 257

Kauffmann G. et al., 2003, MNRAS, 341, 54

Kimm T., Cen R., 2013, ApJ, 776, 35

Kirkpatrick J. D. et al., 2011, ApJS, 197, 19

Knapp G. R. et al., 2004, AJ, 127, 3553

Koekemoer A. M. et al., 2007, ApJS, 172, 196

Koekemoer A. M. et al., 2013, ApJS, 209, 16

Koekemoer A. M. et al., 2011, ApJS, 197, 36

Kroupa P., 2001, MNRAS, 322, 231

Laureijs R. et al., 2011, preprint (arXiv:1110.3193)

Law D. R., Steidel C. C., Shapley A. E., Nagy S. R., Reddy N. A., Erb D. K., 2012, ApJ, 745, 85

Lawrence A. et al., 2007, MNRAS, 379, 1599

Lehnert M. D., Bremer M., 2003, ApJ, 593, 630

Lilly S. J., Le Fèvre O., Hammer F., Crampton D., 1996, ApJ, 460

Loeb A., 2010, How Did the First Stars and Galaxies Form? Princeton University Press

Lorenzoni S., Bunker A. J., Wilkins S. M., Caruana J., Stanway E. R., Jarvis M. J., 2012, MNRAS, 429, 150

Lorenzoni S., Bunker A. J., Wilkins S. M., Stanway E. R., Jarvis M. J., Caruana J., 2011, MNRAS, 414, 1455

Madau P., 1995, ApJ, 441, 18

Madau P., Dickinson M., 2014, ARA&A, 52, 415

Madau P., Ferguson H., Dickinson M., Giavalisco M., Steidel C., Fruchter A., 1996, MNRAS, 283, 1388

Madau P., Pozzetti L., Dickinson M., 1998, ApJ, 498, 106

Maio U., Ciardi B., Dolag K., Tornatore L., Khochfar S., 2010, MNRAS, 407, 1003

Massey R., Stoughton C., Leauthaud A., Rhodes J., Koekemoer A., Ellis R., Shaghoulian E., 2010, MNRAS, 401, 371

Masters D. et al., 2012, ApJ, 752, L14

McCracken H. J. et al., 2010, ApJ, 708, 202

McCracken H. J. et al., 2013, The Messenger, 154, 29

McCracken H. J. et al., 2012, A&A, 544

McCracken H. J. et al., 2007, ApJS, 172, 314

McGreer I. D. et al., 2013, ApJ, 768, 105

McLure R. J., Cirasuolo M., Dunlop J. S., Foucaud S., Almaini O., 2009, MNRAS, 395, 2196

McLure R. J. et al., 2006, MNRAS, 372, 357

McLure R. J. et al., 2013, MNRAS, 432, 2696

McLure R. J., Dunlop J. S., Cirasuolo M., Koekemoer A. M., Sabbi E., Stark D. P., Targett T. A., Ellis R. S., 2010, MNRAS, 403, 960

McLure R. J. et al., 2011, MNRAS, 418, 2074

Meneux B. et al., 2009, A&A, 505, 463

Momjian E., Carilli C. L., Walter F., Venemans B., 2014, AJ, 147, 6

Montero-Dorta A. D., Prada F., 2009, MNRAS, 399, 1106

Moretti A. et al., 2014, A&A, 563, A46

Mortlock A. et al., 2013, MNRAS, 433, 1185

Mortlock D. J. et al., 2011, Nat, 474, 616

Muñoz J. A., Loeb A., 2008, MNRAS, 386, 2323

Muzzin A. et al., 2013, ApJ, 777, 18

Neistein E., Dekel A., 2008, MNRAS, 388, 1792

Noeske K. G. et al., 2007, ApJ, 660, L43

Oesch P. A. et al., 2010a, ApJ, 709, L21

Oesch P. A. et al., 2010b, ApJ, 709, L16

Oesch P. A. et al., 2012, ApJ, 759, 135

Oesch P. A. et al., 2013, ApJ, 773, 75

Oesch P. A. et al., 2014, ApJ, 786, 108

Oke J. B., 1974, ApJS, 27, 21

Oke J. B., Gunn J. E., 1983, ApJ, 266, 713

Ono Y. et al., 2013, ApJ, 777, 155

Ono Y. et al., 2012, ApJ, 744, 83

Ono Y., Shimasaku K., Dunlop J., Farrah D., McLure R., Okamura S., 2010, ApJ, 724, 1524

Osterbrock D. E., Ferland G. J., 2006, Astrophysics of gaseous nebulae and active galactic nuclei

Ota K. et al., 2014, preprint (arXiv:1405.5387)

Ouchi M. et al., 2013, ApJ, 778, 102

Ouchi M. et al., 2009a, ApJ, 706, 1136

Ouchi M. et al., 2009b, ApJ, 696, 1164

Ouchi M. et al., 2005, ApJ, 620, L1

Ouchi M. et al., 2008, ApJS, 176, 301

Ouchi M. et al., 2010, ApJ, 723, 869

Paardekooper J.-P., Khochfar S., Dalla C. V., 2013, MNRAS: Letters, 429, L94

Page M. J., Simpson C., Mortlock D. J., Warren S. J., Hewett P. C., Venemans B. P., McMahon R. G., 2014, MNRAS: Letters, 440, L91

Patel M., 2010, PhD thesis, Imperial College London

Patten B. M. et al., 2006, ApJ, 651, 502

Peng Y. et al., 2010, ApJ, 721, 193

Pentericci L. et al., 2014, ApJ, 793, 113

Pirzkal N. et al., 2009, ApJ, 695, 1591

Planck Collaboration et al., 2014, A&A, 571

Press W. H., Schechter P., 1974, ApJ, 187, 425

Press W. H., Teukolsky S. A., Vetterling W. T., Flannery B. P., 1992, Numerical recipes in FORTRAN. The art of scientific computing, Cambridge University Press

Reed D. S., Bower R., Frenk C. S., Jenkins A., Theuns T., 2007, MNRAS, 374, 2

Rees M. J., Ostriker J. P., 1977, MNRAS, 179, 541

Riechers D. A. et al., 2013, Nat, 496, 329

Robertson B. E., Ellis R. S., Dunlop J. S., McLure R. J., Stark D. P., 2010, Nat, 468, 49

Robertson B. E. et al., 2013, ApJ, 768, 71

Rogers A. B., McLure R. J., Dunlop J. S., 2013, MNRAS, 429, 2456

Rogers A. B. et al., 2014, MNRAS, 440, 3714

Ryan R. E. et al., 2011, ApJ, 739, 83

Rykoff E. S. et al., 2008, MNRAS: Letters, 387, L28

Salim S., Lee J. C., 2012, ApJ, 758, 134

Salpeter E. E., 1955, ApJ, 121, 161

Salvaterra R., Ferrara A., Dayal P., 2011, MNRAS, 414, 847

Salvato M. et al., 2011, ApJ, 742, 61

Sanders D. B. et al., 2007, ApJS, 172, 86

Sanders R. L. et al., 2014, preprint (arXiv:1408.2521)

Saunders W., Rowan-Robinson M., Lawrence A., Efstathiou G., Kaiser N., Ellis R. S., Frenk C. S., 1990, MNRAS, 242, 318

Schaerer D., 2002, A&A, 382, 28

Schaerer D., Boone F., Zamojski M., Staguhn J., Dessauges-Zavadsky M., Finkelstein S., Combes F., Richard J., 2014, preprint (arXiv:1407.5793)

Schechter P., 1976, ApJ, 203, 297

Schenker M. A., Ellis R. S., Konidaris N. P., Stark D. P., 2014, ApJ, 795, 20

Schenker M. A. et al., 2013, ApJ, 768, 196

Schenker M. A., Stark D. P., Ellis R. S., Robertson B. E., Dunlop J. S., McLure R. J., Kneib J.-P., Richard J., 2012, ApJ, 744, 179

Schinnerer E. et al., 2010, ApJS, 188, 384

Schlegel D. J., Finkbeiner D. P., Davis M., 1998, ApJ, 500, 525

Schmidt K. B. et al., 2014, ApJ, 786, 57

Schmidt M., 1968, ApJ, 151, 393

Scoville N. et al., 2007a, ApJS, 172, 38

Scoville N. et al., 2007b, ApJS, 172, 1

Shang Z. et al., 2011, ApJS, 196, 2

Shibuya T. et al., 2014, ApJ, 788, 74

Shimasaku K., Ouchi M., Furusawa H., Yoshida M., Kashikawa N., Okamura S., 2005, Pub. of the Ast. Soc. of Japan, 57, 447

Silk J., 1977, ApJ, 211, 638

Silk J., Mamon G. A., 2012, RAA, 12, 917

Skibba R. A. et al., 2014, ApJ, 784, 128

Smit R. et al., 2014, ApJ, 784, 58

Smith D. J. B. et al., 2012, MNRAS, 427, 703

Sobral D., Best P. N., Matsuda Y., Smail I., Geach J. E., Cirasuolo M., 2012, MNRAS, 420, 1926

Soifer B. T., Sanders D. B., Madore B. F., Neugebauer G., Danielson G. E., Elias J. H., Lonsdale C. J., Rice W. L., 1987, ApJ, 320, 238

Stanway E. R., Bremer M. N., Lehnert M. D., Eldridge J. J., 2008a, MNRAS, 384, 348

Stanway E. R., Bremer M. N., Squitieri V., Douglas L. S., Lehnert M. D., 2008b, MNRAS, 386, 370

Stanway E. R., Davies L. J. M., 2014, MNRAS, 439, 2474

Stark D. P., Ellis R. S., Bunker A., Bundy K., Targett T., Benson A., Lacy M., 2009, ApJ, 697, 1493

Stark D. P., Ellis R. S., Chiu K., Ouchi M., Bunker A., 2010, MNRAS, 408, 1628

Stark D. P., Ellis R. S., Ouchi M., 2011, ApJ, 728, L2

Stark D. P. et al., 2014a, preprint (arXiv:1408.3649)

Stark D. P. et al., 2014b, MNRAS, 445, 3200

Stark D. P., Schenker M. A., Ellis R., Robertson B., McLure R., Dunlop J., 2013, ApJ, 763, 129

Steidel C. C., Giavalisco M., Pettini M., Dickinson M., Adelberger K. L., 1996, ApJ, 462, L17

Su J. et al., 2011, ApJ, 738, 123

Talia M., Cimatti A., Mignoli M., Pozzetti L., Renzini A., Kurk J., Halliday C., 2014, A&A, 562, A113

Tasca L. A. M. et al., 2009, A&A, 503, 379

Tempel E., Einasto J., Einasto M., Saar E., Tago E., 2009, A&A, 495, 37

Tempel E. et al., 2014, A&A, 566, A1

Tilvi V. et al., 2014, ApJ, 794, 5

Tilvi V. et al., 2013, ApJ, 768, 56

Tojeiro R., Heavens A. F., Jimenez R., Panter B., 2007, MNRAS, 381, 1252

Trenti M. et al., 2011, ApJ, 727, L39

Trenti M. et al., 2012, ApJ, 746, 55

Trenti M., Stiavelli M., 2008, ApJ, 676, 767

Trenti M., Stiavelli M., Bouwens R. J., Oesch P., Shull J. M., Illingworth G. D., Bradley L. D., Carollo C. M., 2010, ApJ, 714, L202

Ueda Y. et al., 2008, ApJS, 179, 124

van der Burg R. F. J., Hildebrandt H., Erben T., 2010, A&A, 523, A74

Venemans B. P. et al., 2013, ApJ, 779, 24

Wilkins S. M., Bunker A. J., Ellis R. S., Stark D., Stanway E. R., Chiu K., Lorenzoni S., Jarvis M. J., 2010, MNRAS, 403, 938

Wilkins S. M. et al., 2013, MNRAS, 435, 2885

Willott C. J. et al., 2009, AJ, 137, 3541

Willott C. J. et al., 2013, AJ, 145, 4

Yan H. et al., 2012, ApJ, 761, 177

Yan H. et al., 2011, ApJ, 728, L22

Yan H.-J., Windhorst R. A., Hathi N. P., Cohen S. H., Ryan R. E., O'Connell R. W., McCarthy P. J., 2010, RAA, 10, 867

Zheng W. et al., 2012, Nat, 489, 406